UNIVERSITY OF CALIFORNIA
SANTA CRUZ

BIOGEOCHEMICAL CYCLING OF MARINE PARTICLES: INSIGHTS FROM THREE RECENT U.S. GEOTRACES CRUISES

A dissertation submitted in partial satisfaction
of the requirements for the degree of

DOCTOR OF PHILOSOPHY

in

OCEAN SCIENCES

by

Yang Xiang

June 2021

The Dissertation of Yang Xiang
is approved:

_____
Professor Phoebe J. Lam, chair

_____
Professor Carl Lamborg

_____
Professor Matthew D. McCarthy

_____
Colleen Hansel, Ph.D.

_____
Quentin Williams
Interim Vice Provost and Dean of Graduate Studies

TABLE OF CONTENTS

LIST OF TABLES

LIST OF FIGURES

ABSTRACT

Biogeochemical cycling of marine particles:

Insights from three recent U.S. GEOTRACES cruises

by

Yang Xiang

Marine particles are an essential component of the marine biological pump (BP). The BP transfers particulate organic matter (POM) produced by phytoplankton at the surface into the ocean interior and exerts a primary control on the atmospheric CO_2 level (Volk & Hoffert, 1985). This classic view of POM transport vertically has dominated our view of particle cycling in the ocean. It has long been known, however, that marine particles are complicated matrixes consisting of phases beyond POM (e.g., Lam et al., 2015), and the transport of particles can be both horizontal and vertical (e.g., Honjo et al., 2010). A limited number of particle concentration and composition measurements globally, however, remain one of the main barriers to understanding the biogeochemical cycling of marine particles and their associated elements and isotopes. This dissertation examines the sources, sinks, and transport of marine particles in recent U.S. GEOTRACES cruises in three ocean basins: the Western Arctic, the South Pacific, and the North Atlantic. Measurements of particle composition and metal chemical speciation are used to investigate the importance of lateral transport of particles and diel cycles of particulate manganese (Mn) in the Western Arctic Ocean, respectively.

Enhancements in Mn oxides in the halocline and high lithogenic particles in the deep ocean point to the significance of lateral transport throughout the water column, while the contrasting difference in particulate Mn average oxidation states during the day and at night suggests rapid redox variations of Mn in the surface Western Arctic Ocean. The Western Arctic Ocean is characterized by the lowest particle flux of the three cruises. Our data with higher spatial and depth resolution show that there are ballast minerals present in particles in the Western Arctic Ocean, unlike what was observed by Honjo et al. (2010) using a handful of ice-tethered sediment traps. The low export fluxes found in the Western Arctic Ocean result from this basin having the smallest particle sizes, lowest particle concentrations and most viscous water. Overall, this dissertation contributes to the growing body of literature on the distribution and biogeochemistry of marine particles in the global ocean.

References

Honjo, S., Krishfield, R. A., Eglinton, T. I., Manganini, S. J., Kemp, J. N., Doherty, K., et al. (2010). Biological pump processes in the cryopelagic and hemipelagic Arctic Ocean: Canada Basin and Chukchi Rise. *Progress in Oceanography*, *85*(3-4), 137-170. https://doi.org/10.1016/j.pocean.2010.02.009

Lam, P. J., Ohnemus, D. C., & Auro, M. E. (2015). Size-fractionated major particle composition and concentrations from the US GEOTRACES North Atlantic Zonal Transect. *Deep Sea Research Part II: Topical Studies in Oceanography*, *116*, 303-320. https://doi.org/10.1016/j.dsr2.2014.11.020

Volk, T., & Hoffert, M. I. (1985). Ocean carbon pumps: analysis of relative strengths and efficiencies in ocean-driven atmospheric CO2 changes. In E. T. Sundquist and W. S. Broecker (Eds.), *The carbon cycle and atmospheric CO2: natural variations Archean to present* (Vol. 32, pp. 99-110). Washington, D. C.: American Geophysical Union. https://doi.org/10.1029/GM032p0099

To my family.

ACKNOWLEDGEMENTS

I would like to thank my advisor Phoebe J. Lam for her tremendous support and help during my entire PhD. I came to the lab as a fresh undergraduate from a different country and had to overcome difficulties in both science and many aspects of daily life, such as the culture and language. I couldn't have completed my PhD and prepared myself for future challenges without Phoebe's help. She has been an incredible advisor and always makes sure to meet with me once a week about my research progress. I am grateful for her financial support so that I don't need to do extra TAs while conducting my research. I would also like to thank my other committee members, Carl Lamborg, Matthew McCarthy, and Colleen Hansel, for their helpful insights in my annual progress meetings and defense. Many thanks to Phoebe for her help on my postdoctoral job applications and to Phoebe, Carl, Amy Gartman, and Adrian Burd for writing recommendation letters.

I sincerely thank all past and current members in the Lam Lab, Maija Heller, Jong-Mi Lee, Kira Mizell, Vinicius Amaral, and Allison Laubach. I learned a lot from you and am grateful to have you all as my lab mates and friends. I valued the time we spent together in synchrotron facilities analyzing samples in the middle of the night, and also enjoyed the cruises we were on as the pump team in the middle of the Pacific Ocean. Special thanks to Jong-Mi, Kira, and Vinicius who overlapped with me during most of my PhD for their generous help and friendships.

Many thanks to my fellow international students and friends in the Ocean Sciences Department, Yuan Shen, Jiani Zheng, Yan Zhang, Xinyun Cui, and Esther Mak. The potluck parties we had and road trips we took have always been some of the best memories in my graduate school life. I would like to thank my cohort, especially Meredith McPherson, Katie Harding, Maria Hamilton, and Kira, for their help and encouragement along this journey. Within the Ocean Science Department, I would also like to thank Rob Franks of the UCSC Marine Analytical Laboratory and Colin Carney of the UCSC Stable Isotope Laboratory for their assistance with the instruments, and the department manager Rondi Robison for her help with logistics. Outside the department, I owe a huge amount of thanks to my friends I get to know from GEOTRACES cruises and conferences, especially Jennifer Kenyon, Janelle Steffen, and Steve Pike. It is my pleasure to get to know you all, and I appreciate the help and joy you brought me. Special thanks to my roommates Kira and John Mizell. Despite staying at home every day in the past year, it is you who made my last year of graduate school so much fun.

Finally, I want to thank my mom, dad, and wife for their continuous support and love during my PhD. The pathway to academia is long and full of uncertainties. Wherever it goes, I hope that I can get together with my family in the near future.

This work was made possible by support from (in alphabetical order): the financial awards (travel and research) and support from the Ocean Science Department at UCSC, the NSF funding for the GN01 cruise to Phoebe J. Lam (grant number: NSF OCE-1535854), the NSF funding for the GP15 cruise management (grant number:

NSF OCE-1657781), the UCSC Chancellor's Dissertation Year Fellowship, the UCSC Non-Resident Tuition Fellowship, the UCSC Regent's Fellowship, and the UCSC-USGS Co-Op funding through Amy Gartman.

The text of this dissertation includes a reprint of the following previously published material in Chapter 1:

Xiang, Y., & Lam, P. J. (2020). Size-fractionated compositions of marine suspended particles in the western Arctic Ocean: Lateral and vertical sources. *Journal of Geophysical Research: Oceans*, *125*(8), e2020JC016144.

The co-author listed in this publication, Phoebe J. Lam, directed and supervised the research which forms the basis for the dissertation.

INTRODUCTION

Marine particles participate in the cycling of most elements in the ocean and are a key parameter in the GEOTRACES program. Sources of particles to the ocean can be either internal (e.g., biological production) or external (e.g., dust deposition, lateral transport from margins, and hydrothermal vents). As an essential component in the marine biological pump, the vertical transport of particulate organic matter (POM) from the surface into the ocean interior (>1000 m) can sequester carbon from the atmosphere on a time scale of centuries, exerting a primary control on the atmospheric CO_2 level (Kwon et al., 2009; Volk & Hoffert, 1985).

In general, marine particles consist of both biogenic and abiotic phases (Bishop et al., 1977; Lam et al., 2015). The major biogenic phases are POM, calcium carbonate ($CaCO_3$) and biogenic silica (opal), and major abiotic phases include lithogenic material and authigenic Fe and Mn (oxyhydr)oxides. The important role of particle composition manifests in particle export and scavenging processes. $CaCO_3$ and lithogenic particles have been suggested to provide a source of excess density and/or protection and promote carbon export into the deep ocean, acting as efficient ballast minerals (Armstrong et al., 2001; Francois et al., 2002; Klaas & Archer, 2002). Additionally, the composition of marine particles is of importance in the scavenging removal of particle-reactive trace elements and isotopes (TEIs). Hayes et al. (2015) examined the partition coefficient (K_d) of two particle-reactive TEIs, thorium-230

(^{230}Th) and protactinium-231 (^{231}Pa), in the North Atlantic and found that the affinity of ^{230}Th and ^{231}Pa is 1 to 3 orders of magnitude higher for Fe and Mn (oxyhydr)oxides than for other major phases.

Separating the particle pool into two size classes (small vs. large particles) can help understand the many roles that particles play in the ocean. Small particles are more abundant than large particles (Jackson et al., 1997; Loisel et al., 2006; Roullier et al., 2014; Stemmann et al., 2008; Stemmann et al., 2004), comprising most of the overall particle mass (Bishop et al., 1977; Lam et al., 2018; Lam et al., 2015; Xiang & Lam, 2020). Based on Stokes' Law, smaller particles tend to sink more slowly compared to larger particles because sinking rates are proportional to the square of particle diameter. Therefore, long-distance lateral flux of particles for hundreds of kilometers from continental margins (Honjo, 1982; Honjo et al., 2010; Hwang et al., 2015; Lamborg et al., 2008) is likely to be dominated by small particles. Given their high abundance and long residence time, small particles are responsible for scavenging particle-reactive TEIs. The two size classes are linked by aggregation and disaggregation, through both physical and biological processes (Burd & Jackson, 2009). Large particles, consisting of phytodetrital aggregates, marine snow, and fecal pellets, tend to dominate the sinking flux (Alldredge & Silver, 1988; Bishop et al., 1977; Ebersbach & Trull, 2008; Fowler & Knauer, 1986; Laurenceau-Cornec et al., 2015; Turner, 2015; Wilson et al., 2013) and remove carbon and particle-associated TEIs from the surface ocean (sinking up to several hundred meters per day; Armstrong et al., 2009), though smaller particles can also be important for vertical flux from oligotrophic systems (Alonso-González et al.,

2010; Baker et al., 2017; Bol et al., 2018; Giering et al., 2016; Riley et al., 2012; Trull et al., 2008).

This dissertation examines the biogeochemical cycling of size-fractionated marine particles in the Western Arctic Ocean and explores the effect of particle composition on the magnitude of vertical mass flux in three major ocean basins. Chapter 1 presents the first dataset of full-ocean-depth concentration and composition of size-fractionated suspended particles in the Western Arctic Ocean. Marked differences between particle composition in the Chukchi Shelf and Arctic Basin are used to discern lateral from vertical particle sources into the Arctic interior. The carbon isotopic signatures of particulate organic carbon suggest that small particles in the subsurface in the central basin consist of a mixture of laterally advected and vertically sinking components. In contrast, large particles in the upper 500 m in most part of central Arctic Ocean are dominated mainly by particles that sank from the surface. The importance of lateral transport is also evident from other tracers, such as enhancements in Mn oxides in the halocline, and high lithogenic particles in the deep ocean. Chapter 2 uses synchrotron X-ray absorption spectroscopy (XAS) to characterize the chemical speciation of a specific particle phase, particulate Mn (pMn), in the surface waters of the Western Arctic Ocean. Higher pMn average oxidation states (AOS) are observed at night compared to in the light, suggesting that oxidation and reduction increases and lowers pMn AOS, respectively. Rates of oxidation and reduction during the day-night cycle are more rapid in the Arctic shelf/slope than the basin, possibly as a result of their differences in temperature, dissolved Mn and microbial communities. Chapter 3

compiles particle composition data from three recent U.S. GEOTRACES cruises in the North Atlantic, the Eastern Tropical South Pacific, and the Western Arctic Ocean. Mass fluxes in three basins are calculated based on Stokes' Law that is modified with a new porosity-size relationship that adds observations from smaller aggregates. The relative importance of particle concentration, composition, size, and hydrography on sinking fluxes is evaluated in these three basins. Particle concentration and composition are more important controls on the variability and magnitude of total mass flux than particle size, as increasing porosity with size and a dominance of smaller particles diminish the size dependence of mass flux.

REFERENCES

Alldredge, A. L., & Silver, M. W. (1988). Characteristics, dynamics and significance of marine snow. *Progress in oceanography*, *20*(1), 41-82. https://doi.org/10.1016/0079-6611(88)90053-5

Alonso-González, I. J., Arístegui, J., Lee, C., Sanchez-Vidal, A., Calafat, A., Fabrés, J., et al. (2010). Role of slowly settling particles in the ocean carbon cycle. *Geophysical Research Letters*, *37*(13). https://doi.org/10.1029/2010gl043827

Armstrong, R. A., Lee, C., Hedges, J. I., Honjo, S., & Wakeham, S. G. (2001). A new, mechanistic model for organic carbon fluxes in the ocean based on the quantitative association of POC with ballast minerals. *Deep Sea Research Part II: Topical Studies in Oceanography*, *49*(1-3), 219-236. https://doi.org/10.1016/S0967-0645(01)00101-1

Armstrong, R. A., Peterson, M. L., Lee, C., & Wakeham, S. G. (2009). Settling velocity spectra and the ballast ratio hypothesis. *Deep Sea Research Part II: Topical Studies in Oceanography*, *56*(18), 1470-1478. https://doi.org/10.1016/j.dsr2.2008.11.032

Baker, C. A., Henson, S. A., Cavan, E. L., Giering, S. L. C., Yool, A., Gehlen, M., et al. (2017). Slow-sinking particulate organic carbon in the Atlantic Ocean: Magnitude, flux, and potential controls. *Global Biogeochemical Cycles*, *31*(7), 1051-1065. https://doi.org/10.1002/2017gb005638

Bishop, J. K. B., Edmond, J. M., Ketten, D. R., Bacon, M. P., & Silker, W. B. (1977). The chemistry, biology, and vertical flux of particulate matter from the upper 400 m of the equatorial Atlantic Ocean. *Deep Sea Research*, *24*(6), 511-548. https://doi.org/10.1016/0146-6291(77)90526-4

Bol, R., Henson, S. A., Rumyantseva, A., & Briggs, N. (2018). High-frequency variability of small-particle carbon export flux in the Northeast Atlantic. *Global Biogeochemical Cycles*, *32*(12), 1803-1814. https://doi.org/10.1029/2018gb005963

Burd, A. B., & Jackson, G. A. (2009). Particle aggregation. *Annual Review of Marine Science*, *1*, 65-90. https://doi.org/10.1146/annurev.marine.010908.163904

Ebersbach, F., & Trull, T. W. (2008). Sinking particle properties from polyacrylamide gels during the KErguelen Ocean and Plateau compared Study (KEOPS): Zooplankton control of carbon export in an area of persistent natural iron inputs in the Southern Ocean. *Limnology and Oceanography*, *53*(1), 212-224. https://doi.org/10.4319/lo.2008.53.1.0212

Fowler, S. W., & Knauer, G. A. (1986). Role of large particles in the transport of elements and organic compounds through the oceanic water column. *Progress in oceanography*, *16*(3), 147-194. https://doi.org/10.1016/0079-6611(86)90032-7

Francois, R., Honjo, S., Krishfield, R., & Manganini, S. (2002). Factors controlling the flux of organic carbon to the bathypelagic zone of the ocean. *Global Biogeochemical Cycles*, *16*(4), 34-31-34-20. https://doi.org/10.1029/2001gb001722

Giering, S. L. C., Sanders, R., Martin, A. P., Lindemann, C., Möller, K. O., Daniels, C. J., et al. (2016). High export via small particles before the onset of the North Atlantic spring bloom. *Journal of Geophysical Research: Oceans*, *121*(9), 6929-6945. https://doi.org/10.1002/2016jc012048

Hayes, C. T., Anderson, R. F., Fleisher, M. Q., Vivancos, S. M., Lam, P. J., Ohnemus, D. C., et al. (2015). Intensity of Th and Pa scavenging partitioned by particle chemistry in the North Atlantic Ocean. *Marine Chemistry*, *170*, 49-60. https://doi.org/10.1016/j.marchem.2015.01.006

Honjo, S. (1982). Seasonality and interaction of biogenic and lithogenic particulate flux at the Panama Basin. *Science*, *218*(4575), 883-884. https://doi.org/10.1126/science.218.4575.883

Honjo, S., Krishfield, R. A., Eglinton, T. I., Manganini, S. J., Kemp, J. N., Doherty, K., et al. (2010). Biological pump processes in the cryopelagic and hemipelagic Arctic Ocean: Canada Basin and Chukchi Rise. *Progress in Oceanography*, *85*(3-4), 137-170. https://doi.org/10.1016/j.pocean.2010.02.009

Hwang, J., Kim, M., Manganini, S. J., McIntyre, C. P., Haghipour, N., Park, J., et al. (2015). Temporal and spatial variability of particle transport in the deep Arctic Canada Basin. *Journal of Geophysical Research: Oceans*, *120*(4), 2784-2799. https://doi.org/10.1002/2014jc010643

Jackson, G. A., Maffione, R., Costello, D. K., Alldredge, A. L., Logan, B. E., & Dam, H. G. (1997). Particle size spectra between 1 μm and 1 cm at Monterey Bay determined using multiple instruments. *Deep Sea Research Part I: Oceanographic Research Papers*, *44*(11), 1739-1767. https://doi.org/10.1016/S0967-0637(97)00029-0

Klaas, C., & Archer, D. E. (2002). Association of sinking organic matter with various types of mineral ballast in the deep sea: Implications for the rain ratio. *Global Biogeochemical Cycles*, *16*(4), 63-61-63-14. https://doi.org/10.1029/2001GB001765

Kwon, E. Y., Primeau, F., & Sarmiento, J. L. (2009). The impact of remineralization depth on the air–sea carbon balance. *Nature Geoscience*, *2*(9), 630-635. https://doi.org/10.1038/ngeo612

Lam, P. J., Lee, J. M., Heller, M. I., Mehic, S., Xiang, Y., & Bates, N. R. (2018). Size-fractionated distributions of suspended particle concentration and major phase composition from the US GEOTRACES Eastern Pacific Zonal Transect (GP16). *Marine Chemistry*, *201*, 90-107. https://doi.org/10.1016/j.marchem.2017.08.013

Lam, P. J., Ohnemus, D. C., & Auro, M. E. (2015). Size-fractionated major particle composition and concentrations from the US GEOTRACES North Atlantic Zonal Transect. *Deep Sea Research Part II: Topical Studies in Oceanography*, *116*, 303-320. https://doi.org/10.1016/j.dsr2.2014.11.020

Lamborg, C. H., Buesseler, K. O., Valdes, J., Bertrand, C. H., Bidigare, R., Manganini, S., et al. (2008). The flux of bio- and lithogenic material associated with sinking particles in the mesopelagic "twilight zone" of the northwest and North Central Pacific Ocean. *Deep Sea Research Part II: Topical Studies in Oceanography*, *55*(14-15), 1540-1563. https://doi.org/10.1016/j.dsr2.2008.04.011

Laurenceau-Cornec, E. C., Trull, T. W., Davies, D. M., Bray, S. G., Doran, J., Planchon, F., et al. (2015). The relative importance of phytoplankton aggregates and zooplankton fecal pellets to carbon export: insights from free-drifting sediment trap deployments in naturally iron-fertilised waters near the Kerguelen Plateau. *Biogeosciences*, *12*(4), 1007-1027. https://doi.org/10.5194/bg-12-1007-2015

Loisel, H., Nicolas, J. M., Sciandra, A., Stramski, D., & Poteau, A. (2006). Spectral dependency of optical backscattering by marine particles from satellite remote sensing of the global ocean. *Journal of Geophysical Research: Oceans*, *111*(C9). https://doi.org/10.1029/2005JC003367

Riley, J. S., Sanders, R., Marsay, C., Le Moigne, F. A. C., Achterberg, E. P., & Poulton, A. J. (2012). The relative contribution of fast and slow sinking particles to ocean carbon export. *Global Biogeochemical Cycles*, *26*(1), n/a-n/a. https://doi.org/10.1029/2011gb004085

Roullier, F., Berline, L., Guidi, L., Durrieu De Madron, X., Picheral, M., Sciandra, A., et al. (2014). Particle size distribution and estimated carbon flux across the Arabian Sea oxygen minimum zone. *Biogeosciences*, *11*(16), 4541-4557. https://doi.org/10.5194/bg-11-4541-2014

Stemmann, L., Eloire, D., Sciandra, A., Jackson, G. A., Guidi, L., Picheral, M., & Gorsky, G. (2008). Volume distribution for particles between 3.5 to 2000 µm

in the upper 200 m region of the South Pacific Gyre. *Biogeosciences*, *5*(2), 299-310. https://doi.org/10.5194/bg-5-299-2008

Stemmann, L., Jackson, G. A., & Ianson, D. (2004). A vertical model of particle size distributions and fluxes in the midwater column that includes biological and physical processes—Part I: model formulation. *Deep Sea Research Part I: Oceanographic Research Papers*, *51*(7), 865-884. https://doi.org/10.1016/j.dsr.2004.03.001

Trull, T. W., Bray, S. G., Buesseler, K. O., Lamborg, C. H., Manganini, S., Moy, C., & Valdes, J. (2008). In situ measurement of mesopelagic particle sinking rates and the control of carbon transfer to the ocean interior during the Vertical Flux in the Global Ocean (VERTIGO) voyages in the North Pacific. *Deep Sea Research Part II: Topical Studies in Oceanography*, *55*(14), 1684-1695. https://doi.org/10.1016/j.dsr2.2008.04.021

Turner, J. T. (2015). Zooplankton fecal pellets, marine snow, phytodetritus and the ocean's biological pump. *Progress in Oceanography*, *130*, 205-248. https://doi.org/10.1016/j.pocean.2014.08.005

Volk, T., & Hoffert, M. I. (1985). Ocean carbon pumps: analysis of relative strengths and efficiencies in ocean-driven atmospheric CO2 changes. In E. T. Sundquist and W. S. Broecker (Eds.), *The carbon cycle and atmospheric CO2: natural variations Archean to present* (Vol. 32, pp. 99-110). Washington, D. C.: American Geophysical Union. https://doi.org/10.1029/GM032p0099

Wilson, S. E., Ruhl, H. A., & Smith, J., K. L. (2013). Zooplankton fecal pellet flux in the abyssal northeast Pacific: A 15 year time-series study. *Limnology and oceanography*, *58*(3), 881-892. https://doi.org/10.4319/lo.2013.58.3.0881

Xiang, Y., & Lam, P. J. (2020). Size-fractionated compositions of marine suspended particles in the Western Arctic Ocean: Lateral and vertical sources. *Journal of Geophysical Research: Oceans*, *125*(8), e2020JC016144. https://doi.org/10.1029/2020JC016144

CHAPTER 1: SIZE-FRACTIONATED COMPOSITIONS OF MARINE SUSPENDED PARTICLES IN THE WESTERN ARCTIC OCEAN: LATERAL AND VERTICAL SOURCES

Abstract

We present full water depth sections of size-fractionated (1-51 μm; >51 μm) concentrations of suspended particulate matter and major particle phase composition (particulate organic matter (POM), including its carbon isotopic composition (POC-$\delta^{13}C$) and C:N ratio, calcium carbonate ($CaCO_3$), opal, lithogenic particles, and iron and manganese (oxyhydr)oxides from the U.S. GEOTRACES Arctic Cruise (GN01) in the Western Arctic in 2015. Whereas biogenic particles (POM and opal) dominate the upper 1000 m, lithogenic particles are the most abundant particle type at depth. Minor phases such as manganese (Mn) oxides are higher in GN01 than in any other U.S. GEOTRACES cruises so far. Extremely depleted POC-$\delta^{13}C$, as low as ~-32‰, is ubiquitous at the surface of the Western Arctic Ocean as a result of different growth rates of phytoplankton. Moderate penetration of depleted POC-$\delta^{13}C$ to depth indicates active sinking of large particles in the central basin. Lateral transport from the Chukchi shelf is also of significance in the Western Arctic, as is evident from increases in biogenic silica to POC ratios and Mn oxide concentrations in the halocline, as well as lithogenic element contents in the deep waters. Our study supports previous suggestions of the near absence of $CaCO_3$ in the Arctic Basin. This study presents the

first data set of concentration and composition of suspended particles in the Western Arctic Ocean, and sheds new light on the vertical and lateral processes that govern particle distribution in this enclosed ocean basin.

1. Introduction

The Arctic Ocean is characterized by extremely broad shelf areas and sea ice cover and thus has profoundly different particle cycling compared to other ocean basins. The Canada Basin has the lowest measured biogenic fluxes of any region of the global ocean (Honjo et al., 2010). It is estimated that only about 1-2% of the surface new production can reach the deep Canada Basin (Hwang et al., 2015). With little particle flux coming from above, lateral processes from the surrounding seem to dominate the particle transport in the Arctic Ocean (Fahl & Nöthig, 2007; Honjo et al., 2010; Hwang et al., 2008; Hwang et al., 2015). Increases in the vertical fluxes with depth are frequently observed in the deep Arctic Ocean (Fahl & Nöthig, 2007; Forest et al., 2015; Honjo et al., 2010; Hwang et al., 2008; Hwang et al., 2015; Lalande et al., 2016; O'Brien et al., 2013). Particles transported laterally from the shelves are characterized by a high fraction of lithogenic material (~80%) and old radiocarbon ages (~1900 years) (Hwang et al., 2008; Hwang et al., 2015). In addition, distinct chemical signatures within the laterally transported material are also manifested in other compositional variables. For example, elevated particulate organic matter (POM) concentrations in the upper halocline of the Western Arctic Basin appear to originate from the shelf (Bates et al., 2005). Plumes of laterally advected iron (Fe) in different phases, including

suspended leachable particulate, dissolved and total dissolvable Fe, are also observed to reside in upper halocline water (Aguilar-Islas et al., 2013; Cid et al., 2012; Hioki et al., 2014; Nakayama et al., 2011).

Different origins, concentrations, and compositions of particles in the Arctic are bound to set up an entirely unique dynamic of particle cycling compared to most ocean basins, which will undoubtedly influence the scavenging and removal of particle-reactive trace elements and isotopes (TEIs). Both particle concentrations and composition are crucial for scavenging and removal of particle-reactive TEIs. The number of surface sites to bind TEIs on particle surfaces is thought to scale approximately with particle concentration (Honeyman et al., 1988). The number of surface sites is also influenced by particle composition, since some particle phases, such as Fe and Mn (oxyhydr)oxides, have specific surface areas orders of magnitude higher than others (Davis & Leckie, 1978; Toner et al., 2005).

Although there has been some work examining the composition of sinking particles from sediment traps (Fahl & Nöthig, 2007; Honjo et al., 2010; Hwang et al., 2008; Hwang et al., 2015; Lalande et al., 2016; O'Brien et al., 2011; O'Brien et al., 2006; O'Brien et al., 2013), no previous studies have focused on the concentration and composition of suspended particles in the deep Arctic Ocean. This study presents the first set of full water column suspended particle concentration and composition in the Arctic Ocean, spanning the highly productive Chukchi Shelf to the perennially ice-covered and oligotrophic Western Arctic basins. Our measurements of size-fractionated suspended particle concentration and composition in the Western Arctic

Ocean improve understanding of the strength and efficiency of the biological pump, and shed light on unique particle provenance and transport. They give novel insight into both internal processes (e.g., manganese oxide precipitation in the halocline) and external sources (e.g., lateral transport of lithogenic material to deep waters) in particle cycling in the Western Arctic Ocean. Furthermore, these measurements will also provide a crucial baseline before major climatic changes fundamentally alter the Arctic. Insights gained from this study about particle sources and transport may have implications for other regions, especially those with broad productive margins juxtaposed against oligotrophic basins, such as the Gulf of Mexico, the Mediterranean Sea, and the South China Sea.

2. Methods

2.1 Cruise track and hydrography

The 2015 U.S. GEOTRACES Arctic cruise (GN01) focused on the Western Arctic Ocean with comprehensive coverage of both shallow shelves and deep basins (Figure 1.1a). The cruise sailed from Dutch Harbor, Alaska, to the North Pole and returned to Dutch Harbor onboard the U.S. Coast Guard Cutter (USCGC) Healy (HLY1502) between August 9 and October 11, 2015. The cruise was in a clockwise direction, starting and ending on the shallow shelf and slopes. The northbound leg covered the Chukchi Abyssal Plain, the Makarov Basin and the North Pole in the Amundsen Basin, whereas the southbound leg encompassed both the Makarov Basin and the Canada Basin. A total of 66 stations were occupied, including both

GEOTRACES and Repeat Hydrography stations. In-situ pump particles were sampled from 20 GEOTRACES stations (Figure 1.1a).

Extensive continental shelves make up more than half (53%) of the overall area in the Arctic Ocean (Jakobsson, 2002). This number is much higher than the typical fraction of 9.1-17.7% in other oceans (Menard & Smith, 1966). Despite small percentages with regard to the global ocean volume and surface area, the Arctic Ocean receives up to 11% of the annual global riverine freshwater discharge (Aagaard & Carmack, 1989). The Arctic deep basin is divided into two major sub-basins (Eurasian Basin and Canadian Basin) by the Lomonosov Ridge that runs between the New Siberian Islands and Greenland. The Alpha and Mendeleev ridges sub-divide the Canadian (Amerasian) Basin into the Canada and Makarov basins, and the Eurasian Basin is further separated by the Gakkel Ridge into the Nansen and Amundsen basins.

The Arctic Ocean connects to the North Pacific via the shallow (~50 m deep) Bering Strait (Coachman & Barnes, 1961) and communicates with the North Atlantic Ocean through the Fram Strait, the Barents Sea and the Canadian Arctic Archipelago (CAA) (e.g., Aagaard & Carmack, 1989; Aagaard et al., 1991; Jones et al., 1995; Rudels, 1987; Rudels et al., 1999; Woodgate et al., 2001). The cold and fresh Pacific inflow contributes about 30% of the annual freshwater input in the Arctic Ocean with a reference salinity of 34.8 (Serreze et al., 2006), whereas relatively warm and salty (S~34.8) Atlantic inflow dominates with respect to heat and mass fluxes (Beszczynska-Möller et al., 2011; Dickson et al., 2008). Both inflows are substantially modified on the shelves (Pacific: Bering/Chukchi; Atlantic: Barents/Siberia) through interactions

with shelf sediments, river runoff, sea ice formation and melting processes before flowing into the basin interior (Bauch et al., 2016; Bluhm et al., 2015; Cooper et al., 1997; Jones & Anderson, 1986; Karcher & Oberhuber, 2002; Moore & Smith, 1986; Rudels et al., 2004; Yamamoto-Kawai et al., 2005). The modified Pacific water brings nutrient-rich waters into the Western Arctic Ocean and leads to the formation of the upper halocline (Jones & Anderson, 1986). The upper halocline (UHL), or Pacific halocline, is mainly confined to the Canadian Basin (Carmack et al., 1997; Jones et al., 1998; Shimada et al., 2005), and is composed of near-freezing, relatively salty (S~33.1) Pacific Winter Water and warmer, relatively fresh (31<S<33) Pacific Summer Water (Jones & Anderson, 1986; Steele et al., 2004). The lower halocline (LHL), or Atlantic halocline, is Atlantic-water derived, characterized by higher salinities (33.9<S<34.7) and low nutrient concentrations (<14 μM silicate) in the Western Arctic Ocean (Jones & Anderson, 1986; Salmon & Mcroy, 1994). In our cruise, pronounced silicate concentrations within the halocline (>15 μM) only appear in the Canada Basin and part of the Makarov Basin and are absent from the Amundsen Basin (Cutter et al., 2019). Overlying the well-defined halocline, the abundant presence of freshwater builds up an extremely cold (θ near freezing), fresh (S<32) and stratified Polar Mixed Layer (PML) in the upper 30-70 m in the Western Arctic Ocean as a result of seasonal sea ice melting and river runoff (Jones & Anderson, 1986; Lansard et al., 2012; Macdonald et al., 1989), whereas the PML in the Amundsen Basin is relatively saltier (S<33), owing to more influences from surface Atlantic water (Rudels et al., 1996; Rudels et al., 2004). The warmer (θ> 0˚C) so-called Atlantic Layer is below the unique halocline structure,

dominating intermediate depths (down to ~800 m), and following a cyclonic circulation that is topographically steered around the Arctic in both the Eurasian and Canadian basins (Rudels et al., 1994). Below the Atlantic Layer are the deep and bottom waters. Communication between the deep Eurasian and Canadian Basins is achieved mostly via overflow through the gaps in the Lomonosov Ridge and partly via the boundary flow along the Eurasian shelves into the Canadian Basin (Jones et al., 1995). The residence time of the deep Canadian Basin (>2500 m) calculated using radiocarbon data is about 450 years, longer than the 250 year age of the Eurasian Basin (Schlosser et al., 1997).

2.2 Particle sampling

Size-fractionated particles were collected using dual-flow McLane Research in-situ pumps (WTS-LV). More details about filter holders and deployments were described in Lam et al. (2018), Ohnemus and Lam (2015) and in Appendix 1 of this dissertation (Bishop et al., 2012; Black et al., 2018; Cutter et al., 2010; Planquette & Sherrell, 2012).

Large size fraction particles were collected from the 51 μm prefilters from both filter holders, and they are referred to as "LSF", representing particles >51 μm. The prefilters are upstream of paired 1 μm quartz fiber Whatman QMA and paired 0.8 μm polyethersulfone Supor™ filters. Only the top filter of each was analyzed, and defines the small size fraction, referred to as "SSF" (1-51 μm for the QMA; 0.8-51 μm for the Supor). Bottom filters capture a portion of the submicron particle size (Bishop et al.,

2012), but they were not analyzed in this study. Total particles (>1 μm) are defined as the sum of the two size fractions (Total= LSF+ SSF).

Sea ice algae were collected from multiple ice cores taken at Stations 39, 42, and 43. At each station, the bottom 15- 20 cm of four ice cores were combined and melted in filtered seawater. Approximately 1- 2 L subsamples of the melted slurry was filtered onto separate 25 mm filters for analysis of particulate organic carbon (POC) and particulate inorganic carbon (PIC) (QMA filters) and bSi and lithogenic materials (0.8 μm Supor filters). Filters were dried in an oven at 60 °C (QMA) or in a laminar flow bench (Supor). Filtered seawater alone was also filtered onto each filter type to act as a process and sorption blank.

2.3 Particle Composition

Analytical methods for POC, particulate nitrogen (PN), $\delta^{13}C$ of POC, PIC, and biogenic silica (bSi) are as described in Lam et al. (2018) for samples measured at UCSC. Briefly, POC, PN, and $\delta^{13}C$ of POC were determined by combustion in an elemental analyzer followed by detection by isotope ratio mass spectrometry; PIC was measured by coulometry; and bSi was measured using flow injection analysis of an alkaline leach (Barão et al., 2015; DeMaster, 1981; Hedges et al., 2002; Lam et al., 2011; Lam et al., 2018; Lam et al., 2015; Mortlock & Froelich, 1989). Particulate trace metals were measured by high-resolution inductively coupled mass spectrometry (ICP-MS) of a digest solution from a hot refluxing method using a mixture of hydrofluoric and nitric acids (Cullen & Sherrell, 1999; Ohnemus et al., 2014; Planquette & Sherrell,

2012). More details about these methods are in Appendix 1 of this dissertation. Derived particle phases (lithogenic particles and Fe and Mn oxyhydroxides) and derived suspended particulate mass (SPM) are explained below.

2.3.1 Lithogenic particles (Litho)

Aluminum (Al) is highly abundant in the crust and relatively invariant between two main lithogenic sources, upper continental crust (UCC Al = 8.04 wt%) and bulk continental crust (BCC Al = 8.41 wt%) (Taylor & McLennan, 1995), and therefore serves as an appropriate tracer for lithogenic particles. Dissolved Al is known to be subject to particle scavenging (Orians & Bruland, 1986), however, which could lead to overestimates of lithogenic material based on measurements of particulate Al. Indeed, adsorptive scavenging was estimated to represent more than 50% of surface ocean particulate Al in the Indian and Southern Oceans where lithogenic input was small (Barrett et al., 2018). In an environment with more lithogenic input, leachable aluminum within and offshore of the California Current is much lower, about 10% of the total particulate aluminum (Berger et al., 2008). Applying the same weak acid leach to particles collected from Teflon-coated GO-FLO bottles in this cruise, leachable Al was 16.9 ± 11.7% of total particulate Al (Twining et al., 2019).

However, it is likely that such an operationally defined weak-acid leach would also access aluminosilicate structures, leading to an overestimate of scavenged trace metals. Al scavenging experiments showed adsorption of 6.67×10^{-3} mol Al/mol Si onto diatom frustules (Koning et al., 2007). Applying this ratio to observed biogenic Si

in SSF predicts low scavenged Al in the Western Arctic, with a median of about 1.7% of overall SSF particulate Al. This number serves as a lower limit of scavenged Al, for it only represents the proportion of adsorption onto biogenic silica. To be consistent with the lithogenic calculations from the previous two GEOTRACES cruises, we assumed that most of particulate Al originates from lithogenic sources and use UCC Al wt% to calculate concentrations of lithogenic particles in the Western Arctic Ocean.

$$\text{LITHO [μg/L]=Al [nmol/L]}\times 27\times 10^{-3}\ \text{[μg/nmol]/ 0.0804 [μg Al/μg UCC]}$$

2.3.2 Fe and Mn (oxyhydr)oxides

Excess Fe and Mn beyond their lithogenic contributions were assumed to be Fe and Mn (oxyhydr)oxides and calculated by subtracting the lithogenic Fe and Mn from the totals. The UCC Fe/Al (0.211) and Mn/Al (0.00367) ratios were used in the lithogenic corrections. We conducted a sensitivity study to show that the UCC Fe/Al ratio is the only method to generate most reasonable percentages of excess particulate Fe over the total particulate iron in the Western Arctic Basin (LSF: 34.5 ± 19.1%; SSF: 35.9 ± 15.8%) (Appendix 1.1). It is slightly low, but comparable to the 53.0 ± 12.8% of labile particulate Fe accessed via a weak acid leach in GO-FLO bottle particles in the Western Arctic Basin (Twining et al., 2019). The difference between lithogenic corrections and the weak acid leach, if real, is likely to be the contribution from the lithogenic iron pool in the leach. The SSF biogenic Fe in the Western Arctic Ocean, as a potential pool of excess Fe, was estimated to be of minor importance (median fraction

of biogenic Fe of all samples= 0.5%), calculated using the global average Fe:P ratios of phytoplankton (Twining & Baines, 2013) and observed particulate P.

Iron oxyhydroxides are treated as $Fe(OH)_3$ (ferrihydrite approximation) and Mn oxides are as MnO_2 (birnessite approximation). We apply the formula weights of 106.9 g $Fe(OH)_3$/mol Fe and 86.9 g MnO_2/mol Mn, respectively. By applying UCC Fe/Al and Mn/Al ratios, we minimize the negative values in $Fe(OH)_3$ and MnO_2. Fewer than 1% of SSF $Fe(OH)_3$ and MnO_2 values are negative. Most negative values appear in the calculations of LSF $Fe(OH)_3$, accounting for just 7% of all samples. Negative numbers were all set to 0 in the calculation of particle mass.

$$Fe(OH)_3\ [\mu g/L]=\left(Fe\ [nM]-\left(Al\ [nM]\times 0.211\ [nmol\ Fe/nmol\ Al]\right)\right)$$
$$\times 106.9\ [ng\ Fe(OH)_3/nmol\ Fe]\times [10^{-3}\ \mu g/ng]$$
$$MnO_2\ [\mu g/L]=\left(Mn\ [nM]-\left(Al\ [nM]\times 0.00367\ [nmol\ Mn/nmol\ Al]\right)\right)$$
$$\times 86.9\ [ng\ MnO_2/nmol\ Mn]\times [10^{-3}\ \mu g/ng]$$

2.3.3 Suspended particulate mass (SPM)

Direct comparisons between gravimetric and chemical dry weight have been made in the equatorial Atlantic, and they were found to be quite similar to each other (Bishop et al., 1977). In this paper, the chemical dry weight is used to estimate SPM for each size fraction, as the sum of all major particle composition, which is the sum of POM, $CaCO_3$, opal, lithogenic material (Litho), and Fe and Mn (oxyhydr)oxides.

$$SPM\ [\mu g/L]=POM\ [\mu g/L]+ CaCO_3\ [\mu g/L]+ opal\ [\mu g/L]+ Litho\ [\mu g/L]$$

$$+ Fe(OH)_3\ [\mu g/L] + MnO_2\ [\mu g/L]$$

2.3.4 Blank subtractions, detection limits and error estimations

'Dipped blank' filters were complete filter sets (prefilter on top of paired QMA or paired Supor filters) that were deployed at each cast as process blanks. Prior to the deployment, these filters were sandwiched in a 1 μm polyester mesh filter, placed into acid-leached perforated polypropylene containers, and attached to a pump frame with plastic cable ties. All dipped blank filters were exposed to seawater for the same amount of time, processed, and analyzed as regular samples. As process blanks, dipped blank filters were used for blank subtraction, determination of detection limits, and calculations of uncertainties.

Outliers in dipped blanks (db) for each measurement type were excluded using Chauvenet's criterion (Glover et al., 2011). The median of db filters, except for LSF bSi, was then used in blank subtraction to take into account the adsorption and potential particle loadings from non-targeted depths, especially from the surface ocean during pump recovery. There were anomalously high bSi concentrations of LSF dipped blanks, which were also observed in the GA03 NAZT and GP16 EPZT sections (Lam et al., 2018; Lam et al., 2015). Blank corrections for LSF bSi were made by subtracting the median of LSF failed pump values (pumps with less than 5% of typical water volume filtered). The detection limit was defined as three times the standard deviation of the dipped blank filters. The percentage of samples that fall below the detection limit for each parameter in both size fractions is listed in Appendices 1.9 and 1.10.

Errors were estimated based on the standard deviation of all dipped blank filters. For pTM, analyses on duplicates were frequently conducted, and errors were calculated by propagating two major errors: uncertainty in the db subtraction, and uncertainty from the variability of digestion and particle distribution. Errors in derived parameters are calculated based on rules of error propagation.

3. Results

3.1 Distributions of size-fractionated particle concentration and composition

3.1.1 Particulate Organic Carbon (POC)

Concentrations of particulate organic carbon (POC) at shelf and slope stations range from 0.2 to 9.5 μmol/L for SSF (mean ± s.d. = 2.3 ± 2.7 μmol/L; n= 32) and 0.1 to 20.4 μmol/L for LSF (mean ± s.d. = 1.5 ± 3.7 μmol/L; n= 32) (Figures 1.2a & 1.3a). Extremely high concentrations of POC are observed at Station 6: SSF POC concentrations as high as 9.5 μmol/L are observed near the bottom (Figure 1.2a), whereas the most abundant LSF POC of 20.4 μmol/L appears at the surface (Figure 1.3a). The LSF POC at Stations 60, 61 and 66 close to the Hanna Shoal, ranging from 0.1 to 4.4 μmol/L, are comparable to concentrations of >53 μm POC reported at similar locations in the summer (Bates et al., 2005; Moran et al., 2005). Close to Point Hope, surface concentrations of total POC at Station 6 from this study and from Bates et al. (2005) are both more than 20 μmol/L. Over the northern Bering and Chukchi shelves, the range of total POC is also generally of a similar magnitude to existing measurements (Goñi et al., 2019; Wyatt et al., 2013).

In the central basin, POC concentrations in the upper 100 m are much lower (SSF: 0.5 ± 0.2 μmol/L; LSF: 0.1 ± 0.1 μmol/L) than shelf values and decrease rapidly offshore (Figures 1.2a & 1.3a). A slight local maximum in POC concentrations in the halocline generally exists throughout the Western Arctic Basin, especially in the Chukchi Abyssal Plain. Near-bottom concentration enhancements are detected close to the continental margins and the deep ridges in both size fractions. The lowest concentrations of POC in the basin are detected in the deep Canada Basin at Stations 48 and 52. Total POC concentrations at Station 56 in the Canada Basin are comparable to suspended POC concentrations collected via in-situ pump reported at the same location in 2008 (Appendix 1.2) (Griffith et al., 2012).

3.1.2 Biogenic Silica (bSi)

As for POC, biogenic silica (bSi) concentrations are much higher in the shelf/slope regions (Figures 1.2b & 1.3b) due to the abundance of diatoms in phytoplankton assemblages on the Chukchi Shelf (Balch et al., 2014; Coupel et al., 2012; Giesbrecht et al., 2019; Joo et al., 2012; Laney & Sosik, 2014; Sukhanova et al., 2009). Total bSi concentrations over the shelf increase with depth: bSi concentrations within the euphotic zone are mostly less than 1 μmol/L, whereas in the bottom nepheloid layers (BNLs), total bSi concentrations vary from 1.5 to 15.7 μmol/L. This range is comparable to a previous study over the Western Arctic shelves showing maximum values of 4.8- 9.5 μmol/L within the BNLs (Wyatt et al., 2013). Similar to POC, bSi concentrations decrease rapidly towards the North Pole and also with depth

in the central basin, but bSi concentrations are usually lower than POC, especially in the SSF (Figures 1.2b & 1.3b). Concentrations of total bSi are generally less than 0.1 μmol/L and often lower than 0.01 μmol/L below 1000 m in the central basin, in line with other suspended bSi measurements in the Canada Basin (Varela et al., 2016; Wyatt et al., 2013). A hotspot of LSF POC and bSi at the subsurface of Station 52 co-locates with a maximum of the potential temperature (Figures 1.1b & 1.3a-b), probably indicating the influence from the summer Pacific halocline water (Shimada et al., 2001; Steele et al., 2004). At Station 48 in the marginal ice zone, elevated SSF bSi concentrations are found throughout the upper 300 m (Figure 1.2b). Obvious intrusions of high bSi plumes into the deep are observed at entirely ice-covered stations, especially at Stations 38 and 43.

3.1.3 Lithogenic Particles

As the tracer for lithogenic materials, particulate aluminum (pAl) concentrations are much higher over the shelf/slope than in the basin (Figures 1.2c & 1.3c). Shelf and slope pAl concentrations can reach as high as 5.98×10^{3} μmol/L for SSF (mean ± s.d. = $7.14\times10^{2} \pm 1.52\times10^{3}$ μmol/L; n=33) and 2.49×10^{3} μmol/L for LSF ($3.01\times10^{2} \pm 5.73\times10^{2}$ μmol/L; n=31). Prominent plumes of pAl from nepheloid layers over the slopes are transported into the central basin. When compared with labile particulate aluminum (LPAl) at similar locations over the slope (Cid et al., 2012), our total pAl concentrations, varying from 37.1 to 243 nmol/L at corresponding depths of Station 60, are generally about one order of magnitude higher, consistent with a

relatively small proportion of scavenged Al in the Western Arctic as alluded to earlier. In the central basin, unlike the biogenic particle phases, pAl concentrations generally increase with depth. Enrichments of pAl are observed at most stations in the vicinity of the continental margin, seafloor, and ridges, though they are more prominent in the SSF. The most pronounced increase in pAl concentrations in the deep basin exists in the BNLs of Stations 14 and 19 in the Chukchi Abyssal Plain. The SSF pAl concentrations are generally more elevated in the Makarov Basin than those in the Canada Basin. To the best of our knowledge, there have not been any other direct measurements of suspended particulate aluminum in the Western Arctic Ocean.

It is noteworthy that lithogenic materials appear to have unique features at the North Pole in the Amundsen Basin, characterized by an intermediate (~500 m) maximum averaging 7.0 nmol/L, and elevated concentrations below 1500 m, averaging 14.3 nmol/L (Figure 1.2c). The intermediate lithogenic maximum suggests recent interactions with the Eurasian shelves in the Amundsen Basin, such as would be expected from a general circulation of Atlantic water counter-clockwise along the Eurasian margin and along the Lomonosov Ridge out towards the Fram Strait (Jones, 2001; Rudels et al., 1994). Such features are not as prominent in the LSF, presumably because of sinking of large particles during lateral transport (Figure 1.3c). The strong topographic steering of circulation in the deep Amundsen Basin can lead to prominent BNLs, and may explain the elevated lithogenic particles on the Eurasian side of the Lomonosov Ridge (see section 4.1).

3.1.4 Particulate Inorganic Carbon (PIC)

Particulate inorganic carbon (PIC) is much lower in concentration compared to other biogenic particle phases (Figures 1.2d & 1.3d). It confirms previous observations of the absence of coccolithophores and their coccoliths in the Arctic Basin (Honjo et al., 2010; O'Brien et al., 2011; Poulin et al., 2010). On the shelf and slope, concentrations of PIC vary from below the detection limit to 202.6 nmol/L in the SSF and 104.6 nmol/L in the LSF. The highest concentrations of LSF PIC on the shelf/slope regions are observed at the surface of Station 1 in the Bering Sea as a result of biological production. At Stations 61 and 66 over the Hanna Shoal, total PIC concentrations are elevated and approach about 150 nmol/L in the BNLs, whereas are less than 40 nmol/L in the subsurface. These values are within the range of PIC concentrations observed at similar locations over Hanna Shoals in the Chukchi Sea (Balch et al., 2014).

Prominent subsurface maxima of LSF PIC in the central basin are observed at Stations 19 and 26 at about 50 m (Figure 1.3d), consistent with the abundance of planktonic foraminifera tests at 50- 100 m in the Makarov Basin in a recent plankton tow observation (Ding et al., 2014). Indeed, subsurface maxima of LSF PIC are found at most stations, whereas this feature is missing in any other LSF phase (Figure 1.3a-c), suggesting in-situ production of large PIC below the surface. There is virtually no elevation of the LSF PIC near the bottom in the Makarov and Amundsen Basin. In contrast, enrichments of SSF PIC in the deep exist throughout all basins, with the highest concentration observed in resuspended sediments at Station 14 (Figures 1.2d & 1.3d).

3.1.5 Suspended Particulate Mass (SPM)

Suspended particulate mass (SPM) concentrations are characterized by remarkably high concentrations on the shelf (SSF: 414.0 ± 795.4 μg/L; LSF: 168.7 ± 286.0 μg/L) but low in the basin (Figure 1.4). Extremely high SSF SPM concentrations (~3000 μg/L) are found in the bottom nepheloid layers of Stations 2 and 6 (Figure 1.4b). A prominent BNL originates from Station 60 on the Chukchi slope into the Canada Basin at about 600 m with extremely high particle loads (SSF: 791.5 μg/L; LSF: 114.5 μg/L), exceeding the surface SSF SPM concentrations by a factor of four. In general, our measurements of SPM concentrations using the sum of all major particle phases in the Chukchi Sea shelf fall in the range of earlier studies in which SPM was determined gravimetrically (Reynolds et al., 2016). In the central basin, SPM concentrations for both size fractions, especially the SSF, show a general pattern of enhanced concentrations near the boundaries, either the surface, slope, or bottom. Total SPM concentrations range from 1.6 to 6.9 μg/L below 500 m at Station 43 over the Alpha Ridge and are ~2 μg/L near the bottom of the Canada Basin, comparable to measurements reported at similar locations in the central Arctic Basin (Bacon et al., 1989; Ehn et al., 2019). Concentrations of most particle phases are slightly higher in the Makarov Basin, leading to overall higher SSF SPM there (Figures 1.2-1.4).

3.1.6 Fe and Mn oxyhydroxides

Other particle phases with lower concentrations also show some intriguing features in the Western Arctic Ocean. $Fe(OH)_3$ has the highest concentrations over the shelf (SSF: 105 μg/L; LSF:17.0 μg/L) and decreases dramatically offshore (Figures 1.2e & 1.3e). Similar to pAl, $Fe(OH)_3$ concentrations are generally more enriched at the North Pole in the Amundsen Basin throughout the water column than Makarov and Canada basins. Combined with elevated lithogenic particles at corresponding depths, we hypothesize that this deep $Fe(OH)_3$ plume at the North Pole is also sourced from the strong BNLs due to the deep topography-steered circulation.

Unlike all other major particle phases, MnO_2 is the only particle phase that has lower concentrations on the shelf than in the basin (Figures 1.2f & 1.3f). Interestingly, notably high concentrations of MnO_2 appear in the Western Arctic halocline, especially for SSF, and can extend far into the basin interior (Figure 1.2f). High concentrations of MnO_2 from the bottom nepheloid layers at various depths over the slope are also observed.

3.2 Distribution and basin variability of the relative particle composition

Compositional fractions of particles in the SSF and LSF are calculated by normalizing each particle phase by SPM concentrations. Nepheloid layers mostly consist of lithogenic material in the basin (Figure 1.5c), but have both high opal and lithogenic fractions in the shelf and slope (Figure 1.5b-c). The dominance of minerals in the composition of small particles near the seafloor over the Chukchi Sea shelf is also observed with optical backscattering (Reynolds et al., 2016). Relative

concentrations of SSF $Fe(OH)_3$ ($fFe(OH)_3$) are usually enhanced in nepheloid layers (Figure 1.5e). Surface samples in shelf/slope regions are mostly dominated by POM with the median mass fraction (fPOM) of 72.0% (Figure 1.5a).

In the basin, POM dominates the SSF particle composition in the upper 1000 m of the water column and generally decreases with depth (Figure 1.5a & Appendix 1.3). The SSF opal is the next most important phase in the upper water column, accounting for >35% of SSF SPM at several stations (Figure 1.5b & Appendix 1.3). Below 1000 m, SSF particles are generally dominated by lithogenic materials, with a mean fraction of lithogenic particles (fLitho) of 61.6 ± 18.0% (n= 64) (Figure 1.5c & Appendix 1.3). The contributions from $CaCO_3$, $Fe(OH)_3$, and MnO_2 to SSF SPM are much lower compared to other major particle phases (Figure 1.5d-f & Appendix 1.3). The SSF $CaCO_3$ usually accounts for less than 2% of SSF particle mass. Relative concentrations of SSF MnO_2 in the Canadian Basin are generally more than 2%. Plumes of MnO_2 in the Pacific halocline (Figure 1.2f) lead to elevated $fMnO_2$, accounting for ~9% of SSF particle mass. Below the halocline, SSF $fMnO_2$ remains high in the deep, reaching more than 5% at intermediate depths in the Canada Basin (Figure 1.5f). The SSF $Fe(OH)_3$ generally has the lowest contribution to SSF particle mass, but is relatively higher (~2% of particle mass) below 1000 m at the North Pole in the Amundsen Basin. Besides the relatively high $fFe(OH)_3$, the North Pole station is unique in having the lowest fraction of MnO_2 ($fMnO_2$).

In the LSF, POM is significantly less abundant than in the SSF overall (t-test; $p< 0.001$), and only accounts for 20.5 ± 13.4% (n=30) of LSF SPM over the shelf/slope.

The patchier distribution of LSF fPOM (Figure 1.6a) partly results from the occasional uneven particle distribution on deep LSF filters. It is interesting that the LSF fraction of POM does not decrease with depth as quickly as that observed in the SSF (Figure 1.6a & Appendix 1.3). The LSF opal is of a greater fraction than SSF ($p < 0.001$). In the central basin, LSF opal accounts for 48.0 ± 15.9% (n= 111) of LSF particle mass in the upper 1000 m. High values of the fraction of opal (fOpal) (>60%) can extend to more than 1000 m at Stations 38 and 43 (Figure 1.6b). The LSF fOpal is similar in the Amundsen and Canada Basins, and both decrease rapidly with depth (Appendix 1.3), especially at intermediate depths. The relative concentrations of lithogenic particles below 1000 m in the LSF (46.0 ± 20.1%; n= 66) are significantly less than in the SSF ($p < 0.001$), but lithogenic particles still dominate particle composition of large particles in the deep (Figure 1.6c & Appendix 1.3). Compared to SSF particles, what is also evident is that low LSF fLitho (<10%) in the surface extends deeper into the interior, suggesting that large particles derived from surface production with low fLitho are sinking. Similar to the SSF, fLitho in the LSF is consistently elevated below 1900 m at the North Pole in the Amundsen Basin (Figures 1.5c, 1.6c & Appendix 1.3). The LSF fraction of $CaCO_3$ is much higher than SSF $fCaCO_3$ ($p < 0.001$). In the Canada Basin between 1000 and 2500 m, $fCaCO_3$ often makes up ~40% of particle mass (Figure 1.6d); this is due to both slightly enhanced LSF CaCO3 but also very low LSF SPM. The LSF $Fe(OH)_3$ is typically a small portion of the LSF SPM (Figure 1.6e).

Although LSF $fMnO_2$ does not have halocline enrichments, it is similar to SSF for making up a relatively high fraction (>4 %) of SPM below 1000 m (Figures 1.5f,

1.6f & Appendix 1.3). We hypothesize that high $fMnO_2$ in the deep Canada Basin partly explains the drawdown of rare earth elements below 1000 m when compared to its source from the Atlantic Ocean (Yang & Haley, 2016). The source of high MnO_2 in the central Arctic Basin is discussed in section 4.2. The lowest LSF and SSF $fMnO_2$ in the deep are both found in the Amundsen Basin (Appendix 1.3).

3.3 Distributions of POC-$\delta^{13}C$ and C/N ratios in the Western Arctic Ocean

The carbon isotopic composition of POC (POC-$\delta^{13}C$) in both SSF and LSF is heavier on the shelf than in the basin (Figure 1.7a-b). Such contrasting shelf and basin differences in the surface POC-$\delta^{13}C$ are in good agreement with previous measurements reported in the Western Arctic Ocean (Zhang et al., 2012). In shelf/slope regions, SSF POC-$\delta^{13}C$ is -23.9 ± 1.8‰ (n= 21) and LSF $\delta^{13}C$ is -24.8 ± 2.2‰ (n= 24). The SSF POC-$\delta^{13}C$ over the slope at 121 m at Station 10 is -21.3‰ (Figure 1.7b), closely resembling the value of -21.2‰ reported in the Chukchi Sea sediments (Naidu et al., 1993). The most enriched LSF $\delta^{13}C$ of -20.2‰ is observed at the surface at Station 6 (Figure 1.7a), comparable to values reported over the Chukchi Shelf (Gradinger, 2009; Zhang et al., 2012).

In the basin, the most striking feature found is the extremely depleted $\delta^{13}C$ in the Polar Mixed Layer (PML), as low as -32‰, in both size fractions in the basin (Figure 1.7a-b). Such depleted surface $\delta^{13}C$ values were also observed in the Arctic Ocean in several other studies (Alling et al., 2012; Brown et al., 2014; Goñi et al., 2005; Griffith et al., 2012; Pineault et al., 2013; Winterfeld et al., 2015). Below the PML,

both SSF and LSF POC-$\delta^{13}C$ are more enriched close to the margin than in the central basin, and isotopically enriched POC-$\delta^{13}C$ values appear to extend into the interior.

Both SSF and LSF C/N molar ratios on the shelf and slope (SSF: 6.5 ± 1.1; LSF: 8.5 ± 1.9) are similar to the typical Redfield Ratio (~6.6) (Redfield, 1963) and a revised global estimate of C/N ratio (~8.3) by Sterner et al. (2008), respectively (Appendix 1.4). In the basin, overall SSF and LSF C/N molar ratios are 6.4 ± 2.6 and 11.2 ± 4.4, respectively. The SSF C/N molar ratios (7.0 ± 0.9) in the upper 200 m are generally comparable to the Redfield Ratio but significantly lower compared to LSF C/N ratios (10.1 ± 1.6; $p < 0.001$). The LSF C/N ratios at the North Pole (<200 m), 9.4 ± 0.9 (n=4), are similar to C/N ratios in large sinking particles collected in the upper 200 m of the Amundsen Basin (Tamelander et al., 2013). The C/N ratios are also comparable to values reported in total suspended particles in the nearby Chukchi Sea and central Arctic Ocean (Frigstad et al., 2014). Below the surface, SSF C/N ratios generally decrease with depth, whereas LSF C/N ratios increase with depth in the upper 3000 m and drop below 3000 m (Appendix 1.4). Indeed, high C/N ratios in export fluxes in the deep Canada Basin were detected in several sediment trap studies (Honjo et al., 2010; O'Brien et al., 2006). It is also interesting to note that in the deep ocean, the Makarov Basin generally has higher C/N ratios in both size fractions compared to those in the Canada Basin (Appendix 1.4).

4. Discussion

Several unique behaviors of particles in the Western Arctic Ocean are noticeable, including the abundance of lithogenic particles in the deep ocean, different distributions between shelf and basin, and contributions from sea ice algae and/or rivers. Sections below will further discuss these with respect to sources, sinks, and internal cycles.

4.1 Origin of lithogenic particles in the Arctic Ocean

The high lithogenic contributions to deep particles in the Arctic basin demands some attention, especially since the Arctic Ocean is away from primary dust sources, and atmospheric input only plays a minor role in the distribution of lithogenic elements, such as Al (Marsay et al., 2018). Particulate aluminum (pAl) was used previously as a tracer for sediment resuspension in the deep Canada Basin (Hwang et al., 2015). Here we define nepheloid layers as elevations in particulate aluminum concentrations above 9 and 1 nmol/L for SSF and LSF, respectively (Figures 1.2 & 1.3). These nepheloid layers, especially those below 1000 m, are characterized by high lithogenic contents, 68.7 ± 8.7% (n=15) and 78.0 ± 7.9% (n=15) in the LSF and SSF, respectively (Figures 1.5c & 1.6c). The thickness of these nepheloid layers varies from about 100 m to more than 1000 m in both size fractions. It is also noticeable that nepheloid layers below 3000 m are more abundant and widespread in large particles than in small particles.

Newly settled sediments from rivers and biological production on the Arctic shelf are readily remobilized (O'Brien et al., 2011). Resuspension of shelf sediments into benthic layers facilitates the lateral transport into the slope and basin. The

mechanisms involved in such transport include thermohaline convection (Forest et al., 2015; Forest et al., 2007; Forest et al., 2008), current surges (Forest et al., 2016; Forest et al., 2015; Forest et al., 2007; Forest et al., 2008), wind-driven upwelling and downwelling (Forest et al., 2016; Forest et al., 2015; O'Brien et al., 2011), mesoscale eddies (Ashjian et al., 2005; Forest et al., 2015; Forest et al., 2008; Kadko et al., 2008; Llinás et al., 2009; Mathis et al., 2007; O'Brien et al., 2011; O'Brien et al., 2013; Pickart et al., 2005; Watanabe et al., 2014), and dirty sea ice (e.g., Darby, 2003; Dethleff, 2005; Eicken et al., 1997). Internal waves in the Arctic Ocean can also be of significance locally in transporting particles, such as in the eastern Fram Strait (Sanchez-Vidal et al., 2015), but are weaker compared to those at low latitudes (e.g., D'Asaro & Morison, 1992; Guthrie et al., 2013). Sediment-rich dense shelf water incorporates resuspended sediments over the slope, cascades downslope, and ultimately is advected along an isopycnal off the slope (e.g., Forest et al., 2007; Shapiro et al., 2003). We speculate that density-driven shelf water cascading in winter might be the major source of high lithogenic particles in the central Arctic Basin. Other processes, such as cascading events in different seasons (Ivanov et al., 2004), and the seasonal offset between major convection events and concentrations of suspended shelf sediments (Kipp et al., 2020), however, could also contribute to the lateral lithogenic fluxes.

Intermediate nepheloid layers (INLs) emanating from the continental slope with enrichments in both size fractions of pAl (Figures 1.2-1.3, 1.5c & 1.6c) are ubiquitous at mid-depth, offering compelling evidence for the lateral transport of suspended particles in the Arctic Ocean. The transport of particles into the interior basin appears

to occur in the form of extensive clouds, and its intensity varies with depth (Hwang et al., 2015). The dense water formed in coastal polynyas close to the Barrow Canyon (Cavalieri & Martin, 1994; Weingartner et al., 1998; Winsor & Björk, 2000) and steep topography could augment sediment transport into the deep. Indeed, more pronounced INLs on the slope of the southbound leg with high concentrations and fractions of lithogenic contents at all depths are observed (Figures 1.2-1.3, 1.5c & 1.6c), although we cannot discount the possibility that this is just an artifact of different sampling resolutions.

In the deep Arctic basins, sediments are often transported by turbidity currents (Campbell & Clark, 1977; Hunkins & Kutschale, 1965; Stein & Fahl, 2004; Wahsner et al., 1999), sometimes hundreds of kilometers in the Canada Basin before being terminated by hills or ridges, such as the Alpha Ridge (Mosher et al., 2012). Despite acting as barriers to terminate sediments transported by turbidity currents, rough topographic features can also generate BNLs as they can alter bottom current velocities over seamounts and abyssal hills (Turnewitsch et al., 2013). Indeed, the North Pole station in the Amundsen Basin has the strongest BNLs observed in the central Arctic because of the influence of the Lomonosov Ridge. Likewise, the more complicated topography in the Makarov Basin relative to the Canada Basin leads to more intense bottom nepheloid layers (Figures 1.5c & 1.6c). It is also noteworthy that BNLs over the Mendeleev Ridge are more prominent than those over the Alpha Ridge, probably as a result of faster bottom currents (Hunkins et al., 1969) and/or the closer proximity of the continental margins to the Mendeleev Ridge.

4.2 Shelf sources of Fe and Mn oxyhydroxides to the Western Arctic basin

High concentrations of manganese oxides in the halocline, especially in the SSF, are worth noting (Figures 1.2f & 1.3f). Compared with the previous two U.S. GEOTRACES cruises in the North Atlantic and East Pacific, both absolute and relative concentrations of manganese oxides in the Western Arctic basin are generally higher, almost an order of magnitude higher than even the hydrothermal input from the East Pacific Rise (Lam et al., 2018; Lam et al., 2015). What is the source of such high manganese oxides in the Arctic?

Primary productivity in the Chukchi Sea is among the highest in the Arctic Ocean and orders of magnitude higher than in the central Arctic basin (e.g., Codispoti et al., 2013; Grebmeier et al., 2006; Springer & Mcroy, 1993). Extremely high POC export fluxes are observed in the shallow Chukchi Sea (Black, 2018; Lalande et al., 2007; Lepore et al., 2007; Moran et al., 1997; Moran et al., 2005). The oxidization of organic matter in these sediments depletes oxygen and requires alternate electron acceptors such as nitrate (Granger et al., 2018), and Mn and Fe oxides (Aguilar-Islas et al., 2013; Cid et al., 2012; Froelich et al., 1979; Hioki et al., 2014; Kondo et al., 2016; Nakayama et al., 2011; Nishimura et al., 2012; Vieira et al., 2019). Reductively dissolved manganese (Mn^{2+} and/or Mn^{3+}) and iron (Fe^{2+}) are generated in porewater and diffuse into the overlying seawater (e.g., Elrod et al., 2004; Heller, 2020; Lohan & Bruland, 2008; Madison et al., 2013; Oldham et al., 2017; Richard et al., 2013). Assuming simple oxidation kinetics of Fe(II) by O_2 (Millero et al., 1987) and conditions

in near-bottom waters of Station 66 on the Chukchi shelf (pH 7.79, S= 31.5 psu, T= 1.38°C, O_2= 344 μmol/kg), the oxidation half life for Fe(II) is 5.5 hours, which is shorter than the water mass residence time on the shelf (Woodgate, 2018). The fast oxidation kinetics of dissolved Fe(II) in oxygenated waters results in local oxidation and precipitation of Fe at the sediment/water interface or in the water column near the shelf/slope regions (Aguilar-Islas et al., 2013; Santana-Casiano et al., 2005), whereas the slow oxidation kinetics of Mn(II) allows for the transport of dissolved Mn to the slope and basin before it re-precipitates (Morgan, 2005; Richard et al., 2013). Along-shelf currents, together with mid-depth circulation, facilitate the lateral transport of Mn into the interior (Ye et al., 2019).

Our data show that both LSF and SSF $Fe(OH)_3$ have high concentrations in the shelf and slope regions and decrease rapidly towards the basin (Figures 1.2e & 1.3e). As described above, this could be from in-situ oxidation and precipitation within the water column, or resuspension of sedimentary $Fe(OH)_3$ on the shelf. In contrast, shelf MnO_2 concentrations are low, with no MnO_2 detected within prominent bottom nepheloid layers at shelf Stations 6 and 61, but MnO_2 concentrations in slope nepheloid layers are much higher (Figures 1.2f & 1.3f). Our observations are in good agreement with a recent study illustrating a nearly 100% export of dissolved Mn but a much less effective transport of dissolved Fe off the shelf into the central Arctic Basin (Vieira et al., 2019). The shelf depletion and slope/basin enrichment of MnO_2 observed in the water column are also consistent with a previous study of surface sediments by Macdonald and Gobeil (2012) where they showed an interesting pattern of particulate

Mn distribution in the Western Arctic Ocean: there was virtually no non-lithogenic particulate Mn (MnO_2) in shelf sediments, higher MnO_2 in basin sediments, and the highest values at slope stations. Interestingly, high concentrations of MnO_2 in both size fractions appear and persist in the Pacific-derived halocline in the basin, with the highest in the Chukchi Abyssal Plain (Figures 1.2f & 1.3f). The discontinuity in the distribution of MnO_2, especially in the SSF, can be attributed to not sampling along the MnO_2 transport pathway, and episodic transport events, such as mesoscale eddies (Kadko et al., 2008; Pickart et al., 2005; Zhao et al., 2014). Our preliminary work of particulate manganese speciation using synchrotron-based X-ray absorption spectroscopy supports the lack of authigenic Mn(III/IV) oxides on the shelf and dominance of Mn(III/IV) oxides at the slope and basin stations. Taken together, we hypothesize that most particulate Mn in the central Arctic Basin are authigenic Mn(III/IV) oxides that formed in situ in the water column, likely over the continental slope, once the Pacific inflow subducted from the shelf into the interior. These Mn oxides are transported laterally within the Pacific-derived halocline before they finally sink to the deep ocean. Manganese oxides in the Arctic halocline and deep water lead to strong scavenging of various particle-reactive TEIs, including dissolved cobalt, vanadium, ^{210}Po and ^{210}Pb (Bam et al., 2020; Bundy et al., 2020; Whitmore et al., 2019). This hypothesis is consistent with the ubiquitous occurrence of dark brown layers of sedimentary Mn oxides during interglacial times in the central Arctic Ocean (e.g., Löwemark et al., 2014; März et al., 2011).

The observation of no MnO_2 formation on the shelf is intriguing, given extremely high concentrations of ambient dissolved Mn (Bundy et al., 2020; Hatta & Measures, 2016; Jensen et al., 2018; Kondo et al., 2016; Vieira et al., 2019). It is likely to result from one or more of the following: 1) the loss of Mn oxides during photoreduction; 2) the incompleteness of Mn oxidation due to its slow oxidation kinetics; and 3) the inhibition of Mn oxidation by H_2O_2. Firstly, the loss of Mn oxides is likely to be faster than their formation due to Mn photoreduction at the surface of the Chukchi Sea. Direct photoreduction of Mn oxides is thermodynamically feasible at seawater pH (Sherman, 2005), as is the indirect reduction of Mn oxides mediated by humic acid in the presence of sunlight (Spokes & Liss, 1995). In the photic zone of subtropical waters, photoreduction rates of Mn oxides exceed the microbial Mn(II) oxidation rate (Sunda & Huntsman, 1988; Sunda et al., 1983), leading to high concentrations of dissolved Mn^{2+} in the surface. Accordingly, Mn oxides might only be formed when water parcels exit the upper, well-illuminated Arctic shelf and enter the dark halocline. The importance of photoreduction in the Western Arctic Ocean is further supported by higher concentrations of SSF MnO_2 over the shelf in the southbound leg, sampled in October with limited light, compared to the northbound leg (Figure 1.2f), sampled in August with 24-h light, where light penetrated the water column to within ~10 m of the sediments at Station 6 on the Chukchi shelf (Landing et al., 2017). Secondly, the time scale of the oxidation of dissolved Mn on the Chukchi Shelf may be long relative to the ~4.5 month residence time of water masses in the Chukchi Sea (Woodgate, 2018), preventing precipitation of MnO_2 on the shelf. Mn

oxidation is microbially mediated and may thus be a function of temperature. For example, the Mn(II) oxidation rate by the Mn-oxidizing bacteria, marine *Bacillus* sp. SG-1, was found to decrease with temperature according to the Arrhenius equation (Toyoda & Tebo, 2016). The cold temperatures on the Arctic shelf waters may thus further slow microbial Mn(II) oxidation compared to surface waters in non-polar regions. Lastly, Mn oxidation and reduction are also closely coupled with reactive oxygen species (ROS) (Hansel et al., 2012; Learman et al., 2013; Learman et al., 2011a; Learman et al., 2011b), which can be photochemically or biologically produced. For example, hydrogen peroxide (H_2O_2) is known to inhibit the formation of Mn(IV) oxides through a back reaction with Mn(III) (Learman et al., 2013). Although cold temperatures and lower light levels in Arctic waters would be expected to decrease photochemical H_2O_2 production rates compared to low latitudes (Kieber et al., 2014; Yocis et al., 2000), ROS produced by phytoplankton (Diaz & Plummer, 2018; Hansard et al., 2010; Rose et al., 2010; Rose et al., 2008; Rusak et al., 2011) and marine heterotrophic bacteria (Diaz et al., 2013; Learman et al., 2011a; Learman et al., 2011b) could be important. Future studies on the coupling between Mn and ROS are necessary to help fully understand the redox cycles of Mn in the Arctic.

4.3 Insights on the C cycle in the Western Arctic Ocean

4.3.1 Determinations of carbon sources in surface waters

The most striking observation in our dataset is the contrast between the extremely depleted POC-$\delta^{13}C$ values in the surface waters of the Arctic basin, and the

more enriched POC-$\delta^{13}C$ values of the shelf and slope (Figure 1.7). The temperature may play a crucial role in giving rise to distinct shelf and basin end members, as it influences concentrations of dissolved CO_2 in the seawater (e.g., Rau et al., 1989) as well as growth rates (e.g., Fry, 1996). In the specific case of the Western Arctic Ocean, the temperature effect on isotopic fractionation might not reflect the dissolved CO_2 concentration, since aqueous CO_2 and isotope fractionation do not correlate significantly (Brown et al., 2014). Our dataset shows the most depleted carbon isotopic values at the surface associated with the lowest temperature and nutrients in the Arctic basin, and more enriched POC-$\delta^{13}C$ values on the shelf and slope reflect either higher temperature or nutrients in general (Appendix 1.5). We suggest the basinward decrease in the carbon isotopic values to result at least in part from the decrease in phytoplankton growth rates in the basin compared to the shelf, due to lower nutrient concentrations (Benthien et al., 2002; Bidigare et al., 1997; Eek et al., 1999; Riebesell et al., 2000) and lower temperature (Fry, 1996), which is consistent with the significant correlation between POC-$\delta^{13}C$ and photosynthetic rates found along a shelf-basin transect in the Western Arctic Ocean (Brown et al., 2014). Indeed, several investigations have also indicated potential connections between low POC-$\delta^{13}C$ in the Arctic basin and slow phytoplankton growth rates (Griffith et al., 2012; Pineault et al., 2013; Tolosa et al., 2013).

A number of investigators have attempted to use the carbon isotopic signatures of potential carbon end-members, including terrestrial sources from rivers and coastal erosion, and marine sources from sea ice algae and high latitude marine phytoplankton,

to trace carbon sources to the Arctic Ocean (Belicka & Harvey, 2009; Goñi et al., 2013; Honjo et al., 2010; Koziorowska et al., 2016; Magen et al., 2010; Naidu et al., 2000; Schubert & Calvert, 2001; Vonk et al., 2012; Vonk et al., 2014). The isotopic signatures of different end members are overlapping (Connelly et al., 2012; Goñi et al., 2005; Gradinger, 2009; Guo & Macdonald, 2006; Iken et al., 2005; McClelland et al., 2016; Parsons et al., 1989; Pineault et al., 2013; Rachold & Hubberten, 1999; Sánchez-García et al., 2011; Stein & Macdonald, 2004; Tremblay et al., 2006b), however, making it difficult to deconvolve sources unambiguously (Figure 1.7e). POC-$\delta^{13}C$ values in waters with high river inputs and slow phytoplankton growth rates, defined as upper 50 m basin samples with the fraction meteoric water (fMET) > 0.1, phosphate < 1 μmol/kg phosphate, and temperature < 0 ˚C, fall within the range of riverine POC (Figure 1.7e). Previous studies have suggested the importance of riverine POC in the Arctic Ocean (Brown et al., 2014; Goñi et al., 2005; Griffith et al., 2012), as Arctic rivers bring in isotopically light organic carbon from C_3 terrestrial vegetation at high latitudes (Goñi et al., 2005; Meyers, 1997; O'Leary, 1988), with an average of about -30‰ in suspended POC from six major rivers in the Arctic (McClelland et al., 2016). Sea ice algae collected in this study at ice Station 46 demonstrate quite depleted POC-$\delta^{13}C$ as well, -28.3‰, comparable to values reported by Pineault et al. (2013) and Iken et al. (2005), which were in the range of -27.1 to 11.4‰ and -28.3 to -24.7‰, respectively, but cannot explain our most depleted observations in the basin samples (Figure 1.7e).

Correlations between POC-$\delta^{13}C$, the fraction of meteoric water, and the fraction of sea ice melting (Pasqualini et al., 2017) in the upper 50 m are examined to further

test the importance of contributions from riverine POC and sea ice algae. We speculate that external carbon sources cannot help explain the difference between shelf and basin POC-$\delta^{13}C$. Our data show no significant correlation between POC-$\delta^{13}C$ and the fraction of meteoric water in the upper 50 m, suggesting that rivers do not directly supply isotopically depleted POC into the surface Western Arctic (Appendix 1.6). Even within the transpolar drift (TPD), where riverine influences with various dissolved trace elements and dissolved organic matter are most profound (Charette et al., 2020; Kipp et al., 2018; Shen et al., 2016) due to a short advection time scale from the East Siberia Seas (Kipp et al., 2018), no direct input of riverine POC to the central Arctic is observed (Appendix 1.6). Likewise, no significant correlations are found between the fraction of sea ice melt and POC-$\delta^{13}C$ in the central Arctic Ocean (data not shown), consistent with the observation of limited influence from the ice melting on the surface mixed layer POC-$\delta^{13}C$ in the Western Arctic Ocean (Brown et al., 2014).

Although DIC-$\delta^{13}C$ of Arctic rivers can be quite depleted due to the degradation of terrestrial organic carbon (e.g., around -8‰ in the Lena River) (Alling et al., 2012), riverine DIC-$\delta^{13}C$ is enriched during the mixing between river and Arctic surface seawater, resulting in the most depleted Arctic surface signatures found within the TPD of ~0.5‰ (Ko & Quay, 2020). Assuming a classic isotope fractionation of -24‰ between DIC and phytoplankton (Alling et al., 2012; Mook & Tan, 1991), this slightly depleted river-influenced DIC substrate would not explain the observed POC-$\delta^{13}C$ of ~-30‰ in the PML.

On the whole, we hypothesize that the slow phytoplankton growth rate is the main controlling factor of the extremely depleted carbon isotopic signatures observed throughout the PML in the central Western Arctic. It is believed that inputs from sea ice and rivers, either directly as riverine POC, or indirectly as DIC substrates for photosynthesis, are of minor significance in determining the characteristic values of surface POC-$\delta^{13}C$ in the central basin.

4.3.2 Carbon sources to the subsurface

Because of the dramatic difference in the POC-$\delta^{13}C$ of phytoplankton on the Chukchi shelf (~-24.0‰) compared to phytoplankton in the Western Arctic basin (~-29.5‰), we can use these signatures to diagnose lateral vs. vertical transport of POC in each size fraction to the mesopelagic. The LSF POC-$\delta^{13}C$ values at depth in the central basin are as depleted as the surface (Figure 1.7a). In contrast, the SSF $\delta^{13}C$ values fall between enriched isotopic values from the shelf/slope and depleted values from the surface (Figure 1.7b). If we ignore potential isotopic enrichments due to hydrolytic fractionation (Close, 2019) and treat mesopelagic POC as a two end-member mixing curve between shelf/slope derived enriched POC-$\delta^{13}C$ and PML derived depleted POC-$\delta^{13}C$ in the upper 50 m, we can estimate the contribution from lateral transport for each size fraction in the upper 600 m throughout the basin (Figure 1.7c-d). The median of POC-$\delta^{13}C$ for all shelf/slope stations except Station 1 (LSF: -24.6‰; SSF: -23.3‰) and the upper 50 m for all basin stations (LSF: -29.1‰; SSF: -29.5‰) are used as two representative end members.

Overall, the fraction of laterally-sourced POC is higher in the SSF than in the LSF, consistent with a generally faster sinking of large particles due to larger radii. Near the margin, high fractions of laterally-sourced POC are detected in both size fractions (Figure 1.7c-d). At Stations 14 and 19, more than 80% of the SSF POC in the upper 600 m are sourced from the shelf and slope. Strong lateral influences are still observed in the central basin for the SSF, accounting for up to 87% of the POC at Station 48 (Figure 1.7c). At Station 30, a mean of 46% of subsurface SSF POC in the basin is derived from lateral transport from the shelf/slope, and 54% is derived from vertical sinking from the PML.

In the center part of the Arctic Basin between Station 26 and 56, the fraction of LSF POC sourced from the shelf/slope is very low, averaging 12%, implying the dominance of vertically sinking LSF particles (Figure 1.7c). These POC-δ^{13}C-based conclusions are consistent with those based on low LSF fLitho proposed in section 3.2 (Figure 1.6c).

The differences between LSF and SSF POC-δ^{13}C in the subsurface are unlikely to originate from different isotope fractionations for small vs. large phytoplankton (Burkhardt et al., 1999; Popp et al., 1998; Rau et al., 1996). The LSF and SSF POC-δ^{13}C in the central basin differ by only ~0.5‰ in the PML but by ~2-3‰ in the subsurface. We hypothesize that the increasing absolute differences between two size fractions with depth in the central basin reflect the lateral input of heavier POC-δ^{13}C in the SSF and little subsurface exchange between LSF and SSF.

4.3.3 Carbon sources to the deep Arctic interior

Unfortunately, carbon stable isotope data deeper than 600 m were below the detection limit due to the extremely low abundance of POC. The C/N ratios provide more insights on the provenance of carbon into the deep Western Arctic Basin. It was noted that high C/N values on the Beaufort Shelf could reflect the influence of the refractory materials from land (O'Brien et al., 2006). Compared to most other studies on elemental composition, our sampling covers full ocean depth, and concentrations extend over 1-3 orders of magnitude, which helps resolve the behavior of carbon and nitrogen at very low concentrations. Here, we used two different methods to interpret the C/N stoichiometry: 1) determining the slope and intercept of POC vs. PN in all particles; 2) calculating C/N ratios using POC and PN concentrations directly.

In order to take into account different pools of organic matter, we applied a linear model by plotting POC vs. PN in sinking particles following Lamborg et al. (2008), with the slope indicating the ratio of moles of C per mole of N lost to remineralization, and the intercept indicating the more refractory component (Figure 1.8). The slope should approach the average C/N ratios of the particles if the intercept is near zero. However, a significant intercept could lead to differences between the slope and ratios, especially at low concentrations of POC and PN. For example, one might have a C:N slope that is 6.6, the canonical Redfield value, but a positive intercept, indicating that there is a pool of POC that remains even after all PN has been remineralized. Because of this pool of refractory POC, calculated C/N ratios would be increasingly higher than Redfield as POC and PN concentrations decrease. Indeed,

particles with high C/N ratios are often dominated by land-derived biomacromolecules, such as lignin and cellulose (Hedges et al., 1986). In another example, one might find a C:N slope that is higher than Redfield, but with no (a zero) intercept. In this case, there is no refractory component, but yet both the slope and the ratio, which would approach each other, would be above Redfield, for example as a result of nutrient limitation (Copin-Montégut, 2000; Gervais & Riebesell, 2001; Körtzinger et al., 2001).

Both SSF and LSF in the Western Arctic Basin show a very good correlation between POC and PN (R^2= 0.97 and 0.98 in SSF and LSF, respectively) (Figure 1.8). The slopes in both size fractions (SSF: 7.4 ± 0.1; LSF: 8.7 ± 0.1) are significantly (95% confidence) above the typical Redfield value of 6.6 (Redfield, 1963). The intercept in the SSF is negative ($-1.9\times10^{-2} \pm 4.6\times10^{-3}$), suggesting a refractory PN component, whereas LSF has a slightly positive intercept ($2.1\times10^{-3} \pm 6.2\times10^{-4}$), indicating a refractory POC pool.

The POC: PN relationship for the LSF shows a change in slope at low POC and PN (Figure 1.8a). Low concentrations of LSF POC (< 8.0×10^{-3} μM) and PN (< 6.0×10^{-4} μM), typically from deep (>3000 m) waters, have a steeper C:N slope (12.6 ± 1.2) and an intercept ($-3.4\times10^{-4}\pm 4.5\times10^{-4}$) that is not statistically different from zero. This suggests the importance of a different population of large organic particles in deep waters with higher C/N ratios than particles that dominate in shallower waters. Indeed, this pool of large organic matter in the deep Canada Basin is characterized by much older radiocarbon ages of sinking particles than suspended particles (Griffith et al., 2012). The median C/N ratio calculated directly from LSF POC and PN concentrations

in the basin is 10.4, in between the characteristic C:N slopes for shallow (8.7) and deep (12.6) large particles. The elevated LSF C/N ratios observed in the deep (Appendix 1.4) could be explained by the increasing predominance of refractory carbon with depth in the upper 3000 m as fresh organic matter, with lower C/N ratios, is remineralized during sinking. This refractory carbon pool can originate from either vertical or lateral processes: it can be derived from C-rich sea ice algae, or terrestrial inputs from rivers and/or surrounding margins (Engel & Passow, 2001; Frigstad et al., 2014; Hwang et al., 2008; Meiners et al., 2003).

A single slope applies to all SSF data regardless of the abundance (Figure 1.8b). The apparent refractory pool of nitrogen in small particles as suggested by the negative intercept in the SSF could be explained by a pool of inorganic nitrogen, since no discrimination between inorganic and organic nitrogen was made in the measurements. Schubert and Calvert (2001) found that inorganic nitrogen, in the form of ammonium bound to the clay illite, represented 34%- 63% of the total nitrogen in surface sediments in the central Arctic basin. The presumed longer residence time and much higher lithogenic concentrations in SSF (Figure 1.2c) could explain why more apparent inorganic nitrogen sorption is seen in the SSF compared to the LSF. We estimated the contribution of inorganic nitrogen to C/N ratios in SSF particles in the Western Arctic Ocean by applying the minimum (34%) and maximum (63%) fraction of adsorbed inorganic nitrogen to the lithogenic fraction (fLitho) of small particles, which generally increases with depth (Figure 1.6c & Appendix 1.3). Corrections for inorganic nitrogen do not lead to significant changes to the C:N slope of SSF (7.3 ± 0.1), nor do they

generate a change in the slopes as was seen for deep LSF particles (Appendix 1.7). However, the inorganic nitrogen corrections do lead to intercepts that are closer to zero (correction using 34%: $-6.2\times10^{-3} \pm 4.3\times10^{-3}$; correction using 63%: $4.1\times10^{-3} \pm 4.1\times10^{-3}$), arguing against a significant refractory organic nitrogen pool.

A power function model, as an alternative to the linear model, has been used in several studies to take into account the change in C/N ratios with varying POC and PN concentrations (Frigstad et al., 2014; Sterner et al., 2008). The power relationships between POC and PN in both size fractions (SSF with minimum and maximum inorganic N correction: $POC= 8.23\times PN^{1.06}$ & $POC= 6.78\times PN^{0.980}$; LSF with no correction: $POC= 6.78\times PN^{0.930}$; Figure 1.8 & Appendix 1.7) are generally similar to those of previous studies in the Arctic Ocean (Frigstad et al., 2014; Goñi et al., 2019).

In the SSF, the median of C/N ratios of all basin samples is 6.5. When we correct for inorganic particulate nitrogen as described above, the corrections increase the median C/N ratios to 6.9 to 7.5, depending on the magnitude of the correction (Appendix 1.4), comparable to the slope of SSF POC and PN in the basin (Figure 1.8b). It is interesting that regardless of corrections, there seem to be three pools of SSF C/N ratios: high in nepheloid layers, low in the deep ocean, and moderate in the surface, none of which are Redfieldian (Appendix 1.4). We speculate that low C/N ratios found below 1000 m in the Canada Basin and below 2000 m in the Makarov and Amundsen Basin are indications of heterotrophic bacteria growing in situ, characterized by low C:N ratios due to widespread carbon limitation (Zimmerman et al., 2014). Given the filter pore size of 1 μm used in this study, bacteria may not have been quantitatively

collected, but particle-associated bacteria in the Arctic Ocean (Garneau et al., 2009; Kellogg & Deming, 2009; Ortega-Retuerta et al., 2012), and clogging of particles on the filter surface, which decreases the effective pore size during sampling, ensure that some portion of bacteria are likely to be captured. Indeed, it has been shown that similar GF/F filters (0.7 μm) capture a significant proportion of bacteria (Hollibaugh et al., 1991; Lee & Fuhrman, 1987).

In general, it can be concluded that both SSF and LSF C/N ratios are above the Redfield ratio in the Western Arctic Basin, with LSF C/N ratios further above Redfield compared to the SSF, especially in the deep basin. The more abundant C/N ratios lower than the Redfield in the SSF results from the dominance of marine heterotrophic bacteria in the deep ocean.

4.4 Potential sources and dissolution of biogenic silica in the Western Arctic Ocean

Sources and sinks of other biogenic particle phases, such as biogenic silica, are also important for understanding changes in the biological pump in a rapidly changing Arctic. Tremblay et al. (2006a) observed minor vertical attenuation in the biogenic silica flux in the upper 150 m in the northern Baffin Bay, in contrast to a rapid decrease in POC flux with depth. Molar ratios of biogenic silica to POC (bSi:POC) are widely used for studying the efficiency of POC export by diatoms (e.g., Benitez-Nelson et al., 2007; Buesseler et al., 2001; Rembauville et al., 2016).

In this study, the bSi:POC ratios (mol: mol) are 0.24 ± 0.07 (n=3) in >1 μm surface particles on the Chukchi Shelf, and increase with depth toward the shelf sediments (Figure 1.9c). For context, surface bSi:POC ratios on the Chukchi Shelf are comparable to those in iron-replete field incubations reported off the California coast (Hutchins & Bruland, 1998). In contrast, our sea ice algae samples collected from ice cores in the central Arctic basin have significantly lower bSi:POC ratios (0.04 ± 0.02; n=3) than the Chukchi Shelf surface ($p < 0.05$). Ice algae bSi:POC ratios are statistically indistinguishable from upper 30 m SSF bSi:POC (0.05 ± 0.02; n=11) in the basin, but are below the range of observed LSF bSi:POC (0.11- 2.28) (Figure 1.9b).

In the water column, the bSi:POC ratios in both size fractions in the basin increase with depth toward maxima generally at or below the halocline, between 150 and 400 m for SSF and between 150 to 800 m for LSF (Figure 1.9a-b). The bSi:POC ratios then decrease with depth to values similar to those found in the upper 30m. The decrease in bSi:POC ratios between the subsurface maxima and the low baseline in the deep (>1000 m) is unexpected, as it implies a faster loss of bSi than POC with depth (Figure 1.9a-b). Possible processes to explain the puzzling decrease in bSi:POC ratios with depth include: 1) a non-steady-state profile in which the subsurface bSi:POC max represents a pulse of sinking particles from previous blooms characterized by high bSi:POC; 2) the lateral transport of high bSi:POC shelf particles in the halocline; 3) fast bSi dissolution in the intermediate water; and 4) inputs of POC in the deep.

First, we examine the possibility that sporadic sinking of sea ice diatoms can contribute to the subsurface bSi:POC maximum, especially in the LSF. The widespread

deposition of the centimeter-sized *Melosira arctica* has been observed in the central Arctic, even in late September (Boetius et al., 2013). Several sediment trap studies also captured the presence of *M. arctica* cells in the Arctic Ocean (Fahl & Nöthig, 2007; Lalande et al., 2014; Zernova et al., 2000). We occasionally observed long filaments of *M. arctica* attached to the bottom of sea ice, but the ice cores processed here had no visual evidence of *M. arctica*. Boetius et al. (2013) estimated Si:P uptake ratios from nutrient inventories at stations that were dominated by *M. arctica,* from which we estimate a bSi:POC of *M. arctica* of 0.15 ± 0.10 (n=5). In the subsurface maximum, measured bSi:POC values in the LSF are generally significantly higher than this (~0.5-2) (Figure 1.9b), suggesting that if a pulse of sinking *M. arctica* is responsible for this feature, it would have to be sinking slowly enough for the POC to be preferentially regenerated, or to be sloughed off from sea ice as empty frustules. The return to low bSi:POC below 1000 m in both size fractions would be explained by this slowly sinking pulse not yet reaching the deep ocean, and/or an increase in the bSi dissolution rate at depth.

Secondly, we examine the plausibility of lateral transport of particles from shelves and slopes characterized by high bSi:POC (Figure 1.9c). How is it possible that shelf and slope-derived particles survive transport for thousands of kilometers within the halocline to the central Arctic? The mean ventilation time scale of the Arctic halocline with respect to the Chukchi Shelf is about 20 years (Kipp et al., 2019), which is too long compared to the time scale of sinking (~months using Stokes sinking velocities for typical diatoms) for halocline bSi to survive transport to the central basin.

Episodic mixing events with much shorter time scales may play a key role in transporting particles into the central basin. For example, eddies in the Western Arctic Ocean, with lifetimes of several months (Kadko et al., 2008; Pickart et al., 2005; Zhao et al., 2014), may promote the lateral transport of shelf-derived particles in the halocline. Moreover, particles in the halocline may have also reached neutral buoyancy due to the existence of exopolysaccharides (e.g., transparent exopolymer particles, TEP) whose density can be lower than that of seawater (Azetsu-Scott & Passow, 2004), thereby extending their residence times (MacIntyre et al., 1995; Mari et al., 2017). Indeed, a high proportion of TEP in organic matter on the Chukchi Shelf has been observed, and it has been suggested that shelf produced TEP has the potential to be transported laterally to the basin in the halocline (Yamada et al., 2015). Because of seasonality in shelf production, the lateral supply of TEP-containing bSi may arrive in pulses. The observed subsurface maxima in bSi:POC may represent a recent pulse of shelf and slope-derived bSi from the current season, leaving the low baseline bSi:POC ratios in the deep unchanged. We speculate that the observed bSi:POC maxima in the subsurface migrate downward as the season progresses.

Thirdly, we examine the hypothesis that bSi dissolves more quickly than POC remineralizes in intermediate waters. Previous attempts to detect in-situ bSi dissolution using Si isotopes in the Western Arctic Ocean were inconclusive (Varela et al., 2016). Based on expected timescales given dissolution kinetics of biogenic silica, we find it conceivable that bSi dissolution rates could be faster than POC remineralization rates at intermediate depths and lead to decreasing bSi:POC. It has long been known that the

dissolution kinetics of bSi in the water column depends strongly on temperature (Hurd & Takahashi, 1983; Kamatani & Riley, 1979) and the degree of opal undersaturation (Van Cappellen & Qiu, 1997). The Atlantic layer at intermediate depths is warmer and has lower dissolved silicate concentrations and thus a higher degree of undersaturation, and should thus have higher bSi dissolution rates (Middag et al., 2009) than the cold, Si-rich Pacific-derived halocline. Dissolution experiments conducted at 2 °C on Norwegian Sea sediment trap samples at 1000 m indicate rate constants of 1.4 yr^{-1} and 2.6 yr^{-1} for the degree of undersaturation from dissolved silicate concentrations of 30 μM in the Pacific halocline and 10 μM in the Atlantic layer, respectively (März et al., 2015; Rickert et al., 2002). Applying an Arrhenius-type temperature dependency and assuming a 60 kJ/mol activation energy (Rickert et al., 2002, equation 10) adjusts these rates to 1.1 yr^{-1} and 2.2 yr^{-1} for the -1.0°C halocline and 0.4°C Atlantic layer (Figure 1b), respectively, or equivalently, e-folding timescales of ~11 months in the halocline and ~5 months in the Atlantic layer. The difference in timescales of dissolution is consistent with better preservation during lateral transport in the halocline than during sinking in the Atlantic layer. However, in order for bSi:POC to decrease with depth, the bSi dissolution rate must be faster than POC remineralization. Inverse estimates of POC remineralization rate constants between 250- 4500 m in the Northwest Atlantic ranged from 0.5- 4.4 yr^{-1}, or a timescale of ~3 months to 2 years (Murnane et al., 1994). Given that bSi dissolution timescales of ~5 months are on the low end of the POC remineralization timescales in the Atlantic layer, a decrease of bSi:POC ratios can occur during sinking below halocline depths.

Lastly, additional sources of particles in the deep ocean characterized by low bSi:POC ratios could also play a role. Unlike at halocline depths where more labile POC from the shallow shelf is degraded quickly and generates high bSi:POC ratios, terrigenous POC from the deep slope transported below the halocline is characterized by slower degradation rates and therefore, could contribute to lower bSi:POC ratios in the deep. Likewise, a substantial contribution from in situ DIC fixation due to chemoautotrophy in the suspended POC pool in the central Arctic basins, accounting for up to 22% at intermediate depths (Griffith et al., 2012), will also help decrease bSi:POC ratios.

To summarize, explaining the distribution of bSi:POC ratios requires the consideration of both vertical and horizontal transport processes. We speculate that the subsurface feature of elevated bSi:POC in both size fractions most likely results from TEP-mediated lateral transport of shelf and slope- derived particles at halocline depths, and subsequent fast dissolution of bSi during sinking through the Atlantic layer below. The broader LSF bSi:POC subsurface maximum compared to SSF (Figure 1.9b) is consistent with expected faster sinking of large particles during lateral transport within the halocline.

5. Summary and Conclusions

The Arctic Ocean is characterized by unique particle composition and concentrations not only in different basins, but also throughout the water column. In most respects, two sub-basins in the Canadian Basin, the Canada and Makarov Basin,

are similar in their major particle composition. The North Pole in the Amundsen Basin is quite different from the Canadian Basin, with its higher absolute and relative concentrations of lithogenic materials and Fe oxyhydroxides. Overall, POM and opal dominate the SSF and LSF SPM in the upper 1000 m, respectively, and lithogenic material is the most abundant particle phase in both size fractions below 1000 m.

We summarize the major processes governing the composition and internal cycling of small and large particles in the Western Arctic in Figure 1.10. Small and large particles not only have distinct compositions, but differ somewhat in their sources and transport. In surface waters, slow phytoplankton growth rates related to cold temperature and low nutrients, lead to extremely depleted carbon isotopic signatures in both LSF and SSF particles in the Polar Mixed Layer. In the subsurface, prominent intermediate nepheloid layers (INLs) detach from the continental slope and are transported laterally into the interior. Enrichments in Mn oxide but deficiencies of Fe oxyhydroxides in the SSF are frequently observed in the well-defined Pacific-derived halocline, as a result of differences in the oxidation kinetics of Mn and Fe. In the deep ocean, turbidity currents are presumed to be one of the important mechanisms to transport particles laterally. Benthic nepheloid layers (BNLs), characterized by high lithogenic materials, are frequently observed close to the continental margins and over the deep-sea ridges.

Although large particle concentrations are low in the central Arctic, their chemical compositions indicate that those that are present do sink: POC-$\delta^{13}C$ data suggest that while small particles in the subsurface in the central basin consist of a

mixture of laterally advected and vertically sinking components, large particles in the upper 500 m are dominated mainly by particles that sank from the surface, possibly in the form of nearly empty diatom frustules. The biological pump in the ice-covered central Arctic Basin may not be particularly strong, but it is not completely ineffective (Honjo et al., 2010). In addition to vertical sinking processes, maximum ratios of bSi:POC at around halocline depths suggest that there could be a lateral supply of bSi-rich, POC-poor particles in the halocline, even for large particles. Hypothesized mechanisms for the long-distance lateral transport of large particles include transparent exopolymer particles (TEP) mediated transport within the halocline through episodic mixing events, such as mesoscale eddies. More evidence on the lateral transport of large particles is given through the elemental stoichiometry. Degraded large POC in the deep (>~3000 m), characterized by high molar C:N ratios (12.6) and extremely old radiocarbon ages (Griffith et al., 2012; Hwang et al., 2008), are likely a mixture of laterally advected particles from surrounding margins (Hwang et al., 2008) and resuspended large particles from sediments or resuspended small particles that might have aggregated. Unlike large particles, C:N ratios in small particles decrease with depth, and together with the POC-$\delta^{13}C$ signatures (Griffith et al., 2012), suggest the increasing importance of bacterial carbon in the deep rather than detrital POC from overlying production, especially in the deep Canada Basin.

Because of the juxtaposition of highly productive shelf waters next to oligotrophic basin waters in the Arctic Ocean, the chemical composition of particles originating from the shelf are distinct from those in the basin and offer a means by

which their contributions can be discerned. We find that both lateral transport and vertical sinking are of significance and exist for both small and large particles, with small and large particles influenced more by lateral transport and vertical sinking, respectively. The lateral process can cover thousands of kilometers in distance, most evident at halocline and in the bottom ~1000 m, even for large particles. It is likely that ongoing and future changes in sea ice extent and seasonality in the Arctic will influence particle sources and transport. We recommend that particle composition be used in future investigations in the Arctic to monitor variations in lateral and vertical processes on a seasonal and yearly basis, thereby helping us understand the change in the biological carbon pump in the context of rapidly changing climate in the Arctic Ocean.

Our work contributes to the growing body of literature on the significance of lateral transport of particles of all types in a wide variety of regions. Previous studies on the lateral transport of particles from the margins into the interior basins have typically examined lithogenic particles in deep waters (e.g., Fahl & Nöthig, 2007; Ho et al., 2011; Honjo, 1982; Honjo et al., 2010; Hwang et al., 2010; Hwang et al., 2008; Hwang et al., 2015) or authigenic Fe and Mn oxides (Lam & Bishop, 2008; Lam et al., 2006) at the shelf break. It is generally more difficult to distinguish laterally transported margin-derived biogenic particles from those produced in the basin, but a few studies have done this in the Northwest Atlantic, the Sea of Okhotsk, and the Canary Current region (Alonso-González et al., 2009; Falkowski et al., 1994; Hwang et al., 2009; Nakatsuka et al., 2004). The simultaneous measurement of lithogenic, authigenic, and

biogenic particle phases provides a number of potential tracers to distinguish lateral from vertical sources, and could potentially be used to understand the significance of the lateral flux in the global ocean.

Acknowledgments

This work was supported by NSFOCE-1535854 to PJL. We would like to thank Greg Cutter, Dave Kadko, Bill Landing, and everyone on board the USCGC icebreaker Healy for well organizing the GN01 Arctic GEOTRACES cruise. We also thank the Oceanographic Data Facility (ODF) at Scripps Institution of Oceanography for providing silicate concentrations. Special thanks to Erin Black, Maija Heller, Lauren Kipp, and Steven Pike in the pump group for helping to collect particle samples. Thanks to Benjamin S. Twining, Peter Morton, and Sara Rauschenberg for providing leachable particulate Al and Fe results (funded by NSFOCE-1435862 to Benjamin S. Twining and NSFOCE-1436019 to Peter L. Morton). The National High Magnetic Field Laboratory is supported by the National Science Foundation through DMR-1644779 and the State of Florida. We thank the editor and two anonymous reviewers for their suggestions and comments which helped improve this manuscript. We sincerely thank Vinicius Amaral, Luna Ewald, Jong-Mi Lee, and Kira Mizell for the continuous assistance in both lab work and data analysis, and Colin Carney of the UCSC Stable Isotope Laboratory and Rob Franks of the UCSC Marine Analytical Laboratory for their assistance with the instruments. Many thanks to Colleen Hansel, Carl Lamborg, and Matthew D. McCarthy for their insights in the discussion. All size-fractionated

particle concentration and composition data described above are available on the Biological and Chemical Oceanography Data Management Office website (https://www.bco-dmo.org/dataset/807340).

References

Aagaard, K., & Carmack, E. C. (1989). The role of sea ice and other fresh water in the Arctic circulation. *Journal of Geophysical Research: Oceans*, *94*(C10), 14485-14498. 10.1029/JC094iC10p14485

Aagaard, K., Fahrbach, E., Meincke, J., & Swift, J. H. (1991). Saline outflow from the Arctic Ocean: Its contribution to the deep waters of the Greenland, Norwegian, and Iceland Seas. *Journal of Geophysical Research: Oceans*, *96*(C11), 20433-20441. https://doi.org/10.1029/91JC02013

Aguilar-Islas, A. M., Rember, R., Nishino, S., Kikuchi, T., & Itoh, M. (2013). Partitioning and lateral transport of iron to the Canada Basin. *Polar Science*, *7*(2), 82-99. https://doi.org/10.1016/j.polar.2012.11.001

Alling, V., Porcelli, D., Mörth, C. M., Anderson, L. G., Sanchez-Garcia, L., Gustafsson, Ö., et al. (2012). Degradation of terrestrial organic carbon, primary production and out-gassing of CO2 in the Laptev and East Siberian Seas as inferred from δ13C values of DIC. *Geochimica et Cosmochimica Acta*, *95*, 143-159. https://doi.org/10.1016/j.gca.2012.07.028

Alonso-González, I. J., Arístegui, J., Vilas, J. C., & Hernández-Guerra, A. (2009). Lateral POC transport and consumption in surface and deep waters of the Canary Current region: A box model study. *Global Biogeochemical Cycles*, *23*(2), n/a-n/a. https://doi.org/10.1029/2008gb003185

Ashjian, C. J., Gallager, S. M., & Plourde, S. (2005). Transport of plankton and particles between the Chukchi and Beaufort Seas during summer 2002, described using a Video Plankton Recorder. *Deep Sea Research Part II: Topical Studies in Oceanography*, *52*(24-26), 3259-3280. https://doi.org/10.1016/j.dsr2.2005.10.012

Azetsu-Scott, K., & Passow, U. (2004). Ascending marine particles: Significance of transparent exopolymer particles (TEP) in the upper ocean. *Limnology and Oceanography*, *49*(3), 741-748. https://doi.org/10.4319/lo.2004.49.3.0741

Bacon, M. P., Huh, C. A., & Moore, R. M. (1989). Vertical profiles of some natural radionuclides over the Alpha Ridge, Arctic Ocean. *Earth and Planetary Science Letters*, *95*(1-2), 15-22. https://doi.org/10.1016/0012-821X(89)90164-7

Balch, W. M., Bowler, B. C., Lubelczyk, L. C., & Stevens, M. W. (2014). Aerial extent, composition, bio-optics and biogeochemistry of a massive under-ice algal bloom in the Arctic. *Deep Sea Research Part II: Topical Studies in Oceanography*, *105*, 42-58. https://doi.org/10.1016/j.dsr2.2014.04.001

Bam, W., Maiti, K., Baskaran, M., Krupp, K., Lam, P. J., & Xiang, Y. (2020). Variability in 210Pb and 210Po partition coefficients (Kd) along the US GEOTRACES Arctic transect. *Marine Chemistry*, *219*, 103749. https://doi.org/10.1016/j.marchem.2020.103749

Barão, L., Vandevenne, F., Clymans, W., Frings, P., Ragueneau, O., Meire, P., et al. (2015). Alkaline-extractable silicon from land to ocean: A challenge for biogenic silicon determination. *Limnology and Oceanography: Methods*, *13*(7), 329-344. https://doi.org/10.1002/lom3.10028

Barrett, P. M., Resing, J. A., Grand, M. M., Measures, C. I., & Landing, W. M. (2018). Trace element composition of suspended particulate matter along three meridional CLIVAR sections in the Indian and Southern Oceans: Impact of scavenging on Al distributions. *Chemical Geology*, *502*, 15-28. https://doi.org/10.1016/j.chemgeo.2018.06.015

Bates, N. R., Hansell, D. A., Moran, S. B., & Codispoti, L. A. (2005). Seasonal and spatial distribution of particulate organic matter (POM) in the Chukchi and Beaufort Seas. *Deep Sea Research Part II: Topical Studies in Oceanography*, *52*(24-26), 3324-3343. https://doi.org/10.1016/j.dsr2.2005.10.003

Bauch, D., Cherniavskaia, E., & Timokhov, L. (2016). Shelf basin exchange along the Siberian continental margin: Modification of Atlantic Water and Lower Halocline Water. *Deep Sea Research Part I: Oceanographic Research Papers*, *115*, 188-198. https://doi.org/10.1016/j.dsr.2016.06.008

Belicka, L. L., & Harvey, H. R. (2009). The sequestration of terrestrial organic carbon in Arctic Ocean sediments: A comparison of methods and implications for regional carbon budgets. *Geochimica et Cosmochimica Acta*, *73*(20), 6231-6248. https://doi.org/10.1016/j.gca.2009.07.020

Benitez-Nelson, C. R., Bidigare, R. R., Dickey, T. D., Landry, M. R., Leonard, C. L., Brown, S. L., et al. (2007). Mesoscale Eddies Drive Increased Silica Export in the Subtropical Pacific Ocean. *Science*, *316*(5827), 1017-1021. 10.1126/science.1136221

Benthien, A., Andersen, N., Schulte, S., Müller, P. J., Schneider, R. R., & Wefer, G. (2002). Carbon isotopic composition of the C37: 2 alkenone in core top sediments of the South Atlantic Ocean: Effects of CO2 and nutrient concentrations. *Global Biogeochemical Cycles*, *16*(1), 12-11. https://doi.org/10.1029/2001GB001433

Berger, C. J. M., Lippiatt, S. M., Lawrence, M. G., & Bruland, K. W. (2008). Application of a chemical leach technique for estimating labile particulate aluminum, iron, and manganese in the Columbia River plume and coastal

waters off Oregon and Washington. *Journal of Geophysical Research: Oceans*, *113*. https://doi.org/10.1029/2007jc004703

Beszczynska-Möller, A., Woodgate, R., Lee, C., Melling, H., & Karcher, M. (2011). A Synthesis of Exchanges Through the Main Oceanic Gateways to the Arctic Ocean. *Oceanography*, *24*(3), 82-99. https://doi.org/10.5670/oceanog.2011.59

Bidigare, R. R., Fluegge, A., Freeman, K. H., Hanson, K. L., Hayes, J. M., Hollander, D., et al. (1997). Consistent fractionation of 13C in nature and in the laboratory: Growth-rate effects in some haptophyte algae. *Global Biogeochemical Cycles*, *11*(2), 279-292. https://doi.org/10.1029/96GB03939

Bishop, J. K. B., Edmond, J. M., Ketten, D. R., Bacon, M. P., & Silker, W. B. (1977). The chemistry, biology, and vertical flux of particulate matter from the upper 400 m of the equatorial Atlantic Ocean. *Deep Sea Research*, *24*(6), 511-548. https://doi.org/10.1016/0146-6291(77)90526-4

Bishop, J. K. B., Lam, P. J., & Wood, T. J. (2012). Getting good particles: Accurate sampling of particles by large volume in-situ filtration. *Limnology and Oceanography: Methods*, *10*(9), 681-710. https://doi.org/10.4319/lom.2012.10.681

Black, E. E. (2018). An investigation of basin-scale controls on upper ocean export and remineralization (Doctoral dissertation). Retrieved from DSpace (http://hdl.handle.net/1721.1/115781). Boston, MA: Massachusetts Institute of Technology.

Black, E. E., Buesseler, K. O., Pike, S. M., & Lam, P. J. (2018). 234Th as a tracer of particulate export and remineralization in the southeastern tropical Pacific. *Marine Chemistry*, *201*, 35-50. https://doi.org/10.1016/j.marchem.2017.06.009

Bluhm, B. A., Kosobokova, K. N., & Carmack, E. C. (2015). A tale of two basins: An integrated physical and biological perspective of the deep Arctic Ocean. *Progress in Oceanography*, *139*, 89-121. https://doi.org/10.1016/j.pocean.2015.07.011

Boetius, A., Albrecht, S., Bakker, K., Bienhold, C., Felden, J., Fernández-Méndez, M., et al. (2013). Export of algal biomass from the melting Arctic sea ice. *Science*, *339*(6126), 1430-1432. https://doi.org/10.1126/science.1231346

Brown, K. A., McLaughlin, F. A., Tortell, P. D., Varela, D. E., Yamamoto-Kawai, M., Hunt, B., & Francois, R. (2014). Determination of particulate organic carbon sources to the surface mixed layer of the Canada Basin, Arctic Ocean. *Journal of Geophysical Research: Oceans*, *119*, 1084-1102. https://doi.org/10.1002/2013JC009197

Buesseler, K. O., Ball, L., Andrews, J., Cochran, J. K., Hirschberg, D. J., Bacon, M. P., et al. (2001). Upper ocean export of particulate organic carbon and biogenic silica in the Southern Ocean along 170 W. *Deep Sea Research Part II: Topical Studies in Oceanography*, *48*(19-20), 4275-4297. https://doi.org/10.1016/S0967-0645(01)00089-3

Bundy, R. M., Tagliabue, A., Hawco, N. J., Morton, P. L., Twining, B. S., Hatta, M., et al. (2020). Elevated sources of cobalt in the Arctic Ocean. *Biogeosciences Discussions*. https://doi.org/10.5194/bg-2020-84

Burkhardt, S., Riebesell, U., & Zondervan, I. (1999). Effects of growth rate, CO2 concentration, and cell size on the stable carbon isotope fractionation in marine phytoplankton. *Geochimica et Cosmochimica Acta*, *63*(22). https://doi.org/10.1016/S0016-7037(99)00217-3

Campbell, J. S., & Clark, D. L. (1977). Pleistocene turbidites of the Canada abyssal plain of the Arctic Ocean. *Journal of Sedimentary Research*, *47*(2), 657-670. https://doi.org/10.1306/212F7211-2B24-11D7-8648000102C1865D

Carmack, E. C., Aagaard, K., Swift, J. H., MacDonald, R. W., McLaughlin, F. A., Jones, E. P., et al. (1997). Changes in temperature and tracer distributions within the Arctic Ocean: Results from the 1994 Arctic Ocean section. *Deep Sea Research Part II: Topical Studies in Oceanography*, *44*(8), 1487-1502. https://doi.org/10.1016/S0967-0645(97)00056-8

Cavalieri, D. J., & Martin, S. (1994). The contribution of Alaskan, Siberian, and Canadian coastal polynyas to the cold halocline layer of the Arctic Ocean. *Journal of Geophysical Research: Oceans*, *99*(C9), 18343-18362. https://doi.org/10.1029/94JC01169

Charette, M. A., Kipp, L. E., Jensen, L. T., Dabrowski, J. S., Whitmore, L. M., Fitzsimmons, J. N., et al. (2020). The Transpolar Drift as a source of riverine and shelf‐derived trace elements to the central Arctic Ocean. *Journal of Geophysical Research: Oceans*, *125*(5). https://doi.org/10.1029/2019jc015920

Cid, A. P., Nakatsuka, S., & Sohrin, Y. (2012). Stoichiometry among bioactive trace metals in the Chukchi and Beaufort Seas. *Journal of oceanography*, *68*(6), 985-1001. https://doi.org/10.1007/s10872-012-0150-8

Close, H. G. (2019). Compound-specific isotope geochemistry in the ocean. *Annual review of marine science*, *11*, 27-56. https://doi.org/10.1146/annurev-marine-121916-063634

Coachman, L. K., & Barnes, C. A. (1961). The contribution of Bering Sea water to the Arctic Ocean. *Arctic*, *14*(3), 147-161

Codispoti, L. A., Kelly, V., Thessen, A., Matrai, P., Suttles, S., Hill, V., et al. (2013). Synthesis of primary production in the Arctic Ocean: III. Nitrate and phosphate based estimates of net community production. *Progress in Oceanography*, *110*, 126-150. https://doi.org/10.1016/j.pocean.2012.11.006

Connelly, T. L., Deibel, D., & Parrish, C. C. (2012). Biogeochemistry of near-bottom suspended particulate matter of the Beaufort Sea shelf (Arctic Ocean): C, N, P, δ13C and fatty acids. *Continental Shelf Research*, *43*, 120-132. https://doi.org/10.1016/j.csr.2012.05.011

Cooper, L. W., Whitledge, T. E., Grebmeier, J. M., & Weingartner, T. (1997). The nutrient, salinity, and stable oxygen isotope composition of Bering and Chukchi Seas waters in and near the Bering Strait. *Journal of Geophysical Research: Oceans*, *102*(C6), 12563-12573. https://doi.org/10.1029/97jc00015

Copin-Montégut, C. (2000). Consumption and production on scales of a few days of inorganic carbon, nitrate and oxygen by the planktonic community: results of continuous measurements at the Dyfamed Station in the northwestern Mediterranean Sea (May 1995). *Deep Sea Research Part I: Oceanographic Research Papers*, *47*(3), 447-477. https://doi.org/10.1016/S0967-0637(99)00098-9

Coupel, P., Jin, H. Y., Joo, M., Horner, R., Bouvet, H. A., Sicre, M. A., et al. (2012). Phytoplankton distribution in unusually low sea ice cover over the Pacific Arctic. *Biogeosciences*, *9*, 4835–4850. https://doi.org/10.5194/bg-9-4835-2012

Cullen, J. T., & Sherrell, R. M. (1999). Techniques for determination of trace metals in small samples of size-fractionated particulate matter: phytoplankton metals off central California. *Marine Chemistry*, *67*(3-4), 233-247. https://doi.org/10.1016/S0304-4203(99)00060-2

Cutter, G., Andersson, P., Codispoti, L., Croot, P., Francois, R., Lohan, M. C., et al. (2010). Sampling and sample-handling protocols for GEOTRACES cruises. Available

Cutter, G., Kadko, D., & Landing, W. M. (2019). Bottle data from the CTD-ODF carousel on the GEOTRACES Arctic Section cruise (HLY1502) from August to October 2015 (U.S. GEOTRACES Arctic project). *Biological and Chemical Oceanography Data Management Office (BCO-DMO)*, *Dataset version 2019-07-29*. https://doi.org/10.1575/1912/bco-dmo.646825.4.

D'Asaro, E. A., & Morison, J. H. (1992). Internal waves and mixing in the Arctic Ocean. *Deep Sea Research Part A. Oceanographic Research Papers*, *39*(2), S459-S484. https://doi.org/10.1016/S0198-0149(06)80016-6

Darby, D. A. (2003). Sources of sediment found in sea ice from the western Arctic Ocean, new insights into processes of entrainment and drift patterns. *Journal of Geophysical Research: Oceans*, *108*(C8). https://doi.org/10.1029/2002jc001350

Davis, J. A., & Leckie, J. O. (1978). Effect of adsorbed complexing ligands on trace metal uptake by hydrous oxides. *Environmental Science & Technology*, *12*(12), 1309-1315. https://doi.org/10.1021/es60147a006

DeMaster, D. J. (1981). The supply and accumulation of silica in the marine environment. *Geochimica et Cosmochimica acta*, *45*(10), 1715-1732. https://doi.org/10.1016/0016-7037(81)90006-5

Dethleff, D. (2005). Entrainment and export of Laptev Sea ice sediments, Siberian Arctic. *Journal of Geophysical Research: Oceans*, *110*(C7). https://doi.org/10.1029/2004JC002740

Diaz, J. M., Hansel, C. M., Voelker, B. M., Mendes, C. M., Andeer, P. F., & Zhang, T. (2013). Widespread production of extracellular superoxide by heterotrophic bacteria. *Science*, *340*(6137), 1223-1226. https://doi.org/10.1126/science.1237331

Diaz, J. M., & Plummer, S. (2018). Production of extracellular reactive oxygen species by phytoplankton: past and future directions. *Journal of plankton research*, *40*(6), 655-666. https://doi.org/10.1093/plankt/fby039

Dickson, B., Meincke, J., & Rhines, P. (2008). Arctic–subarctic ocean fluxes: defining the role of the northern seas in climate. In B. Dickson, J. Meincke and P. Rhines (Eds.), *Arctic–Subarctic Ocean Fluxes* (pp. 1-13). Dordrecht: Springer. https://doi.org/10.1007/978-1-4020-6774-7

Ding, X., Wang, R., Zhang, H., & Tao, Z. (2014). Distribution, ecology, and oxygen and carbon isotope characteristics of modern planktonic foraminifers in the Makarov Basin of the Arctic Ocean. *Chinese Science Bulletin*, *59*(7), 674-687. https://doi.org/10.1007/s11434-013-0082-8

Eek, M. K., Whiticar, M. J., Bishop, J. K. B., & Wong, C. S. (1999). Influence of nutrients on carbon isotope fractionation by natural populations of Prymnesiophyte algae in NE Pacific. *Deep Sea Research Part II: Topical Studies in Oceanography*, *46*(11-12), 2863-2876. https://doi.org/10.1016/S0967-0645(99)00086-7

Ehn, J. K., Reynolds, R. A., Stramski, D., Doxaran, D., Lansard, B., & Babin, M. (2019). Patterns of suspended particulate matter across the continental margin

in the Canadian Beaufort Sea during summer. *Biogeosciences*, *16*(7), 1583-1605. https://doi.org/10.5194/bg-16-1583-2019

Eicken, H., Reimnitz, E., Alexandrov, V., Martin, T., Kassens, H., & Viehoff, T. (1997). Sea-ice processes in the Laptev Sea and their importance for sediment export. *Continental Shelf Research*, *17*(2), 205-233. https://doi.org/10.1016/S0278-4343(96)00024-6

Elrod, V. A., Berelson, W. M., Coale, K. H., & Johnson, K. S. (2004). The flux of iron from continental shelf sediments: A missing source for global budgets. *Geophysical Research Letters*, *31*(12). https://doi.org/10.1029/2004gl020216

Engel, A., & Passow, U. (2001). Carbon and nitrogen content of transparent exopolymer particles (TEP) in relation to their Alcian Blue adsorption. *Marine Ecology Progress Series*, *219*, 1-10. https://doi.org/10.3354/meps219001

Fahl, K., & Nöthig, E. M. (2007). Lithogenic and biogenic particle fluxes on the Lomonosov Ridge (central Arctic Ocean) and their relevance for sediment accumulation: Vertical vs. lateral transport. *Deep Sea Research Part I: Oceanographic Research Papers*, *54*(8), 1256-1272. https://doi.org/10.1016/j.dsr.2007.04.014

Falkowski, P. G., Biscaye, P. E., & Sancetta, C. (1994). The lateral flux of biogenic particles from the eastern North American continental margin to the North Atlantic Ocean. *Deep Sea Research Part II: Topical Studies in Oceanography*, *41*(2-3), 583-601. https://doi.org/10.1016/0967-0645(94)90036-1

Forest, A., Osborne, P. D., Curtiss, G., & Lowings, M. G. (2016). Current surges and seabed erosion near the shelf break in the Canadian Beaufort Sea: A response to wind and ice motion stress. *Journal of Marine Systems*, *160*, 1-16. https://doi.org/10.1016/j.jmarsys.2016.03.008

Forest, A., Osborne, P. D., Fortier, L., Sampei, M., & Lowings, M. G. (2015). Physical forcings and intense shelf–slope fluxes of particulate matter in the halocline waters of the Canadian Beaufort Sea during winter. *Continental Shelf Research*, *101*, 1-21. https://doi.org/10.1016/j.csr.2015.03.009

Forest, A., Sampei, M., Hattori, H., Makabe, R., Sasaki, H., Fukuchi, M., et al. (2007). Particulate organic carbon fluxes on the slope of the Mackenzie Shelf (Beaufort Sea): Physical and biological forcing of shelf-basin exchanges. *Journal of Marine Systems*, *68*(1-2), 39-54. https://doi.org/10.1016/j.jmarsys.2006.10.008

Forest, A., Sampei, M., Rail, M. E., Gratton, Y., & Fortier, L. (2008). *Winter pulses of Pacific-origin water and resuspension events along the Canadian Beaufort*

slope revealed by a bottom-moored observatory. Paper presented at OCEANS 2008, IEEE, Quebec City, Canada.

Frigstad, H., Andersen, T., Bellerby, R. G. J., Silyakova, A., & Hessen, D. O. (2014). Variation in the seston C:N ratio of the Arctic Ocean and pan-Arctic shelves. *Journal of Marine Systems*, *129*, 214-223. https://doi.org/10.1016/j.jmarsys.2013.06.004

Froelich, P. N., Klinkhammer, G. P., Bender, M. L., Luedtke, N. A., Heath, G. R., Cullen, D., et al. (1979). Early oxidation of organic matter in pelagic sediments of the eastern equatorial Atlantic: suboxic diagenesis. *Geochimica et cosmochimica acta*, *43*(7), 1075-1090. https://doi.org/10.1016/0016-7037(79)90095-4

Fry, B. (1996). 13C/12C fractionation by marine diatoms. *Marine Ecology Progress Series*, *134*, 283-294. https://doi.org/10.3354/meps134283

Garneau, M. È., Vincent, W. F., Terrado, R., & Lovejoy, C. (2009). Importance of particle-associated bacterial heterotrophy in a coastal Arctic ecosystem. *Journal of Marine Systems*, *75*(1-2), 185-197. https://doi.org/10.1016/j.jmarsys.2008.09.002

Gervais, F., & Riebesell, U. (2001). Effect of phosphorus limitation on elemental composition and stable carbon isotope fractionation in a marine diatom growing under different CO2 concentrations. *Limnology and Oceanography*, *46*(3), 497-504. https://doi.org/10.4319/lo.2001.46.3.0497

Giesbrecht, K. E., Varela, D. E., Wiktor, J., Grebmeier, J. M., Kelly, B., & Long, J. E. (2019). A decade of summertime measurements of phytoplankton biomass, productivity and assemblage composition in the Pacific Arctic Region from 2006 to 2016. *Deep Sea Research Part II: Topical Studies in Oceanography*, *162*, 93-113. https://doi.org/10.1016/j.dsr2.2018.06.010

Glover, D. M., Jenkins, W. J., & Doney, S. C. (2011). *Modeling methods for marine science*. Cambridge: Cambridge University Press. https://doi.org/10.1017/CBO9780511975721

Goñi, M. A., Corvi, E. R., Welch, K. A., Buktenica, M., Lebon, K., Alleau, Y., & Juranek, L. W. (2019). Particulate organic matter distributions in surface waters of the Pacific Arctic shelf during the late summer and fall season. *Marine Chemistry*, *211*, 75-93. https://doi.org/10.1016/j.marchem.2019.03.010

Goñi, M. A., O'Connor, A. E., Kuzyk, Z. Z., Yunker, M. B., Gobeil, C., & Macdonald, R. W. (2013). Distribution and sources of organic matter in surface marine

sediments across the North American Arctic margin. *Journal of Geophysical Research: Oceans*, *118*(9), 4017-4035. https://doi.org/10.1002/jgrc.20286

Goñi, M. A., Yunker, M. B., Macdonald, R. W., & Eglinton, T. I. (2005). The supply and preservation of ancient and modern components of organic carbon in the Canadian Beaufort Shelf of the Arctic Ocean. *Marine Chemistry*, *93*(1), 53-73. https://doi.org/10.1016/j.marchem.2004.08.001

Gradinger, R. (2009). Sea-ice algae: Major contributors to primary production and algal biomass in the Chukchi and Beaufort Seas during May/June 2002. *Deep Sea Research Part II: Topical Studies in Oceanography*, *56*(17), 1201-1212. https://doi.org/10.1016/j.dsr2.2008.10.016

Granger, J., Sigman, D. M., Gagnon, J., Tremblay, J. É., & Mucci, A. (2018). On the Properties of the Arctic Halocline and Deep Water Masses of the Canada Basin from Nitrate Isotope Ratios. *Journal of Geophysical Research: Oceans*, *123*(8), 5443-5458. https://doi.org/10.1029/2018jc014110

Grebmeier, J. M., Cooper, L. W., Feder, H. M., & Sirenko, B. I. (2006). Ecosystem dynamics of the Pacific-influenced Northern Bering and Chukchi Seas in the Amerasian Arctic. *Progress in Oceanography*, *71*(2-4), 331-361. https://doi.org/10.1016/j.pocean.2006.10.001

Griffith, D. R., McNichol, A. P., Xu, L., McLaughlin, F. A., Macdonald, R. W., Brown, K. A., & Eglinton, T. I. (2012). Carbon dynamics in the western Arctic Ocean: insights from full-depth carbon isotope profiles of DIC, DOC, and POC. *Biogeosciences*, *9*(3), 1217-1224. https://doi.org/10.5194/bg-9-1217-2012

Guo, L., & Macdonald, R. W. (2006). Source and transport of terrigenous organic matter in the upper Yukon River: Evidence from isotope (δ13C, Δ14C, and δ15N) composition of dissolved, colloidal, and particulate phases. *Global Biogeochemical Cycles*, *20*(2). https://doi.org/10.1029/2005gb002593

Guthrie, J. D., Morison, J. H., & Fer, I. (2013). Revisiting internal waves and mixing in the Arctic Ocean. *Journal of Geophysical Research: Oceans*, *118*(8), 3966-3977. https://doi.org/10.1002/jgrc.20294

Hansard, S. P., Vermilyea, A. W., & Voelker, B. M. (2010). Measurements of superoxide radical concentration and decay kinetics in the Gulf of Alaska. *Deep Sea Research Part I: Oceanographic Research Papers*, *57*(9), 1111-1119. https://doi.org/10.1016/j.dsr.2010.05.007

Hansel, C. M., Zeiner, C. A., Santelli, C. M., & Webb, S. M. (2012). Mn(II) oxidation by an ascomycete fungus is linked to superoxide production during asexual

reproduction. *Proceedings of the National Academy of Sciences*, *109*(31), 12621-12625. https://doi.org/10.1073/pnas.1203885109

Hatta, M., & Measures, C. (2016). *GEOTRACES Arctic Section: Shipboard Determination of Key Trace Elements*. Paper presented at Goldschmidt Conference, Geochemical Society, Yokohama, Japan.

Hedges, J. I., Baldock, J. A., Gélinas, Y., Lee, C., Peterson, M. L., & Wakeham, S. G. (2002). The biochemical and elemental compositions of marine plankton: A NMR perspective. *Marine Chemistry*, *78*(1), 47-63. https://doi.org/10.1016/S0304-4203(02)00009-9

Hedges, J. I., Clark, W. A., Quay, P. D., Richey, J. E., Devol, A. H., & Santos, M. (1986). Compositions and fluxes of particulate organic material in the Amazon River 1. *Limnology and Oceanography*, *31*(4), 717-738. https://doi.org/10.4319/lo.1986.31.4.0717

Heller, M. I. (2020). Dissolved Fe(II) from the southbound leg of the US GEOTRACES Arctic cruise (HLY1502) on USCGC Healy from August to October 2015. *Biological and Chemical Oceanography Data Management Office (BCO-DMO)*, *Dataset version 2020-05-15*. https://doi.org/10.26008/1912/bco-dmo.811614.1.

Hioki, N., Kuma, K., Morita, Y., Sasayama, R., Ooki, A., Kondo, Y., et al. (2014). Laterally spreading iron, humic-like dissolved organic matter and nutrients in cold, dense subsurface water of the Arctic Ocean. *Scientific Reports*, *4*, 6775. https://doi.org/10.1038/srep06775

Ho, T. Y., Chou, W. C., Lin, H. L., & Sheu, D. D. (2011). Trace metal cycling in the deep water of the South China Sea: The composition, sources, and fluxes of sinking particles. *Limnology and Oceanography*, *56*(4), 1225-1243. https://doi.org/10.4319/lo.2011.56.4.1225

Hollibaugh, J. T., Buddemeier, R. W., & Smith, S. V. (1991). Contributions of colloidal and high molecular weight dissolved material to alkalinity and nutrient concentrations in shallow marine and estuarine systems. *Marine Chemistry*, *34*(1-2), 1-27. https://doi.org/10.1016/0304-4203(91)90011-K

Honeyman, B. D., Balistrieri, L. S., & Murray, J. W. (1988). Oceanic trace metal scavenging: the importance of particle concentration. *Deep Sea Research Part A. Oceanographic Research Papers*, *35*(2), 227-246. https://doi.org/10.1016/0198-0149(88)90038-6

Honjo, S. (1982). Seasonality and interaction of biogenic and lithogenic particulate flux at the Panama Basin. *Science*, *218*(4575), 883-884. https://doi.org/10.1126/science.218.4575.883

Honjo, S., Krishfield, R. A., Eglinton, T. I., Manganini, S. J., Kemp, J. N., Doherty, K., et al. (2010). Biological pump processes in the cryopelagic and hemipelagic Arctic Ocean: Canada Basin and Chukchi Rise. *Progress in Oceanography*, *85*(3-4), 137-170. https://doi.org/10.1016/j.pocean.2010.02.009

Hunkins, K., & Kutschale, H. (1965). Quaternary sedimentation in the Arctic Ocean. *Progress in oceanography*, *4*, 89-94. https://doi.org/10.1016/0079-6611(65)90042-X

Hunkins, K., Thorndike, E. M., & Mathieu, G. (1969). Nepheloid layers and bottom currents in the Arctic Ocean. *Journal of Geophysical Research*, *74*(28), 6995-7008. https://doi.org/10.1029/JC074i028p06995

Hurd, D. C., & Takahashi, K. (1983). On the estimation of minimum mechanical loss during an in situ biogenic silica dissolution experiment. *Marine Micropaleontology*, *7*(5), 441-447. https://doi.org/10.1016/0377-8398(83)90019-1

Hutchins, D. A., & Bruland, K. W. (1998). Iron-limited diatom growth and Si: N uptake ratios in a coastal upwelling regime. *Nature*, *393*(6685), 561. https://doi.org/10.1038/31203

Hwang, J., Druffel, E. R. M., & Eglinton, T. I. (2010). Widespread influence of resuspended sediments on oceanic particulate organic carbon: Insights from radiocarbon and aluminum contents in sinking particles. *Global Biogeochemical Cycles*, *24*(4). https://doi.org/10.1029/2010gb003802

Hwang, J., Eglinton, T. I., Krishfield, R. A., Manganini, S. J., & Honjo, S. (2008). Lateral organic carbon supply to the deep Canada Basin. *Geophysical Research Letters*, *35*(11). https://doi.org/10.1029/2008gl034271

Hwang, J., Kim, M., Manganini, S. J., McIntyre, C. P., Haghipour, N., Park, J., et al. (2015). Temporal and spatial variability of particle transport in the deep Arctic Canada Basin. *Journal of Geophysical Research: Oceans*, *120*(4), 2784-2799. https://doi.org/10.1002/2014jc010643

Hwang, J., Manganini, S. J., Montluçon, D. B., & Eglinton, T. I. (2009). Dynamics of particle export on the Northwest Atlantic margin. *Deep Sea Research Part I: Oceanographic Research Papers*, *56*(10), 1792-1803. https://doi.org/10.1016/j.dsr.2009.05.007

Iken, K., Bluhm, B. A., & Gradinger, R. (2005). Food web structure in the high Arctic Canada Basin: evidence from δ13C and δ15N analysis. *Polar Biology*, *28*(3), 238-249. https://doi.org/10.1007/s00300-004-0669-2

Ivanov, V. V., Shapiro, G. I., Huthnance, J. M., Aleynik, D. L., & Golovin, P. N. (2004). Cascades of dense water around the world ocean. *Progress in oceanography*, *60*(1), 47-98. https://doi.org/10.1029/2001GC000302

Jakobsson, M. (2002). Hypsometry and volume of the Arctic Ocean and its constituent seas. *Geochemistry, Geophysics, Geosystems*, *3*(5), 1-18. https://doi.org/10.1029/2001GC000302

Jensen, L., Cullen, J. T., Ball, G. T., Sherrell, R. M., & Fitzsimmons, J. N. (2018). *Dissolved Fe and Mn along US Arctic GEOTRACES GN01: Effects of scavenging in intermediate and deep waters*. Paper presented at Ocean Sciences Meeting, AGU, Portland, Oregon, USA.

Jones, E. P. (2001). Circulation in the arctic ocean. *Polar Research*, *20*(2), 139-146. https://doi.org/10.1111/j.1751-8369.2001.tb00049.x

Jones, E. P., & Anderson, L. G. (1986). On the origin of the chemical properties of the Arctic Ocean halocline. *Journal of Geophysical Research: Oceans*, *91*(C9), 10759. https://doi.org/10.1029/JC091iC09p10759

Jones, E. P., Anderson, L. G., & Swift, J. H. (1998). Distribution of Atlantic and Pacific waters in the upper Arctic Ocean: Implications for circulation. *Geophysical Research Letters*, *25*(6), 765-768. https://doi.org/10.1029/98GL00464

Jones, E. P., Rudels, B., & Anderson, L. G. (1995). Deep waters of the Arctic Ocean: origins and circulation. *Deep Sea Research Part I: Oceanographic Research Papers*, *42*(5), 737-760. https://doi.org/10.1016/0967-0637(95)00013-V

Joo, H. M., Lee, S. H., Jung, S. W., Dahms, H. U., & Lee, J. H. (2012). Latitudinal variation of phytoplankton communities in the western Arctic Ocean. *Deep Sea Research Part II: Topical Studies in Oceanography*, *81-84*, 3-17. https://doi.org/10.1016/j.dsr2.2011.06.004

Kadko, D., Pickart, R. S., & Mathis, J. (2008). Age characteristics of a shelf-break eddy in the western Arctic and implications for shelf-basin exchange. *Journal of Geophysical Research: Oceans*, *113*(C2). https://doi.org/10.1029/2007jc004429

Kamatani, A., & Riley, J. P. (1979). Rate of dissolution of diatom silica walls in seawater. *Marine Biology*, *55*(1), 29-35. https://doi.org/10.1007/BF00391714

Karcher, M. J., & Oberhuber, J. M. (2002). Pathways and modification of the upper and intermediate waters of the Arctic Ocean. *Journal of Geophysical Research: Oceans*, *107*(C6). https://doi.org/10.1029/2000jc000530

Kellogg, C. T. E., & Deming, J. W. (2009). Comparison of free-living, suspended particle, and aggregate-associated Bacterial and Archaeal communities in the Laptev Sea. *Aquatic Microbial Ecology*, *57*, 1-18. https://doi.org/10.3354/ame01317

Kieber, D. J., Miller, G. W., Neale, P. J., & Mopper, K. (2014). Wavelength and temperature-dependent apparent quantum yields for photochemical formation of hydrogen peroxide in seawater. *Environ Sci Process Impacts*, *16*(4), 777-791. https://doi.org/10.1039/c4em00036f

Kipp, L. E., Charette, M. A., Moore, W. S., Henderson, P. B., & Rigor, I. G. (2018). Increased fluxes of shelf-derived materials to the central Arctic Ocean. *Science advances*, *4*(1), eaao1302. https://doi.org/10.1126/sciadv.aao1302

Kipp, L. E., Kadko, D. C., Pickart, R. S., Henderson, P. B., Moore, W. S., & Charette, M. A. (2019). Shelf-basin interactions and water mass residence times in the Western Arctic Ocean: insights provided by radium isotopes. *Journal of Geophysical Research: Oceans*, *124*(5), 3279-3297. https://doi.org/10.1029/2019JC014988

Kipp, L. E., Spall, M. A., Pickart, R. S., Kadko, D. C., Moore, W. S., Dabrowski, J. S., & Charette, M. A. (2020). Observational and Modeling Evidence of Seasonal Trends in Sediment-Derived Material Inputs to the Chukchi Sea. *Journal of Geophysical Research: Oceans*, *125*(5). https://doi.org/10.1029/2019jc016007

Ko, Y. H., & Quay, P. D. (2020). Origin and Accumulation of an Anthropogenic CO2 and 13C Suess Effect in the Arctic Ocean. *Global Biogeochemical Cycles*, *34*(2). https://doi.org/10.1029/2019gb006423

Kondo, Y., Obata, H., Hioki, N., Ooki, A., Nishino, S., Kikuchi, T., & Kuma, K. (2016). Transport of trace metals (Mn, Fe, Ni, Zn and Cd) in the western Arctic Ocean (Chukchi Sea and Canada Basin) in late summer 2012. *Deep Sea Research Part I: Oceanographic Research Papers*, *116*, 236-252. https://doi.org/10.1016/j.dsr.2016.08.010

Koning, E., Gehlen, M., Flank, A. M., Calas, G., & Epping, E. (2007). Rapid post-mortem incorporation of aluminum in diatom frustules: Evidence from chemical and structural analyses. *Marine Chemistry*, *106*(1-2), 208-222. https://doi.org/10.1016/j.marchem.2006.06.009

Körtzinger, A., Koeve, W., Kähler, P., & Mintrop, L. (2001). C: N ratios in the mixed layer during the productive season in the northeast Atlantic Ocean. *Deep Sea Research Part I: Oceanographic Research Papers*, *48*(3), 661-688. https://doi.org/10.1016/S0967-0637(00)00051-0

Koziorowska, K., Kuliński, K., & Pempkowiak, J. (2016). Sedimentary organic matter in two Spitsbergen fjords: Terrestrial and marine contributions based on carbon and nitrogen contents and stable isotopes composition. *Continental Shelf Research*, *113*, 38-46. https://doi.org/10.1016/j.csr.2015.11.010

Lalande, C., Lepore, K., Cooper, L. W., Grebmeier, J. M., & Moran, S. B. (2007). Export fluxes of particulate organic carbon in the Chukchi Sea: A comparative study using 234Th/238U disequilibria and drifting sediment traps. *Marine Chemistry*, *103*(1-2), 185-196. https://doi.org/10.1016/j.marchem.2006.07.004

Lalande, C., Nöthig, E. M., Bauerfeind, E., Hardge, K., Beszczynska-Möller, A., & Fahl, K. (2016). Lateral supply and downward export of particulate matter from upper waters to the seafloor in the deep eastern Fram Strait. *Deep Sea Research Part I: Oceanographic Research Papers*, *114*, 78-89. https://doi.org/10.1016/j.dsr.2016.04.014

Lalande, C., Nöthig, E. M., Somavilla, R., Bauerfeind, E., Shevchenko, V., & Okolodkov, Y. (2014). Variability in under-ice export fluxes of biogenic matter in the Arctic Ocean. *Global Biogeochemical Cycles*, *28*(5), 571-583. https://doi.org/10.1002/2013gb004735

Lam, P. J., & Bishop, J. K. B. (2008). The continental margin is a key source of iron to the HNLC North Pacific Ocean. *Geophysical Research Letters*, *35*(7), n/a-n/a. https://doi.org/10.1029/2008gl033294

Lam, P. J., Bishop, J. K. B., Henning, C. C., Marcus, M. A., Waychunas, G. A., & Fung, I. Y. (2006). Wintertime phytoplankton bloom in the subarctic Pacific supported by continental margin iron. *Global Biogeochemical Cycles*, *20*(1), n/a-n/a. https://doi.org/10.1029/2005gb002557

Lam, P. J., Doney, S. C., & Bishop, J. K. B. (2011). The dynamic ocean biological pump: Insights from a global compilation of particulate organic carbon, CaCO3, and opal concentration profiles from the mesopelagic. *Global Biogeochemical Cycles*, *25*(3). https://doi.org/10.1029/2010gb003868

Lam, P. J., Lee, J. M., Heller, M. I., Mehic, S., Xiang, Y., & Bates, N. R. (2018). Size-fractionated distributions of suspended particle concentration and major phase composition from the US GEOTRACES Eastern Pacific Zonal Transect (GP16). *Marine Chemistry*, *201*, 90-107. https://doi.org/10.1016/j.marchem.2017.08.013

Lam, P. J., Ohnemus, D. C., & Auro, M. E. (2015). Size-fractionated major particle composition and concentrations from the US GEOTRACES North Atlantic Zonal Transect. *Deep Sea Research Part II: Topical Studies in Oceanography*, *116*, 303-320. https://doi.org/10.1016/j.dsr2.2014.11.020

Lamborg, C. H., Buesseler, K. O., Valdes, J., Bertrand, C. H., Bidigare, R., Manganini, S., et al. (2008). The flux of bio- and lithogenic material associated with sinking particles in the mesopelagic "twilight zone" of the northwest and North Central Pacific Ocean. *Deep Sea Research Part II: Topical Studies in Oceanography*, *55*(14-15), 1540-1563. https://doi.org/10.1016/j.dsr2.2008.04.011

Landing, W. M., Cutter, G., & Kadko, D. C. (2017). CTD-ODF profiles from GEOTRACES-Arctic Section cruise HLY1502, August to October 2015 (U.S. GEOTRACES Arctic project). *Biological and Chemical Oceanography Data Management Office (BCO-DMO)*, *Dataset version 2017-05-22*. Retrieved from http://lod.bco-dmo.org/id/dataset/700817

Laney, S. R., & Sosik, H. M. (2014). Phytoplankton assemblage structure in and around a massive under-ice bloom in the Chukchi Sea. *Deep Sea Research Part II: Topical Studies in Oceanography*, *105*, 30-41. https://doi.org/10.1016/j.dsr2.2014.03.012

Lansard, B., Mucci, A., Miller, L. A., Macdonald, R. W., & Gratton, Y. (2012). Seasonal variability of water mass distribution in the southeastern Beaufort Sea determined by total alkalinity and δ18O. *Journal of Geophysical Research: Oceans*, *117*(C3). https://doi.org/10.1029/2011JC007299

Learman, D. R., Voelker, B. M., Madden, A. S., & Hansel, C. M. (2013). Constraints on superoxide mediated formation of manganese oxides. *Front Microbiol*, *4*, 262. https://doi.org/10.3389/fmicb.2013.00262

Learman, D. R., Voelker, B. M., Vazquez-Rodriguez, A. I., & Hansel, C. M. (2011a). Formation of manganese oxides by bacterially generated superoxide. *Nature Geoscience*, *4*(2), 95-98. https://doi.org/10.1038/ngeo1055

Learman, D. R., Wankel, S. D., Webb, S. M., Martinez, N., Madden, A. S., & Hansel, C. M. (2011b). Coupled biotic–abiotic Mn(II) oxidation pathway mediates the formation and structural evolution of biogenic Mn oxides. *Geochimica et Cosmochimica Acta*, *75*(20), 6048-6063. https://doi.org/10.1016/j.gca.2011.07.026

Lee, S., & Fuhrman, J. A. (1987). Relationships between biovolume and biomass of naturally derived marine bacterioplankton. *Applied and environmental microbiology*, *53*(6), 1298-1303. https://doi.org/10.1128/AEM.53.6.1298-1303.1987

Lepore, K., Moran, S. B., Grebmeier, J. M., Cooper, L. W., Lalande, C., Maslowski, W., et al. (2007). Seasonal and interannual changes in particulate organic carbon export and deposition in the Chukchi Sea. *Journal of Geophysical Research: Oceans*, *112*(C10). https://doi.org/10.1029/2006jc003555

Llinás, L., Pickart, R. S., Mathis, J. T., & Smith, S. L. (2009). Zooplankton inside an Arctic Ocean cold-core eddy: Probable origin and fate. *Deep Sea Research Part II: Topical Studies in Oceanography*, *56*(17), 1290-1304. https://doi.org/10.1016/j.dsr2.2008.10.020

Lohan, M. C., & Bruland, K. W. (2008). Elevated Fe (II) and dissolved Fe in hypoxic shelf waters off Oregon and Washington: an enhanced source of iron to coastal upwelling regimes. *Environmental science & technology*, *42*(17), 6462-6468. https://doi.org/10.1021/es800144j

Löwemark, L., März, C., O'Regan, M., & Gyllencreutz, R. (2014). Arctic Ocean Mn-stratigraphy: genesis, synthesis and inter-basin correlation. *Quaternary Science Reviews*, *92*, 97-111. https://doi.org/10.1016/j.quascirev.2013.11.018

Macdonald, R. W., Carmack, E. C., McLaughlin, F. A., Iseki, K., Macdonald, D. M., & O'Brien, M. C. (1989). Composition and modification of water masses in the Mackenzie Shelf Estuary. *Journal of Geophysical Research: Oceans*, *94*(C12), 18057-18070. https://doi.org/10.1029/JC094iC12p18057

Macdonald, R. W., & Gobeil, C. (2012). Manganese Sources and Sinks in the Arctic Ocean with Reference to Periodic Enrichments in Basin Sediments. *Aquatic Geochemistry*, *18*(6), 565-591. https://doi.org/10.1007/s10498-011-9149-9

MacIntyre, S., Alldredge, A. L., & Gotschalk, C. C. (1995). Accumulation of marines now at density discontinuities in the water column. *Limnology and Oceanography*, *40*(3), 449-468. https://doi.org/10.4319/lo.1995.40.3.0449

Madison, A. S., Tebo, B. M., Mucci, A., Sundby, B., & Luther, G. W. (2013). Abundant porewater Mn(III) is a major component of the sedimentary redox system. *Science*, *341*(6148), 875-878. https://doi.org/10.1126/science.1241396

Magen, C., Chaillou, G., Crowe, S. A., Mucci, A., Sundby, B., Gao, A., et al. (2010). Origin and fate of particulate organic matter in the southern Beaufort Sea – Amundsen Gulf region, Canadian Arctic. *Estuarine, Coastal and Shelf Science*, *86*(1), 31-41. https://doi.org/10.1016/j.ecss.2009.09.009

Mari, X., Passow, U., Migon, C., Burd, A. B., & Legendre, L. (2017). Transparent exopolymer particles: Effects on carbon cycling in the ocean. *Progress in Oceanography*, *151*, 13-37. https://doi.org/10.1016/j.pocean.2016.11.002

Marsay, C. M., Kadko, D., Landing, W. M., Morton, P. L., Summers, B. A., & Buck, C. S. (2018). Concentrations, provenance and flux of aerosol trace elements during US GEOTRACES Western Arctic cruise GN01. *Chemical Geology*, *502*, 1-14. https://doi.org/10.1016/j.chemgeo.2018.06.007

März, C., Meinhardt, A. K., Schnetger, B., & Brumsack, H. J. (2015). Silica diagenesis and benthic fluxes in the Arctic Ocean. *Marine Chemistry*, *171*, 1-9. https://doi.org/10.1016/j.marchem.2015.02.003

März, C., Stratmann, A., Matthiessen, J., Meinhardt, A. K., Eckert, S., Schnetger, B., et al. (2011). Manganese-rich brown layers in Arctic Ocean sediments: Composition, formation mechanisms, and diagenetic overprint. *Geochimica et Cosmochimica Acta*, *75*(23), 7668-7687. https://doi.org/10.1016/j.gca.2011.09.046

Mathis, J. T., Pickart, R. S., Hansell, D. A., Kadko, D., & Bates, N. R. (2007). Eddy transport of organic carbon and nutrients from the Chukchi Shelf: Impact on the upper halocline of the western Arctic Ocean. *Journal of Geophysical Research: Oceans*, *112*(C5). https://doi.org/10.1029/2006jc003899

McClelland, J. W., Holmes, R. M., Peterson, B. J., Raymond, P. A., Striegl, R. G., Zhulidov, A. V., et al. (2016). Particulate organic carbon and nitrogen export from major Arctic rivers. *Global Biogeochemical Cycles*, *30*, 629-643. https://doi.org/10.1002/2015GB005351

Meiners, K., Gradinger, R., Fehling, J., Civitarese, G., & Spindler, M. (2003). Vertical distribution of exopolymer particles in sea ice of the Fram Strait (Arctic) during autumn. *Marine Ecology Progress Series*, *248*, 1-13. https://doi.org/10.3354/meps248001

Menard, H. W., & Smith, S. M. (1966). Hypsometry of ocean basin provinces. *Journal of Geophysical Research*, *71*(18), 4305-4325. https://doi.org/10.1029/JZ071i018p04305

Meyers, P. A. (1997). Organic geochemical proxies of paleoceanographic, paleolimnologic, and paleoclimatic processes. *Organic geochemistry*, *27*(5-6), 213-250. https://doi.org/10.1016/S0146-6380(97)00049-1

Middag, R., de Baar, H. J. W., Laan, P., & Bakker, K. (2009). Dissolved aluminium and the silicon cycle in the Arctic Ocean. *Marine Chemistry*, *115*(3-4), 176-195. https://doi.org/10.1016/j.marchem.2009.08.002

Millero, F. J., Sotolongo, S., & Izaguirre, M. (1987). The oxidation kinetics of Fe(II) in seawater. *Geochimica et Cosmochimica Acta*, *51*(4), 793-801. https://doi.org/10.1016/0016-7037(87)90093-7

Mook, W. G., & Tan, F. C. (1991). Stable carbon isotopes in rivers and estuaries. In E. T. Degens, S. Kempe and J. E. Richey (Eds.), *Biogeochemistry of major world rivers. SCOPE Report 42* (pp. 245–264). Chichester, UK: John Wiley & Sons

Moore, R. M., & Smith, J. N. (1986). Disequilibria between 226Ra, 210Pb and 210Po in the Arctic Ocean and the implications for chemical modification of the Pacific water inflow. *Earth and Planetary Science Letters*, *77*(3-4), 285-292. https://doi.org/10.1016/0012-821X(86)90140-8

Moran, S. B., Ellis, K. M., & Smith, J. N. (1997). 234Th/238U disequilibrium in the central Arctic Ocean: implications for particulate organic carbon export. *Deep Sea Research Part II: Topical Studies in Oceanography*, *44*(8), 1593-1606. https://doi.org/10.1016/S0967-0645(97)00049-0

Moran, S. B., Kelly, R. P., Hagstrom, K., Smith, J. N., Grebmeier, J. M., Cooper, L. W., et al. (2005). Seasonal changes in POC export flux in the Chukchi Sea and implications for water column-benthic coupling in Arctic shelves. *Deep Sea Research Part II: Topical Studies in Oceanography*, *52*(24-26), 3427-3451. https://doi.org/10.1016/j.dsr2.2005.09.011

Morgan, J. J. (2005). Kinetics of reaction between O2 and Mn(II) species in aqueous solutions. *Geochimica et Cosmochimica Acta*, *69*(1), 35-48. https://doi.org/10.1016/j.gca.2004.06.013

Mortlock, R. A., & Froelich, P. N. (1989). A simple method for the rapid determination of biogenic opal in pelagic marine sediments. *Deep Sea Research Part A. Oceanographic Research Papers*, *36*(9), 1415-1426. https://doi.org/10.1016/0198-0149(89)90092-7

Mosher, D. C., Shimeld, J., Hutchinson, D., Lebedeva-Ivanova, N., & Chapman, C. B. (2012). Submarine landslides in Arctic sedimentation: Canada basin. In D. C. Mosher, R. C. Shipp, L. Moscardelli, J. D. Chaytor and C. D. P. Baxter (Eds.), *Submarine mass movements and their consequences* (pp. 147-157). Dordrecht: Springer. https://doi.org/10.1007/978-94-007-2162-3_13

Murnane, R. J., Cochran, J. K., & Sarmiento, J. L. (1994). Estimates of particle-and thorium-cycling rates in the northwest Atlantic Ocean. *Journal of Geophysical Research: Oceans*, *99*(C2), 3373-3392. https://doi.org/10.1029/93JC02378

Naidu, A. S., Cooper, L. W., Finney, B. P., Macdonald, R. W., Alexander, C., & Semiletov, I. P. (2000). Organic carbon isotope ratios (δ 13 C) of Arctic Amerasian Continental shelf sediments. *International Journal of Earth Sciences*, *89*(3), 522-532. https://doi.org/10.1007/s005310000121

Naidu, A. S., Scalan, R. S., Feder, H. M., Goering, J. J., Hameedi, M. J., Parker, P. L., et al. (1993). Stable organic carbon isotopes in sediments of the north Bering-south Chukchi seas, Alaskan-Soviet Arctic Shelf. *Continental Shelf Research*, *13*(5-6), 669-691. https://doi.org/10.1016/0278-4343(93)90099-J

Nakatsuka, T., Fujimune, T., Yoshikawa, C., Noriki, S., Kawamura, K., Fukamachi, Y., et al. (2004). Biogenic and lithogenic particle fluxes in the western region of the Sea of Okhotsk: Implications for lateral material transport and biological productivity. *Journal of Geophysical Research: Oceans*, *109*(C9). https://doi.org/10.1029/2003jc001908

Nakayama, Y., Fujita, S., Kuma, K., & Shimada, K. (2011). Iron and humic-type fluorescent dissolved organic matter in the Chukchi Sea and Canada Basin of the western Arctic Ocean. *Journal of Geophysical Research: Oceans*, *116*(C7). https://doi.org/10.1029/2010jc006779

Nishimura, S., Kuma, K., Ishikawa, S., Omata, A., & Saitoh, S. I. (2012). Iron, nutrients, and humic-type fluorescent dissolved organic matter in the northern Bering Sea shelf, Bering Strait, and Chukchi Sea. *Journal of Geophysical Research: Oceans*, *117*(C2). https://doi.org/10.1029/2011JC007355

O'Brien, M. C., Melling, H., Pedersen, T. F., & Macdonald, R. W. (2011). The role of eddies and energetic ocean phenomena in the transport of sediment from shelf to basin in the Arctic. *Journal of Geophysical Research: Oceans*, *116*(C8). https://doi.org/10.1029/2010jc006890

O'Brien, M. C., Macdonald, R. W., Melling, H., & Iseki, K. (2006). Particle fluxes and geochemistry on the Canadian Beaufort Shelf: Implications for sediment transport and deposition. *Continental Shelf Research*, *26*(1), 41-81. https://doi.org/10.1016/j.csr.2005.09.007

O'Brien, M. C., Melling, H., Pedersen, T. F., & Macdonald, R. W. (2013). The role of eddies on particle flux in the Canada Basin of the Arctic Ocean. *Deep Sea Research Part I: Oceanographic Research Papers*, *71*, 1-20. https://doi.org/10.1016/j.dsr.2012.10.004

O'Leary, M. H. (1988). Carbon Isotopes in Photosynthesis. *BioScience*, *38*(5), 328-336. https://doi.org/10.2307/1310735

Ohnemus, D. C., Auro, M. E., Sherrell, R. M., Lagerström, M., Morton, P. L., Twining, B. S., et al. (2014). Laboratory intercomparison of marine particulate digestions including Piranha: a novel chemical method for dissolution of polyethersulfone filters. *Limnology and Oceanography: Methods*, *12*(8), 530-547. https://doi.org/10.4319/lom.2014.12.530

Ohnemus, D. C., & Lam, P. J. (2015). Cycling of lithogenic marine particles in the US GEOTRACES North Atlantic transect. *Deep Sea Research Part II: Topical Studies in Oceanography*, *116*, 283-302. https://doi.org/10.1016/j.dsr2.2014.11.019

Oldham, V. E., Mucci, A., Tebo, B. M., & Luther, G. W. (2017). Soluble Mn(III)–L complexes are abundant in oxygenated waters and stabilized by humic ligands. *Geochimica et Cosmochimica Acta*, *199*, 238-246. https://doi.org/10.1016/j.gca.2016.11.043

Orians, K. J., & Bruland, K. W. (1986). The biogeochemistry of aluminum in the Pacific Ocean. *Earth and Planetary Science Letters*. https://doi.org/10.1016/0012-821X(86)90006-3

Ortega-Retuerta, E., Jeffrey, W. H., Babin, M., Bélanger, S., Benner, R., Marie, D., et al. (2012). Carbon fluxes in the Canadian Arctic: patterns and drivers of bacterial abundance, production and respiration on the Beaufort Sea margin. *Biogeosciences*, *9*(9), 3679-3692. https://doi.org/10.5194/bg-9-3679-2012

Parsons, T. R., Webb, D. G., Rokeby, B. E., Lawrence, M., Hopky, G. E., & Chiperzak, D. B. (1989). Autotrophic and heterotrophic production in the Mackenzie River/Beaufort Sea estuary. *Polar Biology*, *9*(4), 261-266. https://doi.org/10.1007/BF00263774

Pasqualini, A., Schlosser, P., Newton, R., & Koffman, T. N. (2017). U.S. GEOTRACES Arctic Section Ocean Water Hydrogen and Oxygen Stable Isotope Analyses. *Interdisciplinary Earth Data Alliance (IEDA)*, *Dataset version 1.0*. https://doi.org/10.1594/IEDA/100633.

Pickart, R. S., Weingartner, T. J., Pratt, L. J., Zimmermann, S., & Torres, D. J. (2005). Flow of winter-transformed Pacific water into the Western Arctic. *Deep Sea Research Part II: Topical Studies in Oceanography*, *52*(24-26), 3175-3198. https://doi.org/10.1016/j.dsr2.2005.10.009

Pineault, S., Tremblay, J. É., Gosselin, M., Thomas, H., & Shadwick, E. (2013). The isotopic signature of particulate organic C and N in bottom ice: Key influencing factors and applications for tracing the fate of ice-algae in the Arctic Ocean. *Journal of Geophysical Research: Oceans*, *118*(1), 287-300. https://doi.org/10.1029/2012jc008331

Planquette, H., & Sherrell, R. M. (2012). Sampling for particulate trace element determination using water sampling bottles: methodology and comparison to in situ pumps. *Limnology and Oceanography: Methods*, *10*(5), 367-388. https://doi.org/10.4319/lom.2012.10.367

Popp, B. N., Laws, E. A., Bidigare, R. R., Dore, J. E., Hanson, K. L., & Wakeham, S. G. (1998). Effect of Phytoplankton Cell Geometry on Carbon Isotopic Fractionation. *Geochimica et Cosmochimica Acta*, *62*(1), 69–77. https://doi.org/10.1016/S0016-7037(97)00333-5

Poulin, M., Daugbjerg, N., Gradinger, R., Ilyash, L., Ratkova, T., & von Quillfeldt, C. (2010). The pan-Arctic biodiversity of marine pelagic and sea-ice unicellular eukaryotes: a first-attempt assessment. *Marine Biodiversity*, *41*(1), 13-28. https://doi.org/10.1007/s12526-010-0058-8

Rachold, V., & Hubberten, H. W. (1999). Carbon isotope composition of particulate organic material in East Siberian rivers. In H. Kassens, H. A. Bauch, I. A. Dmitrenko, H. Eicken, H. W. Hubberten, M. Melles, J. Thiede and L. A. Timokhov (Eds.), *Land-ccean systems in the Siberian Arctic* (pp. 223-238). Berlin: Springer. https://doi.org/10.1007/978-3-642-60134-7_21

Rau, G. H., Riebesell, U., & Wolf-Gladrow, D. (1996). A model of photosynthetic 13C fractionation by marine phytoplankton based on diffusive molecular CO2 uptake. *Marine Ecology Progress Series*, *133*, 275–285. https://doi.org/10.3354/meps133275

Rau, G. H., Takahashi, T., & Des Marais, D. J. (1989). Latitudinal variations in plankton δ13C: implications for CO2 and productivity in past oceans. *Nature*, *341*(6242), 516. https://doi.org/10.1038/341516a0

Redfield, A. C. (1963). The influence of organisms on the composition of seawater. *The sea*, *2*, 26-77

Rembauville, M., Manno, C., Tarling, G. A., Blain, S., & Salter, I. (2016). Strong contribution of diatom resting spores to deep-sea carbon transfer in naturally iron-fertilized waters downstream of South Georgia. *Deep Sea Research Part I: Oceanographic Research Papers*, *115*, 22-35. https://doi.org/10.1016/j.dsr.2016.05.002

Reynolds, R. A., Stramski, D., & Neukermans, G. (2016). Optical backscattering by particles in Arctic seawater and relationships to particle mass concentration, size distribution, and bulk composition. *Limnology and Oceanography*, *61*(5), 1869-1890. https://doi.org/10.1002/lno.10341

Richard, D., Sundby, B., & Mucci, A. (2013). Kinetics of manganese adsorption, desorption, and oxidation in coastal marine sediments. *Limnology and Oceanography*, *58*(3), 987-996. https://doi.org/10.4319/lo.2013.58.3.0987

Rickert, D., Schlüter, M., & Wallmann, K. (2002). Dissolution kinetics of biogenic silica from the water column to the sediments. *Geochimica et Cosmochimica Acta*, *66*(3), 439-455. https://doi.org/10.1016/S0016-7037(01)00757-8

Riebesell, U., Burkhardt, S., Dauelsberg, A., & Kroon, B. (2000). Carbon isotope fractionation by a marine diatom: dependence on the growth-rate-limiting resource. *Marine Ecology Progress Series*, *193*, 295-303. https://doi.org/10.3354/meps193295

Rose, A. L., Godrant, A., Godrant, A., Furnas, M., & Waite, T. D. (2010). Dynamics of nonphotochemical superoxide production in the Great Barrier Reef lagoon. *Limnology and Oceanography*, *55*(4), 1521-1536. https://doi.org/10.4319/lo.2010.55.4.1521

Rose, A. L., Webb, E. A., Waite, T. D., & Moffett, J. W. (2008). Measurement and implications of nonphotochemically generated superoxide in the equatorial Pacific Ocean. *Environmental science & technology*, *42*(7), 2387-2393. https://doi.org/10.1021/es7024609

Rudels, B. (1987). On the mass balance of the Polar Ocean, with special emphasis on the Fram Strait. *Norsk Polarinstitutt Skrifter*, *188*, 1-53

Rudels, B., Anderson, L. G., & Jones, E. P. (1996). Formation and evolution of the surface mixed layer and halocline of the Arctic Ocean. *Journal of Geophysical Research: Oceans*, *101*(C4), 8807-8821. https://doi.org/10.1029/96jc00143

Rudels, B., Friedrich, H. J., & Quadfasel, D. (1999). The Arctic circumpolar boundary current. *Deep Sea Research Part II: Topical Studies in Oceanography*, *46*(6-7), 1023-1062. https://doi.org/10.1016/S0967-0645(99)00015-6

Rudels, B., Jones, E. P., Anderson, L. G., & Kattner, G. (1994). On the intermediate depth waters of the Arctic Ocean. *The polar oceans and their role in shaping the global environment*, 33-46. https://doi.org/10.1029/GM085p0033

Rudels, B., Jones, E. P., Schauer, U., & Eriksson, P. (2004). Atlantic sources of the Arctic Ocean surface and halocline waters. *Polar Research*, *23*(2), 181-208. https://doi.org/10.1111/j.1751-8369.2004.tb00007.x

Rusak, S. A., Peake, B. M., Richard, L. E., Nodder, S. D., & Cooper, W. J. (2011). Distributions of hydrogen peroxide and superoxide in seawater east of New Zealand. *Marine Chemistry*, *127*(1-4), 155-169. https://doi.org/10.1016/j.marchem.2011.08.005

Salmon, D. K., & Mcroy, C. P. (1994). Nutrient-based tracers in the western Arctic: a new lower holocline water defined. *Washington DC American Geophysical*

Union Geophysical Monograph Series, *85*, 47-61. https://doi.org/10.1029/GM085p0047

Sánchez-García, L., Alling, V., Pugach, S., Vonk, J., Van Dongen, B., Humborg, C., et al. (2011). Inventories and behavior of particulate organic carbon in the Laptev and East Siberian seas. *Global Biogeochemical Cycles*, *25*(2). https://doi.org/10.1029/2010gb003862

Sanchez-Vidal, A., Veres, O., Langone, L., Ferré, B., Calafat, A., Canals, M., et al. (2015). Particle sources and downward fluxes in the eastern Fram strait under the influence of the west Spitsbergen current. *Deep Sea Research Part I: Oceanographic Research Papers*, *103*, 49-63. https://doi.org/10.1016/j.dsr.2015.06.002

Santana-Casiano, J. M., González-Dávila, M., & Millero, F. J. (2005). Oxidation of Nanomolar Levels of Fe(II) with Oxygen in Natural Waters. *Environmental Science & Technology*, *39*(7), 2073-2079. https://doi.org/10.1021/es049748y

Schlosser, P., Kromer, B., Ekwurzel, B., Bönisch, G., McNichol, A., Schneider, R., et al. (1997). The first trans-Arctic 14C section: comparison of the mean ages of the deep waters in the Eurasian and Canadian basins of the Arctic Ocean. *Nuclear Instruments and Methods in Physics Research Section B: Beam Interactions with Materials and Atoms*, *123*(1-4), 431-437. https://doi.org/10.1016/S0168-583X(96)00677-5

Schubert, C. J., & Calvert, S. E. (2001). Nitrogen and carbon isotopic composition of marine and terrestrial organic matter in Arctic Ocean sediments:: implications for nutrient utilization and organic matter composition. *Deep Sea Research Part I: Oceanographic Research Papers*, *48*(3), 789-810. https://doi.org/10.1016/S0967-0637(00)00069-8

Serreze, M. C., Barrett, A. P., Slater, A. G., Woodgate, R. A., Aagaard, K., Lammers, R. B., et al. (2006). The large-scale freshwater cycle of the Arctic. *Journal of Geophysical Research: Oceans*, *111*(C11). https://doi.org/10.1029/2005jc003424

Shapiro, G. I., Huthnance, J. M., & Ivanov, V. V. (2003). Dense water cascading off the continental shelf. *Journal of Geophysical Research: Oceans*, *108*(C12). https://doi.org/10.1029/2002jc001610

Shen, Y., Benner, R., Robbins, L. L., & Wynn, J. G. (2016). Sources, Distributions, and Dynamics of Dissolved Organic Matter in the Canada and Makarov Basins. *Frontiers in Marine Science*, *3*. https://doi.org/10.3389/fmars.2016.00198

Sherman, D. M. (2005). Electronic structures of iron(III) and manganese(IV) (hydr)oxide minerals: Thermodynamics of photochemical reductive dissolution in aquatic environments. *Geochimica et Cosmochimica Acta*, *69*(13), 3249-3255. https://doi.org/10.1016/j.gca.2005.01.023

Shimada, K., Carmack, E. C., Hatakeyama, K., & Takizawa, T. (2001). Varieties of shallow temperature maximum waters in the western Canadian Basin of the Arctic Ocean. *Geophysical Research Letters*, *28*(18), 3441-3444. https://doi.org/10.1029/2001GL013168

Shimada, K., Itoh, M., Nishino, S., McLaughlin, F., Carmack, E., & Proshutinsky, A. (2005). Halocline structure in the Canada basin of the arctic ocean. *Geophysical Research Letters*, *32*(3). https://doi.org/10.1029/2004gl021358

Spokes, L. J., & Liss, P. S. (1995). Photochemically induced redox reactions in seawater, I. Cations. *Marine chemistry*, *49*(2-3), 201-213. https://doi.org/10.1016/0304-4203(95)00006-D

Springer, A. M., & Mcroy, C. P. (1993). The paradox of pelagic food webs in the northern Bering Sea—III. Patterns of primary production. *Continental shelf research*, *13*(5-6), 575-599. https://doi.org/10.1016/0278-4343(93)90095-F

Steele, M., Morison, J., Ermold, W., Rigor, I., Ortmeyer, M., & Shimada, K. (2004). Circulation of summer Pacific halocline water in the Arctic Ocean. *Journal of Geophysical Research: Oceans*, *109*(C2). https://doi.org/10.1029/2003JC002009

Stein, R., & Fahl, K. (2004). The Laptev Sea: distribution, sources, variability and burial of organic carbon. In R. Stein and R. W. Macdonald (Eds.), *The organic carbon cycle in the Arctic Ocean* (pp. 213-237). Berlin: Springer-Verlag

Stein, R., & Macdonald, R. W. (2004). *The organic carbon cycle in the Arctic Ocean*. Berlin: Springer. https://doi.org/10.1007/978-3-642-18912-8

Sterner, R. W., Andersen, T., Elser, J. J., Hessen, D. O., Hood, J. M., McCauley, E., & Urabe, J. (2008). Scale - dependent carbon: nitrogen: phosphorus seston stoichiometry in marine and freshwaters. *Limnology and Oceanography*, *53*(3), 1169-1180. https://doi.org/10.4319/lo.2008.53.3.1169

Sukhanova, I. N., Flint, M. V., Pautova, L. A., Stockwell, D. A., Grebmeier, J. M., & Sergeeva, V. M. (2009). Phytoplankton of the western Arctic in the spring and summer of 2002: Structure and seasonal changes. *Deep Sea Research Part II: Topical Studies in Oceanography*, *56*(17), 1223-1236. https://doi.org/10.1016/j.dsr2.2008.12.030

Sunda, W. G., & Huntsman, S. A. (1988). Effect of sunlight on redox cycles of manganese in the southwestern Sargasso Sea. *Deep Sea Research Part A. Oceanographic Research Papers*, *35*(8), 1297-1317. https://doi.org/10.1016/0198-0149(88)90084-2

Sunda, W. G., Huntsman, S. A., & Harvey, G. R. (1983). Photoreduction of manganese oxides in seawater and its geochemical and biological implications. *Nature*, *301*(5897), 234. https://doi.org/10.1038/301234a0

Tamelander, T., Reigstad, M., Olli, K., Slagstad, D., & Wassmann, P. (2013). New production regulates export stoichiometry in the ocean. *PLoS One*, *8*(1), e54027. https://doi.org/10.1371/journal.pone.0054027

Taylor, S. R., & McLennan, S. M. (1995). The geochemical evolution of the continental crust. *Reviews of Geophysics*, *33*(2), 241-265. https://doi.org/10.1029/95RG00262

Tolosa, I., Fiorini, S., Gasser, B., Martín, J., & Miquel, J. C. (2013). Carbon sources in suspended particles and surface sediments from the Beaufort Sea revealed by molecular lipid biomarkers and compound-specific isotope analysis. *Biogeosciences*, *10*(3), 2061-2087. https://doi.org/10.5194/bg-10-2061-2013

Toner, B., Fakra, S., Villalobos, M., Warwick, T., & Sposito, G. (2005). Spatially resolved characterization of biogenic manganese oxide production within a bacterial biofilm. *Appl Environ Microbiol*, *71*(3), 1300-1310. https://doi.org/10.1128/AEM.71.3.1300-1310.2005

Toyoda, K., & Tebo, B. M. (2016). Kinetics of Mn(II) oxidation by spores of the marine Bacillus sp. SG-1. *Geochimica et Cosmochimica Acta*, *189*, 58-69. https://doi.org/10.1016/j.gca.2016.05.036

Tremblay, J. É., Hattori, H., Michel, C., Ringuette, M., Mei, Z. P., Lovejoy, C., et al. (2006a). Trophic structure and pathways of biogenic carbon flow in the eastern North Water Polynya. *Progress in Oceanography*, *71*(2-4), 402-425. https://doi.org/10.1016/j.pocean.2006.10.006

Tremblay, J. É., Michel, C., Hobson, K. A., Gosselin, M., & Price, N. M. (2006b). Bloom dynamics in early opening waters of the Arctic Ocean. *Limnology and Oceanography*, *51*(2), 900-912. https://doi.org/10.4319/lo.2006.51.2.0900

Turnewitsch, R., Falahat, S., Nycander, J., Dale, A., Scott, R. B., & Furnival, D. (2013). Deep-sea fluid and sediment dynamics—Influence of hill-to seamount-scale seafloor topography. *Earth-Science Reviews*, *127*, 203-241. https://doi.org/10.1016/j.earscirev.2013.10.005

Twining, B. S., & Baines, S. B. (2013). The trace metal composition of marine phytoplankton. *Annual Review of Marine Science*, *5*, 191-215. https://doi.org/10.1146/annurev-marine-121211-172322

Twining, B. S., Morton, P. L., & Salters, V. J. (2019). Trace element concentrations (labile and total measurements) in particles collected with GO-Flo bottles and analyzed with ICP-MS from the US GEOTRACES Arctic cruise (HLY1502; GN01) from August to October 2015. *Biological and Chemical Oceanography Data Management Office (BCO-DMO)*, *Dataset version 2019-07-02*. https://doi.org/10.1575/1912/bco-dmo.771474.2.

Van Cappellen, P., & Qiu, L. (1997). Biogenic silica dissolution in sediments of the Southern Ocean. II. Kinetics. *Deep Sea Research Part II: Topical Studies in Oceanography*, *44*(5), 1129-1149. https://doi.org/10.1016/S0967-0645(96)00112-9

Varela, D. E., Brzezinski, M. A., Beucher, C. P., Jones, J. L., Giesbrecht, K. E., Lansard, B., & Mucci, A. (2016). Heavy silicon isotopic composition of silicic acid and biogenic silica in Arctic waters over the Beaufort shelf and the Canada Basin. *Global Biogeochemical Cycles*, *30*(6), 804-824. https://doi.org/10.1002/2015GB005277

Vieira, L. H., Achterberg, E. P., Scholten, J., Beck, A. J., Liebetrau, V., Mills, M. M., & Arrigo, K. R. (2019). Benthic fluxes of trace metals in the Chukchi Sea and their transport into the Arctic Ocean. *Marine Chemistry*, *208*, 43-55. https://doi.org/10.1016/j.marchem.2018.11.001

Vonk, J. E., Sánchez-García, L., van Dongen, B. E., Alling, V., Kosmach, D., Charkin, A., et al. (2012). Activation of old carbon by erosion of coastal and subsea permafrost in Arctic Siberia. *Nature*, *489*(7414), 137-140. https://doi.org/10.1038/nature11392

Vonk, J. E., Semiletov, I. P., Dudarev, O. V., Eglinton, T. I., Andersson, A., Shakhova, N., et al. (2014). Preferential burial of permafrost-derived organic carbon in Siberian-Arctic shelf waters. *Journal of Geophysical Research: Oceans*, *119*(12), 8410-8421. https://doi.org/10.1002/2014jc010261

Wahsner, M., Müller, C., Stein, R., Ivanov, G., Levitan, M., Shelekhova, E., & Tarasov, G. (1999). Clay - mineral distribution in surface sediments of the Eurasian Arctic Ocean and continental margin as indicator for source areas and transport pathways—a synthesis. *Boreas*, *28*(1), 215-233. https://doi.org/10.1111/j.1502-3885.1999.tb00216.x

Watanabe, E., Onodera, J., Harada, N., Honda, M. C., Kimoto, K., Kikuchi, T., et al. (2014). Enhanced role of eddies in the Arctic marine biological pump. *Nature communications*, *5*, 3950. https://doi.org/10.1038/ncomms4950

Weingartner, T. J., Cavalieri, D. J., Aagaard, K., & Sasaki, Y. (1998). Circulation, dense water formation, and outflow on the northeast Chukchi shelf. *Journal of Geophysical Research: Oceans*, *103*(C4), 7647-7661. https://doi.org/10.1029/98JC00374

Whitmore, L. M., Morton, P. L., Twining, B. S., & Shiller, A. M. (2019). Vanadium cycling in the Western Arctic Ocean is influenced by shelf-basin connectivity. *Marine Chemistry*, *216*, 103701. https://doi.org/10.1016/j.marchem.2019.103701

Winsor, P., & Björk, G. (2000). Polynya activity in the Arctic Ocean from 1958 to 1997. *Journal of Geophysical Research: Oceans*, *105*(C4), 8789-8803. https://doi.org/10.1029/1999JC900305

Winterfeld, M., Laepple, T., & Mollenhauer, G. (2015). Characterization of particulate organic matter in the Lena River delta and adjacent nearshore zone, NE Siberia--Part I: Radiocarbon inventories. *Biogeosciences*, *12*(12), 3769-3788. https://doi.org/10.5194/bg-12-3769-2015

Woodgate, R. A. (2018). Increases in the Pacific inflow to the Arctic from 1990 to 2015, and insights into seasonal trends and driving mechanisms from year-round Bering Strait mooring data. *Progress in Oceanography*, *160*, 124-154. https://doi.org/10.1016/j.pocean.2017.12.007

Woodgate, R. A., Aagaard, K., Muench, R. D., Gunn, J., Björk, G., Rudels, B., et al. (2001). The Arctic Ocean boundary current along the Eurasian slope and the adjacent Lomonosov Ridge: Water mass properties, transports and transformations from moored instruments. *Deep Sea Research Part I: Oceanographic Research Papers*, *48*(8), 1757-1792. https://doi.org/10.1016/S0967-0637(00)00091-1

Wyatt, S. N., Crawford, D. W., Wrohan, I. A., & Varela, D. E. (2013). Distribution and composition of suspended biogenic particles in surface waters across Subarctic and Arctic Seas. *Journal of Geophysical Research: Oceans*, *118*(12), 6867-6880. https://doi.org/10.1002/2013jc009214

Yamada, Y., Fukuda, H., Uchimiya, M., Motegi, C., Nishino, S., Kikuchi, T., & Nagata, T. (2015). Localized accumulation and a shelf-basin gradient of particles in the Chukchi Sea and Canada Basin, western Arctic. *Journal of Geophysical Research: Oceans*, *120*(7), 4638-4653. https://doi.org/10.1002/2015JC010794

Yamamoto-Kawai, M., Tanaka, N., & Pivovarov, S. (2005). Freshwater and brine behaviors in the Arctic Ocean deduced from historical data of δ18O and alkalinity (1929–2002 A.D.). *Journal of Geophysical Research: Oceans*, *110*(C10). https://doi.org/10.1029/2004jc002793

Yang, J., & Haley, B. (2016). The profile of the rare earth elements in the Canada Basin, Arctic Ocean. *Geochemistry, Geophysics, Geosystems*, *17*(8), 3241-3253. https://doi.org/10.1002/2016GC006412

Ye, L., März, C., Polyak, L., Yu, X., & Zhang, W. (2019). Dynamics of manganese and cerium enrichments in Arctic Ocean sediments: a case study from the Alpha Ridge. *Frontiers in Earth Science*, *6*. https://doi.org/10.3389/feart.2018.00236

Yocis, B. H., Kieber, D. J., & Mopper, K. (2000). Photochemical production of hydrogen peroxide in Antarctic waters. *Deep Sea Research Part I: Oceanographic Research Papers*, *47*(6), 1077-1099. https://doi.org/10.1016/S0967-0637(99)00095-3

Zernova, V. V., Nöthig, E. M., & Shevchenko, V. P. (2000). Vertical microalga flux in the northern Laptev Sea (from the data collected by the yearlong sediment trap). *Oceanology*, *40*(6), 801-808

Zhang, R., Chen, M., Guo, L., Gao, Z., Ma, Q., Cao, J., et al. (2012). Variations in the isotopic composition of particulate organic carbon and their relation with carbon dynamics in the western Arctic Ocean. *Deep Sea Research Part II: Topical Studies in Oceanography*, *81-84*, 72-78. https://doi.org/10.1016/j.dsr2.2011.05.005

Zhao, M., Timmermans, M. L., Cole, S., Krishfield, R., Proshutinsky, A., & Toole, J. (2014). Characterizing the eddy field in the Arctic Ocean halocline. *Journal of Geophysical Research: Oceans*, *119*(12), 8800-8817. https://doi.org/10.1002/2014JC010488

Zimmerman, A. E., Allison, S. D., & Martiny, A. C. (2014). Phylogenetic constraints on elemental stoichiometry and resource allocation in heterotrophic marine bacteria. *Environmental Microbiology*, *16*(5), 1398-1410. https://doi.org/10.1111/1462-2920.12329

Figures and Tables

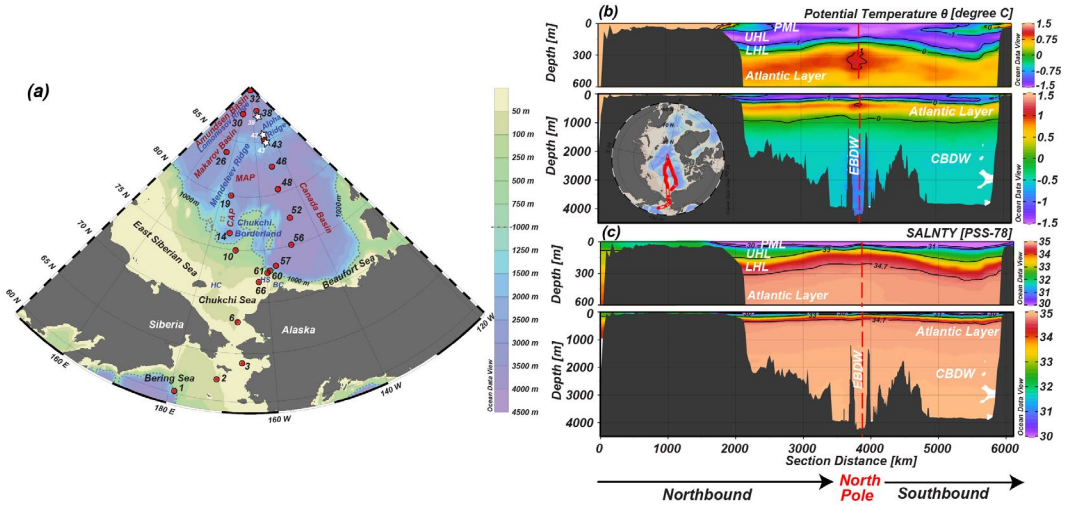

Figure 1.1 Map and hydrography of the GN01 U.S. GEOTRACES cruise in the Western Arctic (Cutter et al., 2019). (a) Station map showing GEOTRACES stations in which in-situ pumps were deployed (red circles; n= 20) plotted on ocean bathymetry (color bar) with 1000 m contour indicated as grey dotted line. Four stations (30, 32, 38, and 43) locate within the fast-flowing Transpolar Drift. Sea ice algae were collected at Stations 39, 42, and 43, marked with white stars and station numbers. Marginal seas, major basins, and key topographic features are labeled in black, dark red and dark blue, respectively. Bering Shelf: Stations 2, and 3; Bering Slope: Station 1; Chukchi Shelf: Stations 6, 61, and 66; Chukchi Slope: Stations 10, and 60; Makarov Basin (MB): Stations 26, 30, 38, and 43; Amundsen Basin (AB): Station 32; Canada Basin (CB): Stations 46, 48, 52, 56, and 57; Chukchi Abyssal Plain (CAP): Stations 14, and 19; HS: Hanna Shoal; HC: Herald Canyon; BC: Barrow Canyon; MAP: Mendeleev Abyssal Plain. (b) The section plot of potential temperature; (c) The section plot of salinity. In (b) and (c), top panels are both the upper 600 m, and bottom panels are the whole water column. The North Pole (Station 32) is marked with the red dashed line. Different water masses are labeled. PML: Polar Mixed Layer; UHL: Upper Halocline; LHL: Lower Halocline; AL: Atlantic Layer; CBDW: Canadian Basin Deep Water; EBDW: Eurasian Basin Deep Water.

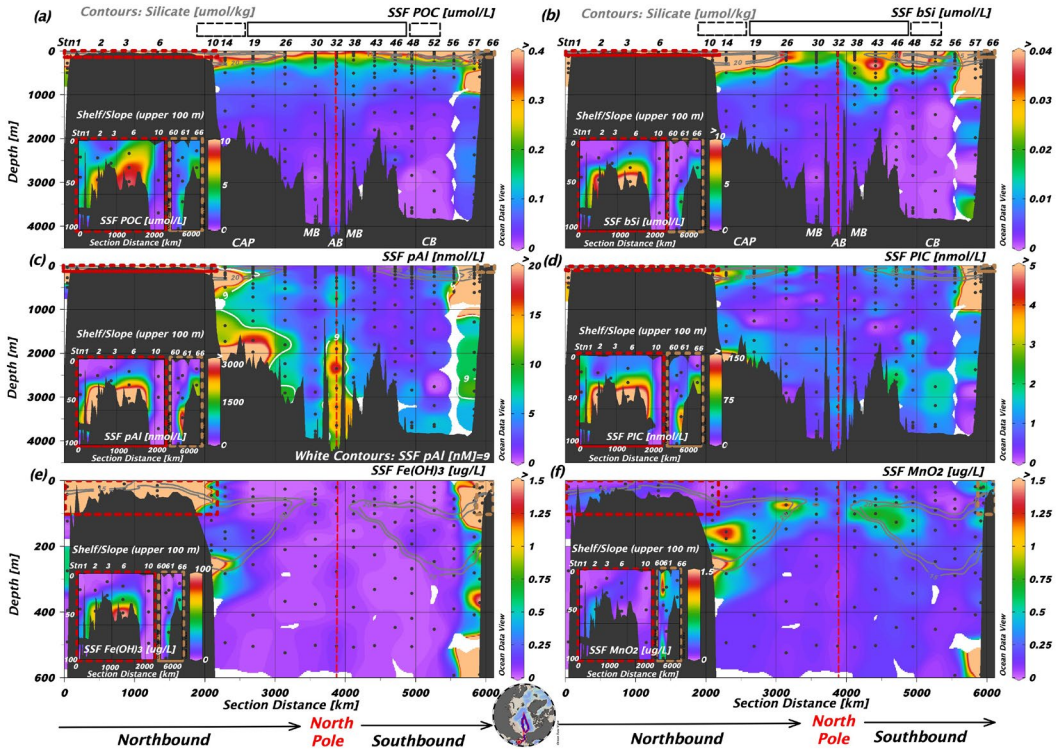

Figure 1.2 Section plots of small size fraction (SSF; 1-51 µm) major particle composition in the whole water column (a-d) and the upper 600 m (e-f). (a) Particulate organic carbon (POC) (µmol/L); (b) Biogenic silica (bSi) (µmol/L); (c) Particulate aluminum (pAl) (nmol/L); (d) Particulate inorganic carbon (PIC) (nmol/L); (e) Fe oxyhydroxides ($Fe(OH)_3$) (µg/L); (f) Mn oxides (MnO_2) (µg/L). Insets highlighted with dark red, and brown dotted rectangles in the bottom left corner are expanded sections of the upper 100 m at northbound and southbound shelf/slope stations, respectively. Note much higher color scales in insets. Grey contours are silicate concentrations of 15 and 20 µmol/kg, indicating the intrusion of the modified Pacific water. Bottom nepheloid layers (BNLs), defined where pAl > 9 nmol/L in the SSF, are indicated by white contour lines in (c). Station numbers are labeled on the top of each panel. Rectangles with dashed and solid black outline on the top margin indicate the marginal ice zone (MIZ) and fully ice-covered stations, respectively. Abbreviations as in Figure 1.1.

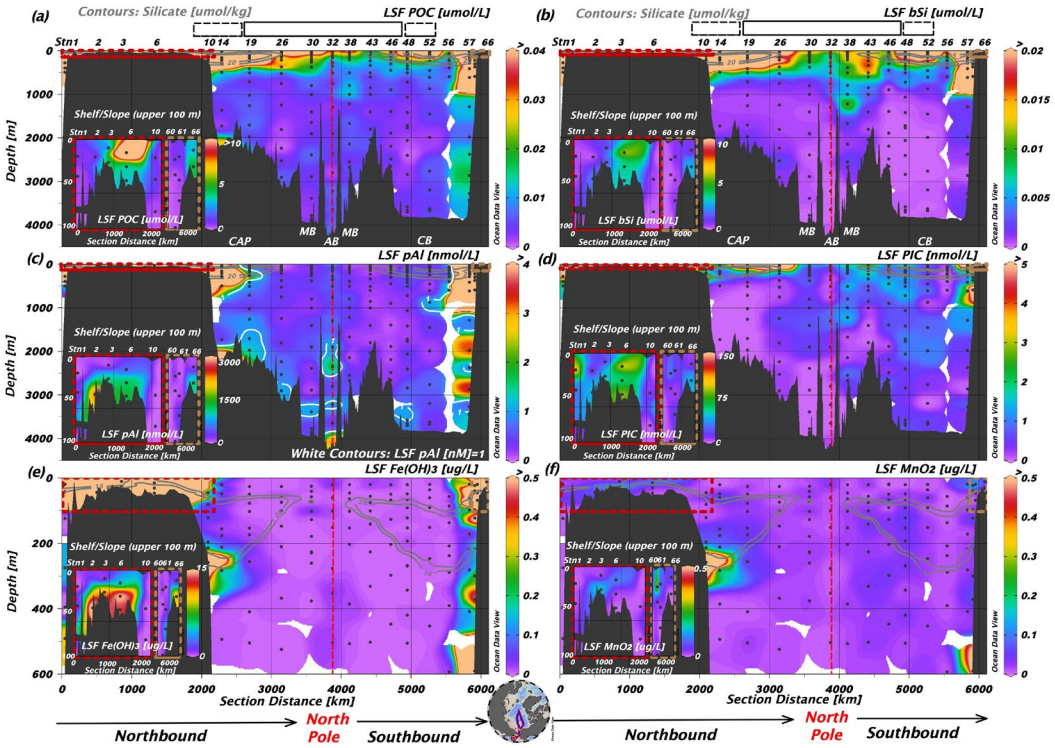

Figure 1.3 Section plots of large size fraction (LSF; >51 µm) major particle composition in the whole water column (a-d) and the upper 600 m (e-f). (a) Particulate organic carbon (POC) (µmol/L); (b) Biogenic silica (bSi) (µmol/L); (c) Particulate aluminum (pAl) (nmol/L); (d) Particulate inorganic carbon (PIC) (nmol/L); (e) Fe oxyhydroxides ($Fe(OH)_3$) (µg/L); (f) Mn oxides (MnO_2) (µg/L). Bottom nepheloid layers (BNLs), defined where pAl > 1 nM in the LSF, are indicated by white contour lines in (c). Panel arrangements, insets, and notations as for Figure 1.2.

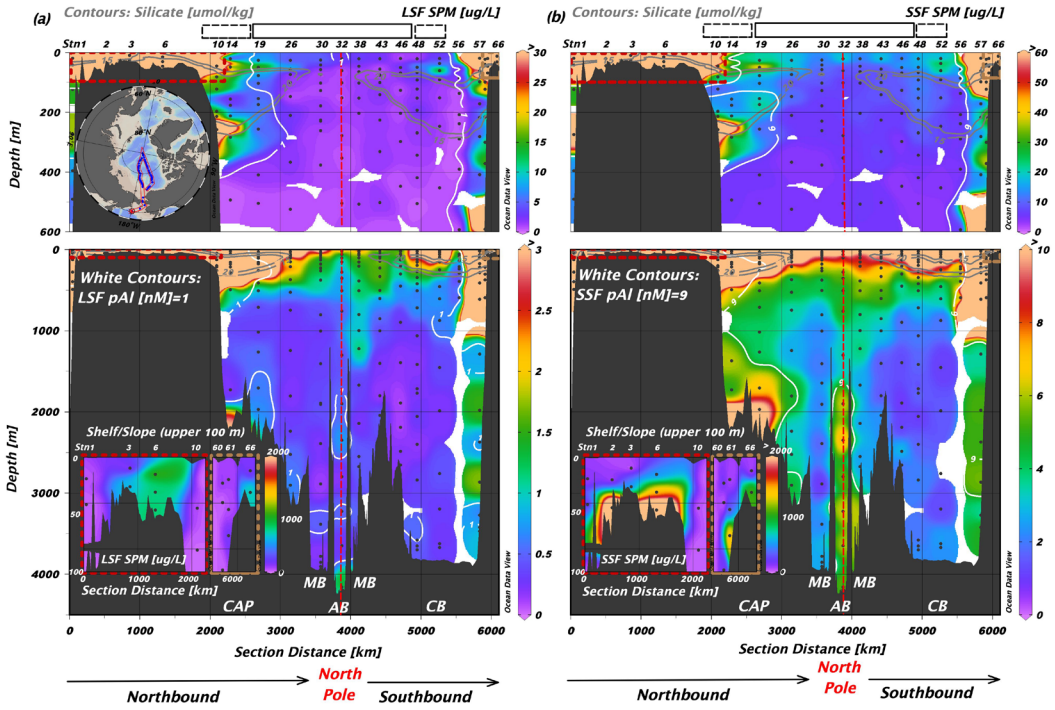

Figure 1.4 Section plots of suspended particulate mass (SPM) (µg/L) in the upper 600 m (top panels) and the whole water column (bottom panels). (a) large size fraction (LSF; >51 µm); (b) small size fraction (SSF; 1-51 µm). White contour lines show locations of BNLs, as defined in Figures 1.2 and 1.3. Panel insets and notations as for Figures 1.2 and 1.3. Note scale changes between panels and insets.

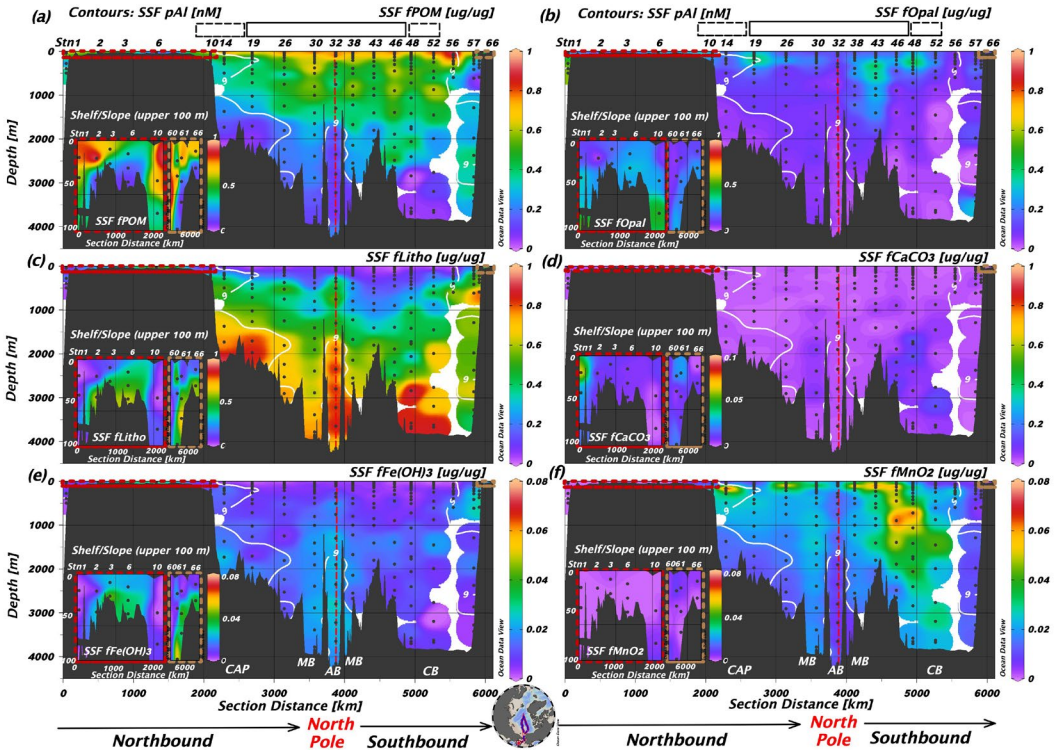

Figure 1.5 Section plots of relative particle composition (weight fraction of SPM that is the particle phase) for the major phases in the SSF in the whole water column (g/g). (a) the fraction of particulate organic matter (fPOM); (b) the fraction of opal (fOpal); (c) the fraction of lithogenic particles (fLitho); (d) the fraction of calcium carbonate ($fCaCO_3$); (e) the fraction of Fe oxyhydroxides ($fFe(OH)_3$); (f) the fraction of Mn oxides ($fMnO_2$). White contour lines show locations of BNLs, as defined in Figure 1.2. Panel arrangements, insets, and notations as for Figure 1.2.

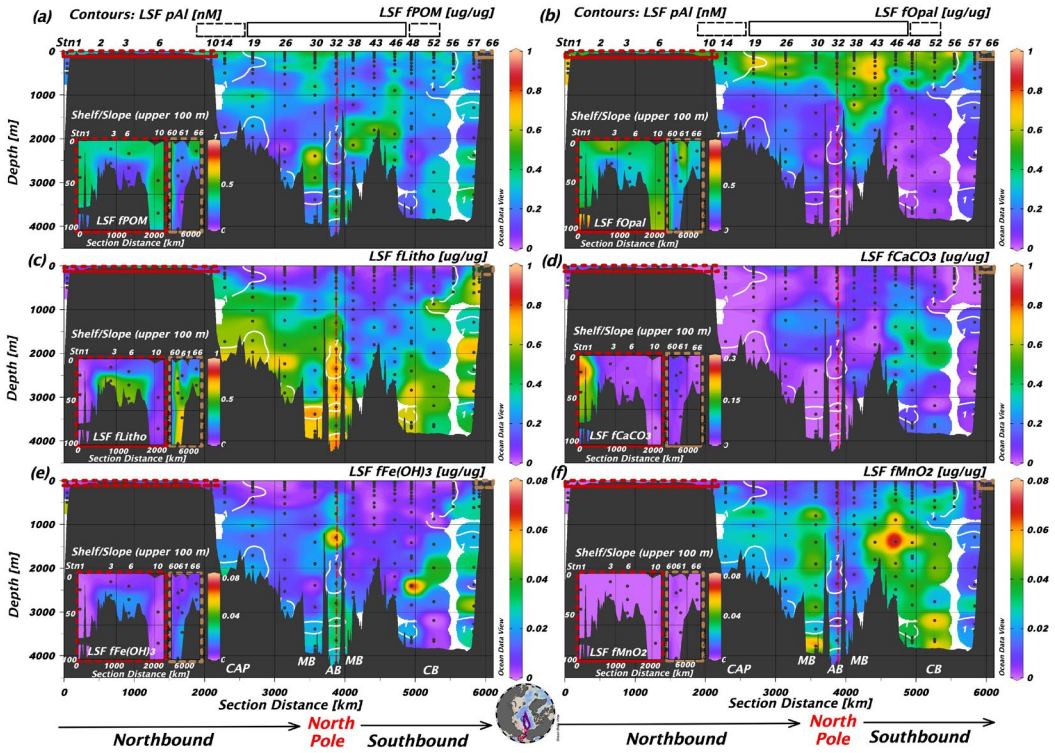

Figure 1.6 Section plots of relative particle composition for the major phases in the LSF in the whole water column (g/g). (a) the fraction of particulate organic matter (fPOM); (b) the fraction of opal (fOpal); (c) the fraction of lithogenic particles (fLitho); (d) the fraction of calcium carbonate ($fCaCO_3$); (e) the fraction of Fe oxyhydroxides ($fFe(OH)_3$); (f) the fraction of Mn oxides ($fMnO_2$). White contour lines show locations of BNLs, as defined in Figure 1.3. Panel arrangements, insets, and notations as for Figure 1.3.

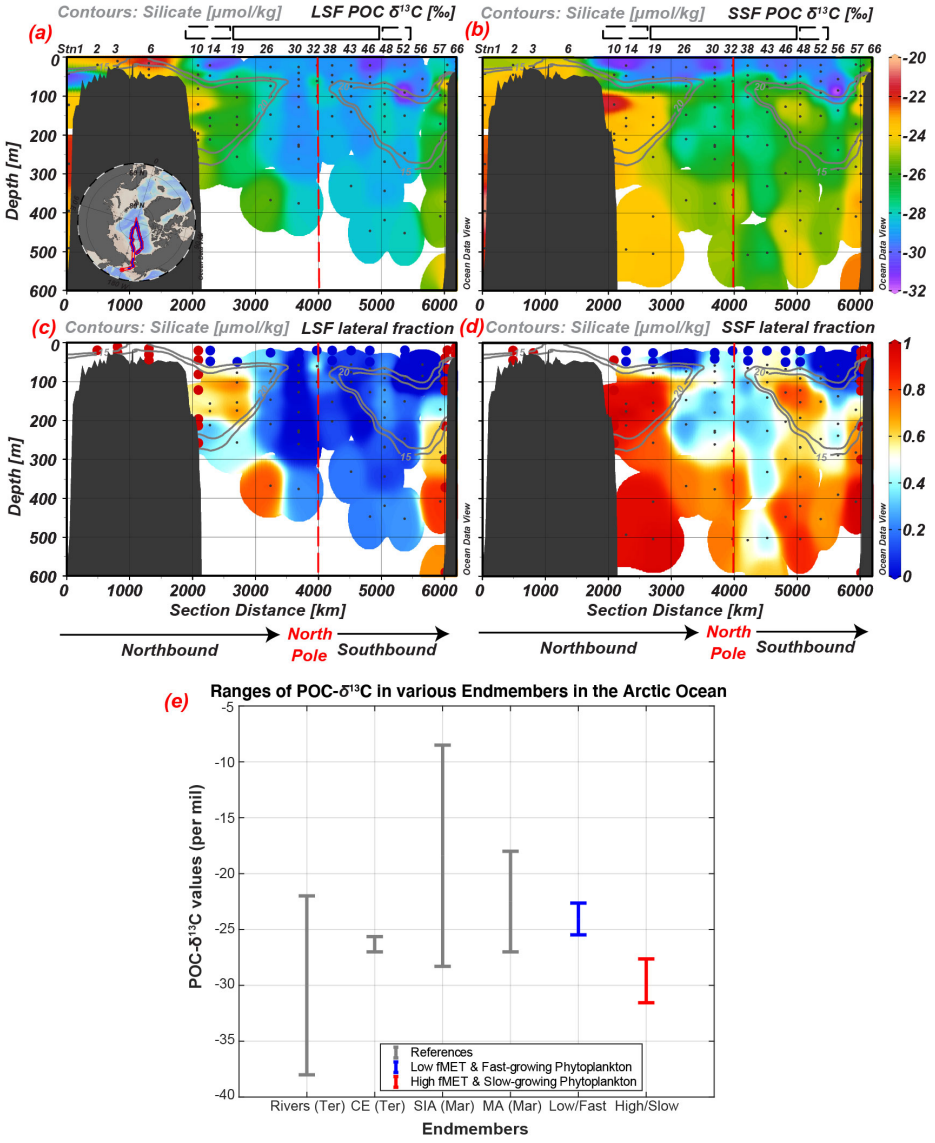

Figure 1.7 Summary of POC-δ^{13}C values and the fraction of lateral transport in size-fractionated particles in the upper 600 m. Section plots of POC-δ^{13}C in the (a) LSF and (b) SSF; section plots of the fraction of lateral transport below 50 m in the central basin in the (c) LSF and (d) SSF. The fraction of lateral transport is derived from a two end-member mixing model between shelf/slope POC-δ^{13}C and POC-δ^{13}C in the PML. End members are calculated as the median of POC-δ^{13}C in the shelf/slope, and upper 50 m of the PML, and shown as colored dots with values of 1 and 0, respectively. Note that blue-white-red color bars are used in (c) and (d) to more clearly indicate the 50% threshold in the fraction of lateral-derived POC. (e) the range of POC-δ^{13}C values for terrestrial (Rivers and CE: coastal erosion) and marine (SIA: sea ice algae and MA: marine algae) endmembers in the Arctic Ocean from the literature (grey bars) and for size-fractionated samples from this work in the basin (<50 m) with low fractions of

meteoric (fMET) and fast growth rates (low/fast—blue bars; ≤0.1 in fMET, ≥1 µmol/kg phosphate and ≥0 ˚C in temperature), and samples in the basin (<50 m) with high fMET and slow growth rates in phytoplankton (high/slow—red bars; >0.1 in fMET, <1 µmol/kg phosphate and <0 ˚C in temperature).

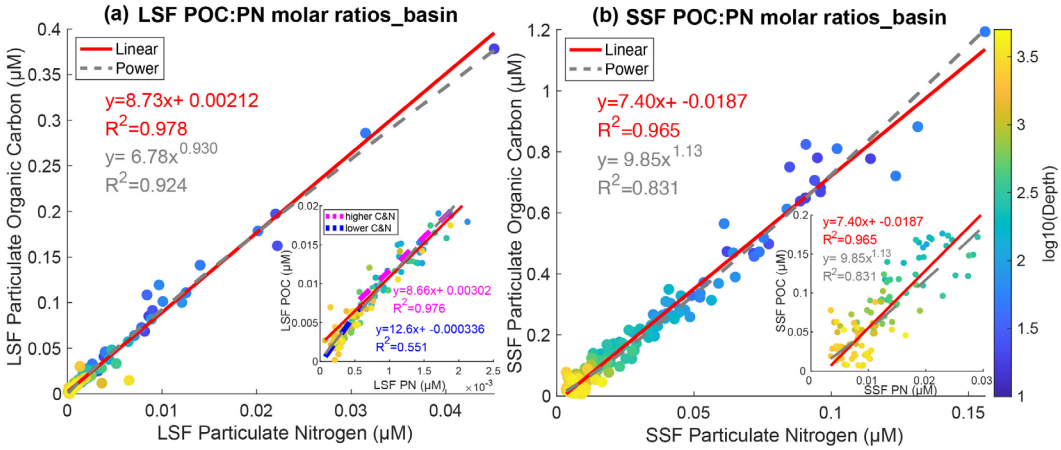

Figure 1.8 Correlations between POC and PN in the basin stations in LSF (a) and SSF (b) are shown with units all in µM. All data points are above detection limits and color-coded with log base 10 of the sampling depth (unit: m). The reduced major axis (Model II linear fit) and power-law fit are used in the regression. The LSF power function is fitted without two extremely low C/N ratio samples to be more representative of the overall trend. Red solid and grey dashed lines are fitted with all data in the basin. Expanded plots at low concentrations are plotted separately in the bottom right. In (a), at low concentrations, LSF data are fitted differently. Two regression equations are used, with the dark blue dotted line fitting data at the low end and the magenta fitting the rest. Regression equations are displayed with the colors matching with fit lines.

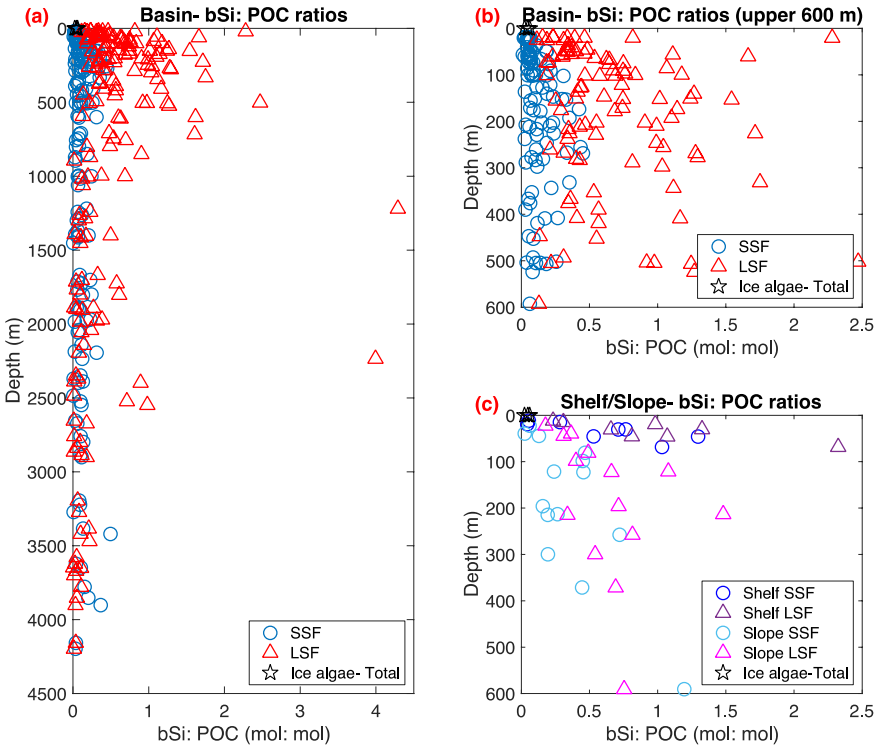

Figure 1.9 Vertical profiles of size-fractionated bSi:POC molar ratios (unit: mol:mol) at basin and Chukchi shelf/slope stations. Only data above the detection limit are used here. (a) bSi:POC ratios in the entire water column in the basin; (b) bSi:POC ratios in the upper 600 m in the basin; (c) bSi:POC ratios over the shelf and slope. Sea ice algae bSi:POC at the surface of Stations 39, 42 and 43 are shown in black pentagrams.

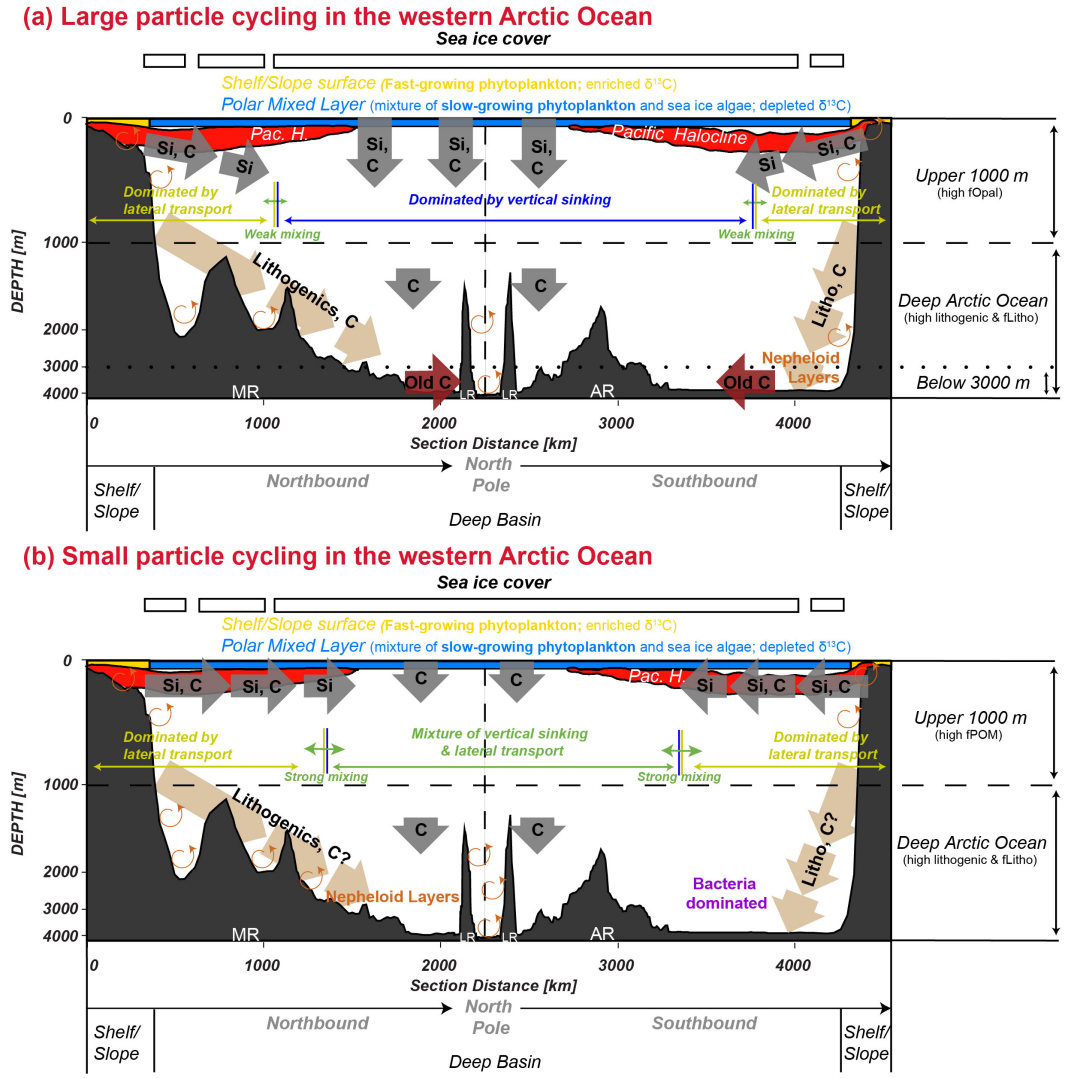

Figure 1.10 Schematic of size-fractionated particles sources and transport in the Western Arctic Ocean for (a) the large size-fraction (LSF) and (b) the small size-fraction (SSF). Note that the depth is strongly stretched to the top to better represent upper ocean processes. Key water masses and processes are indicated by various colors: the thin gold rectangle represents the shelf/slope surface, whereas the thin blue one represents the Polar Mixed Layer; the red plume at about 200 m shows the Pacific-derived halocline; the horizontal grey dashed line at 1000 m separates the Atlantic layer and deep Arctic Ocean; vertical and lateral transport are illustrated with block arrows, with biogenic particle transport in grey, lithogenic particle transport in tan and old LSF carbon with relatively high C/N ratios below 3000 m (dotted line) in maroon. The length of the arrows in each category qualitatively reflect the relative magnitude of fluxes for each process. Nepheloid layers as defined by pAl content (see section 4.1) are shown as orange spirals; bacterial dominance in the SSF in the deep Canada Basin based on low C/N is indicated with purple; the color of the notations in the subsurface

reflects the average POC-$\delta^{13}C$ for that size fraction (see color bar for Figure 1.7a-b), and implies the extent of mixing between the lateral and vertical component of POC: (a) POC-$\delta^{13}C$ of LSF is depleted (dark blue color), suggesting that vertical sinking dominates; (b) POC-$\delta^{13}C$ of SSF is more enriched in the central Arctic (green color), suggesting that vertical sinking and lateral transport are equally important.

CHAPTER 2: DIEL REDOX CYCLE OF MANGANESE IN THE SURFACE ARCTIC OCEAN

Abstract

Knowledge of the chemical speciation of particulate manganese (pMn) is important for understanding the biogeochemical cycling of Mn and other particle-reactive elements. Here, we present the synchrotron-based X-ray spectroscopy derived average oxidation state (AOS) of pMn in the surface Arctic Ocean collected during the U.S. GEOTRACES Arctic cruise (GN01) in 2015. We show that the pMn AOS at the time of sampling is less than 2.4 during the day and more than ~3.0 at night, suggesting that reduction and oxidation lowers and increases pMn AOS, respectively. Examination of AOS as a function of sampling time relative to dawn suggests diel redox variations of pMn within the Polar Mixed Layer, with more rapid rates of light-dependent reduction and oxidation at Arctic shelf/slope compared to basin stations.

1 Introduction

Manganese (Mn) is the 3rd most abundant transition metal in Earth's crust and exists in three oxidation states (II, III, and IV) in the ocean. Mn is an essential element to life and used to catalyze the oxidation of water to O_2 in Photosystem II (Yano et al., 2006) by phytoplankton, and to detoxify cells from superoxide radicals via the

antioxidant enzyme Mn superoxide dismutase (Peers & Price, 2004). Oxidation from dissolved Mn(II) to particulate Mn(III/IV) oxides is known to proceed through two sequential one-electron reactions (Luther, 2005). The final oxidation product, Mn(III/IV) oxide, is a strong natural oxidant and is also known as the "scavenger of the sea" (Goldberg, 1954; Tebo et al., 2004). Although Mn is an important micronutrient for phytoplankton growth, dissolved Mn is often characterized by maximum concentrations at the surface ocean (van Hulten et al., 2017) due to photoreduction of Mn(III/IV) oxides (Sunda & Huntsman, 1987, 1994; Sunda et al., 1983) and is thus not typically limiting, except for in the Southern Ocean (Browning et al., 2021; Middag et al., 2013).

Recent GEOTRACES cruises have demonstrated that the Arctic Ocean is enriched in Mn because of riverine, sedimentary and hydrothermal sources (Charette et al., 2020; Colombo et al., 2020; Jensen et al., 2020; Middag et al., 2011; Xiang & Lam, 2020). The Mn concentration distribution in the Western Arctic Ocean is characterized by surface maxima in the Polar Mixed Layer in the dissolved phase and distinct elevations at halocline depths in the particulate phase (Jensen et al., 2020; Xiang & Lam, 2020). Investigations of Mn cycling in the Arctic Ocean have generally focused on processes spanning time scales of several months to years during transport from shelves to central basins. However, a diel cycle in the concentrations of Mn, in both dissolved and particulate phases, has been observed in the coastal Northwest Atlantic Ocean (Oldham et al., 2020; Sunda & Huntsman, 1990).

Here, we use synchrotron-based X-ray absorption spectroscopy (XAS) to examine the chemical speciation of particulate Mn (pMn) and its relationship with light during the U.S. GEOTRACES Arctic cruise (GN01) in 2015. We take advantage of sampling times that spanned a range of light conditions to reconstruct a pseudo-diel cycle. This study is one of few that focuses on the oxidation state of pMn in the ocean (Hermans et al., 2019; Lee et al., 2021; Oldham et al., 2021), and the first one in the Arctic Ocean. Lee et al. (2021) showed that changes in pMn speciation in the near- vs. far-field 15˚S East Pacific Rise hydrothermal plume were associated with differences in its scavenging affinity for other trace elements and isotopes. Therefore, insights gained in this work help us understand the diel cycling of Mn and potentially also of other pMn-associated elements in the surface Arctic Ocean. Furthermore, since the light-dependent cycling of pMn found in the Arctic Ocean is likely to also occur elsewhere, this may have implications for Mn limitation in the Southern Ocean.

2 Materials and Methods

2.1 Marine particle sampling and chemical analysis

Marine particles were sampled using dual-flow McLane Research in-situ pumps (WTS-LV) during the U.S. Arctic GEOTRACES cruise (GN01) between 9 August and 11 October 2015 (Figure 2.1). The day-night cycle varied tremendously over the course of the cruise due to changes in sampling latitude and season, with the length of night ranging from 0 to ~14 hours (Supplementary Table 1).

Particles (0.8-51 μm) were collected with paired 0.8 μm pore-size polyethersulfone Supor™ filters that were downstream of a 51 μm pore-size polyester pre-filter. The typical time of pumping in the water column was 3-4 hours. Concentrations of pMn were measured by high-resolution inductively coupled mass spectrometry after total digestion (Xiang & Lam, 2020).

2.2 Synchrotron X-ray Absorption Spectroscopy (XAS) analysis

Surface samples collected at ~20 m from 13 stations (3 shelf, 1 slope, and 9 basin), together with one sample within the benthic nepheloid layer (BNL) over the shelf, were analyzed by bulk XAS at the Stanford Synchrotron Radiation Lightsource (SSRL) Beamline 11-2. Prior to exposure to the light source, a subsample of the original filter (usually 1/32 of the whole, equivalent to ~12.5 L of pumped seawater) was rolled into multiple layers to maximize the signal from dilute marine particle samples. The speciation of pMn was determined by X-ray Absorption Near Edge Structure (XANES) spectroscopy using a liquid nitrogen cryostat. Averaged spectra were background removed, normalized and deglitched using the SIXPACK software package (Webb, 2005). No obvious shifts of XANES peaks were observed within 10-20 scans in all samples analyzed, indicating no Mn photoreduction had taken place during analysis (Appendix 2.1).

Overall, there are 18 Mn mineral references in our library (Appendix 2.7), including spectra of Mn minerals that we collected at Beamline 11-2 (e.g., pyroxmangite ($Mn^{II}SiO_3$), hureaulite ($Mn^{II}_5(PO_3OH)_2(PO_4)_2 \cdot 4H_2O$)), those shared by

collaborators (e.g., δ-$Mn^{IV}O_2$, feitknechtite ($Mn^{III}OOH$), Mn(II)-citrate), and the most reduced surface sample, GT11010s at Station 26, which was smoothed using a smoothing parameter of 2 using SIXPACK. Linear combination fitting (LCF) of sample XANES spectra in the energy range of 6520-6600 eV was conducted using different combinations of Mn mineral references using the Least Sq. Fitting module in SIXPACK (Webb, 2005) and the goodness of the fits was evaluated by the magnitude of the R-factor (Newville, 2001). The pMn average oxidation state (AOS) was calculated as a weighted average of Mn(II), Mn(III), and Mn(IV) using the LCF fractions of three end-member Mn references chosen to represent each oxidation state. The Mn references used as end members for AOS calculations were GT11010s-Mn(II), feitknechtite ($Mn^{III}OOH$), and δ-$Mn^{IV}O_2$. We chose these three Mn reference minerals for the following two reasons. First, compared to the most reduced surface sample GT11010s, none of the other Mn(II) references in our library, including a number of Mn silicates and Mn-organic ligand complexes, showed the characteristic absorption peak at 6551 eV as seen in surface pMn samples in the Arctic Ocean (Appendices 2.2 & 2.8). Secondly, to choose appropriate oxidized Mn mineral references for our surface Arctic dataset, we applied LCF to the XANES spectrum of a pMn sample from the dark halocline (GT10800s; 176 m at Station 14) thought to be dominated by oxidized pMn (c.f., Xiang & Lam, 2020), also analyzed at Beamline 11-2. The LCF of this sample with two endmembers, feitknechtite ($Mn^{III}OOH$) and δ-$Mn^{IV}O_2$, led to a low R factor of 7.56×10^{-4} (Appendix 2.3), suggesting that these two references are reasonable choices to represent Mn(III) and Mn(IV) in the Western Arctic Ocean. Indeed,

feitknechtite ($Mn^{III}OOH$), and δ-$Mn^{IV}O_2$ are commonly used as Mn(III/IV) reference compounds in lab settings (Learman et al., 2011) and other ocean environments (Hermans et al., 2019; Lee et al., 2021; Oldham et al., 2021). We also would like to note that the primary purpose of calculating AOS is to define a metric to describe the variation in the speciation of pMn in the surface Arctic, rather than to give an accurate and precise estimate of pMn AOS. Given the lack of sample duplicates and beam time, the uncertainties in the values of pMn AOS calculated from the XANES spectra could not be formally assessed during this study. However, major variations in spectral features are clear and consistent with the trend of calculated pMn AOS (Figure 2.2).

2.3 Environmental parameters

Environmental parameters that can affect Mn redox cycling such as pH, temperature, oxygen, and light levels (Kim et al., 2012; Sunda & Huntsman, 1994; Toyoda & Tebo, 2016; Von Langen et al., 1997) were measured on the Oceanographic Data Facility (ODF) CTD rosette during the cruise (Landing et al., 2017; Woosley et al., 2017). For light levels, photosynthetically available radiation (PAR; light within 400-700nm) data was collected by a QCP-2300-HP Biospherical PAR sensor. Since PAR data was collected on a different cast than particle samples, the solar zenith angle (SZA), defined as the angle between the sun and the vertical plane, is therefore used to estimate the light level in the surface ocean during particle sampling. The SZA is lower than 90˚ when the sun is above the horizon ("daylight"), and larger than 90˚ when the sun is below the horizon ("night"). The SZA was calculated with the National Oceanic and Atmospheric Administration Earth Systems Research Laboratory Solar Position

Calculator (http://www.esrl.noaa.gov/gmd/grad/solcalc/calcdetails.html) by inputting sampling coordinates and times. PAR values from the ODF CTD are negatively correlated with their corresponding SZA at 20 decibars during the daytime (SZA<90˚), and they are relatively constant and small in the dark (SZA>90˚) (Figure 2.3a). The scatter in the relationship between PAR and SZA results from different weather conditions experienced at each station, and variable light attenuation by either ice cover (Stations 19-46: permanent ice cover) or particles in the water column. Despite the scatter, the close relationship between PAR and SZA observed during the ODF CTD casts suggests that the magnitude of SZA is a good proxy for visible light levels at 20 m where surface particles were collected.

3 Results and Discussion

3.1 Surface particulate Mn (pMn) speciation

The surface Arctic has median (range) pMn concentrations of 1.0 (1.1×10^{-1}-18.7) nmol/L (Figure 2.1 & Supplementary Table 1). Surface samples with relatively high pMn concentrations were analyzed by XANES. The XANES spectra show a pronounced maximum x-ray absorption peak either at 6561 eV or 6551 eV (Figure 2.2) which indicates oxidized and reduced pMn, respectively. It is worth noting that oxidized pMn samples (Stations 48, 52, 60) also have a shoulder peak at 6551 eV, reflecting the existence of reduced Mn.

Two distinct x-ray absorption peaks at 6552 and 6557.5 eV occur in the BNL sample (Appendix 2.4). Similar XANES spectra have been observed in estuarine sediments in San Francisco Bay (Carroll et al., 2002) and Baltic Sea sediments (Lenz et al., 2014), potentially suggesting a detrital pool of Mn aluminosilicates. We used the BNL XANES as a likely aluminosilicate reference to fit all surface Arctic samples and found that the aluminosilicate signal is only present at shelf Station 6. The surface sample at Station 6 is dominated by the putative Mn aluminosilicates, with the BNL fraction accounting for 68.11% of the XANES signal (Appendix 2.4), suggesting strong sediment resuspension on the Chukchi Shelf (Xiang & Lam, 2020). To compare the non-aluminosilicate fraction to other surface samples, the BNL fraction was removed from the bulk XANES spectrum, and the residual was renormalized. The BNL-corrected sample at Station 6 has a maximum absorption peak at 6551 eV, like the other reduced pMn (Figure 2.2a).

The pMn AOS estimated from XANES spectra range from 2.00 to 3.17 (Figure 2.1 & Supplementary Table 1). More samples (10 out of 13) were characterized by reduced pMn (AOS <2.9) than oxidized pMn. The most oxidized surface pMn (Station 60) was best fit when the Mn(IV) reference (δ-$Mn^{IV}O_2$) was included in the fits, accounting for 40.5% of pMn (Appendix 2.5).

3.2 Effect of light on pMn speciation

We separate XANES spectra into four groups based on the light level experienced during the 4-hour in-situ sampling and the day-night cycle characterizing

that station. The first group experienced full light during sampling, even if a day-night cycle was present at that station (Stations 6, 43, 57, and 66); pMn is generally reduced in this group (Figure 2.2a). Samples from Stations 43 and 57 also show small peaks at 6561 eV, indicating some presence of oxidized Mn (see section 3.2.2). The second group comprised all surface samples experiencing 24-hour light (Stations 19-38); these spectra exhibit a steep absorption peak at 6551 eV, characteristic of reduced Mn (Figure 2.2b). A small peak at 6560 eV observed at Station 32 is associated with a high Mn(III) fraction of 19.1% and little Mn(IV) (Supplementary Table 1). Station 32, within the fast-flowing Transpolar Drift, is characterized by the shortest transport time from the shelf (~6 months) among all surface stations (Kipp et al., 2018). Thus, it may have received shelf-derived particulate Mn(III/IV) that was transported laterally. The third group of samples were collected in partial darkness and are characterized by reduced Mn (Station 61) or a mixture of reduced and oxidized Mn (Stations 48 and 60) (Figure 2.2c). The more oxidized samples from Stations 48 and 60 experienced a longer period of darkness during sample collection. The fourth group, comprising only one sample (Station 52), was collected in complete darkness. Similar to the more oxidized samples at Stations 48 and 60, pMn at Station 52 is characterized by a mixture of reduced and oxidized Mn (Figure 2.2d).

3.2.1 Relationships between pMn AOS and solar zenith angle

To further describe the relationship between pMn speciation and light, we plot the AOS of pMn against the SZA (Figure 2.3b). We find that pMn is more oxidized

when samples were taken at night (SZA>90˚), whereas it is more reduced when sampled during the day (SZA<90˚). Other environmental parameters, e.g., temperature, dissolved oxygen, and pH, that are known to influence Mn oxidation (Toyoda & Tebo, 2016; Von Langen et al., 1997) and reduction (Kim et al., 2012; Sunda & Huntsman, 1994) kinetics, do not have clear correlations with pMn AOS in the surface Arctic during our cruise (Appendix 2.6). Therefore, light levels appear to be the most important control for pMn AOS in the surface Western Arctic.

3.2.2 Mn redox cycling in the surface Arctic

Diel variations in the redox cycling of Mn have been observed in the coastal Northwest Atlantic Ocean (Oldham et al., 2020; Sunda & Huntsman, 1990). Although our data were not conducted at a single location over a 24-hour period, we treat our dataset as a pseudo-diel study and hypothesize that the high pMn AOS in the dark reflects the oxidation of dissolved Mn into Mn(III/IV) oxides at night (Sunda & Huntsman, 1990), and reduced AOS in the light results from the light-dependent reduction of Mn(III/IV) oxides during the day (Sunda & Huntsman, 1988, 1994; Sunda et al., 1983). Photo-enhanced Mn(II) oxidation in the light mediated by reactions with reactive oxygen species has been reported in other environments and laboratory settings (Hansel & Francis, 2006; Learman et al., 2011; Nico et al., 2002). Although we cannot exclude photo-enhanced oxidation in the surface Arctic Ocean, the net effect of light-dependent reduction suggests higher rates of reduction in the light relative to photo-enhanced oxidation.

Using the SZA data from each station, we compare the time of sampling relative to dawn and dusk (Supplementary Table 1) to examine how fast oxidation and reduction take place. We consider shelf/slope and basin stations separately, since they have very different temperatures (Appendix 2.6) and nutrient levels.

The transition from Mn(III/IV) to Mn(II) upon exposure to sunlight appears to be relatively slow at basin stations. For example, pMn at Station 48, with its sampling midpoint at dawn and final 2 hours of sampling in the light, remains very oxidized (AOS=3.11) (Figure 2.4). Stations 43 and 57, which were fully sampled in the light between hours 1-5 after dawn, are both characterized by lower Mn AOS (2.34 and 2.37, respectively) than Station 48 (Figure 2.4), but slightly higher AOS compared to Stations 19-38 that were collected under 24-hour light conditions (median AOS=2.10) (Figure 2.3b). Longer exposure to light leads to more complete reduction from Mn(III/IV) oxides to Mn(II), and the partially oxidized pMn at Stations 43 and 57 suggests that complete reduction takes more than 5 hours after exposure to light in the oligotrophic Arctic basins.

Mn reduction in the light may occur more quickly at the warmer (0 to 5 °C), more productive shelf stations compared to the cold (-1.5 to -1 °C), oligotrophic basin stations: pMn at Station 61 on the Chukchi Shelf was sampled between -0.8 and 2.2 hrs relative to dawn and its AOS is 2.11. Given that oxidized Mn does form in the dark nearby on the Chukchi Slope at Station 60 (AOS=3.17), we postulate that oxidized Mn also forms at night at Station 61 but is rapidly reduced within the first 2 hours after dawn.

Like for reduction of Mn, the dark oxidation of Mn also appears to occur more quickly at shelf/slope compared to basin stations. Samples in the shelf/slope regions are reduced when sampled about 1.5 hours before dusk (Station 66 pMn AOS = 2.11) but are oxidized when sampled within the first 3 hours after dusk (Station 60), reaching the highest AOS (3.17) observed in the dataset (Figure 2.4). In comparison, although pMn at basin Station 52, collected between hours 2-6 after dusk, has a relatively high AOS of 2.96, it is not as high as at Station 60, despite having spent longer in the dark after dusk. If we restrict our comparisons to basin stations only, however, higher AOS may be found in samples experiencing longer periods of darkness: Station 48 has higher pMn AOS (3.11) after 11.7 hrs of darkness compared to Station 52 (AOS=2.96 after 6.2 hrs of darkness; Figure 2.4).

3.3 Different pMn phases in the surface Arctic

In Sunda and Huntsman (1990)'s study of diel Mn cycling, it was the ascorbate reducible fraction of pMn, i.e., Mn(III/IV) oxides, that exhibited a diel pattern, whereas the ascorbate-resistant pMn remained relatively constant throughout the sampling period. The ascorbate-resistant pMn likely consists of lithogenic Mn silicates and/or other forms of pMn(II), such as organically bound Mn(II) and adsorbed Mn(II).

In the surface of the Western Arctic, both XANES and low concentrations of particulate Al, a lithogenic tracer (cf., Xiang & Lam, 2020), suggest that besides Station 6, lithogenic Mn silicates are of minor importance. Adsorbed Mn(II) is also unlikely to be an important component of surface pMn because reduced pMn samples were poorly

fit with the XANES spectra of four Mn(II)-sorption standards (Appendices 2.2 & 2.8). We hypothesize that the pMn(II) observed in the surface Arctic Ocean, accounting for a median (range) of 86.2% (23.7-100.0%) of total pMn, is likely in the form of a strong organic-complexed Mn(II) that is incorporated by phytoplankton. The identity of this organically bound Mn(II) is yet unknown. Model organic Mn compounds such as Mn(II)-citrate, Mn(II)-EDTA, Mn superoxide dismutase (SOD), or Mn(II)-siderophores are characterized by maximum absorption peaks at higher energies than what we observed in the samples (Appendices 2.2 & 2.8) (Blamey et al., 2018; Gunter et al., 2006; Harrington et al., 2012; Machado et al., 2019).

We envision a conceptual model with a base level of organically bound pMn(II) that remains relatively constant through the day and night. At night, oxidation of ambient dissolved Mn adds pMn(III/IV) to the pMn pool. For the fraction of pMn(III/IV) that survives sinking and remains in the euphotic zone, it is completely reduced and returned to the dissolved Mn pool during daytime. The total pMn concentrations and fractions of Mn(III)+Mn(IV) for oxidized samples from Stations 48, 52 and 60 are 1.1 nM and 74.9%, 1.1 nM and 64.0%, and 18.7 nM and 76.3%, respectively (Supplementary Table 1). Assuming the particulate Mn(III/IV) is derived from nightly oxidation of dissolved Mn(II), we calculate that 0.8 nM of dissolved Mn(II) was oxidized at Station 48, 0.7 nM at Station 52, and 14.3 nM at Station 60. For simplicity, if we further assume that oxidation starts at dusk and loss of pMn by sinking is small, net Mn oxidation rates can be estimated by dividing the concentration of oxidized Mn by the length of darkness experienced from dusk to the end of sampling

at each station (Station 48, 52, and 60: 11.7, 6.2, and 2.9 hrs, respectively). Our estimated net Mn oxidation rates at Station 48, 52 and 60 are 0.070, 0.11, and 4.9 nM/h, respectively. The much slower apparent oxidation rates at basin Stations 48 and 52 might be explained by colder temperatures in the basin (-1.5 °C) compared to 0 °C at Station 60 at the shelf/slope, lower dissolved Mn concentrations (Jensen et al., 2020), and/or by different microbial communities (e.g., Lee et al., 2019) affecting the oxidation. These rates integrating over 2.9-11.7 hours are probably lower than the maximum oxidation rate in the dark in the surface Arctic but are generally comparable with other reported microbially mediated Mn oxidation rates of 0.1-50 nM/h in marine environments (Clement et al., 2009; Dick et al., 2009; Sunda & Huntsman, 1990).

4 Conclusions

The observed relationship between the pMn AOS and SZA stresses the significance of light in the Mn redox cycling in the Western Arctic Ocean. Such a relationship could also exist in other regions globally, but similar synchrotron-based analyses are more challenging due to much lower pMn concentrations compared to the surface Arctic Ocean.

We estimated that the Mn oxidation rate at night in the surface oligotrophic Arctic basins during our cruise is ~0.1 nM/h. Such rates of Mn oxidation take place within the near-freezing (~ -1 ˚C) Polar Mixed Layer in late summer. This study serves as the first study to observe in-situ Mn oxidation at such cold temperatures. The

oxidation of dissolved Mn(II) in the extended polar winter with no sunlight could serve as a significant seasonal Mn removal mechanism out of the surface layer. Assuming that the Mn oxidation rate remains at 0.1 nM/h in the Arctic winter when it is dark 24 hrs a day, and that riverine and benthic sources of dissolved Mn shut down in winter, it would only take ~50 hours (~2 days) to oxidize the entire reservoir of dissolved Mn in the surface Western Arctic Ocean (~5 nM; Jensen et al., 2020) and then sink out of the Polar Mixed Layer. To our knowledge, no measurements of dissolved or particulate Mn exist in the Arctic winter to test this prediction.

The Canadian Basin in the Arctic Ocean is oligotrophic, so phytoplankton are thought to be limited by major rather than minor nutrients like Mn (Codispoti et al., 2013; Hill et al., 2013). However, the rapid removal of dissolved Mn by oxidation in the dark could be significant in the Southern Ocean where recent studies suggest that Mn is a co-limiting nutrient (Browning et al., 2021; Middag et al., 2013). The continual removal of dissolved Mn as particulate Mn(III/IV) oxides in the dark during austral winter should lead to even more severe Mn limitation in the Southern Ocean and could explain why deep winter mixing is unable to replenish surface waters with higher concentrations of dissolved Mn to support the growing season.

Acknowledgments

This work was supported by the Chemical Oceanography program through the National Science Foundation under grant number NSFOCE-1535854 to Phoebe J. Lam. This research was carried out at the Stanford Synchrotron Radiation Lightsource, supported by the U.S. Department of Energy, Office of Science, Office of Basic Energy Sciences under Contract No. DE-AC02-76SF00515. We would like to thank all scientists and crew on board the USCGC icebreaker Healy during the GN01 Arctic GEOTRACES cruise. We thank Susan Becker from the Oceanographic Data Facility at Scripps Institution of Oceanography for providing photosynthetically available radiation data. The ODF hydrographic, PAR, and pH data are available on the Biological and Chemical Oceanography Data Management Office (BCO-DMO) (https://www.bco-dmo.org/dataset/700817 and https://www.bco-dmo.org/dataset/646825). The conversion between voltage and μE/m2/s in PAR data is based on the calibration conducted before the cruise (http://dmoserv3.bco-dmo.org/data_docs/GEOTRACES/Arctic/HLY1502_PAR_QCP2300HP-70444-1506.pdf). Many thanks to Ryan C. Davis for the support at the Beamline 11-2, Carl Lamborg and Colleen Hansel for insights in the discussion, Colleen Hansel for providing XANES reference spectra including δ-MnO_2 and feitknechtite, Jena E. Johnson for Mn silicates reference spectra, Peter Kopittke for Mn citrate and oxalate reference spectra, and Hudson Carvalho for Mn-EDTA reference spectra.

References

Blamey, F. P. C., McKenna, B. A., Li, C., Cheng, M., Tang, C., Jiang, H., et al. (2018). Manganese distribution and speciation help to explain the effects of silicate and phosphate on manganese toxicity in four crop species. *New Phytologist*, *217*(3), 1146-1160. https://doi.org/10.1111/nph.14878

Browning, T. J., Achterberg, E. P., Engel, A., & Mawji, E. (2021). Manganese co-limitation of phytoplankton growth and major nutrient drawdown in the Southern Ocean. *Nature Communications*, *12*(1), 884. https://doi.org/10.1038/s41467-021-21122-6

Carroll, S., O'Day, P. A., Esser, B., & Randall, S. (2002). Speciation and fate of trace metals in estuarine sediments under reduced and oxidized conditions, Seaplane Lagoon, Alameda Naval Air Station (USA). *Geochemical Transactions*, *3*(10), 81-101. https://doi.org/10.1039/B205002A

Charette, M. A., Kipp, L. E., Jensen, L. T., Dabrowski, J. S., Whitmore, L. M., Fitzsimmons, J. N., et al. (2020). The Transpolar Drift as a source of riverine and shelf - derived trace elements to the central Arctic Ocean. *Journal of Geophysical Research: Oceans*, *125*(5). https://doi.org/10.1029/2019jc015920

Clement, B. G., Luther, G. W., & Tebo, B. M. (2009). Rapid, oxygen-dependent microbial Mn(II) oxidation kinetics at sub-micromolar oxygen concentrations in the Black Sea suboxic zone. *Geochimica et Cosmochimica Acta*, *73*(7), 1878-1889. https://doi.org/10.1016/j.gca.2008.12.023

Codispoti, L. A., Kelly, V., Thessen, A., Matrai, P., Suttles, S., Hill, V., et al. (2013). Synthesis of primary production in the Arctic Ocean: III. Nitrate and phosphate based estimates of net community production. *Progress in Oceanography*, *110*, 126-150. https://doi.org/10.1016/j.pocean.2012.11.006

Colombo, M., Jackson, S. L., Cullen, J. T., & Orians, K. J. (2020). Dissolved iron and manganese in the Canadian Arctic Ocean: On the biogeochemical processes controlling their distributions. *Geochimica et Cosmochimica Acta*, *277*, 150-174. https://doi.org/10.1016/j.gca.2020.03.012

Dick, G. J., Clement, B. G., Webb, S. M., Fodrie, F. J., Bargar, J. R., & Tebo, B. M. (2009). Enzymatic microbial Mn(II) oxidation and Mn biooxide production in the Guaymas Basin deep-sea hydrothermal plume. *Geochimica et Cosmochimica Acta*, *73*(21), 6517-6530. https://doi.org/10.1016/j.gca.2009.07.039

Goldberg, E. D. (1954). Marine Geochemistry 1. Chemical Scavengers of the Sea. *The Journal of Geology*, *62*(3), 249-265

Gunter, K. K., Aschner, M., Miller, L. M., Eliseev, R., Salter, J., Anderson, K., & Gunter, T. E. (2006). Determining the oxidation states of manganese in NT2 cells and cultured astrocytes. *Neurobiology of Aging*, *27*(12), 1816-1826. https://doi.org/10.1016/j.neurobiolaging.2005.10.003

Hansel, C. M., & Francis, C. A. (2006). Coupled photochemical and enzymatic Mn(II) oxidation pathways of a planktonic *Roseobacter*-like bacterium. *Applied and Environmental Microbiology*, *72*(5), 3543. https://doi.org/10.1128/AEM.72.5.3543-3549.2006

Harrington, J. M., Parker, D. L., Bargar, J. R., Jarzecki, A. A., Tebo, B. M., Sposito, G., & Duckworth, O. W. (2012). Structural dependence of Mn complexation by siderophores: Donor group dependence on complex stability and reactivity. *Geochimica et Cosmochimica Acta*, *88*, 106-119. https://doi.org/10.1016/j.gca.2012.04.006

Hermans, M., Lenstra, W. K., van Helmond, N. A. G. M., Behrends, T., Egger, M., Séguret, M. J. M., et al. (2019). Impact of natural re-oxygenation on the sediment dynamics of manganese, iron and phosphorus in a euxinic Baltic Sea basin. *Geochimica et Cosmochimica Acta*, *246*, 174-196. https://doi.org/10.1016/j.gca.2018.11.033

Hill, V. J., Matrai, P. A., Olson, E., Suttles, S., Steele, M., Codispoti, L. A., & Zimmerman, R. C. (2013). Synthesis of integrated primary production in the Arctic Ocean: II. In situ and remotely sensed estimates. *Progress in Oceanography*, *110*, 107-125. https://doi.org/10.1016/j.pocean.2012.11.005

Jensen, L. T., Morton, P. L., Twining, B. S., Heller, M. I., Hatta, M., Measures, C. I., et al. (2020). A comparison of marine Fe and Mn cycling: U.S. GEOTRACES GN01 Western Arctic case study. *Geochimica et Cosmochimica Acta*, *288*, 138-160. https://doi.org/10.1016/j.gca.2020.08.006

Kim, K., Yoon, H. I., & Choi, W. (2012). Enhanced dissolution of manganese oxide in ice compared to aqueous phase under illuminated and dark conditions. *Environmental Science & Technology*, *46*(24), 13160-13166. https://doi.org/10.1021/es302003z

Kipp, L. E., Charette, M. A., Moore, W. S., Henderson, P. B., & Rigor, I. G. (2018). Increased fluxes of shelf-derived materials to the central Arctic Ocean. *Science advances*, *4*(1), eaao1302. https://doi.org/10.1126/sciadv.aao1302

Landing, W. M., Cutter, G., & Kadko, D. C. (2017). CTD-ODF profiles from GEOTRACES-Arctic Section cruise HLY1502, August to October 2015 (U.S. GEOTRACES Arctic project). *Biological and Chemical Oceanography Data*

Management Office (BCO-DMO), *Dataset version 2017-05-22*. Retrieved from http://lod.bco-dmo.org/id/dataset/700817

Learman, D. R., Wankel, S. D., Webb, S. M., Martinez, N., Madden, A. S., & Hansel, C. M. (2011). Coupled biotic–abiotic Mn(II) oxidation pathway mediates the formation and structural evolution of biogenic Mn oxides. *Geochimica et Cosmochimica Acta*, *75*(20), 6048-6063. https://doi.org/10.1016/j.gca.2011.07.026

Lee, J., Kang, S. H., Yang, E. J., Macdonald, A. M., Joo, H. M., Park, J., et al. (2019). Latitudinal distributions and controls of bacterial community composition during the summer of 2017 in Western Arctic Surface waters (from the Bering Strait to the Chukchi Borderland). *Scientific Reports*, *9*(1), 16822. https://doi.org/10.1038/s41598-019-53427-4

Lee, J. M., Lam, P. J., Vivancos, S. M., Pavia, F. J., Anderson, R. F., Lu, Y., et al. (2021). Changing chemistry of particulate manganese in the near- and far-field hydrothermal plumes from 15°S East Pacific Rise and its influence on metal scavenging. *Geochimica et Cosmochimica Acta*, *300*, 95-118. https://doi.org/10.1016/j.gca.2021.02.020

Lenz, C., Behrends, T., Jilbert, T., Silveira, M., & Slomp, C. P. (2014). Redox-dependent changes in manganese speciation in Baltic Sea sediments from the Holocene Thermal Maximum: An EXAFS, XANES and LA-ICP-MS study. *Chemical Geology*, *370*, 49-57. https://doi.org/10.1016/j.chemgeo.2014.01.013

Luther, G. W. (2005). Manganese(II) oxidation and Mn(IV) reduction in the environment—two one-electron transfer steps versus a single two-electron step. *Geomicrobiology Journal*, *22*(3-4), 195-203. https://doi.org/10.1080/01490450590946022

Machado, B. A., Gomes, M. H. F., Marques, J. P. R., Otto, R., & de Carvalho, H. W. P. (2019). X-ray spectroscopy fostering the understanding of foliar uptake and transport of Mn by soybean (*Glycine max* L. Merril): Kinetics, chemical speciation, and effects of glyphosate. *Journal of Agricultural and Food Chemistry*, *67*(47), 13010-13020. https://doi.org/10.1021/acs.jafc.9b05630

Middag, R., de Baar, H. J. W., Klunder, M. B., & Laan, P. (2013). Fluxes of dissolved aluminum and manganese to the Weddell Sea and indications for manganese co-limitation. *Limnology and Oceanography*, *58*(1), 287-300. https://doi.org/10.4319/lo.2013.58.1.0287

Middag, R., de Baar, H. J. W., Laan, P., & Klunder, M. B. (2011). Fluvial and hydrothermal input of manganese into the Arctic Ocean. *Geochimica et*

Cosmochimica Acta, *75*(9), 2393-2408. https://doi.org/10.1016/j.gca.2011.02.011

Newville, M. (2001). IFEFFIT: Interactive XAFS analysis and FEFF fitting. *Journal of Synchrotron Radiation*, *8*(2), 322-324. https://doi.org/10.1107/S0909049500016964

Nico, P. S., Anastasio, C., & Zasoski, R. J. (2002). Rapid photo-oxidation of Mn(II) mediated by humic substances. *Geochimica et Cosmochimica Acta*, *66*(23), 4047-4056. https://doi.org/10.1016/S0016-7037(02)01001-3

Oldham, V. E., Chmiel, R., Hansel, C. M., DiTullio, G. R., Rao, D., & Saito, M. A. (2021). Inhibited manganese oxide formation hinders cobalt scavenging in the Ross Sea. *Global Biogeochemical Cycles*, *n/a*(n/a), e2020GB006706. https://doi.org/10.1029/2020GB006706

Oldham, V. E., Lamborg, C. H., & Hansel, C. M. (2020). The spatial and temporal variability of Mn speciation in the coastal Northwest Atlantic Ocean. *Journal of Geophysical Research: Oceans*, *125*(1), e2019JC015167. https://doi.org/10.1029/2019JC015167

Peers, G., & Price, N. M. (2004). A role for manganese in superoxide dismutases and growth of iron-deficient diatoms. *Limnology and Oceanography*, *49*(5), 1774-1783. https://doi.org/10.4319/lo.2004.49.5.1774

Sunda, W. G., & Huntsman, S. A. (1987). Microbial oxidation of manganese in a North Carolina estuary1. *Limnology and Oceanography*, *32*(3), 552-564. https://doi.org/10.4319/lo.1987.32.3.0552

Sunda, W. G., & Huntsman, S. A. (1988). Effect of sunlight on redox cycles of manganese in the southwestern Sargasso Sea. *Deep Sea Research Part A. Oceanographic Research Papers*, *35*(8), 1297-1317. https://doi.org/10.1016/0198-0149(88)90084-2

Sunda, W. G., & Huntsman, S. A. (1990). Diel cycles in microbial manganese oxidation and manganese redox speciation in coastal waters of the Bahama Islands. *Limnology and Oceanography*, *35*(2), 325-338. https://doi.org/10.4319/lo.1990.35.2.0325

Sunda, W. G., & Huntsman, S. A. (1994). Photoreduction of manganese oxides in seawater *Marine Chemistry*, *46*, 133-152. https://doi.org/10.1016/0304-4203(94)90051-5

Sunda, W. G., Huntsman, S. A., & Harvey, G. R. (1983). Photoreduction of manganese oxides in seawater and its geochemical and biological implications. *Nature*, *301*(5897), 234. https://doi.org/10.1038/301234a0

Tebo, B. M., Bargar, J. R., Clement, B. G., Dick, G. J., Murray, K. J., Parker, D., et al. (2004). Biogenic manganese oxides: Properties and mechanisms of formation. *Annual Review of Earth and Planetary Sciences*, *32*(1), 287-328. https://doi.org/10.1146/annurev.earth.32.101802.120213

Toyoda, K., & Tebo, B. M. (2016). Kinetics of Mn(II) oxidation by spores of the marine Bacillus sp. SG-1. *Geochimica et Cosmochimica Acta*, *189*, 58-69. https://doi.org/10.1016/j.gca.2016.05.036

van Hulten, M., Middag, R., Dutay, J. C., de Baar, H., Roy-Barman, M., Gehlen, M., et al. (2017). Manganese in the west Atlantic Ocean in the context of the first global ocean circulation model of manganese. *Biogeosciences*, *14*(5), 1123-1152. https://doi.org/10.5194/bg-14-1123-2017

Von Langen, P. J., Johnson, K. S., Coale, K. H., & Elrod, V. A. (1997). Oxidation kinetics of manganese (II) in seawater at nanomolar concentrations. *Geochimica et Cosmochimica Acta*, *61*(23), 4945-4954. https://doi.org/10.1016/S0016-7037(97)00355-4

Webb, S. M. (2005). SIXPack a graphical user interface for XAS analysis using IFEFFIT. *Physica Scripta*, 1011. https://doi.org/10.1238/physica.topical.115a01011

Woosley, R. J., Millero, F. J., & Takahashi, T. (2017). Internal consistency of the inorganic carbon system in the Arctic Ocean. *Limnology and Oceanography: Methods*, *15*(10), 887-896. https://doi.org/10.1002/lom3.10208

Xiang, Y., & Lam, P. J. (2020). Size‐fractionated compositions of marine suspended particles in the Western Arctic Ocean: Lateral and vertical sources. *Journal of Geophysical Research: Oceans*, *125*(8), e2020JC016144. https://doi.org/10.1029/2020JC016144

Yano, J., Kern, J., Sauer, K., Latimer, M. J., Pushkar, Y., Biesiadka, J., et al. (2006). Where water is oxidized to dioxygen: Structure of the photosynthetic Mn4Ca cluster. *Science*, *314*(5800), 821-825. https://doi.org/10.1126/science.1128186

Figures and Tables

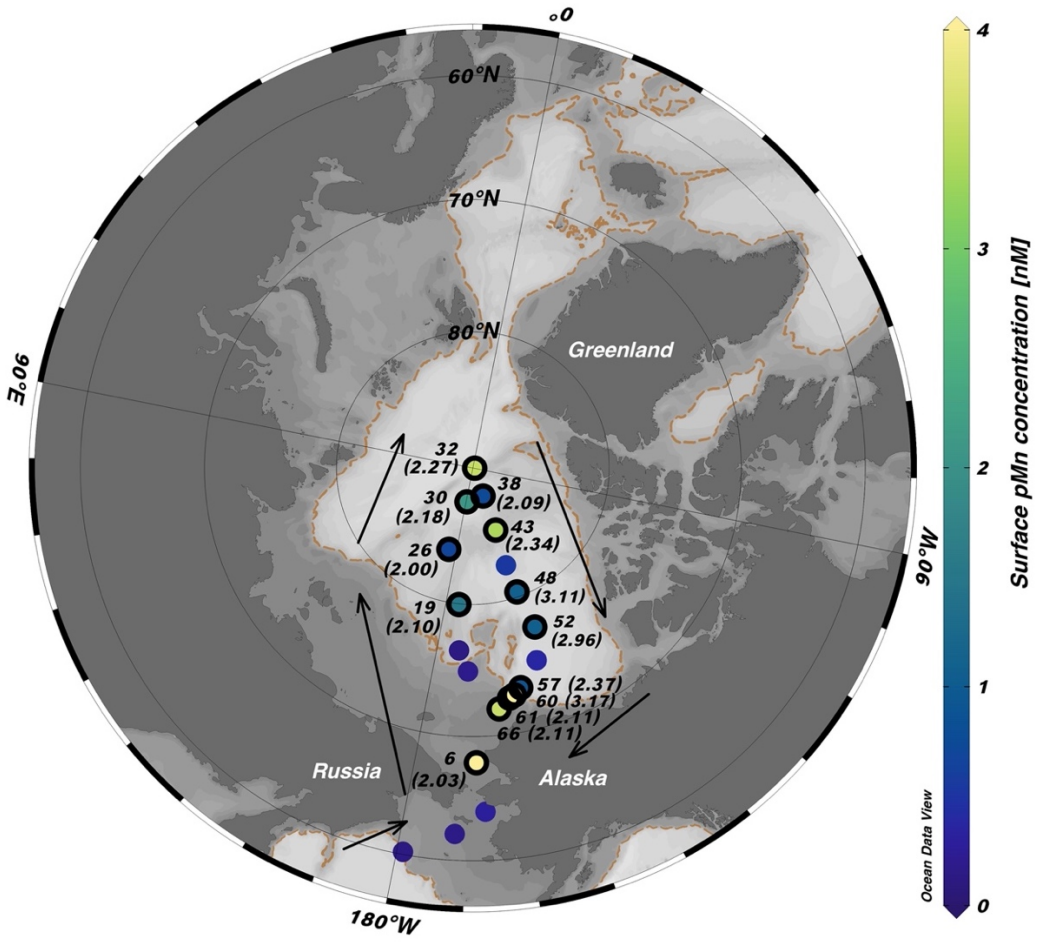

Figure 2.1 Sampling locations of the GN01 cruise (cruise track: clockwise). Colors show the surface particulate Mn (pMn) concentrations (unit: nmol/L). The ocean bathymetry with 1,000 m contour is indicated as brown dashed lines. Samples analyzed by XANES are outlined by thick black circles and labeled by station numbers. Average oxidation states (AOS) of pMn are labeled next to station numbers within the parenthesis.

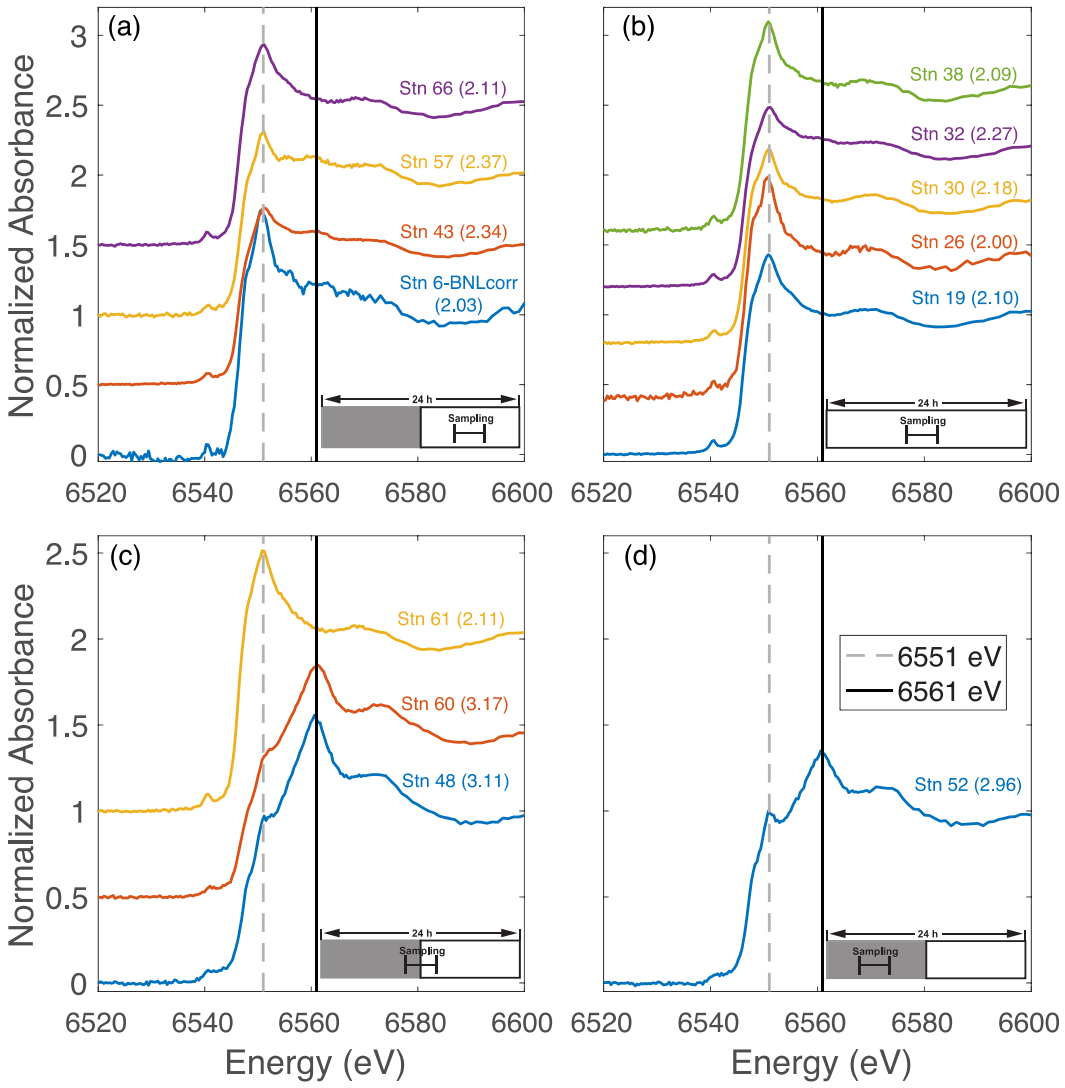

Figure 2.2 Mn K-edge bulk X-ray absorption near edge structure (XANES) spectra of surface pMn analyzed, grouped by different light levels experienced during the sampling and/or on a daily basis. The selection criteria for four groups are displayed as a simple cartoon in the bottom right corner of each subplot, illustrating whether there was a day-night cycle at that station during sampling (white-shaded rectangle) and the light level during sampling (horizontal bar). (a): sampling entirely in the light but experiencing a daily day-night cycle; (b): sampling entirely in the light and experiencing 24-h daily light; (c): sampling partially in the light; (d): sampling entirely

in the dark but experiencing a daily day-night cycle. The pMn AOS for each spectrum is labeled next to station numbers within the parenthesis.

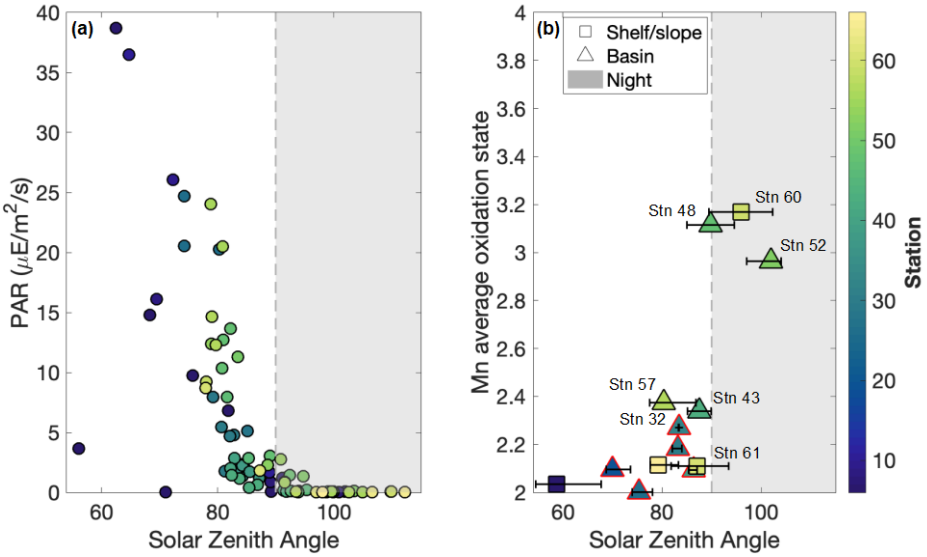

Figure 2.3 The relationships between solar zenith angle (SZA) and photosynthetically available radiation (PAR) measured in the ODF CTD casts at pressure = 20 decibars (a), and between SZA and Mn average oxidation states (AOS) measured on particles collected in the pump casts at ~20 m (b). The triangles in (b) are the SZA at mid-cast and error bars demonstrate the minimum and maximum SZA during particle sampling. Samples collected under 24-h light conditions are outlined in red.

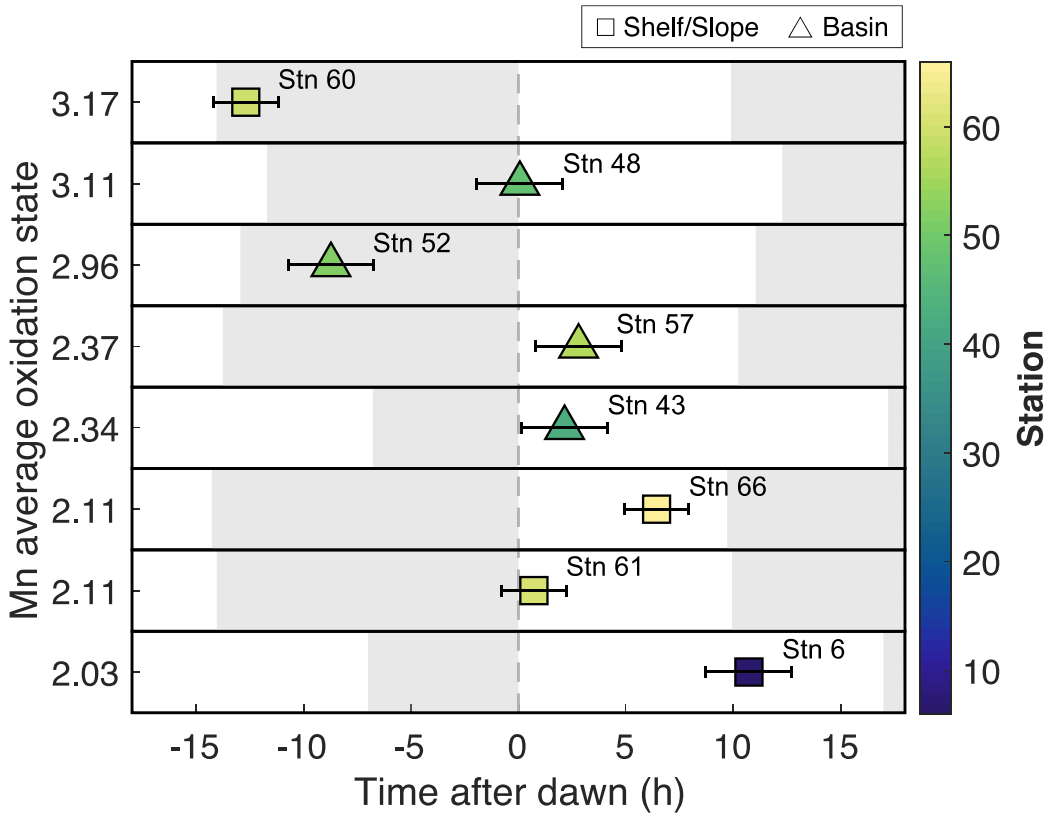

Figure 2.4 The relationship between time after dawn (unit: hour) and pMn average oxidation state (AOS), shown with Y-axis in ranked ascending order of AOS. The length of night is indicated by the shaded rectangle for each station. Note that stations experiencing 24-hr light (Stations 19-38) are not plotted here.

CHAPTER 3: CONTROLS ON SINKING VELOCITIES AND MASS FLUXES OF SIZE-FRACTIONATED MARINE PARTICLES MEASURED DURING RECENT U.S. GEOTRACES CRUISES

Abstract

Chemical composition is an important parameter that influences the sinking velocity of marine particles. Most current studies, however, are limited by either a lack of routine measurements of particle composition or low sampling resolution in the water column. Here, we compile full ocean-depth size-fractionated (1-51 and >51 μm) particle concentration and composition of suspended particulate matter from three recent U.S. GEOTRACES cruises to calculate their corresponding sinking velocity and mass flux. Our model is based on Stokes' Law and incorporates a newly updated power-law relationship between particle size and porosity. The integration of the porosity-size relationship decreases the power applied to size in Stokes' Law to 0.8. The medians of sinking velocity in total particles are 15.4, 15.2, and 7.4 m/d, in the North Atlantic, Eastern Tropical South Pacific, and Western Arctic Ocean, respectively. We examine the relative importance of particle concentration, composition, size, and hydrography on sinking fluxes. Particle concentration is the major control of the variability and magnitude of mass flux, while particle composition is the second most important term. Increasing porosity with aggregate size and a dominance of smaller particles diminishes the importance of the size dependence in mass flux, elevating the

relative importance of composition. Viscosity of seawater can result in up to a factor of two difference in mass flux between polar and tropical oceans. This work serves as one of the first studies to offer quantitative perspectives for the contribution from different factors to mass flux in field observations of marine particles.

1. Introduction

The marine biological carbon pump (BCP) plays a crucial role in the global carbon cycle by fixing carbon dioxide (CO_2) in the surface water into particulate organic matter (POM), which then sinks into the deep ocean (Kwon et al., 2009; Volk & Hoffert, 1985). Particle dynamics in the water column, including particle remineralization, aggregation, and disaggregation, are of significance in modifying and attenuating POM during sinking (Lam & Marchal, 2015). Most of the sinking flux is composed of phytodetrital aggregates, marine snow, and fecal pellets (Alldredge & Silver, 1988; Bishop et al., 1977; Ebersbach & Trull, 2008; Fowler & Knauer, 1986; Laurenceau-Cornec et al., 2015a; Turner, 2015; Wilson et al., 2013). Only a small fraction of POM (~10%) produced at the surface, however, sinks below mesopelagic regions (Martin et al., 1987).

Conceptually, vertical mass flux is estimated as the product of the sinking velocity and particle concentration. It is closely related to particle properties such as concentration, size, and composition. Numerous studies measure POC fluxes using sediment traps (e.g., Buesseler et al., 2007) and POC concentrations using large-volume filtration (e.g., Bishop et al., 1977; Lam et al., 2011). While particle flux should

scale with concentration, this is modulated by variations in sinking speed caused by differences in particle size, shape, and excess density. The importance of particle size on carbon export is apparent from Stokes' Law (Stokes, 1851), which states that the sinking velocity is proportional to the square of particle diameter. Despite only holding for spherical solid particles at low Reynolds number, Stokes' Law has been widely used to characterize the sinking speed of marine particles (e.g., Laurenceau-Cornec et al., 2020; McDonnell & Buesseler, 2010; Omand et al., 2020), giving insights into the complicated system of the BCP. Similar to particle size, particle composition is also known to affect the export flux via its relationship with sinking velocity. The existence of mineral ballast, such as $CaCO_3$ and lithogenic particles, has been suggested to provide a source of excess density and/or protection and promote carbon export into the deep ocean (Armstrong et al., 2001; Francois et al., 2002; Klaas & Archer, 2002). Opal is a less efficient ballast mineral as a result of its lower density and/or higher porosity (Bach et al., 2016; Francois et al., 2002; Iversen & Ploug, 2010; Lam & Bishop, 2007; Lam et al., 2011; Puigcorbé et al., 2015). The ballast effect, however, is still under active debate (Aumont et al., 2017; Boyd & Trull, 2007; Henson et al., 2012; Lam & Bishop, 2007; Le Moigne et al., 2012; Lee et al., 2009; Rosengard et al., 2015), since indirect ecosystem effects are difficult to disentangle from direct effects of mineral density (e.g., Lima et al., 2014).

Thanks to the GEOTRACES program, measurements of particle concentration and composition in the North Atlantic, Eastern Tropical South Pacific, and Western Arctic Ocean have been made in the past decade, covering many different geographic

regions (Lam et al., 2018; Lam et al., 2015; Xiang & Lam, 2020). The three ocean basins are characterized by different particle compositions. This study uses the composition data from these recent U.S. GEOTRACES cruises and applies mass-size and porosity-size power-law functions to calculate the corresponding size-fractionated sinking velocity and mass flux. Despite lacking seasonal resolution, this data offers higher spatial and depth resolution of sinking particle fluxes than existing sediment traps and allows us to investigate the relative importance of particle concentration, composition (density), particle size, and hydrography on particle sinking fluxes. Indeed, the model used here can be adapted to any other size-fractionated particulate phases and trace metals to calculate their corresponding mass fluxes, given the assumption that the specific particulate phase has the same sinking rate as the bulk particles. Insights gained in this study help us understand the role of particle characteristics on carbon flux, which can be applied to other regions in future studies to improve our understanding of the biological pump on a global scale.

2. Materials and Methods

2.1 Cruise tracks and sampling method

As mentioned above, the dataset we analyze here consists of results from three cruises (GA03, GP16 and GN01). The U.S. GEOTRACES North Atlantic Zonal Transect (GA03) cruise was completed with two legs in 2010-2011 in the subtropical North Atlantic (Figure 3.1). The cruise track sampled the Mauritanian Upwelling system, the North Atlantic deep western boundary current, and the Trans-Atlantic

Geotraverse (TAG) hydrothermal plume on the slowly spreading Mid-Atlantic Ridge. The Eastern Pacific Zonal Transect (GP16) cruise was completed in the Eastern Tropical South Pacific Ocean in October–December 2013 (Figure 3.1). The expedition sampled the Peruvian Coastal upwelling region, the oxygen deficient zone (ODZ) off Peru, and the superfast-spreading East Pacific Rise (EPR) hydrothermal plume. The U.S. Arctic cruise (GN01) focused on the Western Arctic Ocean and sampled at both very productive shallow shelves and extremely oligotrophic deep basins in 2015 (Figure 3.1). The Arctic Ocean is characterized by extremely broad continental shelves, consisting of 53% of its overall area (Jakobsson, 2002).

Size-fractionated particles were all sampled using dual-flow McLane Research in-situ pumps (WTS-LV). Large size fraction particles are referred to as "LSF", representing the size fraction of >51 μm, whereas the small size fraction, "SSF", are particles between 1 and 51 μm. Total particles are defined as the sum of both size fractions (Total= LSF+SSF). More details about the cruise hydrography, sample handling and analytical methods of different particle compositions can be found in Lam et al. (2015), Lam et al. (2018), Xiang and Lam (2020).

2.2 Porosity and size relationship

Porosity is defined as the volume fraction of an aggregate that is not occupied by solid matter and tends to increase with particle size (Alldredge & Gotschalk, 1988). It is an essential parameter in the calculation of particle volume and mass flux from size (Jackson et al., 1997; Stemmann et al., 2008). Alldredge and Gotschalk (1988)

pioneered porosity measurements in marine aggregates and found a power-law relationship between the porosity and particle size by direct measurements in-situ:

$$1\text{-}P_i = (8\times10^{-3})\times(d_i/10^3)^{-1.6} \quad (1)$$

where P_i is the particle porosity for size bin i and is unitless, d_i is the equivalent spherical diameter of particles (μm), and 10^3 is the conversion factor between μm and mm. This classic power function was used to calculate particle sinking velocities in many studies (e.g., Burd et al., 2007; Ruiz, 1997). Data points from Alldredge and Gotschalk (1988) were extracted using WebPlotDigitizer (Rohatgi, 2010) for this study. The extracted regression equation is $1\text{-}P_i = (8.2\times10^{-3})\times(d_i/10^3)^{-1.6}$, which is similar to the original one.

In the past 30 years, there have been several additional studies measuring porosity and size of marine aggregates (Figure 3.2) (Bach et al., 2016; Engel et al., 2009; Iversen & Robert, 2015; Lam & Bishop, 2007; Laurenceau-Cornec et al., 2020; Laurenceau-Cornec et al., 2015b; Logan & Alldredge, 1989; Ploug et al., 2008a; Ploug & Passow, 2007; Prairie et al., 2015; Schmidt et al., 2014). A detailed summary of all data sources and analytical methods is listed in Appendix 3.10. Due to the difficulties of measuring size and porosity in-situ in the water column, many of these studies were conducted with aggregates formed in lab roller tanks, while others measured bulk properties from which we estimated particle size distributions. For example, the Lam and Bishop (2007) study estimated porosities of bulk size-fractionated (1-51 μm and >51 μm) particles collected by in-situ filtration in the Southern Ocean. To estimate a mean particle size for each size fraction to associate with estimated porosities, we

used nearby particle size distributions obtained by the Underwater Vision Profiler (UVP) in the Lohafex 2009 and Tara 2011 cruises in the Subantarctic and Antarctic, respectively (Picheral et al., 2017). It is noted that natural aggregates are different from aggregates formed in roller tanks and characterized by smaller sizes (Laurenceau-Cornec et al., 2015b). Further, for a given size, it also seems that natural aggregates have a higher porosity (lower ($1-P_i$)) than similarly-sized lab formed aggregates (Figure 3.2). Since marine particles are all collected in-situ in our dataset, we only use natural marine particles in our updated regression.

Compared to Eq. 1, we also used a different linear regression model. The ordinary least square (OLS) regression used in Alldredge and Gotschalk (1988) is sensitive to changes in x-axis scale (i.e., meter vs. millimeter). Therefore, a Model-II reduced major axis (RMA) regression was used, as implemented in lsqfitgm.m in MATLAB by E.T. Peltzer (https://www.mbari.org/index-of-downloadable-files/). The updated power-law relationship between ($1-P_i$) and particle sizes is:

$$1-P_i = (3.6\times10^{-3})\times(d_i/10^3)^{-1.2} \quad (2)$$

Compared to the original Alldredge and Gotschalk (1988) relationship (Eq. 1), this new relationship has a weaker dependency of porosity with size, but also has a lower coefficient. Logan and Wilkinson (1990) illustrated the relationship between the fractal dimension D_3 and the power exponent b in the porosity-size function, where $D_3=3+b$. The value of the fractal dimension depicts how much space the solid occupies in three dimensions. A pure solid has a fractal dimension of 3. The fractal dimensions in our updated and original Alldredge and Gotschalk (1988) relationship are 1.8 and

1.4, respectively, which means that marine particles in this study are more compact than those in Alldredge and Gotschalk (1988). Despite the higher fractal dimension in our new relationship, the coefficient is lower, resulting in higher porosities over the size range of most marine particles (Figure 3.2). The intersection between Eq. 1 and Eq. 2 occurs at 8.3 mm; therefore, particles smaller than 8.3 mm have a higher porosity (lower $1-P_i$) in the newly compiled porosity-size relationship (Figure 3.2). Additionally, the new relationship predicts a particle size of about 8.6 μm when the porosity approaches 0, compared to 48.9 μm for the original Alldredge and Gotschalk (1988) relationship. We treat particles as pure solids ($P_i=0$) for all sizes below 8.6 μm.

2.3 Particle sinking rate calculation

Assuming spherical particles, laminar flow, and a smooth surface, sinking velocity increases with particle size and excess density (the density difference between solid materials and seawater) according to Stokes' Law:

$$W_i = \frac{g\Delta\rho(d_i/10^6)^2}{18\eta} \quad (3)$$

where W_i is the sinking velocity for size bin i with the unit of m/s, g is the gravitational acceleration in m/s^2, $\Delta\rho$ is the excess density in kg/m^3, 10^6 is the conversion factor between μm and m, and η is the dynamic viscosity of seawater in kg/m/s. Including the effect of non-solid porosity, and assuming that flow through the porous aggregate is negligible (although see section 4.4), Eq. 3 becomes:

$$W_i=(1-P_i)\frac{g\Delta\rho(d_i/10^6)^2}{18\eta} \quad (4)$$

Combing Eqs. 2 and 4 explicitly and using m as the unit for particle size, the sinking velocity is calculated as:

$$W_i=(3.6\times10^{-11.4})\times\frac{g\Delta\rho(d_i)^{0.8}}{18\eta} \quad (5)$$

Since $1-P_i$ decreases (porosity increases) with particle size (Eqs. 1-2), sinking velocities in Eqs. 4-5 have a weaker dependence on the particle size compared to the original Stokes' Law (Eq. 3). As a result, the influence of other parameters, such as the excess density and viscosity, becomes more important. It is also worth noting that a slightly stronger size dependency in sinking velocity occurs with the implementation of the newly compiled porosity and size relationship (Eq. 2) to Eq. 5 when compared to using the original relationship from Alldredge and Gotschalk (1988) (Eq. 1).

The Stokes' Law is only valid at low Reynolds number (Re) in the laminar flow regime, empirically found at Re<0.5 (White, 1974). The Reynolds number is:

$$Re=\frac{\rho_{sw}W(d_i/10^6)}{\eta} \quad (6)$$

where ρ_{sw} is the density of seawater (unit: kg/m^3). With the consideration of increasing porosity with size, however, Stokes' Law is potentially valid at higher Reynolds numbers ($1< Re < 50$) (Laurenceau-Cornec et al., 2020). Indeed, roller-tank aggregates with minerals were best modelled using Stokes' Law with constant and high porosity (99%), and also well described with a form of Stokes' Law modified with a fractal-porosity relationship (Laurenceau-Cornec et al., 2020), similar to our Eq. 5. However,

for aggregates without minerals, the modified Stokes' law with the fractal-porosity relationship modelled the sinking velocity much better than using constant porosity. Even though the observation was not based on naturally formed marine aggregates, it is still our best understanding of the applicability of Stokes' Law to marine particles, and we use Eq. 5 to estimate sinking velocities of our natural mineral-containing particles. It is noteworthy that the fractal-porosity relationship for natural marine aggregates used in this study (Eq. 2) has a lower coefficient but similar fractal dimension compared to artificial aggregates in Laurenceau-Cornec et al. (2020). Lower coefficients can be visualized with Figure 3.2, where natural aggregates seem to have a lower intercept than roller tanks aggregates.

2.3.1 Particle density calculation

Major phases in marine particles include particulate organic matter (POM), opal, lithogenic materials (Litho), calcium carbonate ($CaCO_3$), manganese oxides (MnO_2), and iron oxyhydroxides ($Fe(OH)_3$). The contribution of each particle phase to the overall particle mass, known as the compositional fraction, is calculated by normalizing its concentration with suspended particulate mass (SPM). Compositional fractions in the LSF and SSF are calculated separately and used in the calculations of particle density. The density of the solid portion of particles, $\rho_{particle}$, is calculated as:

$$\rho_{particle}=\rho_{POM}f_{POM}+\rho_{opal}f_{opal}+\rho_{Litho}f_{Litho}+\rho_{CaCO_3}f_{CaCO_3} +\rho_{MnO_2}f_{MnO_2}+\rho_{Fe(OH)_3}f_{Fe(OH)_3} \quad (7)$$

where ρ_{POM}, ρ_{opal}, ρ_{Litho}, ρ_{CaCO_3}, ρ_{MnO_2}, $\rho_{Fe(OH)_3}$ are the densities of each particle phase, and f_{POM}, f_{opal}, f_{Litho}, f_{CaCO_3}, f_{MnO_2}, $f_{Fe(OH)_3}$ are the compositional fractions (by weight) of each particle phase. We use a density of POM ρ_{POM} of 1.05 g/cm^3 (Young, 1994), ρ_{opal} of 2.0 g/cm^3 (Hurd & Theyer, 1977), ρ_{Litho} of 2.70 g/cm^3 (Rixen et al., 2019), ρ_{CaCO_3} of 2.71 g/cm^3, ρ_{MnO_2} of 3.0 g/cm^3, and $\rho_{Fe(OH)_3}$ of 3.96 g/cm^3 (Towe & Bradley, 1967).

2.3.2 Hydrography

Hydrographic data, such as temperature, salinity, dissolved oxygen, and nutrients, were measured in each cruise (Cutter et al., 2019; Schlitzer et al., 2018). The potential density was calculated using the seawater toolbox version 3.3.1 (http://www.cmar.csiro.au/datacentre/ext_docs/seawater.htm) in MATLAB (MathWorks Inc.). Temperature, salinity, and pressure from the bottle data were interpolated linearly to pump depths. The seawater density is a function of temperature, salinity, and pressure, and the gravitational acceleration was derived from latitude and depth. The seawater viscosity was calculated from temperature and salinity based on the equation in Millero (1974).

2.3.3 Data binning

Both SSF (1-51 μm) and LSF (>51 μm) are evenly divided into 25 bins in logarithmic space. Since particles of more than 5 mm are generally rare in the ocean

(Honjo et al., 1995; Shanks & Trent, 1980), we set the upper limit of the LSF to 5 mm. The size range and median for each size bin are summarized in Appendix 3.11. The center of the bin in log space is used in the calculation of sinking speeds and mass fluxes. Since we only have bulk composition information available for the SSF and LSF fractions, we assume that all 25 bins in each size fraction have the same particle composition, and thereby the same particle densities.

2.4 Mass-size spectra

A mass-size spectrum is calculated for each sample in all cruises using the measured bulk SSF and LSF SPM concentrations. All spectra are assumed to be a power function between 1 μm and 5 mm. LSF and SSF SPM concentrations, together with size boundaries in different size fractions (1, 51 and 5000 μm) were used to constrain the relationships:

$$m_i = p d_i^{-q} \tag{8}$$

$$SPM = \frac{\int_{d_1}^{d_2} p d_i^{-q} dd}{10^3} \tag{9}$$

where m_i is the dry mass of particles for each size bin i (unit: g/L/m), SPM is the measured bulk dry suspended particulate mass in each size fraction (unit: g/m^3), 10^3 is the conversion factor between μg/L and g/m^3, d_1 is the lower integration boundary, as 1 μm in the SSF or 51 μm in the LSF, d_2 is the higher integration boundary, as 51 or 5000 μm, and p and q are constant parameters that are determined from the size-fractionated SPM data for each sample. The coefficient q is unitless.

2.5 Mass flux calculation

The mass flux is obtained from the product of SPM concentrations and sinking velocities. The mass flux for each size bin, F_i, is calculated as:

$$F_i = \frac{m_i \times W_i}{10^3} \tag{10}$$

where F_i is with the unit of $g/m^2/s/\mu m$, and 10^3 is the conversion factor between μm and mm. The overall mass flux F is the sum of mass fluxes in all size bins:

$$F = \int_{d_1}^{d_2} \frac{m_i \times W_i}{10^3} dd \tag{11}$$

where F is with the unit of $g/m^2/s$. To convert $g/m^2/s$ to $g/m^2/day$, one needs to multiply by 86400 s/day. The SSF and LSF mass flux are calculated separately for each sample. The total mass flux is the sum of SSF and LSF fluxes.

2.6 Mass-weighted average sinking velocity calculation

The calculation of the mass-weighted average sinking velocity for the SSF and LSF size fractions uses the mass fraction of each size bin to weight the velocity calculated in each size bin. The mass-weighted average sinking velocity WSV (unit: m/s) is computed separately for the SSF (1-51 μm), the LSF (51-5000 μm), and total particles (1-5000 μm) as:

$$WSV = \int_{d_1}^{d_2} \frac{m_i W_i dd}{\int_{d_1}^{d_2} m_i dd} \tag{12}$$

Indeed, the mass flux F of the SSF, LSF, or total particles is the product of the WSV multiplied by SPM concentrations of the respective size fraction:

$$F=WSV\times SPM \quad (13)$$

Derived mass flux and WSV in all size fractions (SSF, LSF, and TOT) from three cruises are summarized in Supplementary Table 2.

2.7 Statistical Analysis

In this paper, two methods of statistical tests are conducted to evaluate whether variables in three oceans are significantly different. The choice of the statistical method depends on the distribution for given datasets. The normality of the data distribution is assessed using the Lilliefors test at the 5% significance level. We use the two-sample t-test ($\alpha=0.05$) to examine statistical differences between variables if they both have a normal distribution. Otherwise, the Wilcoxon rank sum test, also known as the Mann-Whitey U test, is used. Most of our derived parameters are not normally distributed. Thus, unless otherwise specified, the p value shown is from the Wilcoxon rank sum test.

3. Results

3.1 Suspended Particulate Mass (SPM)

LSF, SSF, and total (TOT) SPM concentrations in three basins tend to decrease with depth (Appendix 3.1). In general, the SPM is of higher concentrations in the SSF than LSF (see section 3.4.1). The Chukchi Shelf in the Western Arctic Ocean has the

highest SPM concentrations in all size fractions, reaching 1.1, 3.2, and 4.0 g/m^3 for the LSF, SSF, and TOT respectively, approached only by the bottom nepheloid layer of the western boundary current in the North Atlantic from the GA03 cruise. In contrast, the Canada Basin of the Western Arctic Ocean is characterized by the lowest SPM concentrations in the LSF ($p \ll 0.001$). The SSF and TOT SPM concentrations in the Western Arctic Ocean and Eastern Tropical South Pacific central basin are not statistically different from each other ($p > 0.05$) but are both significantly smaller than the North Atlantic ($p \ll 0.001$). Interestingly, most deviations between the North Atlantic and Eastern Tropical South Pacific occur in the deep ocean: there is less SPM attenuation with depth in the North Atlantic. Inputs from hydrothermal vents are responsible for the small elevation in SPM concentrations at 2500 m in the EPR 15˚S hydrothermal plume in the Eastern Tropical South Pacific. The North Atlantic western boundary has much more prominent bottom nepheloid layers (BNLs) than the Eastern Tropical South Pacific or Western Arctic, as found by Gardner et al. (2018a), Gardner et al. (2018b), and Gardner et al. (2018c).

3.2 Compositional fraction

The LSF and SSF particles have different particle compositions, with their POM and opal fractions differing the most. In general, the LSF POM is less dominant than the SSF, whereas the LSF opal fraction is greater than in the SSF (Appendices 3.2 & 3.3). POM is the dominant particle phase in the upper 500 m in both size fractions and the fraction of POM decreases with depth in all three basins. In contrast, the

fraction of lithogenic material progressively increases with depth (Appendices 3.2 & 3.3). The particulate lithogenic content in the Eastern Tropical South Pacific is significantly smaller than that in the Arctic and North Atlantic ($p \ll 0.001$). Unlike the North Atlantic, which is heavily influenced by Saharan dust input (e.g., Mahowald et al., 2005), the Western Arctic Ocean is far from major dust sources, and the supply of lithogenic aerosol particles into the Arctic Ocean is much smaller (Marsay et al., 2018). The central Arctic Basin receives most of its lithogenic material via lateral fluxes from the margins (Xiang & Lam, 2020). Prominent bottom nepheloid layers in the North Atlantic and the Western Arctic Ocean are characterized by high lithogenic fractions, accounting for over 60% of the SPM. $CaCO_3$, a biogenic mineral of similar density to lithogenic particles (see section 2.3.1), is highest in the Eastern Tropical South Pacific ($p \ll 0.001$) and lowest in the Arctic Ocean in both size fractions ($p \ll 0.001$). The abundance of $CaCO_3$ compensates for a lack of lithogenic particles in the Eastern Tropical South Pacific, leading to relatively similar fractions of Litho+$CaCO_3$ in the three ocean basins (Appendix 3.2). The North Atlantic has the lowest fraction opal ($p \ll 0.001$). High opal fractions are observed in the Eastern Tropical South Pacific and Western Arctic Ocean, whereas a more definite decreasing trend with depth appears in the Western Arctic Ocean (Appendices 3.2 & 3.3). The $Fe(OH)_3$ is generally low but elevated in the EPR 15˚S and TAG hydrothermal plumes where the highest fraction of $Fe(OH)_3$+MnO_2 consists of up to 60% of SPM (Appendix 3.2). Despite the absence of hydrothermal activities, the Western Arctic Ocean is the only basin with a relatively high fraction of MnO_2 (>2%) in the entire water column (Appendix 3.3). The highest

fraction in the SSF (~9%) is found in the upper 500 m in the Western Arctic Ocean coinciding with the Pacific-derived halocline and is even higher than that in the EPR hydrothermal plume. There is no obvious MnO_2 elevation in the TAG plume, despite similar dissolved manganese concentrations between the EPR 15˚S and TAG plumes (Hatta et al., 2015; Resing et al., 2015); therefore, the presence of high concentration and fraction of MnO_2 in the EPR 15˚S but not in the TAG (Lam et al., 2018; Lam et al., 2015) is likely a consequence of the comparative ages of the plumes relative to the timescale of dissolved Mn oxidation (Kipp et al., 2018; Mandernack & Tebo, 1993).

3.3 Fraction-weighted particle density and excess density

Estimated particle densities range from 1.1 to 3.2 g/cm^3 in the three sections and generally increase with depth (Figure 3.3). The highest density is found in the EPR 15˚ S hydrothermal plume. The median for LSF particle densities is 1.8, 2.0, and 2.0 g/cm^3 in the North Atlantic, Eastern Tropical South Pacific, and the Western Arctic Ocean, respectively. The SSF densities are 2.0±0.4, 1.9±0.4, and 1.9±0.4 g/cm^3 (mean±s.d.). Based on the Lilliefors test, LSF densities in the Arctic and Pacific are not normally distributed at the 5% significance level. In contrast, LSF densities in the North Atlantic and all SSF particle densities have normal distributions. The North Atlantic has the lowest LSF densities compared to the other two cruises ($p \ll 0.001$), but its SSF densities are significantly higher than the Western Arctic Ocean (t-test; $p<0.01$). Such contrasting characteristics between size fractions can be partly explained by the

abundance of POM and the lack of opal in the North Atlantic in the LSF (Appendices 3.2 & 3.3).

Both the magnitude and variations of seawater densities are small compared to the particle density in most cases, which leads to relatively consistent differences between particle density and excess densities (Appendix 3.4). Variations in the excess density are controlled by composition effects on particle density, not by variations in the seawater density.

3.4 Mass partitioning

3.4.1 The fraction of mass concentrations in the SSF and LSF

The SSF SPM generally makes up more TOT SPM concentrations than the LSF (Figure 3.4). A higher fraction of small particles with respect to total mass concentrations (fSSF) corresponds to a higher power q in the mass-size spectra. The median (range) fSSF fractions are 76.6% (34.2-97.8%), 78.4% (48.4-93.9%), and 85.5% (11.1-96.5%) in the North Atlantic, Eastern Tropical South Pacific, and the Western Arctic Ocean, respectively. The highest fSSF of 97.8% appears in the BNLs along the western boundary in the North Atlantic (Figure 3.4a). Close to the venting site of the EPR hydrothermal plume, the fSSF is about 70%, implying hydrothermal particles from the EPR partition less towards the SSF than outside the plume (Figure 3.4b) (Lee et al., 2018). The central Arctic Basin is characterized by significantly higher fSSF (more small particles) than the North Atlantic and Eastern Tropical South Pacific ($p \ll 0.001$) (Figure 3.4c), consistent with oligotrophic conditions and subsurface lateral

transport of fine particles in the Western Arctic Ocean (Xiang & Lam, 2020). Interestingly, the lowest fSSF and thereby the largest particles are also in the Western Arctic Ocean, but over the productive Chukchi Shelf (Figure 3.4c).

3.4.2 The mass-size spectra power q

Another means to assess the mass partitioning in size-fractionated particles is to compare the magnitude of the power q in the mass-size spectra (Eq. 8). A higher q indicates a higher fSSF, and thereby more mass distributed to the SSF compared to the LSF. The mass-size spectra formulation also facilitates subsequent calculations of sinking velocities (see section 2.6). The distributions of the two parameters, fSSF and q, look alike (Figure 3.4 & Appendix 3.5). The medians (ranges) of q are 1.3 (0.9-2.0), 1.3 (1.0-1.7), 1.5 (0.6-1.8) in the North Atlantic, Eastern Tropical South Pacific, and the Western Arctic Ocean, respectively.

3.5 Derived variables

3.5.1 Derived mass flux

The LSF mass flux generally decreases with depth and away from the margins, with values ranging over three to four orders of magnitude within each cruise. The medians (5^{th} to 95^{th} percentile range) of LSF mass flux (units of $g/m^2/d$) are 2.0×10^{-1} (2.1×10^{-2}-1.9) in the North Atlantic, 8.9×10^{-2} (2.3×10^{-2}-1.0) in the Eastern Tropical South Pacific, and 4.4×10^{-2} (8.2×10^{-3}-8.7) in the Western Arctic Ocean (Appendix 3.6). In terms of 0-100% range of mass flux over all cruises, it is worth noting that samples

with the highest (88.2 g/m^2/d) and lowest (2.9×10^{-3} g/m^2/d) mass flux are both in the Western Arctic Ocean. The BNLs along the western boundary in the North Atlantic increase the LSF mass flux to about 3.5 g/m^2/d. In the SSF, the mass flux varies one to two orders of magnitude within each cruise. The medians (5^{th}-95^{th}) of SSF mass flux (units of g/m^2/d) are 1.6×10^{-2} (4.5×10^{-3}-8.3×10^{-2}) in the North Atlantic, 6.5×10^{-3} (2.7×10^{-3}-4.4×10^{-2}) in the Eastern Tropical South Pacific, and 4.9×10^{-3} (1.5×10^{-3}-2.7×10^{-1}) in the Western Arctic Ocean (Appendix 3.6). Fluxes of more than 1.0 g/m^2/d are rare in the SSF, only occurring in prominent BNLs, such as on the western margin in the North Atlantic and the Chukchi Shelf in the Western Arctic Ocean.

The distribution of TOT mass fluxes is similar to the LSF (Figure 3.5 & Appendix 3.6). The medians (5^{th}-95^{th}) of TOT mass flux (units of g/m^2/d) are 2.1×10^{-1} (2.5×10^{-2}-2.5) in the North Atlantic, 9.7×10^{-2} (2.7×10^{-2}-1.1) in the Eastern Tropical South Pacific, and 4.9×10^{-2} (1.1×10^{-2}-9.6) in the Western Arctic Ocean (Figure 3.5). The highest (100^{th} percentile) TOT mass flux is over the Chukchi Shelf, reaching 89.6 g/m^2/d. The North Atlantic is characterized by the highest TOT mass flux (Figure 3.5a), and the Western Arctic Ocean has the lowest TOT mass flux ($p\ll0.001$) (Figure 3.5e). It is interesting that high mass fluxes in the upper 500 m near the Peru margin persist hundreds of kilometers offshore in the Eastern Tropical South Pacific, coinciding with the 10 μmol/kg dissolved oxygen contour line (Figure 3.5c). The low attenuation of mass flux in this region is consistent with conclusions drawn from other tracers from the same cruise, such as the ^{230}Th-normalized POC flux and stable isotope of nitrate

($\delta^{15}N_{NO3}$), which both point to less POC regeneration within the Peru oxygen deficient zone (Pavia et al., 2019; Peters et al., 2018).

3.5.2 Derived mass-weighted average sinking velocities

The magnitude of mass-weighted average sinking velocities (WSVs) for each size fraction is determined by the mass fraction and sinking velocity for each size bin (Eq. 12). Sinking velocities, in turn, are dependent on the hydrography, particle composition, and porosity-size relationship. The medians (5^{th}-95^{th} range) of WSVs over all cruises are 60.6 m/d (27.0-103.8 m/d) in the LSF, and 1.4 m/d (4.1×10^{-1}-2.6 m/d) in the SSF (Appendix 3.7). Unlike the mass flux, where the total flux was similar to the LSF flux, WSVs of total particles are less similar to the LSF WSVs: the TOT sinking rates fall between the SSF and LSF, with the median (5^{th}-95^{th}) of 13.5 m/d (3.4- 41.0 m/d; Figure 3.5). This is because the WSVs are an average sinking speed weighted by mass, thus giving more weight to the slowly sinking particles of the more abundant SSF. In contrast, flux is simply integrated across sizes, and the larger size range and faster sinking speeds of the LSF dominate the total flux. In general, we did not find strong evidence for an increasing sinking velocity with depth, in line with observations by Xue and Armstrong (2009) and Nowald et al. (2009).

The LSF WSVs are high near shelf/slope regions in the North Atlantic, but relatively low in the surface and deep basin (Appendix 3.7). The Eastern Tropical South Pacific has relatively uniform distributions of LSF WSVs (Appendix 3.7). The median (5^{th}-95^{th}) of LSF WSVs in the Eastern Tropical South Pacific is 65.7 m/d (42.8-113.0

m/d), not significantly different from the North Atlantic ($p>0.05$), which has the median (5^{th}-95^{th}) of 62.9 m/d (19.5-118.3 m/d). Interestingly, despite having significantly higher LSF particle densities compared to the North Atlantic, the Arctic Ocean is characterized by the lowest LSF sinking rates in all three basins ($p \ll 0.001$) (Appendix 3.7). The median (5^{th}-95^{th}) in the LSF in the Western Arctic Ocean is 46.1 m/d (23.3-90.5 m/d). In this case, the smaller particle size distribution (Figure 3.4 & Appendix 3.5) and greater importance of viscosity relative to gravitational sinking (see section 4.3.2.2) in the Western Arctic Ocean may play a more important role in diminishing sinking velocity.

Similar to the LSF, the Western Arctic Ocean is also characterized by the lowest WSVs in the SSF ($p \ll 0.001$), and the median (5^{th}-95^{th}) is 1.0 m/d (2.4×10^{-1}-2.1 m/d) (Appendix 3.7). However, unlike for the LSF, the SSF WSVs are relatively high in the deep North Atlantic compared to the other basins (Appendix 3.7). The SSF WSVs in the Eastern Tropical South Pacific (median: 1.4 m/d; 5^{th}-95^{th}: 6.4×10^{-1}-2.7 m/d) are significantly lower than the North Atlantic (median: 1.7 m/d; 5^{th}-95^{th}: 8.8×10^{-1}-2.7 m/d) ($p \ll 0.001$) (Appendix 3.7).

The median (5^{th}-95^{th}) of TOT WSVs is 15.4 (4.1-52.2 m/d), 15.2 (6.6-37.0 m/d), and 7.4 m/d (2.3-39.1 m/d) in the North Atlantic, Eastern Tropical South Pacific, and the Western Arctic Ocean, respectively (Figure 3.5). In the central North Atlantic, the TOT WSVs have surface and deep minima of less than 10 m/d (Figure 3.5b). As a consequence of a dominance of very small particles in the BNLs, the TOT WSVs along the deep western boundary are lower than the midwater column values despite much

higher fractions of lithogenic contents. Within the near-field EPR hydrothermal plume (<80 km from the ridge axis) in the Eastern Tropical South Pacific, the TOT WSVs can reach more than 50 m/d (Figure 3.5d) owing to increasing particle densities (Figure 3.3b) from the high oxide fraction (Appendix 3.2) and lower fSSF (more large particles) (Figure 3.4b). The most pronounced gradient in TOT WSVs between the shelf/slope and basin is observed in the Western Arctic Ocean (Figure 3.5f). Overall, the TOT WSVs in the Western Arctic Ocean are significantly lower than the other two oceans ($p \ll 0.001$).

4. Discussion

4.1 Sensitivity tests

Sensitivity tests were conducted with different numbers of size bins, upper size limits for the LSF, and porosity-size relationships. Compared to the latter two, the number of bins is of minor importance in the variations of mass flux and WSVs, and not discussed here. Additionally, according to Eq. 13, for given SPM concentrations, the variability is the same between mass flux and WSVs. Therefore, we only discuss changes in the mass flux term in sensitivity tests below.

The mass-size spectra (Eq. 8) change slightly with different upper size limits in the LSF. The difference in the power q is generally <1.5% if 10 mm is used as the upper size boundary instead of 5 mm. However, mass flux is sensitive to the variations in the upper limit in the LSF. Using the data from the Eastern Tropical South Pacific as an example, if setting the upper size boundary as 10 mm rather than 5 mm, the TOT mass

flux and WSVs are both elevated. The absolute difference ranges from 1.4×10^{-3} to 1.9 g/m^2/d and the median is 3.0×10^{-2} g/m^2/d (Appendix 3.8). The percentage of increase has a median (range) of 30.1% (4.3%-58.9%).

The mass flux is also very sensitive to the choice of the porosity-size relationship. As seen in Figure 3.2, the power-law relationship in the Alldredge and Gotschalk (1988) (P1) has a steeper slope and higher coefficient than the new compilation used in this paper (P2). For particle sizes below 5 mm, the P1 relationship tends to have a higher 1-P, thereby lower P, which leads to higher mass fluxes. If keeping the upper size limit in the LSF as 5 mm, the TOT mass flux derived from the P1 changes by a median of 1.5×10^{-1} g/m^2/d and 156.7% in the absolute and relative increase, respectively, when compared to ones calculated using the P2 relationship (Appendix 3.8).

4.2 Literature comparisons

Most observations of mass fluxes are from sediment traps. Particles collected by sediment traps and large-volume in-situ pumps, however, integrate over different temporal and spatial scales. Moored sediment traps are usually deployed for weeks and months, neutrally buoyant or surface-drifting traps are deployed for days, whereas pumps collect particles for several hours. Longer deployment times allow sediment traps to capture rare fast-sinking particles, but sediment traps tend to under-collect slowly-sinking particles owing to hydrodynamic discrimination (Gustafsson et al., 2004). Pumps sample abundant slowly-sinking particles well, but are less likely to

capture rare, fast-sinking particles. Despite the sampling differences, derived TOT mass fluxes using the pump data in this study are comparable to existing sediment trap studies (Figure 3.6) (Berelson et al., 2015; Honjo et al., 1995; Honjo et al., 2010; Hwang et al., 2015; Torres-Valdés et al., 2014). Note that there are fewer sediment trap studies in the South Pacific and Arctic Oceans as there are in the North Atlantic. Mass fluxes derived from the newly compiled P2 porosity-size power function are closer to sediment trap observations than those using the original P1 relationship. The difference in mass flux between the two porosity-size relationships results from higher porosity for all particles >8.6 μm in the P2 relationship, given an upper size limit of 5 mm in our current study.

Existing measurements of sinking velocities of natural marine particles, direct or indirect, vary by several orders of magnitude, ranging from several meters to thousands of meters per day (Alldredge & Gotschalk, 1988; Alonso-González et al., 2010; Armstrong et al., 2009; Bach et al., 2016; Bach et al., 2019; Berelson, 2001; Briggs et al., 2020; Estapa et al., 2019; Giering et al., 2016; McDonnell & Buesseler, 2010; McDonnell & Buesseler, 2012; Nowald et al., 2009; Peterson et al., 2005; Pilskaln et al., 1998; Riley et al., 2012; Trull et al., 2008; Turner, 2002). Our estimates of TOT WSVs, about 10-30 m/d (Figure 3.5), fall within the range of 2 to 54 m/d measured using gel traps and in situ camera system for particles between 73 and 1400 μm at the Bermuda Atlantic Time-Series (BATS) in the Sargasso Sea (McDonnell & Buesseler, 2012). The TOT WSVs, however, are almost an order of magnitude higher than 2-3 m/d estimated using a thorium (Th) based inverse method in the North Atlantic

(Lerner et al., 2017). Approximations of the sinking velocity derived from ^{230}Th observations are also about 1-3 m/d in other parts of the ocean (Bacon & Anderson, 1982; Krishnaswami et al., 1981; Rutgers van der Loeff & Berger, 1993; Scholten et al., 1995). Puigcorbé et al. (2015) estimated the sinking velocity of total particles as 5±2 m/d based on ^{234}Th data collected with pumps in the Northeast Pacific. In general, the SSF WSVs (~1-3 m/d) are much closer to the values from these Th-based estimates compared to the TOT WSVs (~10-30 m/d). Burd et al. (2007) pointed out that bulk measurements such as particulate ^{234}Th are likely to represent the properties of small particles more than large particles. Adsorption of radionuclides such as thorium is a function of available particle surface area (e.g., Santschi et al., 2006), and should thus be weighted to small particles that have higher surface area to volume ratios. In contrast, in our method, mass flux and WSVs are both mass-based and derived from the particle volume (Eqs. 11&12), which gives more importance to larger particles and thus a higher total sinking velocity.

Alternative chemical tracers, such as chloropigments, have also been used with inverse models to calculate sinking velocities for different size pools. Indeed, sinking rate estimates from a recent chloropigments-based inverse method by Wang et al. (2019) using data from in-situ pumps in the Mediterranean Sea are in good agreement with our study. Their modeled sinking velocities are 66.8±68.6 m/d (mean±s.d.) for large particles (>70 μm), with a range between 7 to 183 m/d, and 1.8±1.9 m/d, for small particles (1-70 μm), ranging between 0.2-5 m/d.

4.3 Controls on the mass flux

The mass flux is calculated as the product of the particle concentration and sinking velocity. Sinking velocity, in turn, depends on composition, size, and hydrography (e.g., viscosity and seawater density). Previous work has mostly focused on different factors impacting particle sinking velocities, such as the role of particle size (Alldredge & Gotschalk, 1988; Engel et al., 2009; Guidi et al., 2008; Iversen & Ploug, 2010; Iversen & Robert, 2015; Laurenceau-Cornec et al., 2020; Laurenceau-Cornec et al., 2015b; McDonnell & Buesseler, 2010; Schmidt et al., 2014), particle composition (Bach et al., 2016; Bach et al., 2019; Engel et al., 2009; Laurenceau-Cornec et al., 2020; Laurenceau-Cornec et al., 2015b; Schmidt et al., 2014), and the hydrographic effects owing to the density discontinuities (Alldredge et al., 2002; Alldredge & Crocker, 1995; Kindler et al., 2010; MacIntyre et al., 1995; Prairie et al., 2013; Prairie et al., 2015). Our comprehensive work examines all of these components governing the mass flux and adds valuable in-situ particle composition data to the existing literature.

4.3.1 Effects of particle concentration and weighted sinking velocities on mass flux

The SPM concentrations and weighted sinking velocities are used to calculate the mass flux (Eq. 13). Of these two factors, the mass flux is better correlated with SPM than with WSVs (Figure 3.7), with the relationships best for the LSF.

The scatter about the relationship between mass flux and SPM reflects the influence of WSV and therefore in the components (particle composition, size, and

hydrography) that contribute to WSV. The scatter is most evident at the low end in the Western Arctic Ocean in the SSF and TOT. The sections below will discuss how particle size, composition, and hydrography affects the sinking velocity and thus the mass flux.

4.3.1.1 Effects of particle size on sinking velocity

It is straightforward to recognize the importance of size in controlling the sinking velocity: according to Stokes' Law, sinking velocities increase with the square of particle diameter. The size effect on sinking velocity is highly dependent on the porosity-size relationship, however. Incorporation of any porosity-size relationship reduces the exponent value in Stokes' Law (Eqs. 3-4), diminishing the importance of particle size. The lower coefficient in the newly compiled porosity-size relationship increases the importance of porosity for particles as small as 8.6 μm, which tends to reduce overall sinking velocities and thus flux compared to the porosity-size relationship from Alldredge and Gotschalk (1988) (Figure 3.6). The integration of the new porosity-size relationship (Figure 3.2) results in a power of ~0.8 applied to particle diameter, which makes the dependence of sinking velocity less sensitive to changes in size than to changes in density.

Additionally, much lower mass partitioning to large particles further reduces the significance of particle size on sinking velocity. In our model, the mass fraction decreases with size due to a negative slope between the mass concentration and size (Eq. 9 & Appendix 3.5). The WSVs are the sum of sinking velocity in each size bin

weighted by its mass fraction (Eq. 12). With porosity, the last LSF size bin (4.2×10^3-5.0×10^3 μm) has sinking velocities of about four orders of magnitude higher than the first bin in the SSF (1.0-1.2 μm), reaching a median of 3.5×10^2 m/d. Its mass fraction, however, is much lower and only accounts for a median of 0.35% in TOT mass concentrations. Therefore, the effects of particle size on the overall mass flux are much less important than the classic perspective from Stokes' Law, due to the existence of porosity, as also proposed by Laurenceau-Cornec et al. (2020), and the dominance of smaller particles.

4.3.1.2 Effects of particle composition on sinking velocity

Several previous studies have shown that incorporation of minerals, such as lithogenic particles and $CaCO_3$, decreases particle size (De La Rocha et al., 2008; Engel et al., 2009; Hamm, 2002; Iversen & Ploug, 2010; Laurenceau-Cornec et al., 2020; Nowald et al., 2015; Passow & De La Rocha, 2006; Passow et al., 2014; Schmidt et al., 2014). Most of these conclusions were drawn from experiments using aggregates formed in lab roller tanks. Natural aggregates may have different behaviors when exposed to minerals.

In our study using natural particles from the full water column, we did not find evidence to support the role of $CaCO_3$ and opal in affecting particle size distribution (Figure 3.8a-b & e-f). We do find, however, that the abundance of small particles (denoted by the magnitude of the exponent q) decreases with lithogenic fraction (Figure 3.8c-d). This relationship is predominantly driven by particles in the deep Western

Arctic Ocean and by the strong bottom nepheloid layers (BNLs) of the western boundary current in the North Atlantic and Chukchi Shelf (Lam et al., 2015; Xiang & Lam, 2020). The Western Arctic Ocean is heavily influenced by lateral transport from sediment resuspension over the Chukchi Shelf and Slope, resulting in high fractions of lithogenic particles below 1000 m (Xiang & Lam, 2020). The association of lithogenic content and small particle size is thus driven by sediment resuspension processes, and not by a decrease in aggregate size caused by lithogenic content. If we exclude the entire GN01, small particles in the North Atlantic and Eastern Tropical South Pacific outside strong BNLs no longer decrease with the lithogenic fraction (Figure 3.8i-j). Indeed, the abundance of large particles may even increase with the SSF lithogenic fractions. Therefore, we postulate that in areas away from sediment resuspension, incorporation of ballast minerals into aggregates is not a primary controlling factor on the particle size distribution.

The sinking velocity increases with excess densities on the basis of Stokes' Law. The densities of $Fe(OH)_3$ and MnO_2 are higher than $CaCO_3$ and lithogenic materials, but they are usually a much smaller fraction of the particulate mass (Appendices 3.2 & 3.3). A few notable exceptions occur in hydrothermal plumes, where they can account for up to 50% of SPM concentrations. The $CaCO_3$ and Litho are often the most important ballast minerals owing to their high densities and abundances. The density of POM (~1.05 g/cm^3) is the lowest among all major phases and similar to seawater density (~1.03 g/cm^3). Given the small value in the excess density, particles with a high fraction of POM sink slowly compared to other types.

It is worth noting that the opal density, ~2.0 g/cm^3, is very similar to the median of overall particle densities in the ocean (see section 3.3), which tend to frequently be a mixture of POM and $CaCO_3$ and/or Litho. Additions of opal into marine aggregates would not lead to substantial increases in excess densities, thereby sinking velocities, and suggest that opal is likely of minor importance in influencing the overall sinking velocity. To increase sinking velocities, particles have to be characterized by elevated fractions of $Fe(OH)_3$, MnO_2, $CaCO_3$ or Litho. Our hypothesis is consistent with Klaas and Archer (2002) where they explain the low correlation between deep POC and opal fluxes as a consequence of the relatively low density of opal compared to $CaCO_3$ and lithogenic particles. The apparent weak ballasting effect of opal has also been attributed to higher aggregate porosities, reduced aggregate compactness, and increased POC lability (Bach et al., 2016; Bach et al., 2019; Francois et al., 2002; Lam & Bishop, 2007; Lam et al., 2011). This work shows that an increase in the fraction of opal is not associated with a higher abundance of larger particles (Figure 3.8e-f & k-l). Direct measurements of opal size and porosity in the future are needed to examine the role of porosity in the opal ballast more carefully.

To summarize, we did not observe any obvious decrease in particle size distribution with incorporation of ballast minerals in natural particles. In this study, effects of particle composition mainly manifest in density of different phases, where $CaCO_3$ and lithogenic particles are generally the two most important ballast minerals that add excess density to POM. The direct ballast effect of opal appears to be very weak, given its similar density to median of particle densities. We cannot exclude other

hypotheses for the weak role of opal in particle flux, such as ecosystem effects (Lima et al., 2014) and POC lability (Lam et al., 2011), however.

4.3.1.3 Effects of hydrography on sinking velocity

Hydrographic parameters in the Stokes' velocity calculation include seawater density, gravitational acceleration, and viscosity. Strong density gradients appear in the upper water column in all three oceans, especially in the Arctic Ocean. A decrease in sinking velocities and accumulations of particles within a thin layer of sharp density gradients has been observed for marine aggregates both in-situ and in laboratory settings (Alldredge et al., 2002; Alldredge & Crocker, 1995; Kindler et al., 2010; MacIntyre et al., 1995; Prairie et al., 2013; Prairie et al., 2015). Elevations of beam attenuation from the transmissometer are generally observed within the pycnocline in all three cruises (Anderson & Fleisher, 2013). Our pump sampling resolution, however, may not be fine enough to capture such features on the scale of a few meters, given the absence of obvious elevations in particle concentrations at the density discontinuities.

The influence of seawater density is incorporated into the calculation of excess densities, but as noted previously, variations in seawater density are usually small compared to variation in particle densities (see section 3.3). Sharp density gradients are generally associated with sharp viscosity gradients, since both parameters depend on temperature and salinity, so the hydrography effects on mass flux mainly manifest in the g/viscosity term (Eq. 3). Gravitational acceleration varies by less than 1% between Arctic and tropical waters. The most variation results from the viscosity, which is

highly temperature-dependent (Millero, 1974). We disregard potential biological contributions to viscosity such as from the release of mucous materials including transparent exopolymer particles (TEP) (Jenkinson, 1986; 1993; Jenkinson & Biddanda, 1995; Seuront et al., 2007; Seuront et al., 2010; Seuront & Vincent, 2008; Seuront et al., 2006).

In the Western Arctic Ocean, the ratios of g/viscosity (g/vis) are lowest in the surface (~5000 m^2/s/kg), highest at about 300 m below the Pacific-derived halocline (~5400 m^2/s/kg) and remain relatively constant in the deep ocean (~5200 m^2/s/kg) (Figure 3.9). In contrast, g/vis ratios are highest in the surface North Atlantic and Eastern Tropical South Pacific (~10000 m^2/s/kg) and decrease rapidly with depth. Higher values of g/vis in the surface (low viscosity) facilitate particle sinking out of the surface where remineralization rates are highest. On the basis of g/viscosity profiles alone, one would expect sinking velocities to slow down with depth in the North Atlantic and Eastern Tropical South Pacific, especially in upper 2000 m, whereas not change much in the Western Arctic Ocean. The fact that WSVs do not decrease with depth in the North Atlantic and Eastern Tropical South Pacific (Figures 3.5b, 3.5d, & Appendix 3.7) is caused by generally increasing excess densities with depth (Figure 3.3). Places with small g/viscosity variations with depth, such as the Western Arctic Ocean, however, have more potential for increasing excess density to increase sinking velocities with depth.

When comparing values of g/vis between three basins, they only differ by <10% in the deep ocean but can be up to 200% different in the upper water column (Figure

3.9). This distinct feature in the high-latitude Arctic Ocean can lead to up to two times smaller sinking velocities and mass fluxes than low-latitude oceans, partly contributing to smaller sinking velocities and mass fluxes in the upper water column in the Arctic Ocean (Appendices 3.6 & 3.7).

4.3.2 The relative importance of hydrography, particle concentration, size, and composition for mass flux

The size-fractionated mass flux is calculated as the sum of mass flux in each size bin (Eq. 11). Equivalently, it can also be expressed as the product of the overall mass concentration and WSVs (Eq. 13). Combining Eqs. 4, 12 and 13, we generate an overall equation with concentration, size, composition, and hydrography terms to calculate mass flux (Eq. 14), which can be used to quantitatively de-convolve the contribution of each effect to the variability and magnitude of mass flux in the SSF and LSF (Table 3.1).

$$F=\left(\int_{d_1}^{d_2}\frac{m_i}{\int_{d_1}^{d_2} m_i dd}\times(1-P_i)\frac{g\Delta\rho(d_i/10^6)^2}{18\eta}dd\right)\times SPM \qquad (14)$$

We define the concentration effect directly as SPM, and the size effect as $\int_{d_1}^{d_2}\frac{m_i}{\int_{d_1}^{d_2} m_i dd}\times(1-P_i)\times(d_i/10^6)^2 dd) = \int_{d_1}^{d_2}\frac{m_i}{\int_{d_1}^{d_2} m_i dd}\times 3.6\times10^{-11.4}\times(d_i)^{0.8}dd$, which includes both the porosity-size relationship and mass partitioning of particles, and is calculated as the sum of contribution from each size bin. The excess density, $\Delta\rho$, is used to represent the composition effect, and the hydrography effect is defined as g/viscosity, g/η. Multiplying all four terms would generate an adjusted mass flux that is 18 times higher

than the actual derived mass flux (unit: $g/m^2/s$). The variability and magnitude of individual terms, therefore, are helpful in understanding their relative importance in determining mass flux. We only focus on the upper 100 m of the water column of all non-shelf stations to assess the importance of these four effects across surface ecosystems. To avoid extreme outliers, we use the range between 5 and 95 percentiles in each term to demonstrate the variability and magnitude of mass flux.

4.3.2.1 Effects on variability of mass flux

The variability of mass flux within each size fraction with respect to hydrography, particle concentration, size, and composition is first evaluated by examining the ratio of the 95^{th} to 5^{th} percentile values for each of these four effects as defined above (Table 3.1). This 95^{th} to 5^{th} percentile ratio is a metric we use to quantify the observed variability in these effects, and thus assess the expected influence each effect may have on the observed variability in mass flux.

SPM shows the highest ratio of the 95^{th} to 5^{th} percentiles in all three cruises, and thus accounts for most of the variability in the mass flux, consistent with good correlations between SPM concentration and mass flux (Figures 3.7a-c, 3.10a-b). The concentration range ratio in the Western Arctic Ocean (44.8 and 10.2 for LSF and SSF, respectively) is much higher than other oceans, demonstrating the enormous SPM range sampled on that cruise (Figure 3.10a-b). Given the much higher SPM concentrations on the Chukchi Slope, we also calculated the ratio between 90 and 5 percentiles for both size fractions in the Western Arctic Ocean, and they are 19.2 and

3.0 for the LSF and SSF, respectively. The adjusted LSF ratio in the Western Arctic Ocean is still the highest among all cruises, whereas the SSF is similar to the North Atlantic and Eastern Tropical South Pacific.

The composition effect has the second highest ratio of the 95^{th} to 5^{th} percentiles. In the North Atlantic, the SSF range ratio for composition is slightly higher than that in the concentration. Particle composition differences may thus be more important than concentration differences for explaining mass flux variability in the SSF.

Surprisingly, the range of variability as a result of the size effect is relatively low in both size fractions, about 1-3 times lower than the composition effect. Despite the strong d_i^2 size dependence in the size term in the Stokes equation, the incorporation of size-dependent porosity reduces this effect to a dependency on $d_i^{0.8}$. Furthermore, not only are larger particles more porous, but they are less abundant than smaller particles (see section 4.3.1.1). Therefore, when comparing the sinking velocity from different locations in the SSF or LSF, samples with a high fSSF (more abundant small particles) do not necessarily correspond to slower sinking velocities because the composition effect can predominate over the size effect. Indeed, the ratio of 95^{th} to 5^{th} percentiles is greater for the composition effect than for the size effect in all cruises, demonstrating that there are greater variations in particle density than in particle size distributions.

The hydrography effect generally has lower 95^{th} to 5^{th} percentile ratios than the size effect. The largest difference between the size and hydrography effects occurs in

the Western Arctic Ocean, due to a combination of increased variability in size and decreased hydrography effect compared to other oceans.

On a global scale including all three cruises, the concentration effect still leads to most variability in the mass flux in the upper 100 m and the composition effect is the second most important term (Table 3.1). The high 95^{th} to 5^{th} percentile ratio for the concentration effect is driven by the very low (5^{th} percentile) concentrations in the Western Arctic Ocean (Figure 3.10a-b). The LSF concentration range is more variable than the SSF, whereas the SSF excess density range is more pronounced than the LSF (Table 3.1). SSF mass flux increases with excess density (Figure 3.10 b&d). LSF mass flux appears to have little relationship with excess density, until one notices that the GA03 and GP16 data do have a relationship, but the GN01 samples from the Western Arctic cluster in a range of relatively high excess density but low mass flux and WSVs (Figure 3.10a&c). This is explained by the influence of the significantly smaller particle size distribution and particle concentrations, and most viscous water in the Arctic compared to the North Atlantic and Eastern Tropical South Pacific. The relatively similar range ratios between the SSF composition and concentration effects lead to less scatter in the overall relationship of excess density *vs.* mass flux than the LSF. Additionally, the ratio of 95^{th} to 5^{th} percentiles for the hydrography effect on a global scale is almost two times higher than that on a regional scale, due to contrasting hydrographic features between polar and tropical oceans (Figure 3.9), which makes the ratio very similar to the size effect (Table 3.1).

4.3.2.2 Effects on magnitude of mass flux

We are also interested in addressing two questions related to the magnitude of mass flux: 1) why is the magnitude of LSF mass flux smallest in the central basin of Western Arctic Ocean? 2) why do LSF particles dominate the TOT mass flux throughout the water column even though they have much smaller mass concentrations than the SSF?

First, we assess the difference in magnitudes between four terms in the upper 100 m across all cruises. Since the LSF flux comprises the majority of TOT mass flux, we only discuss LSF flux here. The LSF mass flux in the upper 100 m in the Western Arctic Ocean is significantly smaller than the other two oceans ($p \ll 0.001$). Indeed, the magnitudes of the concentration and hydrographic effects are smallest in the Western Arctic Ocean (<100 m; $p \ll 0.001$), and the size effect in the Western Arctic Ocean is similar to the Eastern Tropical South Pacific ($p > 0.05$) but both are smaller than the North Atlantic ($p < 0.01$). In contrast, the LSF excess density in the Western Arctic Ocean is significantly larger than the North Atlantic ($p < 0.01$) and similar to the Eastern Tropical South Pacific ($p > 0.05$). The slightly higher excess density in the Western Arctic Ocean compared to the North Atlantic (median excess density in the LSF is 0.7 and 0.5 g/cm^3 in the Western Arctic Ocean and North Atlantic, respectively) cannot compensate for smaller size and hydrographic effects, resulting in the smallest LSF WSVs in the upper 100m in the Western Arctic (median: 37.8 m/d; $p \ll 0.001$; Figure 3.10c). The much lower LSF SPM concentrations in the Western Arctic Ocean further decrease the mass flux (Figure 3.10a). Therefore, the lowest mass fluxes in the Western

Arctic Ocean are not due to a lack of ballast minerals as proposed by (Honjo et al., 2010), but rather to a combination of the smallest particle sizes, the lowest particle concentrations and the most viscous water (lower g/vis) of the three basins. This conclusion also holds true for the rest of the water column.

Secondly, high values of mass flux for LSF compared to SSF result from their much higher sinking velocities than the SSF (Eq. 13). Indeed, we can determine quantitatively which term (size, composition or hydrography) is the main driver elevating sinking velocity over the entire water column. Based on our definition of size effect, the ratios of size effect between LSF and SSF can be calculated as: $\frac{\int_{51}^{5000} \frac{m_i}{\int_{51}^{5000} m_i dd} \times (1-P_i) \times (d_i/10^6)^2 dd}{\int_{1}^{51} \frac{m_i}{\int_{1}^{51} m_i dd} \times (1-P_i) \times (d_i/10^6)^2 dd}$, which is relatively constant, ~41. Given that the ratio of the concentration effect between LSF and SSF over all cruises has a median (5^{th}-95^{th} percentile range) of 0.3 (0.1-0.8), the size alone can more than compensate for lower concentrations in the LSF and lead to higher mass flux. Additionally, the LSF excess densities are slightly higher than the SSF in the upper 100 m (Figure 3.10): the median (5^{th}-95^{th}) ratio of the composition effect between LSF and SSF is 1.8 (0.7-4.8). Since both size fractions experience the same hydrographic parameters, it is the larger particle sizes and, to a lesser degree, denser particles in the LSF that explain the dominance of this size fraction's contribution to the total mass flux.

4.3.2.3 Overall dependency of mass flux on particle size

Since m_i, P_i and Wi are functions of d_i in Eq. 14, we can further substitute Eqs. 2 and 8 into 14 and derive the overall dependency of F on d_i:

$$F=3.6\times10^{-14.4}\times\frac{p\times\Delta\rho\times g}{18\eta}\times\int_{d_1}^{d_2}(d_i)^{0.8-q}dd \quad (15)$$

The integrated mass flux F is calculated using the mass flux spectrum integrated over a size interval $[d_1, d_2]$. We simplify Eq. 15 and define the mass flux as $F=\int_{d_1}^{d_2} f(d)dd$. The mass flux spectrum f(d) is a power function with positive coefficients and an exponent of 0.8-q. For any given particle size, the values of f(d) are always positive, which leads to positive flux F for any size interval.

The median (5^{th}-95^{th}) of mass-size spectra power q over all three cruises is 1.4 (1.1-1.6). Accordingly, the power of f(d) has a median (5^{th} to 95^{th}) of -0.6 (-0.8 to -0.3). Therefore, the mass flux spectrum generally has a negative slope, and the function f(d) decreases with size. The negative sign of the power signifies that the mass flux in any single size bin generally decreases as a function of particle size, similar to the mass-size and number-size spectra, although the absolute magnitude of the power in the mass flux spectrum is much smaller. Noticeably, in some rare cases, the mass flux spectrum can even have a positive slope and increase with size. Over the Chukchi Shelf in the Western Arctic Ocean, there are very low q values (denoted larger particles), reaching as low as 0.6 (Appendix 3.5), which leads to a positive exponent 0.2 in f(d).

4.4 Key assumptions and their limitations

This study relies on several key assumptions: (1) the mass concentration and size follow a power-law relationship; (2) a power function also describes the relationship between porosity and size; (3) the particle composition is the same across the size spectrum within each size fraction for a specific sample; (4) the sinking of particles obeys Stokes' Law. We examine each of these assumptions.

First, due to the difficulties of observing individual particle mass directly, there is not much direct evidence for the application of a single power-law relationship between mass concentration and size. The mass size distribution in this study was derived from bulk measurements of particle mass in two size fractions. Its power law form assumes that the higher abundance of small particles, as confirmed by numerous optical observations of the number size spectrum (e.g., Jackson et al., 1997; Loisel et al., 2006; Roullier et al., 2014; Stemmann et al., 2008; Stemmann et al., 2004), overcomes the greater mass for individual large aggregates, giving rise to a negative slope between the mass concentration and size. Indeed, our data confirm that the mass of particles in the SSF is almost always larger than in the LSF. Applying a single slope to the entire size range is likely an oversimplification for the complex natural assemblage of particles, but hopefully captures the first order distribution of mass.

Secondly, the single power-law function between the porosity and size used in this work is also a simplification of the myriad controls on porosity. Compared to the original equation in Alldredge and Gotschalk (1988), the updated power law in this study incorporates more data points, especially in the smaller end of the size range, as well as different methods for estimating particle porosities. As discussed above in

section 4.1, the derived mass flux is quite sensitive to the choice of porosity-size relationship. More data points are needed in future studies, especially in size range of 0.3 to 1.0 mm (Figure 3.2). It is clear from the considerable scatter in both the original and updated relationships that there are many more controls on porosity than size alone. Given the many mechanisms that produce marine aggregates, including abiotic coagulation and fecal pellet production by a wide variety of animals, it is probable that better estimates of mass fluxes require multiple power functions or a more complicated non-linear relationship.

Thirdly, different particle types (Andrews et al., 2010; Reynolds et al., 2016; Woźniak et al., 2010), and phytoplankton communities (Green et al., 2003a; Green et al., 2003b; Smyth et al., 2019; Stramski et al., 2001) have distinct size distributions, and their corresponding peaks in particle number concentrations do not often occur at the same size. For example, relatively dense lithogenic particles and $CaCO_3$ coccoliths are likely concentrated in the smaller end of the SSF spectrum (e.g., Baumann & Sprengel, 2000; Rea & Hovan, 1995) rather than distributed evenly throughout. Thus, the assumption of constant composition in all size bins within each size fraction necessarily results in monotonic changes in sinking velocity with size in the LSF or SSF that might not exist in reality. Using an average bulk composition would lead to an overestimate of true mass flux if denser particle phases were skewed to smaller particles. Since measuring particle composition at each size bin is not practical due to sampling and analytical limitations, we apply two different densities to the size range within the LSF and SSF, respectively, to estimate the mass flux. A similar strategy

using a single bulk composition was employed by Bach et al. (2016) when calculating the sinking velocity of natural marine aggregates in mesocosms.

Fourthly, the assumption of spherical particles for our Stokes' Law calculations is a simplification, as marine aggregates are not perfect spheres (e.g., Alldredge & Gotschalk, 1988; Engel et al., 2009; McDonnell & Buesseler, 2010). Given the same size and excess density, irregularly shaped aggregates are characterized by lower sinking velocities than spherical ones due to the increased drag (Alldredge & Gotschalk, 1988). Another assumption we made in Stokes' Law calculation is that the flow through the porous aggregate is negligible in order to apply Eq.4. The numerical simulations from Kiørboe et al. (2001), however, suggested that flow occurs in a thin layer at the surface of aggregates, which is borne out by oxygen microsensor measurements within aggregates (Ploug et al., 2008b). Additionally, the presence of TEP can also influence the excess density in sinking velocity estimations. Indeed, much of the space in the porous fraction of aggregates can be occupied by TEP (Ploug & Passow, 2007). TEP is operationally defined as >0.4 μm particles filtered by polycarbonate filters that stain with Alcian Blue (Alldredge et al., 1993; Passow, 2002). The density of TEP is 0.70-0.84 g/cm^3 , lower than seawater (Azetsu-Scott & Passow, 2004). As TEP measurements were not made in our samples, we did not consider its possible influence, but it would be expected to decrease the mass flux estimation.

5. Conclusions

Although this study makes several assumptions to convert suspended particle concentration and composition to mass flux, it predicts mass flux values comparable to various sediment traps studies and gives insights into the controls of export flux on a global scale.

We compile porosity and size measurements of natural marine aggregates from the literature and use a modified Stokes' law with the fractal-porosity relationship to calculate sinking velocity and mass flux. Noticeably, TOT mass fluxes derived from the newly compiled porosity-size power-law relationship are more similar to sediment trap observations than if we were to use the porosity-size relationship for marine snow aggregates only from Alldredge and Gotschalk (1988). The Western Arctic Ocean is characterized by the lowest TOT WSVs and mass fluxes compared to the North Atlantic and Eastern Tropical South Pacific. We did not find evidence for a lack of ballast minerals in the Western Arctic Ocean as proposed by Honjo et al. (2010) to explain low mass fluxes. Instead, the lowest TOT mass fluxes found in the Western Arctic Ocean result from the smallest particle sizes, the lowest particle concentrations and the most viscous water. It does not mean that composition is not important in determining the magnitude of mass flux, but simply that other factors dominate in the Western Arctic. Indeed, away from the Arctic, the LSF mass flux generally increases with excess density (Figure 3.10), though there is no relationship with the prevalence of any specific particle phase (Appendix 3.9).

We also compare the relative importance of particle concentration, composition, size and hydrography effects in the variability and magnitude of mass flux on a global

scale combing all three cruises. Our data suggest that the variability of mass flux within each size fraction (LSF, SSF or TOT) is controlled mostly by particle concentration and composition, and less so by size and hydrography (Table 3.1). While large particles will always have a faster sinking velocity than small particles (all else being equal) and thus explain the important contributions of the LSF to the TOT mass flux, the variations in particle size distribution between samples are smaller than the variations in particle density. This highlights the importance of particle composition, not just size distribution, as key parameters for predicting mass flux.

The particle size distribution is a parameter measured by optical methods that is increasingly used to study the biological carbon pump in various cruises and autonomous platforms (Picheral et al., 2017), including the *Tara* Ocean expedition (Guidi et al., 2016). The conversion from particle size to flux, however, often lacks any direct or indirect information about particle composition (Giering et al., 2020; Stemmann & Boss, 2012). The poor constraints in particle densities might partly explain the discrepancy between sediment trap-measured and UVP-derived mass fluxes (Fender et al., 2019; Guidi et al., 2008). Compared to traditional geochemistry measurements, however, optical devices such as the UVP have advantages of much higher spatial and temporal resolution. To better constrain UVP-derived mass flux estimates, we recommend pairing optics with measurements of particle composition in future investigations, either by sampling simultaneously in the same cruise, or referring to historical measurements. The geochemical determination of particle properties

serves as a calibration to optical proxies, and helps us further understand the biological carbon pump on a global scale.

Acknowledgments

This work was supported by NSFOCE-1535854 to PJL. We would like to thank all chief scientists and everyone on board in the GA03, GP16, and GN01 U.S. GEOTRACES cruises. Special thanks to all people in the pump group for helping to collect particle samples at sea. We sincerely thank past and current members in the Lam lab for the continuous assistance in both lab work and data analysis, and Thomas Weber and Bo Yang for their help in data visualization. We also thank X anonymous reviewers for their suggestions and comments to improve this manuscript. All size-fractionated particle concentration and composition data described above are available on the Biological and Chemical Oceanography Data Management Office website (GA03: https://www.bco-dmo.org/dataset/3871; GP16: https://www.bco-dmo.org/dataset/668083; GN01: https://www.bco-dmo.org/dataset/807340).

References

Alldredge, A. L., Cowles, T. J., MacIntyre, S., Rines, J. E. B., Donaghay, P. L., Greenlaw, C. F., et al. (2002). Occurrence and mechanisms of formation of a dramatic thin layer of marine snow in a shallow Pacific fjord. *Marine Ecology Progress Series*, *233*, 1-12. https://doi.org/10.3354/meps233001

Alldredge, A. L., & Crocker, K. M. (1995). Why do sinking mucilage aggregates accumulate in the water column? *Science of The Total Environment*, *165*(1), 15-22. https://doi.org/10.1016/0048-9697(95)04539-D

Alldredge, A. L., & Gotschalk, C. (1988). In situ settling behavior of marine snow. *Limnology and Oceanography*, *33*(3), 339-351. https://doi.org/10.4319/lo.1988.33.3.0339

Alldredge, A. L., Passow, U., & Logan, B. E. (1993). The abundance and significance of a class of large, transparent organic particles in the ocean. *Deep Sea Research Part I: Oceanographic Research Papers*, *40*(6), 1131-1140. https://doi.org/10.1016/0967-0637(93)90129-Q

Alldredge, A. L., & Silver, M. W. (1988). Characteristics, dynamics and significance of marine snow. *Progress in oceanography*, *20*(1), 41-82. https://doi.org/10.1016/0079-6611(88)90053-5

Alonso-González, I. J., Arístegui, J., Lee, C., Sanchez-Vidal, A., Calafat, A., Fabrés, J., et al. (2010). Role of slowly settling particles in the ocean carbon cycle. *Geophysical Research Letters*, *37*(13). https://doi.org/10.1029/2010gl043827

Anderson, R. F., & Fleisher, M. Q. (2013). Particle beam attenuation coefficient (Cp) data from ODF (Ocean Data Facility) rosette, R/V Knorr KN199-04, KN204-01 in the Subtropical northern Atlantic Ocean, 2010-2011 (U.S. GEOTRACES NAT project). *Biological and Chemical Oceanography Data Management Office (BCO-DMO)*, *Dataset version 2013-11-05*.

Andrews, S., Nover, D., & Schladow, S. G. (2010). Using laser diffraction data to obtain accurate particle size distributions: the role of particle composition. *Limnology and Oceanography: Methods*, *8*(10), 507-526. https://doi.org/10.4319/lom.2010.8.507

Armstrong, R. A., Lee, C., Hedges, J. I., Honjo, S., & Wakeham, S. G. (2001). A new, mechanistic model for organic carbon fluxes in the ocean based on the quantitative association of POC with ballast minerals. *Deep Sea Research Part II: Topical Studies in Oceanography*, *49*(1-3), 219-236. https://doi.org/10.1016/S0967-0645(01)00101-1

Armstrong, R. A., Peterson, M. L., Lee, C., & Wakeham, S. G. (2009). Settling velocity spectra and the ballast ratio hypothesis. *Deep Sea Research Part II: Topical Studies in Oceanography*, *56*(18), 1470-1478. https://doi.org/10.1016/j.dsr2.2008.11.032

Aumont, O., Van Hulten, M., Roy-Barman, M., Dutay, J. C., Éthé, C., & Gehlen, M. (2017). Variable reactivity of particulate organic matter in a global ocean biogeochemical model. *Biogeosciences*, *14*(9), 2321-2341. https://doi.org/10.5194/bg-14-2321-2017

Azetsu-Scott, K., & Passow, U. (2004). Ascending marine particles: Significance of transparent exopolymer particles (TEP) in the upper ocean. *Limnology and Oceanography*, *49*(3), 741-748. https://doi.org/10.4319/lo.2004.49.3.0741

Bach, L. T., Boxhammer, T., Larsen, A., Hildebrandt, N., Schulz, K. G., & Riebesell, U. (2016). Influence of plankton community structure on the sinking velocity of marine aggregates. *Global Biogeochemical Cycles*, *30*(8), 1145-1165. https://doi.org/10.1002/2016GB005372

Bach, L. T., Stange, P., Taucher, J., Achterberg, E. P., Algueró-Muñiz, M., Horn, H., et al. (2019). The influence of plankton community structure on sinking velocity and remineralization rate of marine aggregates. *Global Biogeochemical Cycles*, *33*(8), 971-994. https://doi.org/10.1029/2019gb006256

Bacon, M. P., & Anderson, R. F. (1982). Distribution of thorium isotopes between dissolved and particulate forms in the deep sea. *Journal of Geophysical Research: Oceans*, *87*(C3), 2045-2056. https://doi.org/10.1029/JC087iC03p02045

Baumann, K. H., & Sprengel, C. (2000). Morphological variations of selected coccolith species in a sediment trap north of the Canary Islands. *Journal of Nannoplankton Research*, *22*(3), 185-193

Berelson, W. M. (2001). Particle settling rates increase with depth in the ocean. *Deep Sea Research Part II: Topical Studies in Oceanography*, *49*(1-3), 237-251. https://doi.org/10.1016/S0967-0645(01)00102-3

Berelson, W. M., Haskell II, W. Z., Prokopenko, M., Knapp, A. N., Hammond, D. E., Rollins, N., & Capone, D. G. (2015). Biogenic particle flux and benthic remineralization in the Eastern Tropical South Pacific. *Deep Sea Research Part I: Oceanographic Research Papers*, *99*, 23-34. https://doi.org/10.1016/j.dsr.2014.12.006

Bishop, J. K. B., Edmond, J. M., Ketten, D. R., Bacon, M. P., & Silker, W. B. (1977). The chemistry, biology, and vertical flux of particulate matter from the upper

400 m of the equatorial Atlantic Ocean. *Deep Sea Research*, *24*(6), 511-548. https://doi.org/10.1016/0146-6291(77)90526-4

Boyd, P. W., & Trull, T. W. (2007). Understanding the export of biogenic particles in oceanic waters: Is there consensus? *Progress in Oceanography*, *72*(4), 276-312. https://doi.org/10.1016/j.pocean.2006.10.007

Briggs, N., Dall'Olmo, G., & Claustre, H. (2020). Major role of particle fragmentation in regulating biological sequestration of CO2 by the oceans. *Science*, *367*(6479), 791-793. https://doi.org/10.1126/science.aay1790

Buesseler, K. O., Lamborg, C. H., Boyd, P. W., Lam, P. J., Trull, T. W., Bidigare, R. R., et al. (2007). Revisiting carbon flux through the ocean's twilight zone. *Science*, *316*(5824), 567-570. https://doi.org/10.1126/science.1137959

Burd, A. B., Jackson, G. A., & Moran, S. B. (2007). The role of the particle size spectrum in estimating POC fluxes from Th234/U238 disequilibrium. *Deep Sea Research Part I: Oceanographic Research Papers*, *54*(6), 897-918. https://doi.org/10.1016/j.dsr.2007.03.006

Cutter, G., Kadko, D., & Landing, W. M. (2019). Bottle data from the CTD-ODF carousel on the GEOTRACES Arctic Section cruise (HLY1502) from August to October 2015 (U.S. GEOTRACES Arctic project). *Biological and Chemical Oceanography Data Management Office (BCO-DMO)*, *Dataset version 2019-07-29*. https://doi.org/10.1575/1912/bco-dmo.646825.4.

De La Rocha, C. L., Nowald, N., & Passow, U. (2008). Interactions between diatom aggregates, minerals, particulate organic carbon, and dissolved organic matter: Further implications for the ballast hypothesis. *Global Biogeochemical Cycles*, *22*(4). https://doi.org/10.1029/2007gb003156

Ebersbach, F., & Trull, T. W. (2008). Sinking particle properties from polyacrylamide gels during the KErguelen Ocean and Plateau compared Study (KEOPS): Zooplankton control of carbon export in an area of persistent natural iron inputs in the Southern Ocean. *Limnology and Oceanography*, *53*(1), 212-224. https://doi.org/10.4319/lo.2008.53.1.0212

Engel, A., Szlosek, J., Abramson, L., Liu, Z., & Lee, C. (2009). Investigating the effect of ballasting by CaCO3 in Emiliania huxleyi: I. Formation, settling velocities and physical properties of aggregates. *Deep Sea Research Part II: Topical Studies in Oceanography*, *56*(18), 1396-1407. https://doi.org/10.1016/j.dsr2.2008.11.027

Estapa, M. L., Feen, M. L., & Breves, E. (2019). Direct observations of biological carbon export from profiling floats in the subtropical North Atlantic. *Global*

Biogeochemical Cycles, *33*(3), 282-300. https://doi.org/10.1029/2018gb006098

Fender, C. K., Kelly, T. B., Guidi, L., Ohman, M. D., Smith, M. C., & Stukel, M. R. (2019). Investigating particle size-flux relationships and the biological pump across a range of plankton ecosystem states from coastal to oligotrophic. *Frontiers in Marine Science*, *6*(603). https://doi.org/10.3389/fmars.2019.00603

Fowler, S. W., & Knauer, G. A. (1986). Role of large particles in the transport of elements and organic compounds through the oceanic water column. *Progress in oceanography*, *16*(3), 147-194. https://doi.org/10.1016/0079-6611(86)90032-7

Francois, R., Honjo, S., Krishfield, R., & Manganini, S. (2002). Factors controlling the flux of organic carbon to the bathypelagic zone of the ocean. *Global Biogeochemical Cycles*, *16*(4), 34-31-34-20. https://doi.org/10.1029/2001gb001722

Gardner, W. D., Mishonov, A. V., & Richardson, M. J. (2018a). Decadal comparisons of particulate matter in repeat transects in the Atlantic, Pacific, and Indian Ocean Basins. *Geophysical Research Letters*, *45*(1), 277-286. https://doi.org/10.1002/2017GL076571

Gardner, W. D., Richardson, M. J., & Mishonov, A. V. (2018b). Global assessment of benthic nepheloid layers and linkage with upper ocean dynamics. *Earth and Planetary Science Letters*, *482*, 126-134. https://doi.org/10.1016/j.epsl.2017.11.008

Gardner, W. D., Richardson, M. J., Mishonov, A. V., & Biscaye, P. E. (2018c). Global comparison of benthic nepheloid layers based on 52 years of nephelometer and transmissometer measurements. *Progress in oceanography*, *168*, 100-111. https://doi.org/10.1016/j.pocean.2018.09.008

Giering, S. L. C., Cavan, E. L., Basedow, S. L., Briggs, N., Burd, A. B., Darroch, L. J., et al. (2020). Sinking organic particles in the ocean- flux estimates from in situ optical devices. *Frontiers in Marine Science*, *6*(834). https://doi.org/10.3389/fmars.2019.00834

Giering, S. L. C., Sanders, R., Martin, A. P., Lindemann, C., Möller, K. O., Daniels, C. J., et al. (2016). High export via small particles before the onset of the North Atlantic spring bloom. *Journal of Geophysical Research: Oceans*, *121*(9), 6929-6945. https://doi.org/10.1002/2016jc012048

Green, R. E., Sosik, H. M., & Olson, R. J. (2003a). Contributions of phytoplankton and other particles to inherent optical properties in New England continental shelf

waters. *Limnology and Oceanography*, *48*(6), 2377-2391. https://doi.org/10.4319/lo.2003.48.6.2377

Green, R. E., Sosik, H. M., Olson, R. J., & DuRand, M. D. (2003b). Flow cytometric determination of size and complex refractive index for marine particles: comparison with independent and bulk estimates. *Applied Optics*, *42*(3), 526-541. https://doi.org/10.1364/AO.42.000526

Guidi, L., Chaffron, S., Bittner, L., Eveillard, D., Larhlimi, A., Roux, S., et al. (2016). Plankton networks driving carbon export in the oligotrophic ocean. *Nature*, *532*(7600), 465-470. https://doi.org/10.1038/nature16942

Guidi, L., Jackson, G. A., Stemmann, L., Miquel, J. C., Picheral, M., & Gorsky, G. (2008). Relationship between particle size distribution and flux in the mesopelagic zone. *Deep Sea Research Part I: Oceanographic Research Papers*, *55*(10), 1364-1374. https://doi.org/10.1016/j.dsr.2008.05.014

Gustafsson, Ö., Andersson, P., Roos, P., Kukulska, Z., Broman, D., Larsson, U., et al. (2004). Evaluation of the collection efficiency of upper ocean sub-photic-layer sediment traps: A 24-month in situ calibration in the open Baltic Sea using 234Th. *Limnology and Oceanography: Methods*, *2*(2), 62-74. https://doi.org/10.4319/lom.2004.2.62

Hamm, C. E. (2002). Interactive aggregation and sedimentation of diatoms and clay-sized lithogenic material. *Limnology and Oceanography*, *47*(6), 1790-1795. https://doi.org/10.4319/lo.2002.47.6.1790

Hatta, M., Measures, C. I., Wu, J., Roshan, S., Fitzsimmons, J. N., Sedwick, P. N., & Morton, P. L. (2015). An overview of dissolved Fe and Mn distributions during the 2010–2011 US GEOTRACES north Atlantic cruises: GEOTRACES GA03. *Deep Sea Research Part II: Topical Studies in Oceanography*, *116*, 117-129. https://doi.org/10.1016/j.dsr2.2014.07.005

Henson, S. A., Sanders, R., & Madsen, E. (2012). Global patterns in efficiency of particulate organic carbon export and transfer to the deep ocean. *Global Biogeochemical Cycles*, *26*(1). https://doi.org/10.1029/2011gb004099

Honjo, S., Dymond, J., Collier, R., & Manganini, S. J. (1995). Export production of particles to the interior of the equatorial Pacific Ocean during the 1992 EqPac experiment. *Deep Sea Research Part II: Topical Studies in Oceanography*, *42*(2-3), 831-870. https://doi.org/10.1016/0967-0645(95)00034-N

Honjo, S., Krishfield, R. A., Eglinton, T. I., Manganini, S. J., Kemp, J. N., Doherty, K., et al. (2010). Biological pump processes in the cryopelagic and hemipelagic

Arctic Ocean: Canada Basin and Chukchi Rise. *Progress in Oceanography*, *85*(3-4), 137-170. https://doi.org/10.1016/j.pocean.2010.02.009

Hurd, D. C., & Theyer, F. (1977). Changes in the physical and chemical properties of biogenic silica from the central equatorial Pacific; Part II, Refractive index, density, and water content of acid-cleaned samples. *American Journal of Science*, *277*(9), 1168-1202. https://doi.org/10.2475/ajs.277.9.1168

Hwang, J., Kim, M., Manganini, S. J., McIntyre, C. P., Haghipour, N., Park, J., et al. (2015). Temporal and spatial variability of particle transport in the deep Arctic Canada Basin. *Journal of Geophysical Research: Oceans*, *120*(4), 2784-2799. https://doi.org/10.1002/2014jc010643

Iversen, M. H., & Ploug, H. (2010). Ballast minerals and the sinking carbon flux in the ocean: carbon-specific respiration rates and sinking velocity of marine snow aggregates. *Biogeosciences*, *7*(9), 2613-2624. https://doi.org/10.5194/bg-7-2613-2010

Iversen, M. H., & Robert, M. L. (2015). Ballasting effects of smectite on aggregate formation and export from a natural plankton community. *Marine Chemistry*, *175*, 18-27. https://doi.org/10.1016/j.marchem.2015.04.009

Jackson, G. A., Maffione, R., Costello, D. K., Alldredge, A. L., Logan, B. E., & Dam, H. G. (1997). Particle size spectra between 1 μm and 1 cm at Monterey Bay determined using multiple instruments. *Deep Sea Research Part I: Oceanographic Research Papers*, *44*(11), 1739-1767. https://doi.org/10.1016/S0967-0637(97)00029-0

Jakobsson, M. (2002). Hypsometry and volume of the Arctic Ocean and its constituent seas. *Geochemistry, Geophysics, Geosystems*, *3*(5), 1-18. https://doi.org/10.1029/2001GC000302

Jenkinson, I. R. (1986). Oceanographic implications of non-newtonian properties found in phytoplankton cultures. *Nature*, *323*(6087), 435-437. https://doi.org/10.1038/323435a0

Jenkinson, I. R. (1993). Bulk-phase viscoelastic properties of seawater. *Oceanol. acta*, *16*(4), 317-334

Jenkinson, I. R., & Biddanda, B. A. (1995). Bulk-phase viscoelastic properties of seawater relationship with plankton components. *Journal of Plankton Research*, *17*(12), 2251-2274. https://doi.org/10.1093/plankt/17.12.2251

Kindler, K., Khalili, A., & Stocker, R. (2010). Diffusion-limited retention of porous particles at density interfaces. *Proceedings of the National Academy of Sciences*, *107*(51), 22163-22168. https://doi.org/10.1073/pnas.1012319108

Kiørboe, T., Ploug, H., & Thygesen, U. H. (2001). Fluid motion and solute distribution around sinking aggregates. I. Small-scale fluxes and heterogeneity of nutrients in the pelagic environment. *Marine Ecology Progress Series*, *211*, 1-13. https://doi.org/10.3354/meps211001

Kipp, L. E., Sanial, V., Henderson, P. B., van Beek, P., Reyss, J. L., Hammond, D. E., et al. (2018). Radium isotopes as tracers of hydrothermal inputs and neutrally buoyant plume dynamics in the deep ocean. *Marine Chemistry*, *201*, 51-65. https://doi.org/10.1016/j.marchem.2017.06.011

Klaas, C., & Archer, D. E. (2002). Association of sinking organic matter with various types of mineral ballast in the deep sea: Implications for the rain ratio. *Global Biogeochemical Cycles*, *16*(4), 63-61-63-14. https://doi.org/10.1029/2001GB001765

Krishnaswami, S., Sarin, M. M., & Somayajulu, B. L. K. (1981). Chemical and radiochemical investigations of surface and deep particles of the Indian Ocean. *Earth and Planetary Science Letters*, *54*(1), 81-96. https://doi.org/10.1016/0012-821X(81)90071-6

Kwon, E. Y., Primeau, F., & Sarmiento, J. L. (2009). The impact of remineralization depth on the air–sea carbon balance. *Nature Geoscience*, *2*(9), 630-635. https://doi.org/10.1038/ngeo612

Lam, P. J., & Bishop, J. K. B. (2007). High biomass, low export regimes in the Southern Ocean. *Deep Sea Research Part II: Topical Studies in Oceanography*, *54*(5-7), 601-638. https://doi.org/10.1016/j.dsr2.2007.01.013

Lam, P. J., Doney, S. C., & Bishop, J. K. B. (2011). The dynamic ocean biological pump: Insights from a global compilation of particulate organic carbon, CaCO3, and opal concentration profiles from the mesopelagic. *Global Biogeochemical Cycles*, *25*(3). https://doi.org/10.1029/2010gb003868

Lam, P. J., Lee, J. M., Heller, M. I., Mehic, S., Xiang, Y., & Bates, N. R. (2018). Size-fractionated distributions of suspended particle concentration and major phase composition from the US GEOTRACES Eastern Pacific Zonal Transect (GP16). *Marine Chemistry*, *201*, 90-107. https://doi.org/10.1016/j.marchem.2017.08.013

Lam, P. J., & Marchal, O. (2015). Insights into particle cycling from thorium and particle data. *Annual review of marine science*, *7*, 159-184. https://doi.org/10.1146/annurev-marine-010814-015623

Lam, P. J., Ohnemus, D. C., & Auro, M. E. (2015). Size-fractionated major particle composition and concentrations from the US GEOTRACES North Atlantic Zonal Transect. *Deep Sea Research Part II: Topical Studies in Oceanography*, *116*, 303-320. https://doi.org/10.1016/j.dsr2.2014.11.020

Laurenceau-Cornec, E. C., Le Moigne, F. A. C., Gallinari, M., Moriceau, B., Toullec, J., Iversen, M. H., et al. (2020). New guidelines for the application of Stokes' models to the sinking velocity of marine aggregates. *Limnology and Oceanography*, *65*(6), 1264-1285. https://doi.org/10.1002/lno.11388

Laurenceau-Cornec, E. C., Trull, T. W., Davies, D. M., Bray, S. G., Doran, J., Planchon, F., et al. (2015a). The relative importance of phytoplankton aggregates and zooplankton fecal pellets to carbon export: insights from free-drifting sediment trap deployments in naturally iron-fertilised waters near the Kerguelen Plateau. *Biogeosciences*, *12*(4), 1007-1027. https://doi.org/10.5194/bg-12-1007-2015

Laurenceau-Cornec, E. C., Trull, T. W., Davies, D. M., Christina, L., & Blain, S. (2015b). Phytoplankton morphology controls on marine snow sinking velocity. *Marine Ecology Progress Series*, *520*, 35-56. https://doi.org/10.3354/meps11116

Le Moigne, F. A. C., Sanders, R. J., Villa-Alfageme, M., Martin, A. P., Pabortsava, K., Planquette, H., et al. (2012). On the proportion of ballast versus non-ballast associated carbon export in the surface ocean. *Geophysical research letters*, *39*(15). https://doi.org/10.1029/2012GL052980

Lee, C., Peterson, M. L., Wakeham, S. G., Armstrong, R. A., Cochran, J. K., Miquel, J. C., et al. (2009). Particulate organic matter and ballast fluxes measured using time-series and settling velocity sediment traps in the northwestern Mediterranean Sea. *Deep Sea Research Part II: Topical Studies in Oceanography*, *56*(18), 1420-1436. https://doi.org/10.1016/j.dsr2.2008.11.029

Lee, J. M., Heller, M. I., & Lam, P. J. (2018). Size distribution of particulate trace elements in the U.S. GEOTRACES Eastern Pacific Zonal Transect (GP16). *Marine Chemistry*, *201*, 108-123. https://doi.org/10.1016/j.marchem.2017.09.006

Lerner, P., Marchal, O., Lam, P. J., Buesseler, K., & Charette, M. A. (2017). Kinetics of thorium and particle cycling along the U.S. GEOTRACES North Atlantic Transect. *Deep Sea Research Part I: Oceanographic Research Papers*, *125*, 106-128. https://doi.org/10.1016/j.dsr.2017.05.003

Lima, I. D., Lam, P. J., & Doney, S. C. (2014). Dynamics of particulate organic carbon flux in a global ocean model. *Biogeosciences*, *11*(4), 1177-1198. https://doi.org/10.5194/bg-11-1177-2014

Logan, B. E., & Alldredge, A. L. (1989). Potential for increased nutrient uptake by flocculating diatoms. *Marine Biology*, *101*(4), 443-450. https://doi.org/10.1007/BF00541645

Logan, B. E., & Wilkinson, D. B. (1990). Fractal geometry of marine snow and other biological aggregates. *Limnology and Oceanography*, *35*(1), 130-136. https://doi.org/10.4319/lo.1990.35.1.0130

Loisel, H., Nicolas, J. M., Sciandra, A., Stramski, D., & Poteau, A. (2006). Spectral dependency of optical backscattering by marine particles from satellite remote sensing of the global ocean. *Journal of Geophysical Research: Oceans*, *111*(C9). https://doi.org/10.1029/2005JC003367

MacIntyre, S., Alldredge, A. L., & Gotschalk, C. C. (1995). Accumulation of marines now at density discontinuities in the water column. *Limnology and Oceanography*, *40*(3), 449-468. https://doi.org/10.4319/lo.1995.40.3.0449

Mahowald, N. M., Baker, A. R., Bergametti, G., Brooks, N., Duce, R. A., Jickells, T. D., et al. (2005). Atmospheric global dust cycle and iron inputs to the ocean. *Global Biogeochemical Cycles*, *19*(4), n/a-n/a. https://doi.org/10.1029/2004gb002402

Mandernack, K. W., & Tebo, B. M. (1993). Manganese scavenging and oxidation at hydrothermal vents and in vent plumes. *Geochimica et Cosmochimica Acta*, *57*(16), 3907-3923. https://doi.org/10.1016/0016-7037(93)90343-U

Marsay, C. M., Kadko, D., Landing, W. M., Morton, P. L., Summers, B. A., & Buck, C. S. (2018). Concentrations, provenance and flux of aerosol trace elements during US GEOTRACES Western Arctic cruise GN01. *Chemical Geology*, *502*, 1-14. https://doi.org/10.1016/j.chemgeo.2018.06.007

Martin, J. H., Knauer, G. A., Karl, D. M., & Broenkow, W. W. (1987). VERTEX: carbon cycling in the northeast Pacific. *Deep Sea Research Part A. Oceanographic Research Papers*, *34*(2), 267-285. https://doi.org/10.1016/0198-0149(87)90086-0

McDonnell, A. M., & Buesseler, K. O. (2010). Variability in the average sinking velocity of marine particles. *Limnology and Oceanography*, *55*(5), 2085-2096. https://doi.org/10.4319/lo.2010.55.5.2085

McDonnell, A. M. P., & Buesseler, K. O. (2012). A new method for the estimation of sinking particle fluxes from measurements of the particle size distribution, average sinking velocity, and carbon content. *Limnology and Oceanography: Methods*, *10*(5), 329-346. https://doi.org/10.4319/lom.2012.10.329

Millero, F. J. (1974). Seawater as a multicomponent electrolyte solution. In E. D. Goldberg (Eds.), *The Sea, Volume 5: Marine Chemistry* (pp. 3-80): John Wiley & Sons Inc.

Nowald, N., Fischer, G., Ratmeyer, V., Iversen, M., Reuter, C., & Wefer, G. (2009). *In-situ sinking speed measurements of marine snow aggregates acquired with a settling chamber mounted to the Cherokee ROV*. Paper presented at Oceans 2009-Europe, IEEE.

Nowald, N., Iversen, M. H., Fischer, G., Ratmeyer, V., & Wefer, G. (2015). Time series of in-situ particle properties and sediment trap fluxes in the coastal upwelling filament off Cape Blanc, Mauritania. *Progress in Oceanography*, *137*, 1-11. https://doi.org/10.1016/j.pocean.2014.12.015

Omand, M. M., Govindarajan, R., He, J., & Mahadevan, A. (2020). Sinking flux of particulate organic matter in the oceans: Sensitivity to particle characteristics. *Scientific reports*, *10*(1), 1-16. https://doi.org/10.1038/s41598-020-60424-5

Passow, U. (2002). Transparent exopolymer particles (TEP) in aquatic environments. *Progress in Oceanography*, *55*(3), 287-333. https://doi.org/10.1016/S0079-6611(02)00138-6

Passow, U., & De La Rocha, C. L. (2006). Accumulation of mineral ballast on organic aggregates. *Global Biogeochemical Cycles*, *20*(1). https://doi.org/10.1029/2005gb002579

Passow, U., De La Rocha, C. L., Fairfield, C., & Schmidt, K. (2014). Aggregation as a function of and mineral particles. *Limnology and Oceanography*, *59*(2), 532-547. https://doi.org/10.4319/lo.2014.59.2.0532

Pavia, F. J., Anderson, R. F., Lam, P. J., Cael, B. B., Vivancos, S. M., Fleisher, M. Q., et al. (2019). Shallow particulate organic carbon regeneration in the South Pacific Ocean. *Proceedings of the National Academy of Sciences*, *116*(20), 9753-9758. https://doi.org/10.1073/pnas.1901863116

Peters, B. D., Lam, P. J., & Casciotti, K. L. (2018). Nitrogen and oxygen isotope measurements of nitrate along the US GEOTRACES Eastern Pacific Zonal Transect (GP16) yield insights into nitrate supply, remineralization, and water mass transport. *Marine Chemistry*, *201*, 137-150. https://doi.org/10.1016/j.marchem.2017.09.009

Peterson, M. L., Wakeham, S. G., Lee, C., Askea, M. A., & Miquel, J. C. (2005). Novel techniques for collection of sinking particles in the ocean and determining their settling rates. *Limnology and Oceanography: Methods*, *3*(12), 520-532. https://doi.org/10.4319/lom.2005.3.520

Picheral, M., Colin, S., & Irisson, J. O. (2017). EcoTaxa, a tool for the taxonomic classification of images. Available from: http://ecotaxa.obs-vlfr.fr

Pilskaln, C. H., Lehmann, C., Paduan, J. B., & Silver, M. W. (1998). Spatial and temporal dynamics in marine aggregate abundance, sinking rate and flux: Monterey Bay, central California. *Deep Sea Research Part II: Topical Studies in Oceanography*, *45*(8-9), 1803-1837. https://doi.org/10.1016/S0967-0645(98)80018-0

Ploug, H., Iversen, M. H., & Fischer, G. (2008a). Ballast, sinking velocity, and apparent diffusivity within marine snow and zooplankton fecal pellets: Implications for substrate turnover by attached bacteria. *Limnology and Oceanography*, *53*(5), 1878-1886. https://doi.org/10.4319/lo.2008.53.5.1878

Ploug, H., Iversen, M. H., Koski, M., & Buitenhuis, E. T. (2008b). Production, oxygen respiration rates, and sinking velocity of copepod fecal pellets: direct measurements of ballasting by opal and calcite. *Limnology and Oceanography*, *53*(2), 469-476. https://doi.org/10.4319/lo.2008.53.2.0469

Ploug, H., & Passow, U. (2007). Direct measurement of diffusivity within diatom aggregates containing transparent exopolymer particles. *Limnology and oceanography*, *52*(1), 1-6. https://doi.org/10.4319/lo.2007.52.1.0001

Prairie, J. C., Ziervogel, K., Arnosti, C., Camassa, R., Falcon, C., Khatri, S., et al. (2013). Delayed settling of marine snow at sharp density transitions driven by fluid entrainment and diffusion-limited retention. *Marine Ecology Progress Series*, *487*, 185-200. https://doi.org/10.3354/meps10387

Prairie, J. C., Ziervogel, K., Camassa, R., McLaughlin, R. M., White, B. L., Dewald, C., & Arnosti, C. (2015). Delayed settling of marine snow: Effects of density gradient and particle properties and implications for carbon cycling. *Marine Chemistry*, *175*, 28-38. https://doi.org/10.1016/j.marchem.2015.04.006

Puigcorbé, V., Benitez-Nelson, C. R., Masqué, P., Verdeny, E., White, A. E., Popp, B. N., et al. (2015). Small phytoplankton drive high summertime carbon and nutrient export in the Gulf of California and Eastern Tropical North Pacific. *Global Biogeochemical Cycles*, *29*(8), 1309-1332. https://doi.org/10.1002/2015gb005134

Rea, D. K., & Hovan, S. A. (1995). Grain size distribution and depositional processes of the mineral component of abyssal sediments: Lessons from the North Pacific. *Paleoceanography*, *10*(2), 251-258. https://doi.org/10.1029/94PA03355

Resing, J. A., Sedwick, P. N., German, C. R., Jenkins, W. J., Moffett, J. W., Sohst, B. M., & Tagliabue, A. (2015). Basin-scale transport of hydrothermal dissolved metals across the South Pacific Ocean. *Nature*, *523*(7559), 200-203. https://doi.org/10.1038/nature14577

Reynolds, R. A., Stramski, D., & Neukermans, G. (2016). Optical backscattering by particles in Arctic seawater and relationships to particle mass concentration, size distribution, and bulk composition. *Limnology and Oceanography*, *61*(5), 1869-1890. https://doi.org/10.1002/lno.10341

Riley, J. S., Sanders, R., Marsay, C., Le Moigne, F. A. C., Achterberg, E. P., & Poulton, A. J. (2012). The relative contribution of fast and slow sinking particles to ocean carbon export. *Global Biogeochemical Cycles*, *26*(1), n/a-n/a. https://doi.org/10.1029/2011gb004085

Rixen, T., Gaye, B., Emeis, K., & Ramaswamy, V. (2019). The ballast effect of lithogenic matter and its influences on the carbon fluxes in the Indian Ocean. *Biogeosciences*, *16*(2), 485-503. https://doi.org/10.5194/bg-16-485-2019

Rohatgi, A. (2010). WebPlotDigitizer- Extract data from plots, images, and maps. Available from: https://automeris.io/WebPlotDigitizer/

Rosengard, S. Z., Lam, P. J., Balch, W. M., Auro, M. E., Pike, S., Drapeau, D., & Bowler, B. (2015). Carbon export and transfer to depth across the Southern Ocean Great Calcite Belt. *Biogeosciences*, *12*(13), 3953-3971. https://doi.org/10.5194/bg-12-3953-2015

Roullier, F., Berline, L., Guidi, L., Durrieu De Madron, X., Picheral, M., Sciandra, A., et al. (2014). Particle size distribution and estimated carbon flux across the Arabian Sea oxygen minimum zone. *Biogeosciences*, *11*(16), 4541-4557. https://doi.org/10.5194/bg-11-4541-2014

Ruiz, J. (1997). What generates daily cycles of marine snow? *Deep Sea Research Part I: Oceanographic Research Papers*, *44*(7), 1105-1126. https://doi.org/10.1016/S0967-0637(97)00012-5

Rutgers van der Loeff, M. M., & Berger, G. W. (1993). Scavenging of 230Th and 231Pa near the antarctic polar front in the South Atlantic. *Deep Sea Research Part I: Oceanographic Research Papers*, *40*(2), 339-357. https://doi.org/10.1016/0967-0637(93)90007-P

Santschi, P. H., Murray, J. W., Baskaran, M., Benitez-Nelson, C. R., Guo, L. D., Hung, C. C., et al. (2006). Thorium speciation in seawater. *Marine Chemistry*, *100*(3), 250-268. https://doi.org/10.1016/j.marchem.2005.10.024

Schlitzer, R., Anderson, R. F., Dodas, E. M., Lohan, M., Geibert, W., Tagliabue, A., et al. (2018). The GEOTRACES intermediate data product 2017. *Chemical Geology*, *493*(C), 210-223. https://doi.org/10.1016/j.chemgeo.2018.05.040

Schmidt, K., De La Rocha, C. L., Gallinari, M., & Cortese, G. (2014). Not all calcite ballast is created equal: differing effects of foraminiferan and coccolith calcite on the formation and sinking of aggregates. *Biogeosciences*, *11*(1), 135-145. https://doi.org/10.5194/bg-11-135-2014

Scholten, J. C., Rutgers van der Loeff, M. M., & Michel, A. (1995). Distribution of 230Th and 231Pa in the water column in relation to the ventilation of the deep Arctic basins. *Deep Sea Research Part II: Topical Studies in Oceanography*, *42*(6), 1519-1531. https://doi.org/10.1016/0967-0645(95)00052-6

Seuront, L., Lacheze, C., Doubell, M. J., Seymour, J. R., Van Dongen-Vogels, V., Newton, K., et al. (2007). The influence of Phaeocystis globosa on microscale spatial patterns of chlorophyll a and bulk-phase seawater viscosity. In M. A. van Leeuwe, J. Stefels, S. Belviso, C. Lancelot, P. G. Verity and W. W. C. Gieskes (Eds.), *Phaeocystis, major link in the biogeochemical cycling of climate-relevant elements* (pp. 173-188). Dordrecht: Springer Netherlands. https://doi.org/10.1007/978-1-4020-6214-8_13

Seuront, L., Leterme, S. C., Seymour, J. R., Mitchell, J. G., Ashcroft, D., Noble, W., et al. (2010). Role of microbial and phytoplanktonic communities in the control of seawater viscosity off East Antarctica (30-80° E). *Deep Sea Research Part II: Topical Studies in Oceanography*, *57*(9), 877-886. https://doi.org/10.1016/j.dsr2.2008.09.018

Seuront, L., & Vincent, D. (2008). Increased seawater viscosity, Phaeocystis globosa spring bloom and Temora longicornis feeding and swimming behaviours. *Marine Ecology Progress Series*, *363*, 131-145. https://doi.org/10.3354/meps07373

Seuront, L., Vincent, D., & Mitchell, J. G. (2006). Biologically induced modification of seawater viscosity in the Eastern English Channel during a Phaeocystis globosa spring bloom. *Journal of Marine Systems*, *61*(3), 118-133. https://doi.org/10.1016/j.jmarsys.2005.04.010

Shanks, A. L., & Trent, J. D. (1980). Marine snow: sinking rates and potential role in vertical flux. *Deep Sea Research Part A. Oceanographic Research Papers*, *27*(2), 137-143. https://doi.org/10.1016/0198-0149(80)90092-8

Smyth, T. J., Tarran, G. A., & Sathyendranath, S. (2019). Marine picoplankton size distribution and optical property contrasts throughout the Atlantic Ocean revealed using flow cytometry. *Applied Optics*, *58*(32), 8802-8815. https://doi.org/10.1364/AO.58.008802

Stemmann, L., & Boss, E. (2012). Plankton and particle size and packaging: from determining optical properties to driving the biological pump. *Annual Review of Marine Science*, *4*, 263-290. https://doi.org/10.1146/annurev-marine-120710-100853

Stemmann, L., Eloire, D., Sciandra, A., Jackson, G. A., Guidi, L., Picheral, M., & Gorsky, G. (2008). Volume distribution for particles between 3.5 to 2000 µm in the upper 200 m region of the South Pacific Gyre. *Biogeosciences*, *5*(2), 299-310. https://doi.org/10.5194/bg-5-299-2008

Stemmann, L., Jackson, G. A., & Ianson, D. (2004). A vertical model of particle size distributions and fluxes in the midwater column that includes biological and physical processes—Part I: model formulation. *Deep Sea Research Part I: Oceanographic Research Papers*, *51*(7), 865-884. https://doi.org/10.1016/j.dsr.2004.03.001

Stokes, G. G. (1851). On the effect of the internal friction of fluids on the motion of pendulums. *Transactions of the Cambridge Philosophical Society*, *9*, 8-106

Stramski, D., Bricaud, A., & Morel, A. (2001). Modeling the inherent optical properties of the ocean based on the detailed composition of the planktonic community. *Applied Optics*, *40*(18), 2929-2945. https://doi.org/10.1364/AO.40.002929

Torres-Valdés, S., Painter, S. C., Martin, A. P., Sanders, R., & Felden, J. (2014). Data compilation of fluxes of sedimenting material from sediment traps in the Atlantic Ocean. *Earth System Science Data*, *6*(1), 123-145. https://doi.org/10.5194/essd-6-123-2014

Towe, K. M., & Bradley, W. F. (1967). Mineralogical constitution of colloidal "hydrous ferric oxides". *Journal of Colloid and Interface Science*, *24*(3), 384-392. https://doi.org/10.1016/0021-9797(67)90266-4

Trull, T. W., Bray, S. G., Buesseler, K. O., Lamborg, C. H., Manganini, S., Moy, C., & Valdes, J. (2008). In situ measurement of mesopelagic particle sinking rates and the control of carbon transfer to the ocean interior during the Vertical Flux in the Global Ocean (VERTIGO) voyages in the North Pacific. *Deep Sea Research Part II: Topical Studies in Oceanography*, *55*(14), 1684-1695. https://doi.org/10.1016/j.dsr2.2008.04.021

Turner, J. T. (2002). Zooplankton fecal pellets, marine snow and sinking phytoplankton blooms. *Aquatic microbial ecology*, *27*(1), 57-102. https://doi.org/10.3354/ame027057

Turner, J. T. (2015). Zooplankton fecal pellets, marine snow, phytodetritus and the ocean's biological pump. *Progress in Oceanography*, *130*, 205-248. https://doi.org/10.1016/j.pocean.2014.08.005

Volk, T., & Hoffert, M. I. (1985). Ocean carbon pumps: analysis of relative strengths and efficiencies in ocean-driven atmospheric CO2 changes. In E. T. Sundquist and W. S. Broecker (Eds.), *The carbon cycle and atmospheric CO2: natural variations Archean to present* (Vol. 32, pp. 99-110). Washington, D. C.: American Geophysical Union. https://doi.org/10.1029/GM032p0099

Wang, W. L., Lee, C., & Primeau, F. W. (2019). A Bayesian statistical approach to inferring particle dynamics from in-situ pump POC and chloropigment data from the Mediterranean Sea. *Marine Chemistry*, *214*, 103654. https://doi.org/10.1016/j.marchem.2019.04.006

White, F. M. (1974). *Viscous fluid flow*. New York: McGraw-Hill Inc.

Wilson, S. E., Ruhl, H. A., & Smith, J., K. L. (2013). Zooplankton fecal pellet flux in the abyssal northeast Pacific: A 15 year time-series study. *Limnology and oceanography*, *58*(3), 881-892. https://doi.org/10.4319/lo.2013.58.3.0881

Woźniak, S. B., Stramski, D., Stramska, M., Reynolds, R. A., Wright, V. M., Miksic, E. Y., et al. (2010). Optical variability of seawater in relation to particle concentration, composition, and size distribution in the nearshore marine environment at Imperial Beach, California. *Journal of Geophysical Research: Oceans*, *115*(C8). https://doi.org/10.1029/2009jc005554

Xiang, Y., & Lam, P. J. (2020). Size-fractionated compositions of marine suspended particles in the Western Arctic Ocean: Lateral and vertical sources. *Journal of Geophysical Research: Oceans*, *125*(8), e2020JC016144. https://doi.org/10.1029/2020JC016144

Xue, J., & Armstrong, R. A. (2009). An improved "benchmark" method for estimating particle settling velocities from time-series sediment trap fluxes. *Deep Sea Research Part II: Topical Studies in Oceanography*, *56*(18), 1479-1486. https://doi.org/10.1016/j.dsr2.2008.11.033

Young, J. R. (1994). Functions of coccoliths. In A. Winter and W. G. Siesser (Eds.), *Coccolithophores* (pp. 63-82). Cambridge, UK: Cambridge University Press

Figures and Tables

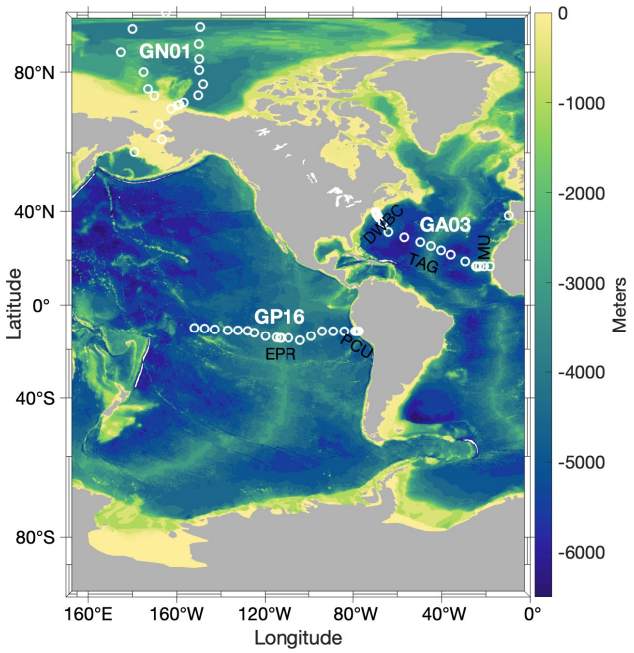

Figure 3.1 Station map of three U.S. GEOTRACES cruises in which in-situ pump were deployed. The color bar is ocean bathymetry. The GA03 is the North Atlantic Zonal Transect, GP16 is the Eastern Pacific Zonal Transect, and GN01 is the Arctic cruise. MU: Mauritanian Upwelling; TAG: Trans-Atlantic Geotraverse hydrothermal plume; DWBC: deep western boundary current; PCU: Peruvian Coastal Upwelling; EPR: East Pacific Rise (EPR) hydrothermal plume.

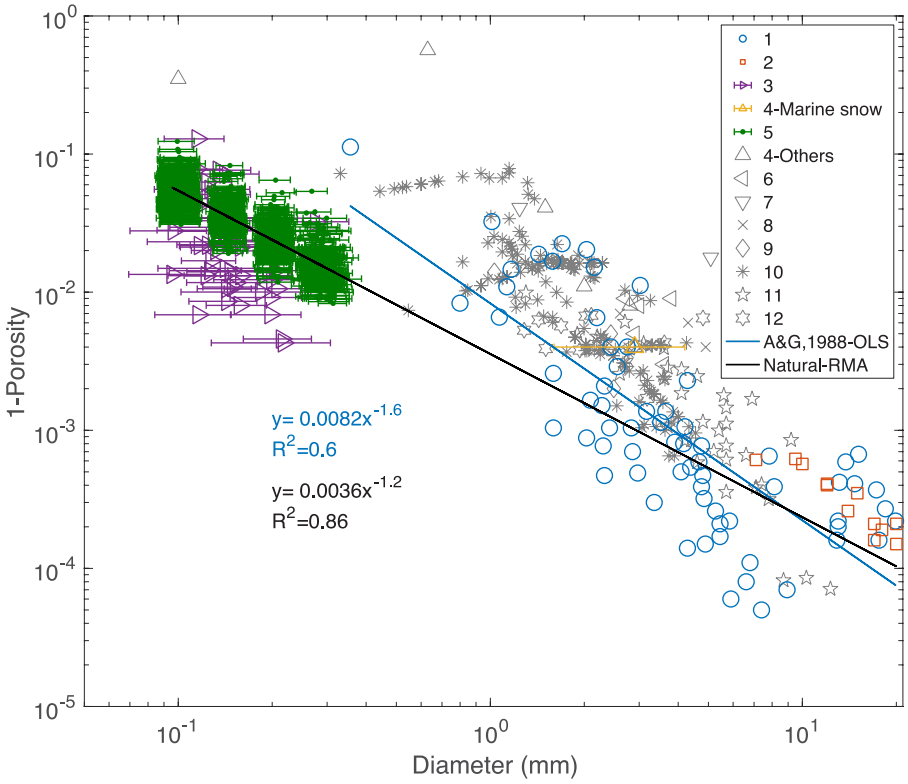

Figure 3.2 A newly compiled porosity-size relationship from literature. Data points outlined in gray are aggregates formed in lab roller tanks, whereas colored symbols are natural marine aggregates. The ordinary least square (OLS) and reduced major axis (RMA) regression are used to fit data from Alldredge and Gotschalk (1988) and all natural aggregates, respectively. Regression equations are displayed with the colors matching with fit lines. 1: Alldredge and Gotschalk (1988); 2: Logan and Alldredge (1989); 3: Lam and Bishop (2007); 4: Ploug et al. (2008a); 5: Bach et al. (2016); 6: Ploug and Passow (2007); 7: Engel et al. (2009); 8: Schmidt et al. (2014); 9: Prairie et al. (2015); 10: Iversen and Robert (2015); 11: Laurenceau-Cornec et al. (2015b); 12: Laurenceau-Cornec et al. (2020).

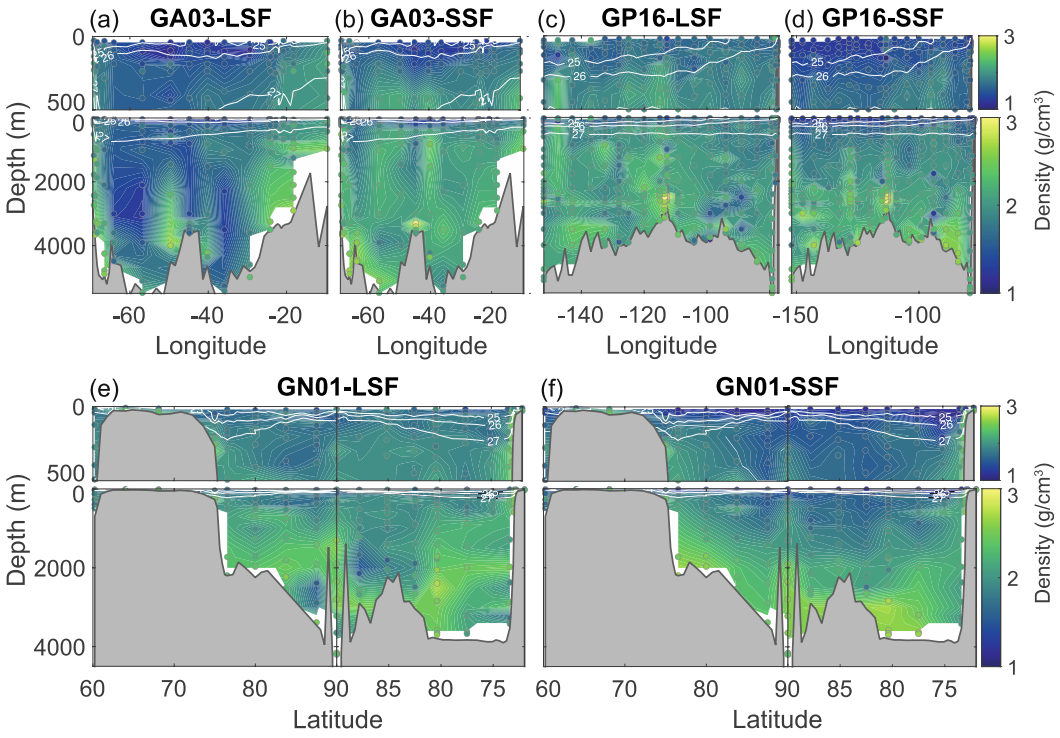

Figure 3.3 LSF (>51 μm) and SSF (1-51 μm) particle densities (unit: g/cm^3) in three cruises. (a): GA03 LSF; (b): GA03 SSF; (c): GP16 LSF; (d): GP16 SSF; (e) GN01 LSF; (f): GN01 SSF. The top panel in each subplot is the upper 500 m, and the lower panel is the entire water column. Pump sampling depths with actual data are shown with colored dots outlined in gray, on top of interpolated values that are plotted on model grids. Both actual and interpolated values are assigned with the same color bar. Thick white contours are potential density anomaly of 25, 26 and 27 kg/m^3, and thin white lines are 50 evenly spaced contour lines within the range of the color scale. In GN01, northbound and southbound legs are connected, and the North Pole station (90˚N) is shown in the center.

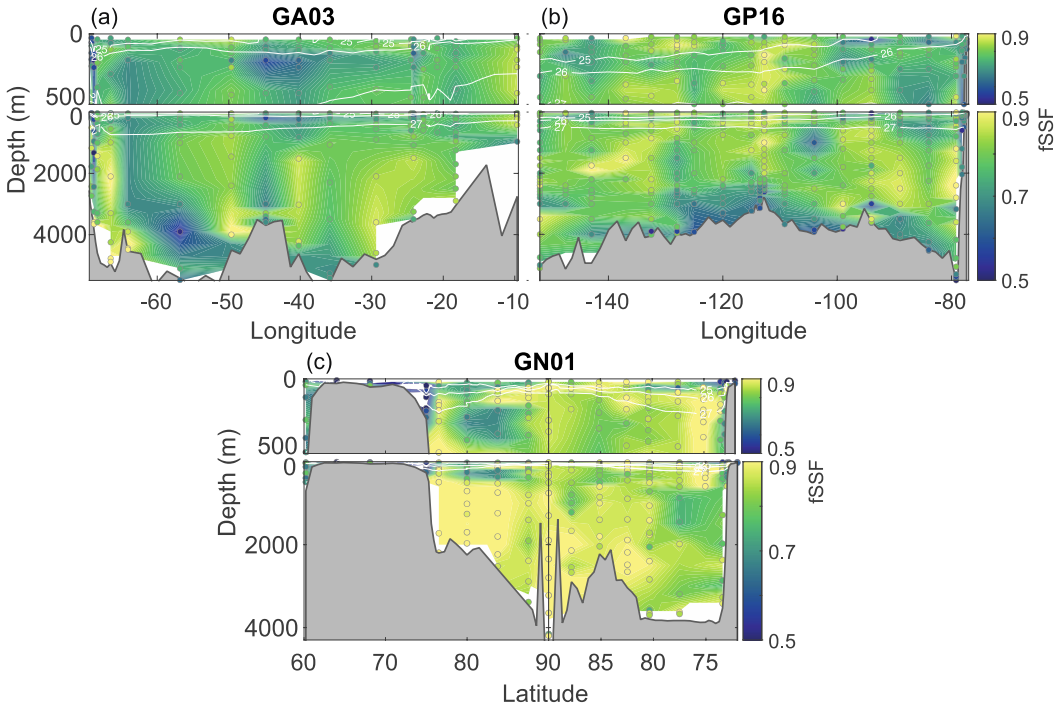

Figure 3.4 Fraction of SSF in TOT (>1 μm) mass concentrations in three cruises. (a): GA03; (b): GP16; (c) GN01. The top panels in each subplot is the upper 500 m, and the lower panel is the entire water column.

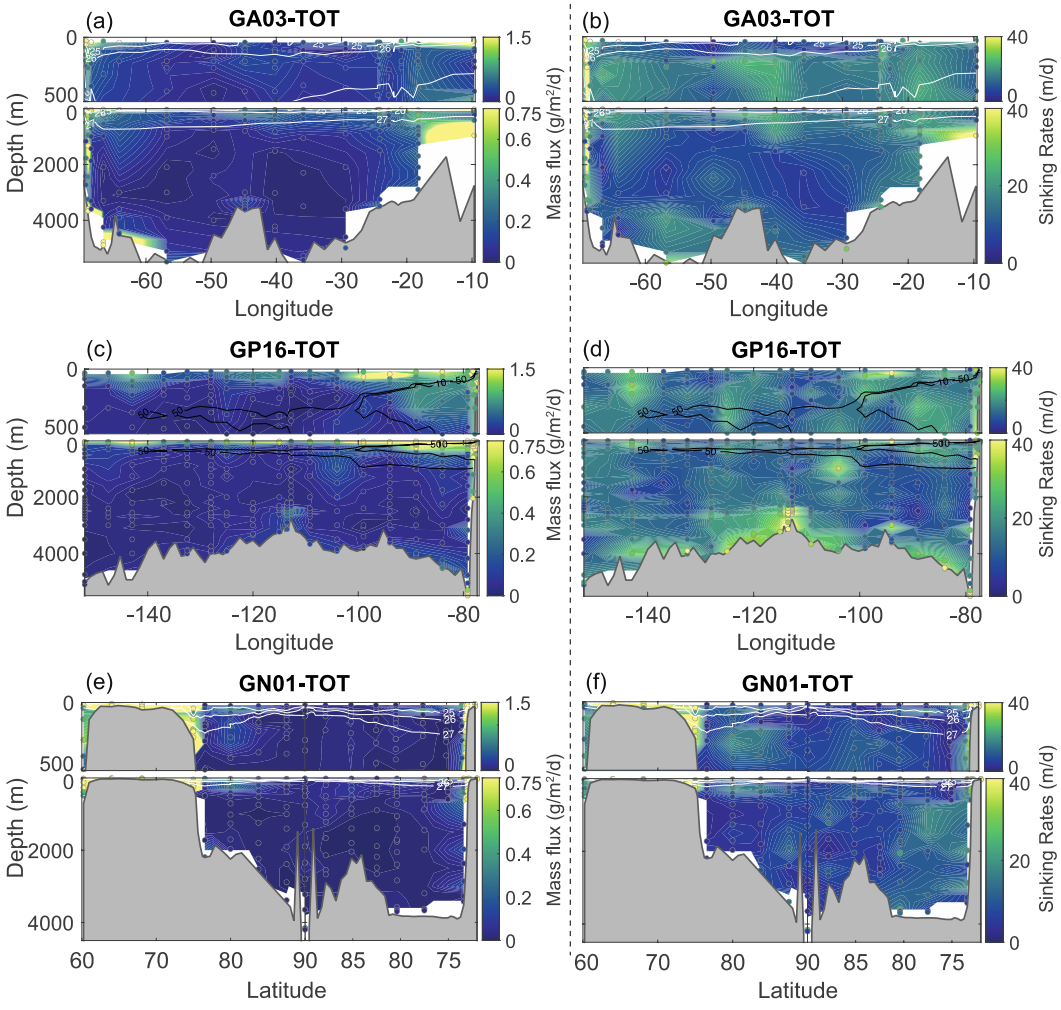

Figure 3.5 Derived mass flux (unit: g/m^2/d) in TOT particles (a, c, e), and derived mass-weighted average sinking velocity (unit: m/d) in TOT particles in three cruises (b, e, f). (a)-(b): GA03; (c)-(d): GP16; (e)-(f): GN01. Thick white contours are potential density anomaly of 25, 26 and 27 kg/m^3, and thick black contours in the GP16 are dissolved oxygen concentrations of 10 and 50 μmol/kg. Note that color scales are the same for all cruises but are different between the upper 500 m (top panels) and the whole water column (bottom panels) in the TOT mass flux.

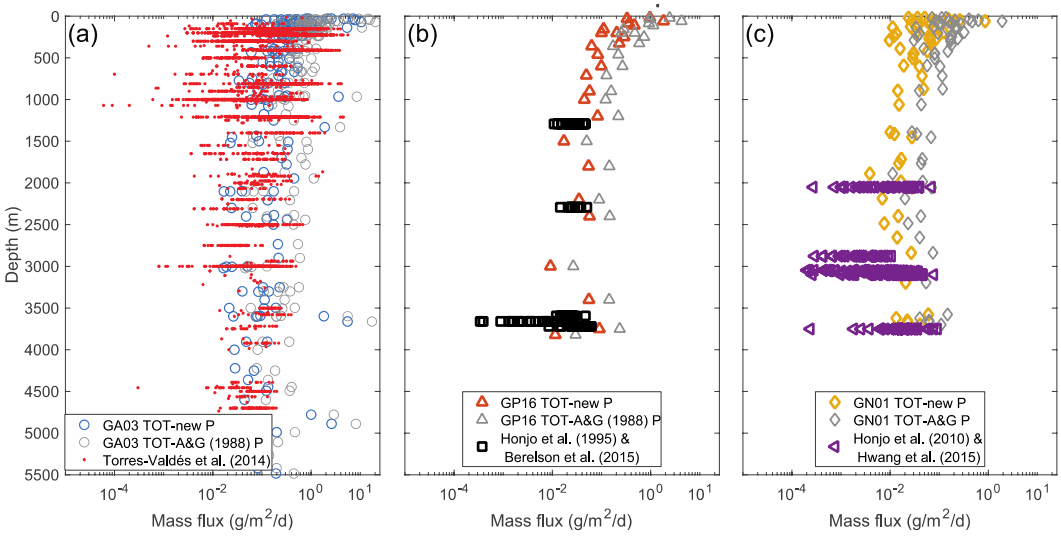

Figure 3.6 Comparisons between pump-derived and sediment trap-measured TOT mass flux (unit: g/m^2/d) in three cruises. (a): GA03; (b): GP16; (c): GN01. Mass fluxes calculated from the porosity-size relationship in Alldredge and Gotschalk (1988) are in gray. All GA03 stations are used to compared with data from Torres-Valdés et al. (2014), which covers both North and South Atlantic and includes many types of sediment traps. Only Stations 13-14 and 29-30 in the GP16 are used in (b) to compare with Station 12 in Honjo et al. (1995) and Stations 5 and 7 in Berelson et al. (2015). The TOT mass flux in Stations 46-56 in the Canada Basin in the GN01 are shown in (c). Sediment traps in both Honjo et al. (2010) and Hwang et al. (2015) were deployed at 75˚N, 150˚W in the center of Canada Basin.

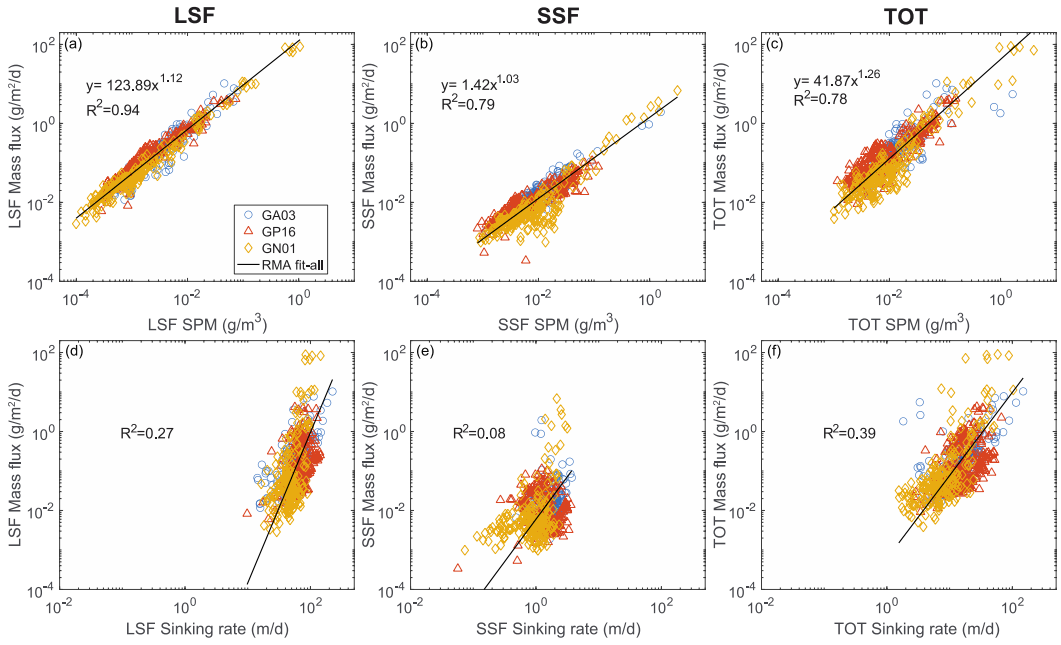

Figure 3.7 Relationships between size-fractionated SPM concentrations and mass flux (a-c), and between mass-weighted average sinking velocity (WSVs) and mass flux (d-f). The (a) and (d) are LSF, (b) and (e) are SSF, (c) and (f) are TOT. The reduced major axis (Model II linear fit) is used in the regression. Regression equations are displayed in (a)-(c), whereas only the coefficient of determination R^2 is shown in (d)-(f).

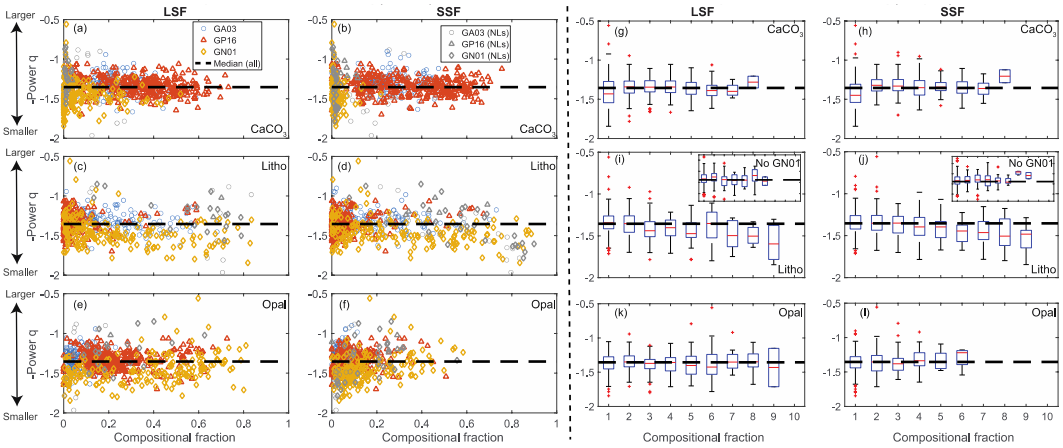

Figure 3.8 Scatter (a-f) and box plots (g-l) between size-fractionated (LSF: left; SSF: right) compositional fraction and negative power exponent q (-q) in the mass-size spectra. Three major ballast minerals, $CaCO_3$, Litho and opal, are shown in the top, middle and bottom panels, respectively. The black dashed line is the median of all -q in each size fraction from all cruises. Nepheloid layers (NLs) are defined as any

lithogenic concentrations of >5 µg/L in both size fractions and plotted in gray in the scatter plots. Compositional fractions are binned for every 10% between 0 and 100% in the box plots, excluding all NLs samples. The red segment inside the rectangle indicates the median and whiskers above and below the box show values of the minimum and maximum. Outliers are shown with red plus signs. Insets in (i) and (j) are plots excluding data from the GN01.

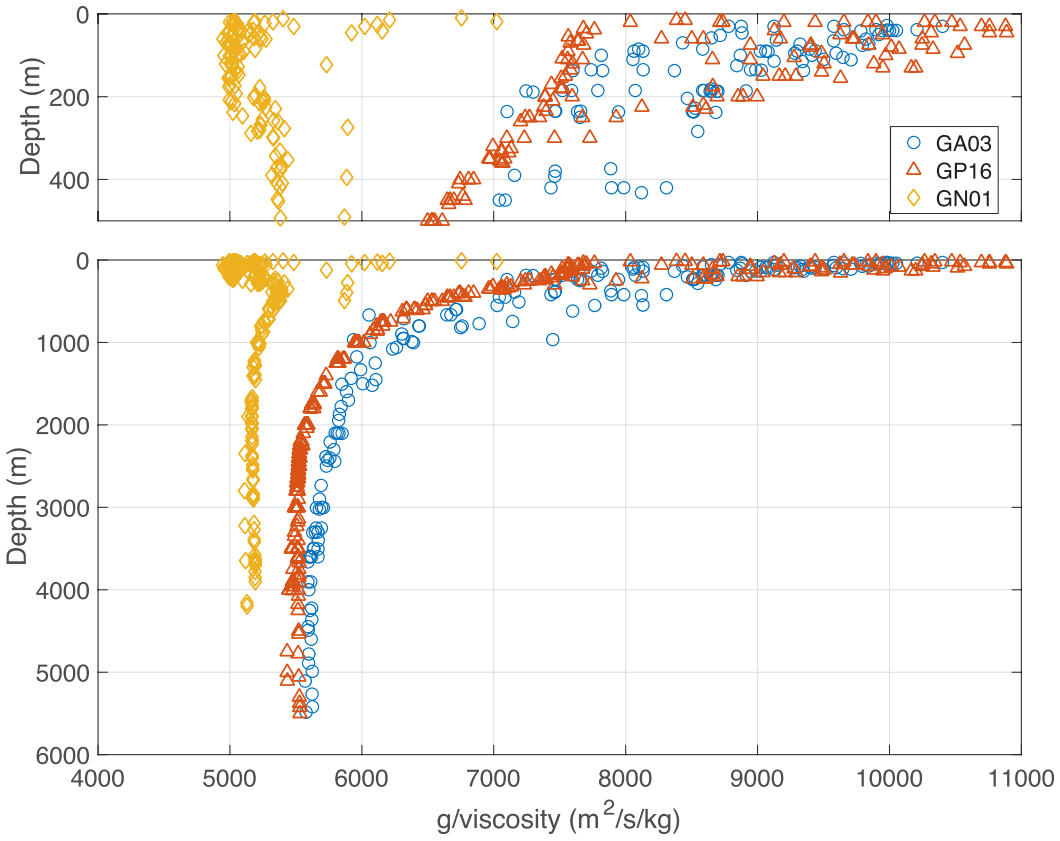

Figure 3.9 Profiles of hydrographic parameter g/ viscosity (unit: $m^2/s/kg$) in the upper 500 m (top panel) and the whole water column (bottom panel) in three cruises.

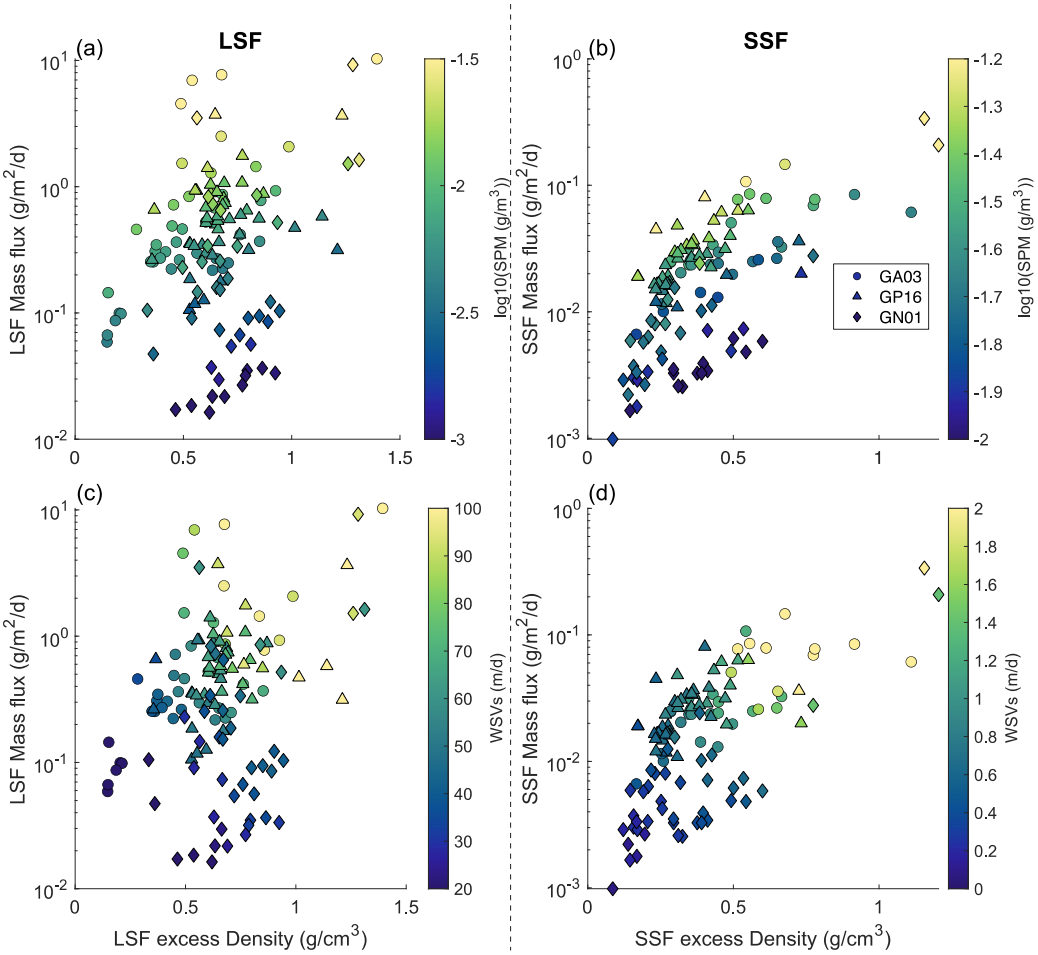

Figure 3.10 Scatter plots between size-fractionated (LSF: left; SSF: right) excess density and mass flux in the upper 100 m of all non-shelf stations (bottom depth>200 m). The color bars are log10(SPM) on the top row (a-b), and mass-weighted average sinking velocity (WSVs) on the second row (c-d). Note that the y axes and color bar for SPM are in logarithmic scale.

Table 3.1 The Contributions from Different Factors to the Variation of Mass Flux (<100 m)

Cruise	Effects	LSF		SSF	
		5-95%ile range (median)	95/5 range ratios	5-95%ile range (median)	95/5 range ratios
GA03	Concentration [unit: g/m^3]	4.1×10^{-3}-6.3×10^{-2} (7.5×10^{-3})	15.5	1.4×10^{-2}-4.7×10^{-2} (2.5×10^{-2})	3.4
	Size [unit: m^2]	2.0×10^{-9}-3.8×10^{-9} (2.4×10^{-9})	1.9	4.9×10^{-11}-9.2×10^{-11} (5.9×10^{-11})	1.9
	Composition [unit: kg/m^3]	1.5×10^{2}-9.5×10^{2} (4.9×10^{2})	6.3	2.5×10^{2}-9.0×10^{2} (4.5×10^{2})	3.5
	Hydrography [unit: m^2/s/kg]	8.1×10^{3}-1.0×10^{4} (9.4×10^{3})	1.3	8.1×10^{3}-1.0×10^{4} (9.4×10^{3})	1.3
GP16	Concentration [unit: g/m^3]	2.6×10^{-3}-2.3×10^{-2} (7.7×10^{-3})	9.1	1.7×10^{-2}-5.9×10^{-2} (2.9×10^{-2})	3.5
	Size [unit: m^2]	1.7×10^{-9}-2.7×10^{-9} (2.2×10^{-9})	1.6	4.1×10^{-11}-6.6×10^{-11} (5.3×10^{-11})	1.6
	Composition [unit: kg/m^3]	4.9×10^{2}-1.2×10^{3} (6.5×10^{2})	2.4	2.1×10^{2}-5.9×10^{2} (3.1×10^{2})	2.8
	Hydrography [unit: m^2/s/kg]	7.7×10^{3}-1.1×10^{4} (9.7×10^{3})	1.4	7.7×10^{3}-1.1×10^{4} (9.7×10^{3})	1.4
GN01	Concentration [unit: g/m^3]	8.7×10^{-4}-3.9×10^{-2} (3.0×10^{-3})	44.8	8.4×10^{-3}-8.6×10^{-2} (1.5×10^{-2})	10.2
	Size [unit: m^2]	1.4×10^{-9}-3.1×10^{-9} (2.0×10^{-9})	2.2	3.3×10^{-11}-7.6×10^{-11} (4.9×10^{-11})	2.3
	Composition [unit: kg/m^3]	4.2×10^{2}-1.3×10^{3} (6.8×10^{2})	3.0	1.3×10^{2}-9.3×10^{2} (2.9×10^{2})	7.0
	Hydrography [unit: m^2/s/kg]	5.0×10^{3}-5.3×10^{3} (5.1×10^{3})	1.1	5.0×10^{3}-5.3×10^{3} (5.1×10^{3})	1.1
Global	Concentration [unit: g/m^3]	9.8×10^{-4}-4.1×10^{-2} (6.5×10^{-3})	42.1	9.3×10^{-3}-5.3×10^{-2} (2.4×10^{-2})	5.7
	Size [unit: m^2]	1.6×10^{-9}-3.2×10^{-9} (2.3×10^{-9})	2.0	3.9×10^{-11}-7.7×10^{-11} (5.5×10^{-11})	2.0
	Composition [unit: kg/m^3]	2.8×10^{2}-1.1×10^{3} (6.5×10^{2})	4.1	1.6×10^{2}-7.7×10^{2} (3.5×10^{2})	4.9
	Hydrography [unit: m^2/s/kg]	5.0×10^{3}-1.1×10^{4} (8.9×10^{3})	2.1	5.0×10^{3}-1.1×10^{4} (8.9×10^{3})	2.1

CONCLUSIONS

The international GEOTRACES program has greatly improved our understanding of dissolved and particulate trace elements and their isotopes (TEIs) in the ocean over the past decade. This dissertation uses published datasets of particles from three recent U.S. GEOTRACES cruises in the North Atlantic (GA03; Lam et al., 2015), Eastern Tropical South Pacific (GP16; Lam et al., 2018), and Western Arctic Ocean (GN01; Xiang & Lam, 2020), and gives novel insights into the role of particle composition in the biological carbon pump and scavenging of particle-reactive elements.

This dissertation generates the first dataset of full-ocean-depth concentration and composition of size-fractionated suspended particles in the Western Arctic Ocean, and offers a baseline for future research to address how ongoing climate change influences marine particle cycling as sea ice melts in the Arctic Ocean. The geochemical determination of particle concentration and composition of field samples is the basis for the major conclusions in this dissertation. The significance of lateral transport in the Western Arctic Ocean is revealed thanks to the marked differences in particle composition between the Chukchi Shelf and Arctic Basin, and between surface and deep oceans, clearly differentiating each of these potential sources (Chapter 1). A diel redox cycle of Mn was concluded based on the relationship between light levels and the particulate Mn average oxidation states that were determined by synchrotron-

based X-ray absorption spectroscopy techniques (Chapter 2). Finally, different particle phases are characterized by varying densities, thereby influencing the sinking velocity according to Stokes' Law. Since vertical mass flux is calculated as the product of the sinking velocity and particle concentration, measuring the distribution of particle composition and concentration is essential for quantifying the sinking flux into the deep ocean in three ocean basins (Chapter 3).

Previous studies have demonstrated the significance of lateral transport of particles in the Western Arctic Ocean using bottom-moored sediment traps (Fahl & Nöthig, 2007; Honjo et al., 2010; Hwang et al., 2008; Hwang et al., 2015). With full ocean-depth particle measurements, this dissertation further suggests that the lateral transport of particles is indeed important throughout the water column from the subsurface to the deep ocean in the Western Arctic Ocean. Compared to the other two cruises in the North Atlantic and Eastern Tropical South Pacific, small particle sizes and viscous water in the Western Arctic Ocean decrease sinking rates of particles and facilitate the lateral transport for longer distances. Additionally, the ubiquitous occurrence of dark brown layers of sedimentary Mn oxides during interglacial times in the Arctic Ocean (e.g., Löwemark et al., 2014; März et al., 2011) suggests an interesting Mn cycle in this basin. This dissertation demonstrates that the Arctic Ocean has high absolute and relative concentrations of Mn oxides throughout the water column due to a shelf source of reductively dissolved Mn, which is then oxidized to Mn oxides in the basin. Likewise, this dissertation also serves as one of the few field studies showing a diel cycle of Mn in the surface ocean (Oldham et al., 2020; Sunda & Huntsman, 1990)

and the first study to give evidence of in-situ Mn oxidation within the cold (~-1 ˚C) Polar Mixed Layer in the Arctic Ocean.

Currently, particle data in the Arctic Ocean are skewed towards the summer season. Particle cycling in the Arctic Ocean in the polar winter with extended darkness and heavy ice cover could be completely different. No measurements of particles, however, exist in the Arctic to test this hypothesis. To achieve a more thorough understanding on marine particle cycling in the Arctic Ocean, future research needs to sample throughout the year to discern the diurnal, seasonal, and annual variability of particle cycling in the Arctic Ocean. New instrumental approaches and autonomous platforms, such as Argo floats equipped with multiple biogeochemical sensors in the Biogeochemical-Argo (BGC-Argo) project (Claustre et al., 2020), could give additional insights into the particle cycling and of particular importance in the Arctic winter where there are few datasets available from traditional oceanographic cruises.

References

Claustre, H., Johnson, K. S., & Takeshita, Y. (2020). Observing the Global Ocean with Biogeochemical-Argo. *Annual Review of Marine Science*, *12*(1), 23-48. https://doi.org/10.1146/annurev-marine-010419-010956

Fahl, K., & Nöthig, E. M. (2007). Lithogenic and biogenic particle fluxes on the Lomonosov Ridge (central Arctic Ocean) and their relevance for sediment accumulation: Vertical vs. lateral transport. *Deep Sea Research Part I: Oceanographic Research Papers*, *54*(8), 1256-1272. https://doi.org/10.1016/j.dsr.2007.04.014

Honjo, S., Krishfield, R. A., Eglinton, T. I., Manganini, S. J., Kemp, J. N., Doherty, K., et al. (2010). Biological pump processes in the cryopelagic and hemipelagic Arctic Ocean: Canada Basin and Chukchi Rise. *Progress in Oceanography*, *85*(3-4), 137-170. https://doi.org/10.1016/j.pocean.2010.02.009

Hwang, J., Eglinton, T. I., Krishfield, R. A., Manganini, S. J., & Honjo, S. (2008). Lateral organic carbon supply to the deep Canada Basin. *Geophysical Research Letters*, *35*(11). https://doi.org/10.1029/2008gl034271

Hwang, J., Kim, M., Manganini, S. J., McIntyre, C. P., Haghipour, N., Park, J., et al. (2015). Temporal and spatial variability of particle transport in the deep Arctic Canada Basin. *Journal of Geophysical Research: Oceans*, *120*(4), 2784-2799. https://doi.org/10.1002/2014jc010643

Lam, P. J., Lee, J. M., Heller, M. I., Mehic, S., Xiang, Y., & Bates, N. R. (2018). Size-fractionated distributions of suspended particle concentration and major phase composition from the US GEOTRACES Eastern Pacific Zonal Transect (GP16). *Marine Chemistry*, *201*, 90-107. https://doi.org/10.1016/j.marchem.2017.08.013

Lam, P. J., Ohnemus, D. C., & Auro, M. E. (2015). Size-fractionated major particle composition and concentrations from the US GEOTRACES North Atlantic Zonal Transect. *Deep Sea Research Part II: Topical Studies in Oceanography*, *116*, 303-320. https://doi.org/10.1016/j.dsr2.2014.11.020

Löwemark, L., März, C., O'Regan, M., & Gyllencreutz, R. (2014). Arctic Ocean Mn-stratigraphy: genesis, synthesis and inter-basin correlation. *Quaternary Science Reviews*, *92*, 97-111. https://doi.org/10.1016/j.quascirev.2013.11.018

März, C., Stratmann, A., Matthiessen, J., Meinhardt, A. K., Eckert, S., Schnetger, B., et al. (2011). Manganese-rich brown layers in Arctic Ocean sediments: Composition, formation mechanisms, and diagenetic overprint. *Geochimica et Cosmochimica Acta*, *75*(23), 7668-7687. https://doi.org/10.1016/j.gca.2011.09.046

Oldham, V. E., Lamborg, C. H., & Hansel, C. M. (2020). The spatial and temporal variability of Mn speciation in the coastal Northwest Atlantic Ocean. *Journal of Geophysical Research: Oceans*, *125*(1), e2019JC015167. https://doi.org/10.1029/2019JC015167

Sunda, W. G., & Huntsman, S. A. (1990). Diel cycles in microbial manganese oxidation and manganese redox speciation in coastal waters of the Bahama Islands. *Limnology and Oceanography*, *35*(2), 325-338. https://doi.org/10.4319/lo.1990.35.2.0325

Xiang, Y., & Lam, P. J. (2020). Size-fractionated compositions of marine suspended particles in the Western Arctic Ocean: Lateral and vertical sources. *Journal of Geophysical Research: Oceans*, *125*(8), e2020JC016144. https://doi.org/10.1029/2020JC016144

APPENDIX 1: SUPPORTING INFORMATION FOR CHAPTER 1

Methods

- Particle sampling

At most of the stations, two casts of 8 pumps each and two filter holders per pump were deployed to collect samples at 16 depths throughout the water column. At super stations, a 24-depth profile was obtained with three casts. The targeted depths of the wire-out were verified by a self-recording Seabird 19plus CTD at the end of the line and an RBR pressure logger attached to the pump at the middle of the line. The RBR was used for all casts in the entire cruise whereas the CTD was only deployed in the northbound leg due to electronic problems. 142 mm-diameter "mini-MULVFS" style filter holders, with multiple stages and baffle systems designed to prevent large particle loss and promote even particle distribution (Bishop et al., 2012), were used. One filter holder/flowpath was loaded with a Sefar polyester mesh prefilter (51 μm pore size) and paired Whatman QMA quartz fiber filters (1 μm pore size) in series ("QMA-side"). The other filter holder/flowpath was also loaded with a 51 μm prefilter, but it was followed by paired 0.8 μm Pall Supor800 polyethersulfone filters ("Supor-side"). A 150 μm Sefar polyester mesh was placed underneath all 51 μm prefilters and QMA filters as a support to facilitate filter handling. All filters and filter holders were acid leached before use based on the recommended methods in the GEOTRACES sample and sample-handling protocols (Cutter et al., 2010). QMA filters were pre-combusted at 450 ˚C for 4 hours after acid leaching.

For LSF particulate organic carbon (POC), the entire >51 μm prefilter from the Supor side was rinsed using 0.2 μm-filtered seawater onto a 25 mm 1 μm Ag filter for later analysis (Black et al., 2018). All other LSF parameters were measured from the QMA-side prefilter, including LSF biogenic silica (bSi), particulate inorganic carbon (PIC) and particulate trace metals (pTM). LSF bSi and PIC were measured directly from the prefilter subsamples, whereas LSF trace metals were analyzed on particles rinsed from 1/8 of the prefilter using trace-metal clean 0.2 μm-filtered surface seawater onto a 25 mm 0.8 μm Supor filter because of relatively high trace metal blanks in prefilters (Planquette & Sherrell, 2012). SSF POC and PIC were measured from the QMA filter; SSF bSi and lithogenic particles were measured from subsamples of the Supor filter.

- Particle composition

i. Particulate organic carbon (POC) and particulate nitrogen (PN)

POC and PN sample processing was similar to what was described in Lam et al. (2018). Samples were fumed in a desiccator with concentrated HCl and dried in the oven at 60 ˚C overnight, and then pelletized with tin discs. Tin disc encapsulated samples, from either one 25 mm-diameter punch from the top SSF QMA filters or the entire LSF silver filters, were measured using a CE Instruments NC 2500 model Carbon/Nitrogen Analyzer interfaced to a ThermoFinnigan Delta Plus XP isotope ratio mass spectrometer (IRMS) at the Stable Isotope Laboratory at University of California, Santa Cruz. Isotopic results obtained from the IRMS were calibrated using reference

materials Acetanilide (C_8H_9NO). The effect of dissolved organic carbon sorption is corrected with isotopic values of dipped blanks. The isotopic data are expressed in the standard delta notation (δ) as per mil deviations (‰) with respect to international standards of Pee Dee Belemnite (PDB) and atmospheric nitrogen. The precision of the internal standard (Pugel) analyzed along with the samples in the run is 0.07‰ for $\delta^{13}C$ and 0.14‰ for $\delta^{15}N$.

Particulate organic matter (POM) was calculated from POC by multiplying a weight ratio of 1.88 g POM/g POC (Lam et al., 2011; Lam et al., 2018; Lam et al., 2015), determined by Nuclear Magnetic Resonance (NMR) measurements of the phytoplankton biochemical composition (Hedges et al., 2002).

$$\text{POM}\left[\frac{\mu g}{L}\right] = \text{POC}\,[\mu M] \times 12\left[\frac{\mu g\ \text{POC}}{\mu mol\ \text{POC}}\right] \times 1.88\,[\frac{g\ \text{POM}}{g\ \text{POC}}]$$

ii. Particulate inorganic carbon (PIC)

A UIC Carbon dioxide coulometer was used for PIC measurement. Briefly, PIC on SSF QMA punches or 1/16 LSF QMA-side prefilter was converted to CO_2 by addition of 2 N sulfuric acid. CO_2 produced is carried by a gas stream into a coulometer cell where CO_2 is quantitatively absorbed by a cathode solution, reacted to form a titratable acid and measured based on the change in current. The mass concentration of $CaCO_3$ was calculated from PIC using a constant weight ratio:

$$CaCO_3\left[\frac{\mu g}{L}\right] = \text{PIC}\,[\mu M] \times 100.08\left[\frac{\mu g\ CaCO_3}{\mu mol\ \text{PIC}}\right]$$

iii. Biogenic silica (bSi)

An alkaline leach with 0.2 M NaOH at 85˚C was used to leach bSi for both size fractions prior to the measurement on a Lachat QuikChem 8000 Flow Injection Analyzer at UCSC. A 4-h time-series leaching approach was applied to all samples below 500 m to take into account the contribution from lithogenic Si (Lam et al., 2018), where lithogenic Si was of significance in the overall measurement. The intercept of all points in the time series was calculated with linear regression and used to best represent the bSi concentrations, assuming bSi is completely dissolved in 1 hour, and lithogenic Si is dissolved at a constant rate during the leach (Barão et al., 2015; DeMaster, 1981).

A hydrated form of silica as $SiO_2 \cdot (0.4\ H_2O)$ was assumed in order to calculate the mass concentrations of opal (Mortlock & Froelich, 1989):

$$\text{Opal}\ \left[\frac{\mu g}{L}\right] = \text{bSi}\ [\mu M] \times 67.2\ \left[\frac{\mu g\ \text{opal}}{\mu mol\ \text{bSi}}\right]$$

iv. Particulate trace metals (pTM)

The digestion method of pTM is based on a refluxing method (Cullen & Sherrell, 1999; Planquette & Sherrell, 2012) with light modifications similar to the “Piranha method” in Ohnemus et al. (2014). In brief, the Supor filter was adhered to the wall by surface tension in a 15 mL flat-bottom screw-cap Savillex vial to avoid immersion. After 4-h refluxing at 110 ˚C with an ultrapure (ARISTAR® or Optima^{TM} grade) 50% HNO_3/10% HF (v/v) mixture, digestion acids were transferred into secondary vials and

heated to near dryness. The residue was heated in 50% HNO_3/15% H_2O_2 (v/v) to dryness at 110 ˚C. The final residue was re-dissolved with 2 ml 5% HNO_3 spiked with 1 ppb In. Two certified reference materials (BCR-414 and PACS-2) were digested routinely alongside the samples to assure the quality of each digestion. Sample solutions were analyzed using an Element XR high-resolution ICP-MS (Thermo Scientific) at the UCSC Plasma Analytical Facility. Mean recoveries of all measured trace metals for BCR-414 and PACS-2 are 116% and 96%, respectively (Appendix 1.8). Pump samples were also exchanged with GO-FLO particle group and differences found to be within 5% for Fe and Mn.

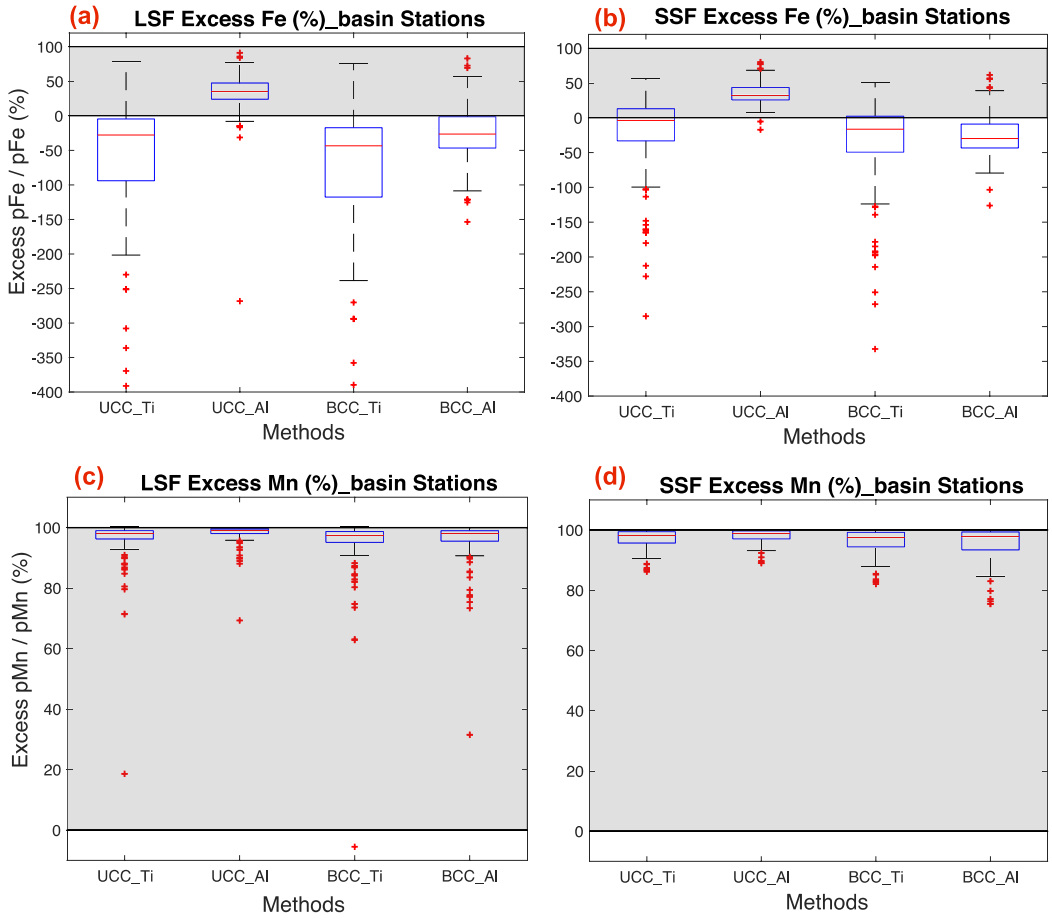

Appendix 1.1 Box plots of the fraction of excess Fe (top) and Mn (bottom) at all basin stations. (a) LSF (>51 µm) excess Fe (%); (b) SSF (1-51 µm) excess Fe (%); (c) LSF excess Mn (%); (d) SSF excess Mn (%). The X axis illustrates four different methods, a combination between UCC and BCC, and Ti and Al, to calculate the excess Fe and Mn. Note that areas of 0 to 100% are highlighted in grey. The red segment inside the rectangle indicates the median and whiskers above and below the box show values of the minimum and maximum. Outliers are shown with red plus signs.

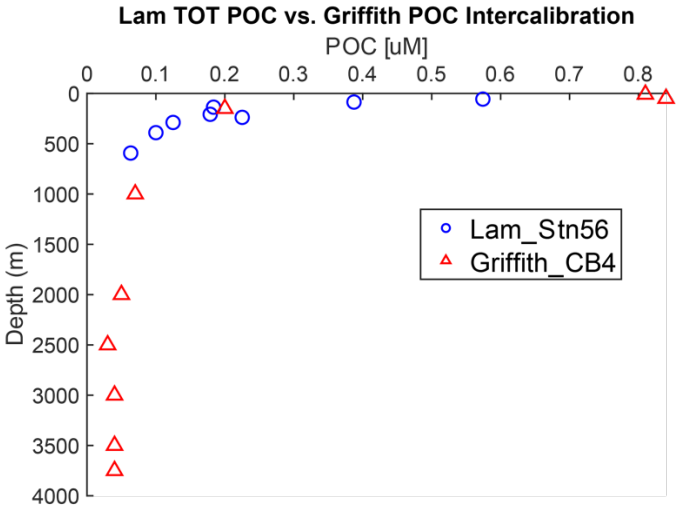

Appendix 1.2 Intercalibration of suspended POC concentrations (unit: μM) between this study and Griffith et al. (2012) at the same location in the Canada Basin (75˚N, 150˚W). Both POC samples were collected by in-situ pumps and total particles (>1 μm) are defined as the sum of the two size fractions (TOT= LSF+ SSF). Note that there was no size fractionation in Griffith et al. (2012), and samples were collected with GF/F filters (pore size: 0.7 μm).

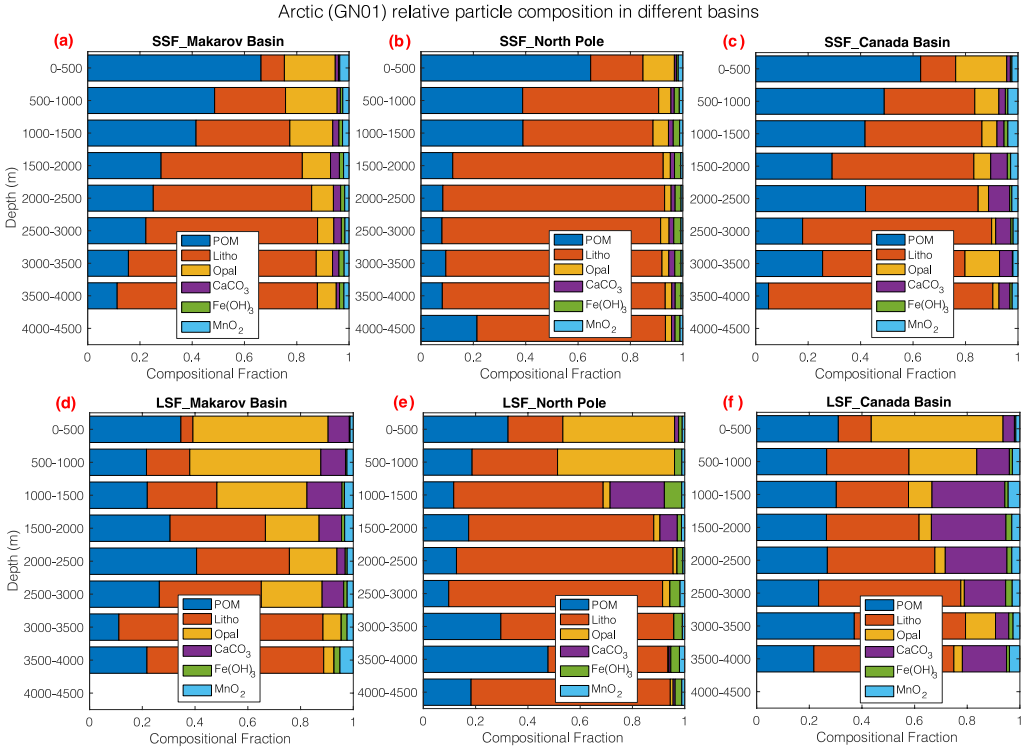

Appendix 1.3 Stacked bar graphs of size-fractionated relative particle composition in the (a, d) Makarov (N= 4 stations), (b, e) Amundsen (North Pole Station 32), and (c, f) Canada (N= 5 stations) basins of the Arctic. a-c and d-f are relative particle composition data from SSF and LSF, respectively. Each bin in a-f shows the mean fraction of each particle phase for all samples in the 500 m depth bin of the specified basin. Different colors represent different particle composition.

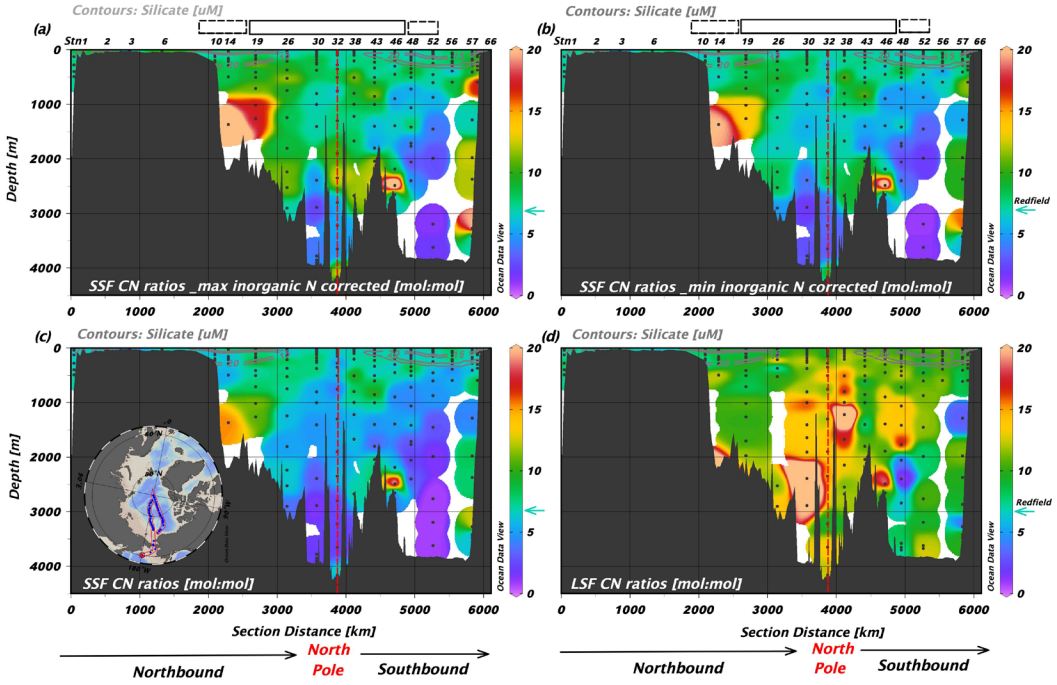

Appendix 1.4 Section plots of POC/PN ratios (mol/mol) in both SSF and LSF in the whole water column. (a) SSF C/N ratios corrected for 63% inorganic nitrogen; (b) SSF C/N ratios corrected for 34% inorganic nitrogen; (c) SSF C/N ratios without any correction; (d) LSF C/N ratios without any correction. Color bars are set the same for all, ranging from 0 to 20.

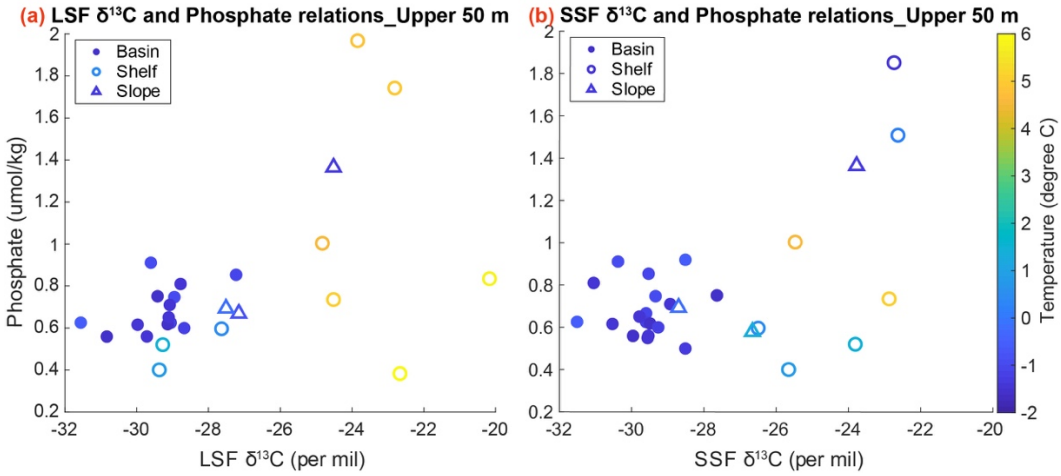

Appendix 1.5 Scatter plots of POC-$\delta^{13}C$ (unit: ‰) against nutrient concentrations (phosphate; µmol/kg) in the upper 50 m from all stations with symbols color-coded by temperature. (a) LSF POC-$\delta^{13}C$ vs. phosphate; (b) SSF POC-$\delta^{13}C$ vs. phosphate. Basin, shelf, and slope stations are drawn with filled dots, empty dots, and empty triangles, respectively. Note that no $\delta^{13}C$ data are available at station 6 in the SSF and data from station 1 in the Bering Sea are excluded.

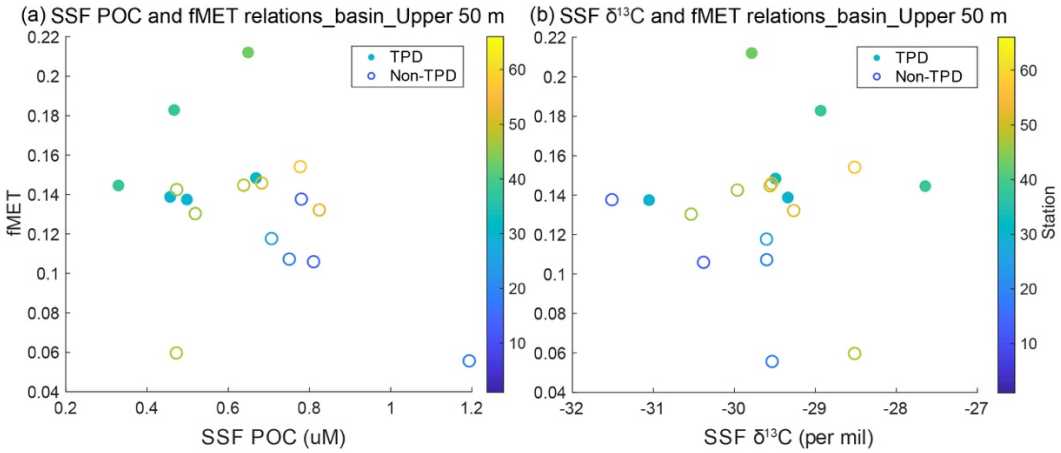

Appendix 1.6 Scatter plots of (a) SSF POC concentrations (µM) and (b) POC-$\delta^{13}C$ (‰) against the fraction of meteoric water (fMET) in the upper 50 m from basin stations (Stations 14-57) only. Stations within (Stations 30, 32, 38 & 43) and outside the transpolar drift (TPD) are plotted as filled and open circles, respectively, and the color bar indicates station number. No significant fits are found in all data.

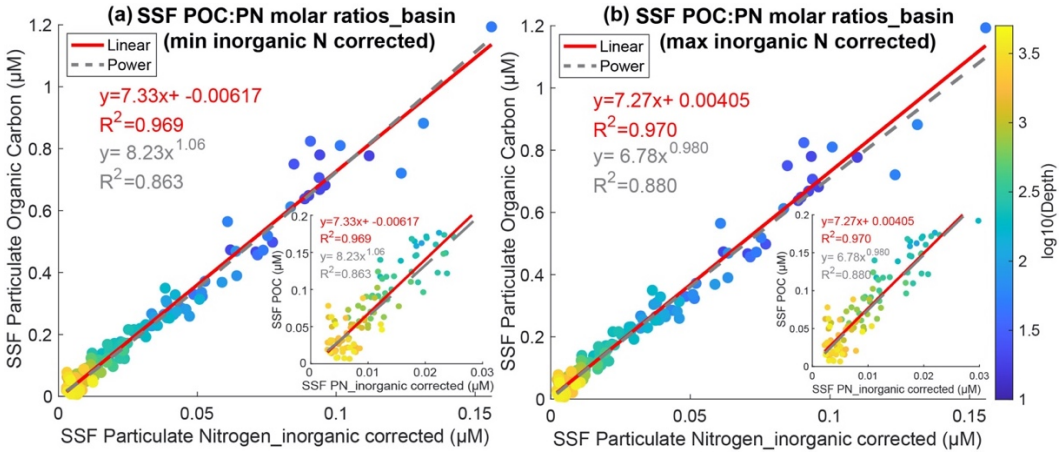

Appendix 1.7 Correlations between SSF POC and inorganic nitrogen corrected PN in the basin stations in SSF are shown with units all in μM. (a) correction based on 34% of inorganic nitrogen adsorbed (the minimum correction); (b) correction based on 63% of inorganic nitrogen adsorbed (the maximum correction). All data points are color-coded with log base 10 of the sampling depth (unit: m). The reduced major axis (Model II) and power-law fit are used in the regression. Red solid and grey dashed lines are fitted with all data in the basin. Expanded plots at low concentrations are plotted separately in the bottom right. Regression equations are displayed with colors matching with fit lines.

Appendix 1.8 Recoveries of the two certified reference materials (CRMs), BCR-414 and PACS-2, from all digestions. N/A indicate elements for which a certified number is not available. Recoveries are shown in percentage relative to certified values or informational values. Uncertainties for all recovered values are ±1 standard deviation, if available. Note that measured Ti recoveries in BCR-414 (*) are quite different from 100%, but they agree well with those previously reported by Ohnemus et al. (2014), indicating a possible error in the informational value. Note that the mean relative recovery for BCR-414 was calculated excluding Ti.

	BCR-414	PACS-2
	relative recovery (%)	relative recovery (%)
Ag	N/A	106 ± 20
Al	123 ± 12	94 ± 7
Ba	129 ± 9	120 ± 9
Cd	111 ± 14	97 ± 11
Co	115 ± 9	92 ± 7
Cu	113 ± 9	95 ± 7
Fe	111 ±10	86 ± 6
Mn	105 ± 11	90 ± 6
Mo	131 ± 10	86 ± 9
Nd	N/A	104 ± 9
Ni	118 ± 11	91 ± 10
P	96 ± 10	102 ± 11
Pb	108 ± 13	89 ± 7
Sc	116 ± 10	96 ± 7
Ti	298 ± 26*	85 ± 7
V	130 ± 11	96 ± 8
Y	N/A	91 ± 7
Zn	118 ± 12	100 ± 9
Mean	116	96

Appendix 1.9 The median and standard deviation (std) of SSF dipped blanks (db), and the percent of SSF samples that fell below the detection limit (DL). The median of shelf/slope and basin db are used in the blank subtraction for particulate trace metals (pTM). For other particle composition calculations, the median and standard deviation of SSF db at all stations are used. The DL was defined as three times the standard deviation of the dipped blanks.

	unit for median and std	Small size fraction (SSF)				
		median db (shelf)	median db (basin)	std db (shelf)	std db (basin)	% below detection limit (overall)
Al	pmol	24656.55	3410.31	58529.76	11942.66	6.99%
Fe	pmol	21526.05	2397.48	12157.44	1465.20	0.44%
Mn	pmol	1677.40	542.08	2987.74	304.02	1.31%
PIC	nmol C	593.36		350.30		22.32%
bSi	nmol Si	152.62		89.34		3.29%
POC	umol C	41.48		15.59		8.58%
PN	umol N	8.92		4.10		14.16%
POC-$\delta^{13}C$	permil	-29.73		2.21		N/A

Appendix 1.10 Same as Appendix 1.9 but for the large size fraction (LSF).

	unit for median and std	Large size fraction (LSF)				
		median db (shelf)	median db (basin)	std db (shelf)	std db (basin)	% below detection limit (overall)
Al	pmol	122151.01	15851.32	88822.49	14500.79	6.11%
Fe	pmol	27430.94	5482.84	22397.50	5425.49	9.17%
Mn	pmol	963.84	380.23	937.32	443.13	2.18%
PIC	nmol C	927.88		591.22		53.91%
bSi	nmol Si	228.56		264.7		26.89%
POC	umol C	2.17		0.61		3.00%
PN	umol N	0.20		0.089		13.30%
POC-$\delta^{13}C$	permil	-22.50		0.83		N/A

APPENDIX 2: SUPPORTING INFORMATION FOR CHAPTER 2

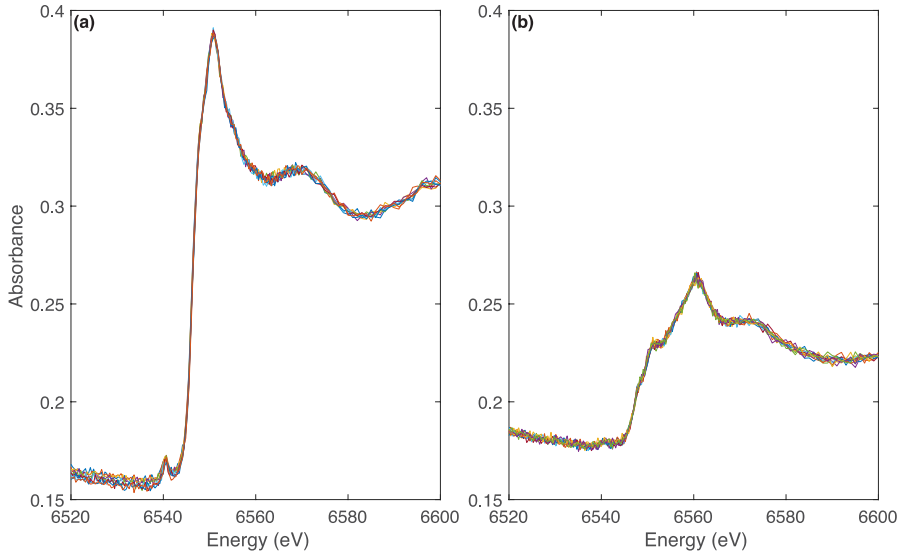

Appendix 2.1 Raw Mn spectra of (a) one reduced pMn sample at Station 19 (9 scans over 1.5 hours) and (b) one oxidized sample at Station 48 (12 scans over 2 hours). No obvious energy shifts were observed in either sample over the course of the analyses, indicating no clear X-ray beam-induced photoreduction.

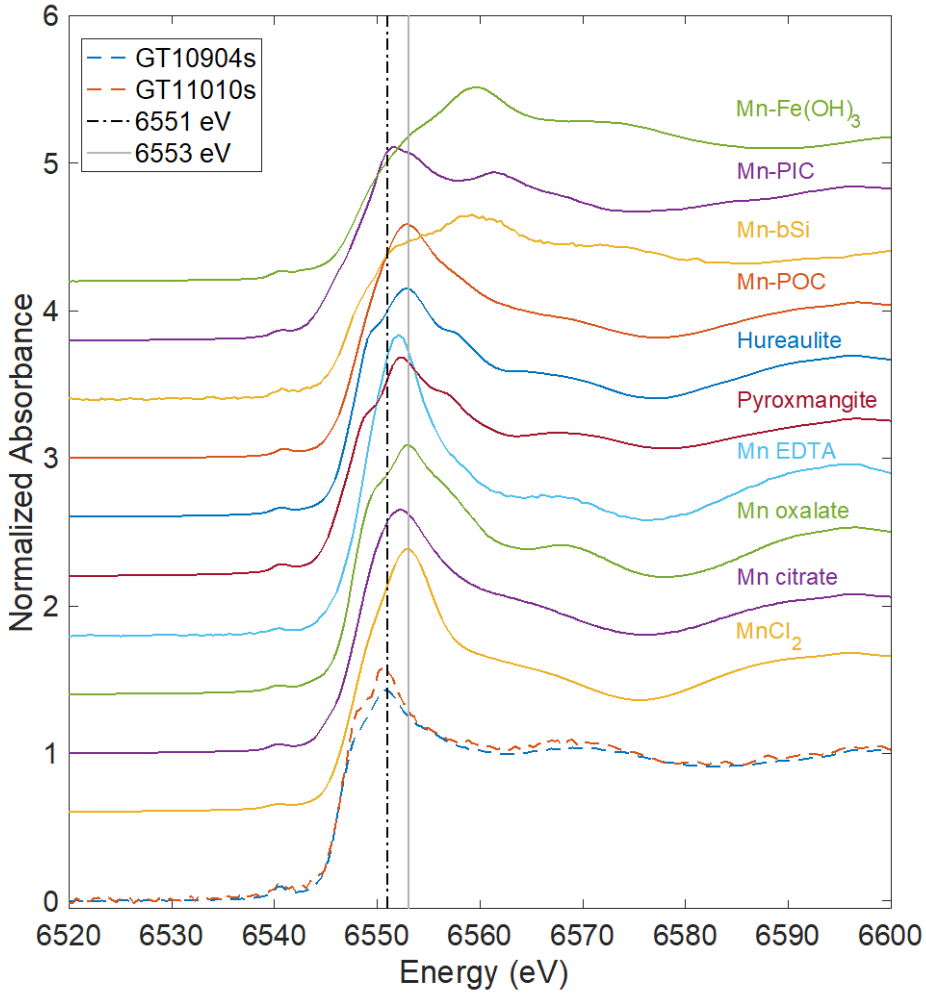

Appendix 2.2 XANES spectra of the two most reduced surface samples, GT11010s at Station 26 and GT10904s at Station 19 (spectra with dashed lines), and six Mn(II) mineral references and four $MnCl_2$ adsorption standards (spectra with solid lines). Mn(II) references plotted include inorganic Mn ($MnCl_2$), organically bound Mn (Mn-citrate, -oxalate, and -EDTA), Mn silicates (Pyroxmangite), and Mn phosphates (Hureaulite). Mn-citrate and -oxalate spectra were obtained at the Australian Synchrotron (Blamey et al., 2018). We applied +1 eV energy shift observed in hausmannite ($Mn^{II}Mn^{III}{}_2O_4$) XANES spectrum to correct for the energy difference between SSRL and the Australian Synchrotron. Mn EDTA was measured at the Brazilian Synchrotron Light Laboratory (LNLS) (Machado et al., 2019). No obvious energy offset was observed between SSRL and LNLS based on Mn foil standards. Sorbed Mn standards we made and ran at Beamline 11-2 at SSRL include four major particle phases, particulate organic carbon (POC), biogenic silica (bSi), particulate inorganic carbon (PIC), and ferrihydrite (Lee et al., 2021). Vertical black dash-dot and grey solid lines at 6551 eV and 6553 eV, respectively, for reference.

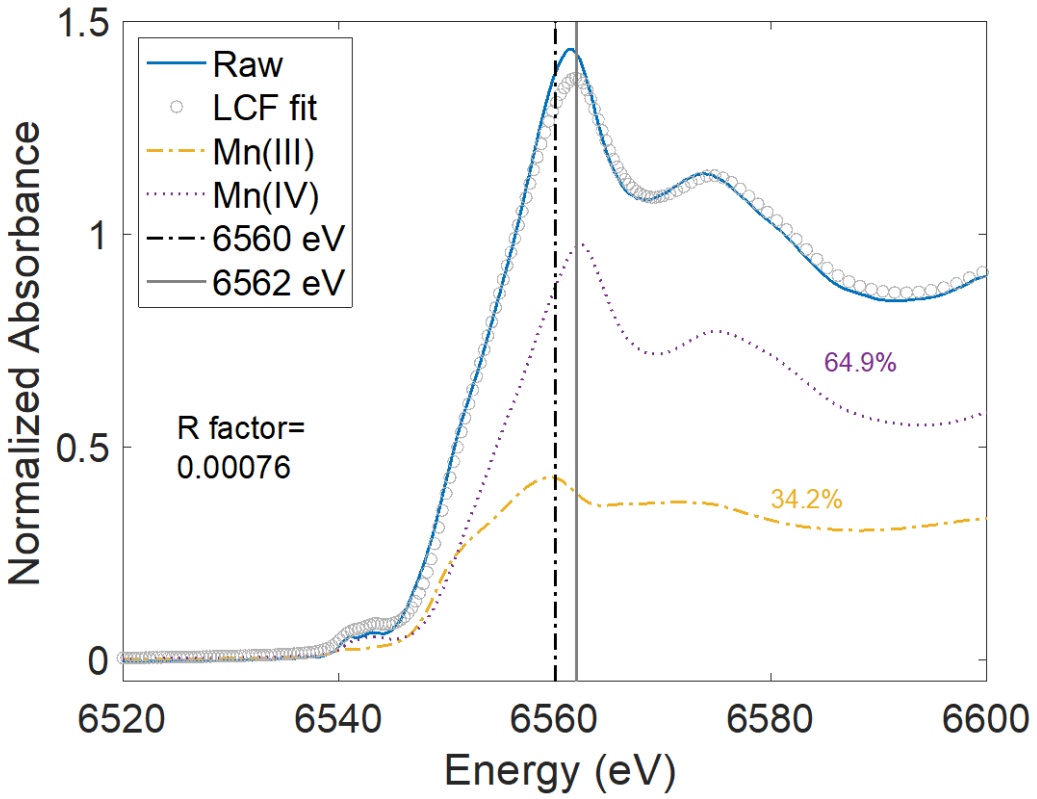

Appendix 2.3 Linear combination fit for the most oxidized sample GT10800s in the halocline at Station 14 using Mn(III) (feitknechtite), and Mn(IV) (δ-MnO_2) as Mn references. The fit fractions for different references and R factor for the fit are displayed. Vertical black dash-dot and grey solid lines at 6560 eV and 6562 eV, respectively, for reference.

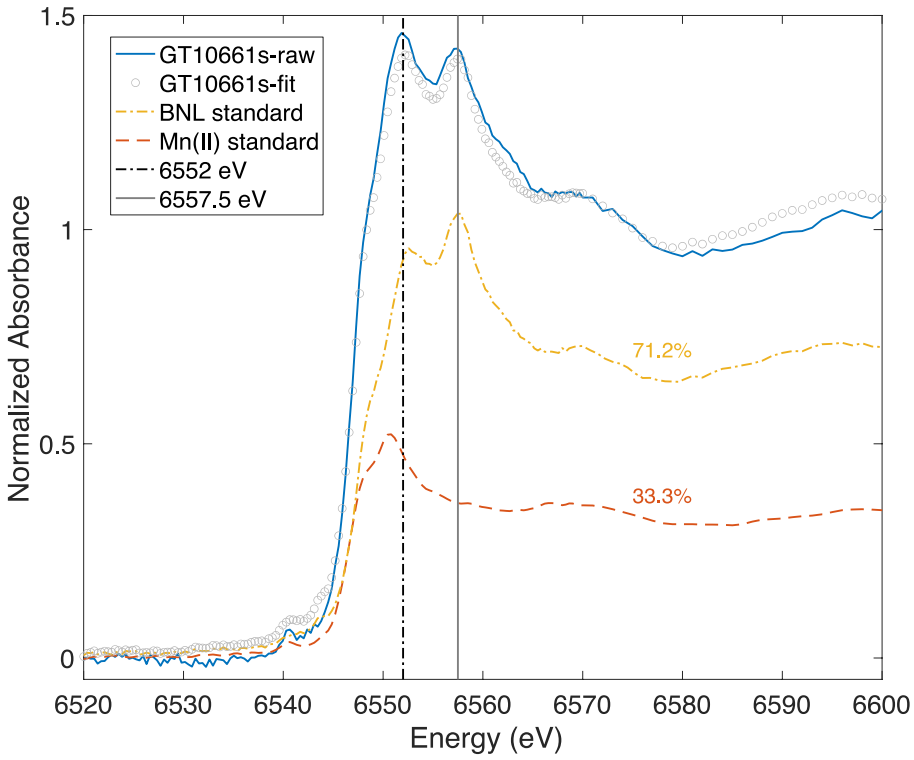

Appendix 2.4 Linear combination fit (LCF) for surface sample GT10661s at Station 6 with the benthic nepheloid layer (BNL) sample (GT12276s), Mn(II) (GT11010s), Mn(III) (feitknechtite), and Mn(IV) (δ-MnO2) references in the LCF. The fraction of the BNL reference (assumed to be Mn silicates) in the fit is 71.20% (68.11% if normalized to 1), and Mn(II) (GT11010s) is 33.34% (31.89% if normalized to 1). The fractions of feitknechtite and δ-MnO_2 are negligible. The R factor is 0.0014. Vertical black dash-dot and grey solid lines at 6552 eV and 6557.5 eV, respectively, for reference.

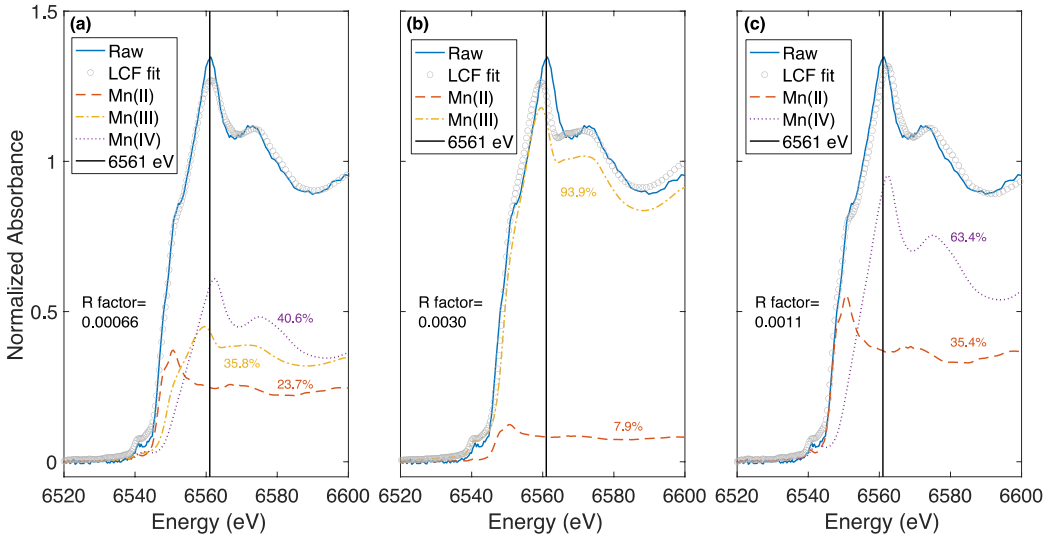

Appendix 2.5 Linear combination fit for oxidized sample GT12240s at Station 60 with (a) Mn(II) (GT11010s), Mn(III) (feitknechtite), and Mn(IV) (δ-MnO_2) references, (b) GT11010s and feitknechtite only, and (c) GT11010s and δ-MnO_2 only in the fit. The fractions for different references (not normalized to 1) and R factor for the fit are displayed in each subplot. Better fits are characterized by smaller R factors. Vertical black solid lines at 6561 eV for reference.

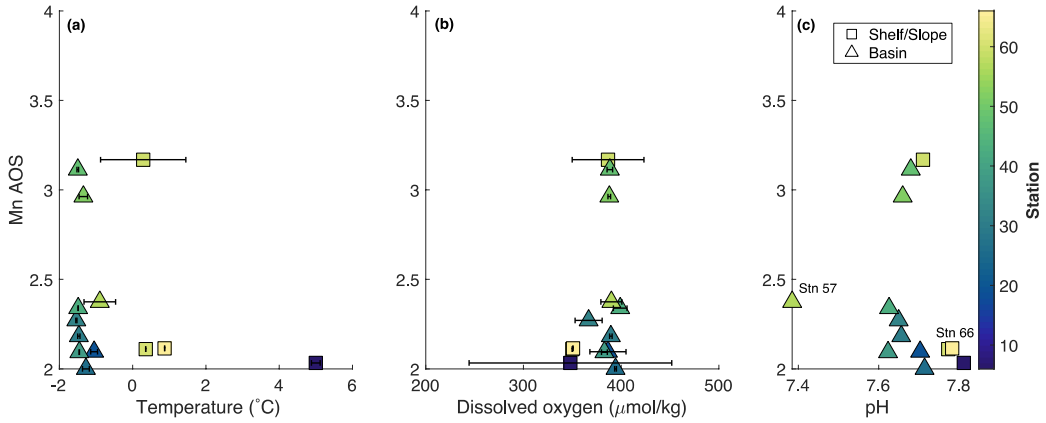

Appendix 2.6 Scatter plots between Mn Average Oxidation State (AOS) from pumps and hydrographic parameters (a) Temperature (˚C); (b) dissolved oxygen (μmol/kg); (c) pH from the CTD rosette at pressure = 20 decibars. Mn AOS were determined on particles collected from pump casts. Temperature and oxygen were collected from sensors mounted on the ODF CTD rosette and are plotted as the mean (marker) and standard deviation (error bars) of all CTD casts (N=1-7) from that station; pH was

determined from discrete samples from one of the ODF CTD casts (Woosley et al., 2017) and linearly interpolated to 20 decibars. The multiple ODF CTD casts at each station generally spanned a similar range of light conditions as experienced by pump casts, so the mean and range should be a good indication of temperature and dissolved oxygen during particle sampling. Measurements of pH were only made from one ODF CTD cast, but this was fortuitously frequently at similar light conditions as the pump cast, except for stations 57 and 66, when the pH data were from nighttime and the pump casts were during the day. The lowest pH observed at 20 decibars is from Station 57 (7.38), but it may not indicate strong remineralization in-situ at night, since the pH values measured at night in the surface of more productive slope Station 60 and shelf Station 66 are both higher than 7.65. Such low pH values can be reached within the strong benthic nepheloid layer (BNL) at shelf Station 61. Likely, the large pH difference between Station 57 and other basin station is due to lateral transport of a low pH water mass from the shelf BNL to Station 57.

Appendix 2.7 Mn mineral references in the current library (N=18).

Reference name	Formula
Mn(II) oxide	$Mn^{II}O$
Mn(II) sulfide	$Mn^{II}S$
Hureaulite	$Mn^{II}_5(PO_3OH)_2(PO_4)_2 \cdot 4H_2O$
Pyroxmangite	$Mn^{II}SiO_3$
Chalcophanite_CH	$ZnMn^{IV}_3O_7 \cdot 3H_2O$
δ-MnO_2_CH	δ-$Mn^{IV}O_2$
Feitknechtite_CH	$Mn^{III}O(OH)$
GT11010s-Mn(II)	Unknown Mn(II) phases
Hausmannite_CH	$Mn^{II}Mn^{III}_2O_4$
Manganese chloride_CH	$Mn^{II}Cl_2$
Mn foil_CH	Mn^0
Mn citrate_PK	Mn(II)-citrate
Mn oxalate_PK	Mn(II)-oxalate
Mn EDTA_HC	Mn(II)-EDTA
DBK1 spessartine_22_24_fl_JJ	$Mn^{II}_3Al_2(SiO_4)_3$
Hotazel_Braunite_009_fl_JJ	$Mn^{II}Mn^{III}_6(SiO_4)O_8$
PiemontiteGRR_039_fl_JJ	$\{Ca_2\}\{Al_2Mn^{III}\}(Si_2O_7)(SiO_4)O(OH)$
PiemontitieGRR_2_040_fl_JJ	$\{Ca_2\}\{Al_2Mn^{III}\}(Si_2O_7)(SiO_4)O(OH)$

Appendix 2.8 Summary of white line positions for Mn superoxide dismutase (SOD), adsorbed, inorganic and organically-bound Mn XANES reference spectra. No references were found with a white line as low as observed for GT11010s.

Name	White line position	Sources
GT11010s (the most reduced surface sample)	6551 eV	This study
Mn adsorption standard (particulate inorganic carbon)	6552 eV	Lee et al. (2021)
Pyroxmangite	6552 eV	Lee et al. (2021)
Mn(II) citrate_PK	6552 eV	Blamey et al. (2018)
Mn(II) EDTA_HC	6552 eV	Machado et al. (2019)
Mn adsorption standard (particulate organic carbon)	6553 eV	Lee et al. (2021)
Hureaulite	6553 eV	Lee et al. (2021)
$MnCl_2$_CH	6553 eV	Learman et al. (2011)
Mn(II) oxalate_PK	6553 eV	Blamey et al. (2018)
Mn(II)-Siderophores	6553 eV	Harrington et al. (2012)
Mn-SOD	6554 eV	Gunter et al. (2006)
Mn adsorption standard (biogenic silica)	6559 eV	Lee et al. (2021)
Mn adsorption standard (ferrihydrite)	6560 eV	Lee et al. (2021)

APPENDIX 3: SUPPORTING INFORMATION FOR CHAPTER 3

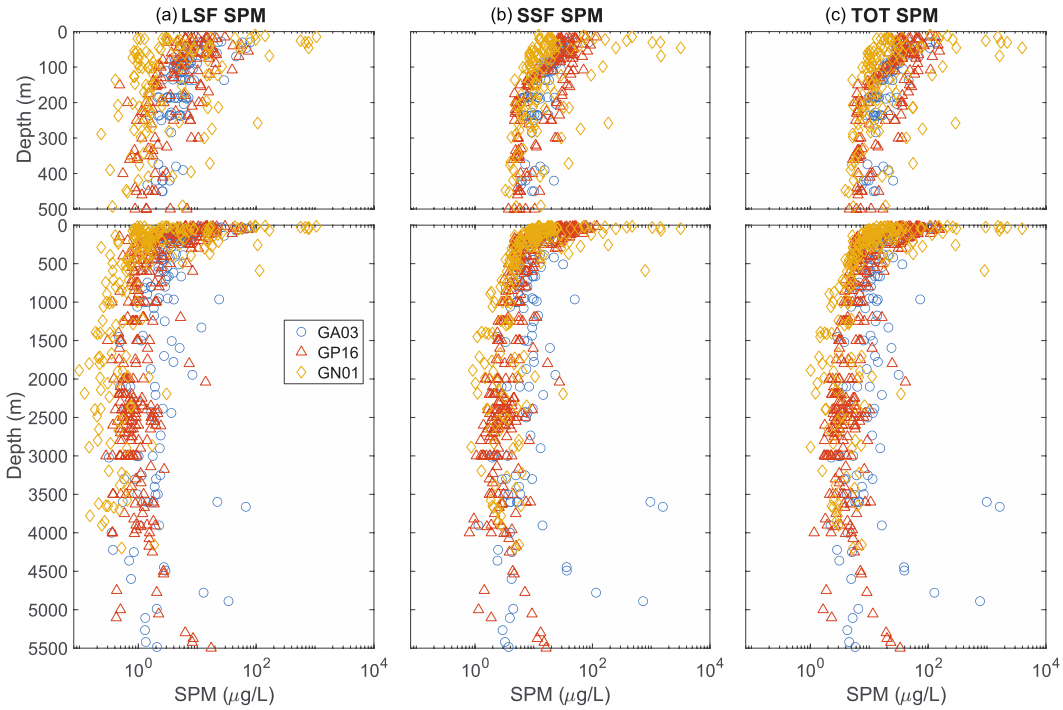

Appendix 3.1 Depth profiles of size-fractionated SPM concentrations (unit: μg/L) in the upper 500 m (top panels) and the whole water column (bottom panels) in all three basins. (a): LSF (>51 μm); (b): SSF (1-51 μm); (c): TOT (>1 μm).

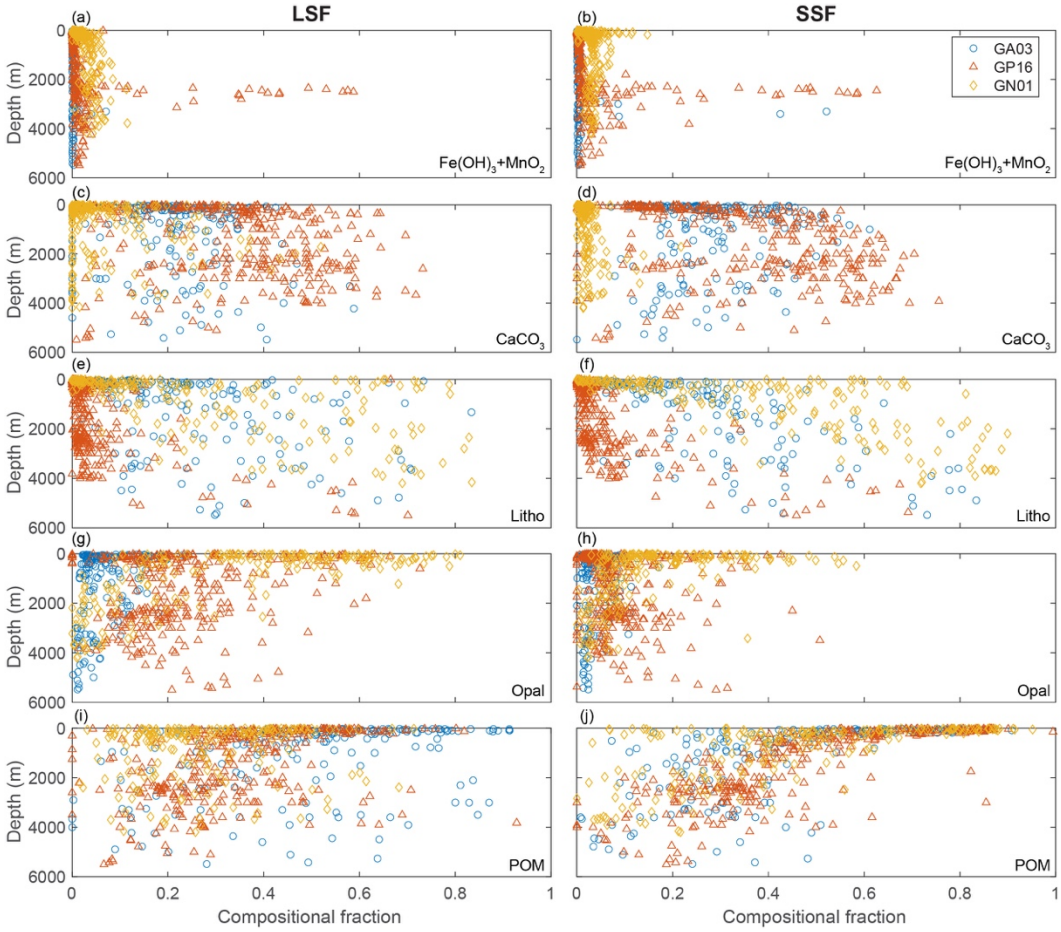

Appendix 3.2 Depth profiles of size-fractionated compositional fractions in the LSF (left panels) and SSF (right panels) in all three basins. (a)-(b): the sum of fractions of iron and manganese (oxyhydr)oxides ($Fe(OH)_3 + MnO_2$); (c)-(d): the fractions of calcium carbonate ($CaCO_3$); (e)-(f): the fractions of lithogenic materials (Litho); (g)-(h): the fraction of opal; (i)-(j): the fraction of particulate organic matter (POM).

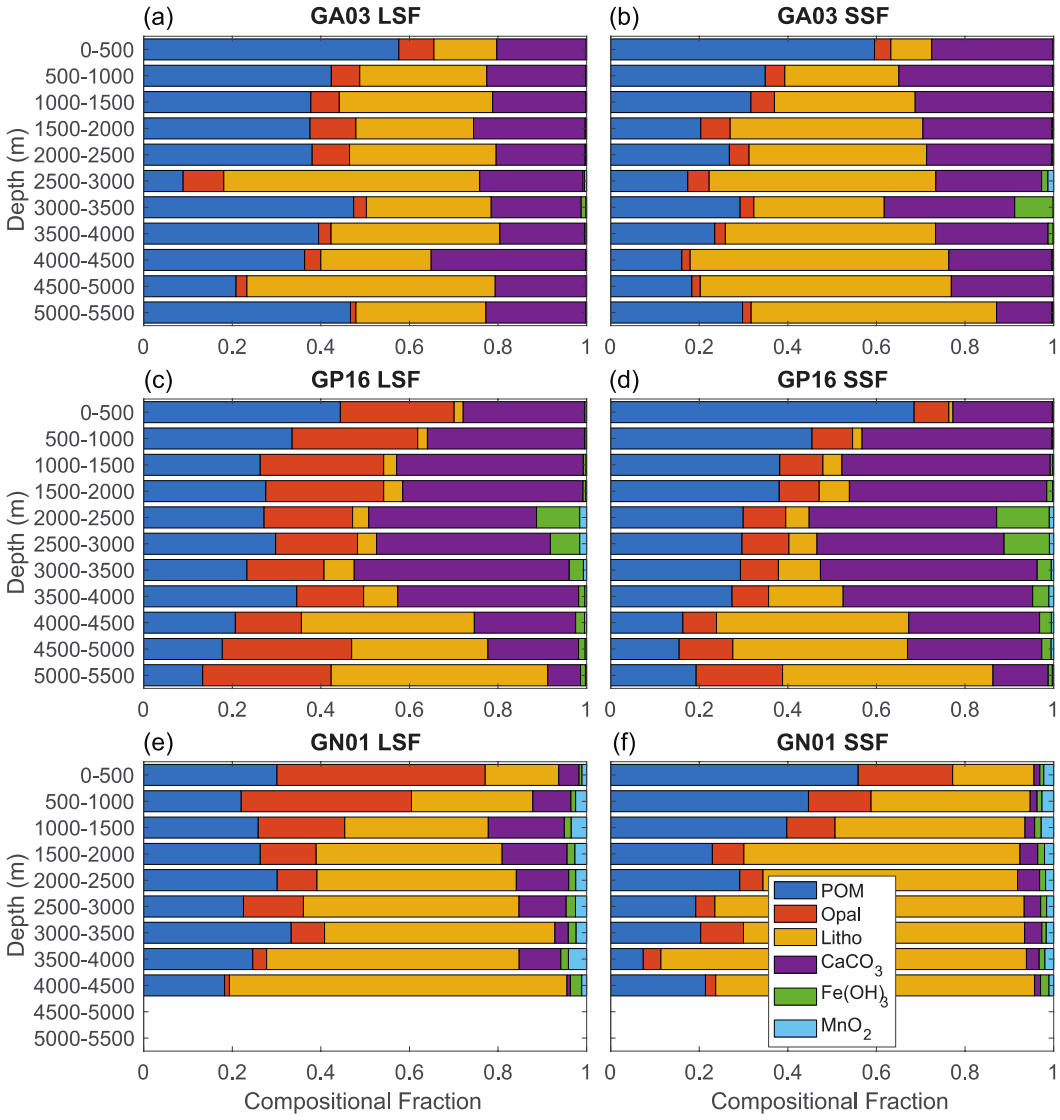

Appendix 3.3 Stacked bar graphs of the change in size-fractionated compositional fractions in all cruises with depth. The left panels are the LSF and right panels are the SSF. Each 500 m depth bin shows the mean compositional fraction over the entire cruise. The blue is the compositional fraction of POM, orange is the fraction of opal, yellow is the fraction of lithogenic, purple is $CaCO_3$, green is Fe oxyhydroxides and light blue is Mn oxides. (a)-(b): GA03; (c)-(d): GP16; (e)-(f): GN01.

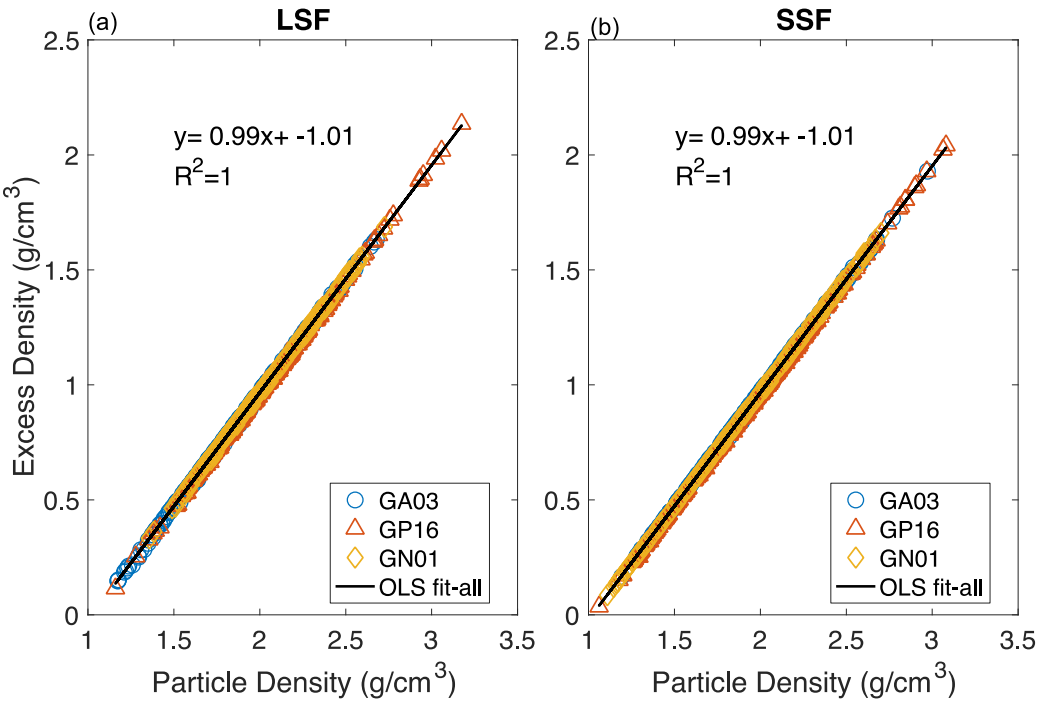

Appendix 3.4 Size-fractionated particle density (unit: g/cm^3) vs. excess density (unit: g/cm^3) in three cruises. (a): LSF; (b): SSF. The ordinary least square (OLS) fit is used in the regression. Regression equations are displayed in each panel.

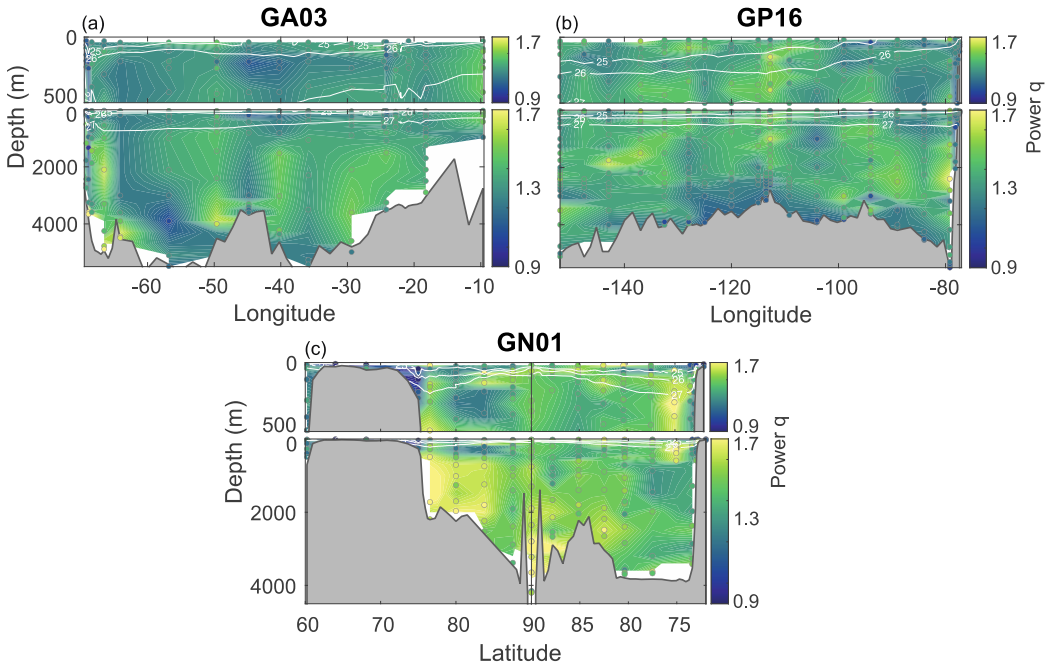

Appendix 3.5 The power exponent q of the mass-size spectra in three cruises. (a): GA03; (b): GP16; (c): GN01. The top panels in each subplot show the upper 500 m, and the lower panels show the entire water column. Thick white contours are potential density anomaly of 25, 26 and 27 kg/m^3.

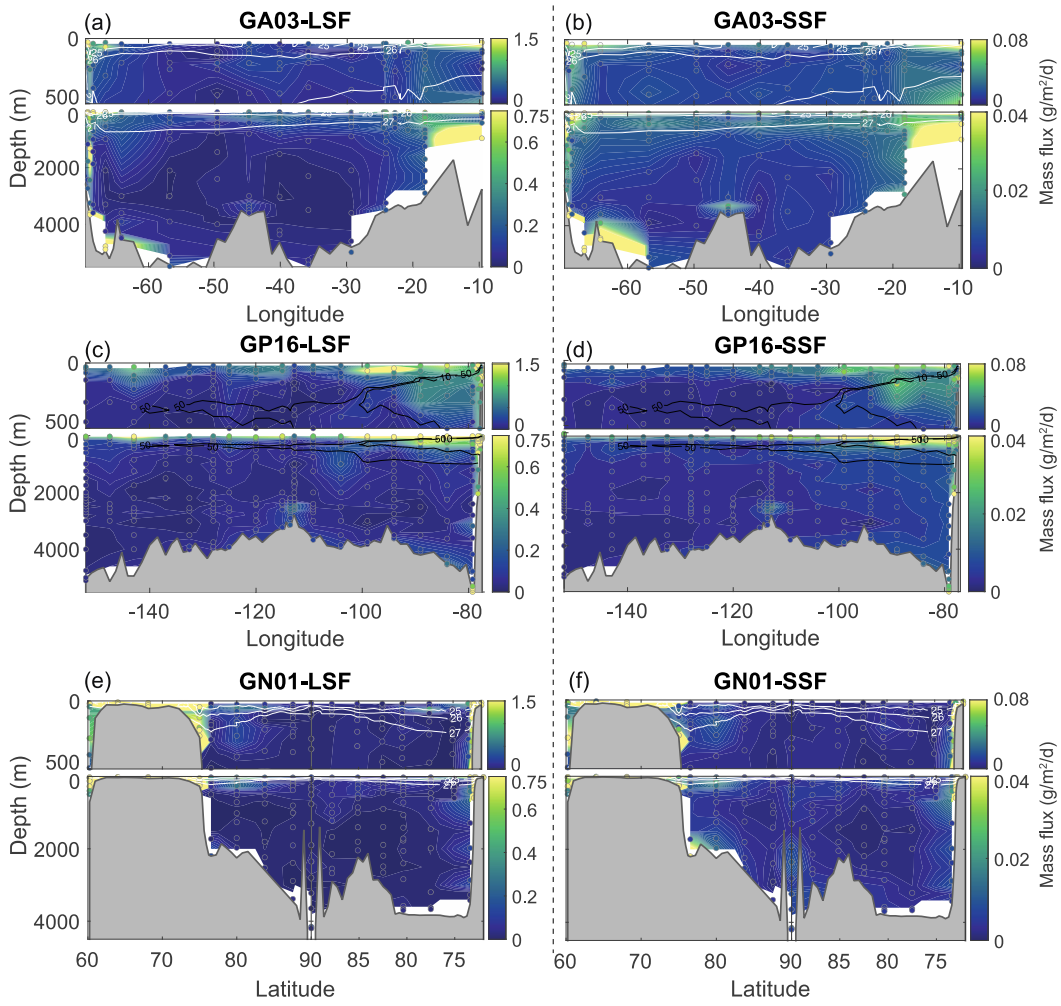

Appendix 3.6 Derived mass flux (unit: g/m^2/d) in the LSF (left panels) and SSF (right panels) in three cruises. (a): GA03 LSF; (b): GA03 SSF; (c): GP16 LSF; (d): GP16 SSF; (e): GN01 LSF; (f): GN01 SSF. Thick white contours are potential density anomaly of 25, 26 and 27 kg/m^3, and thick black contours in the GP16 are dissolved oxygen concentrations of 10 and 50 μmol/kg. Note that color scales are the same for each size fractions in all cruises but are different between the LSF and SSF, and between the upper 500 m and the entire water column.

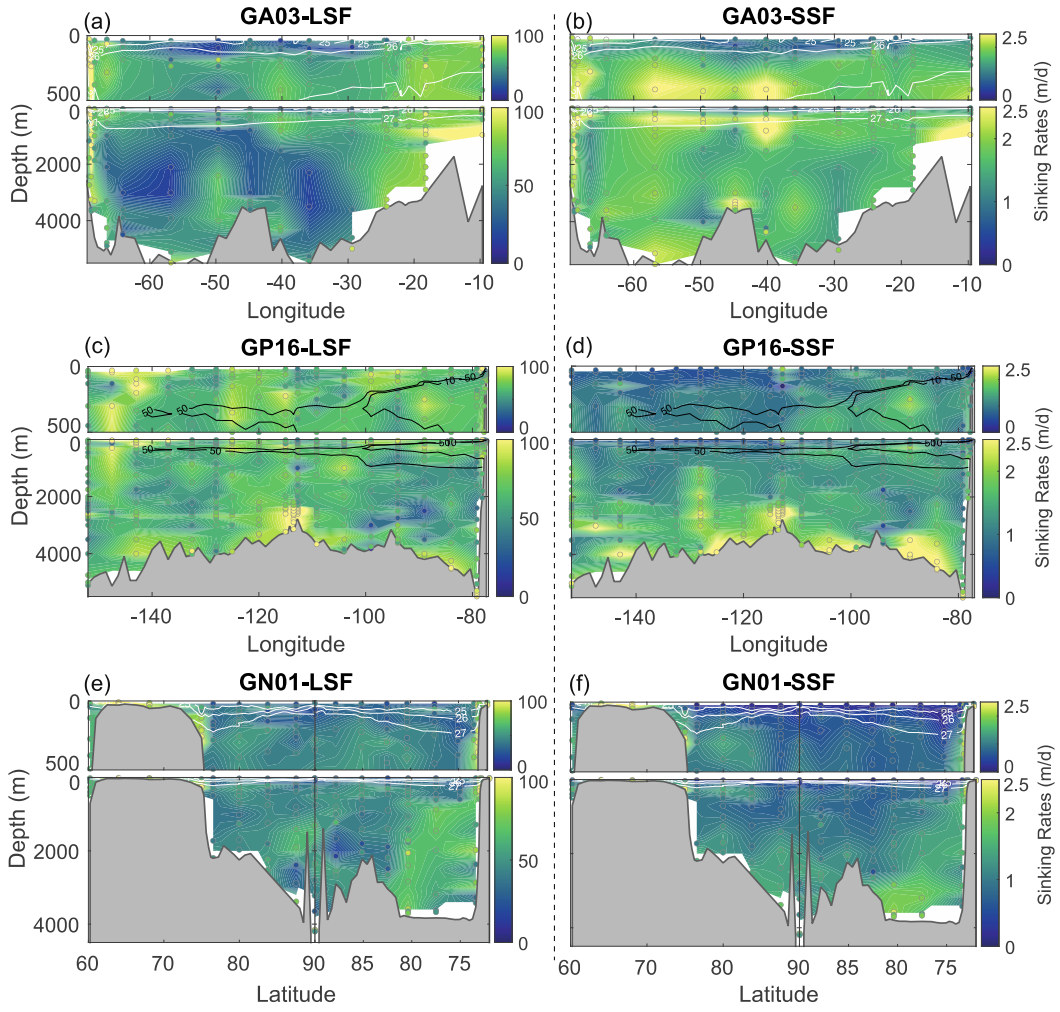

Appendix 3.7 Derived mass-weighted average sinking velocity (unit: m/d) in the LSF (left panels) and SSF (right panels) in three cruises. (a): GA03 LSF; (b): GA03 SSF; (c): GP16 LSF; (d): GP16 SSF; (e) GN01 LSF; (f): GN01 SSF. Contours as for Appendix 3.6.

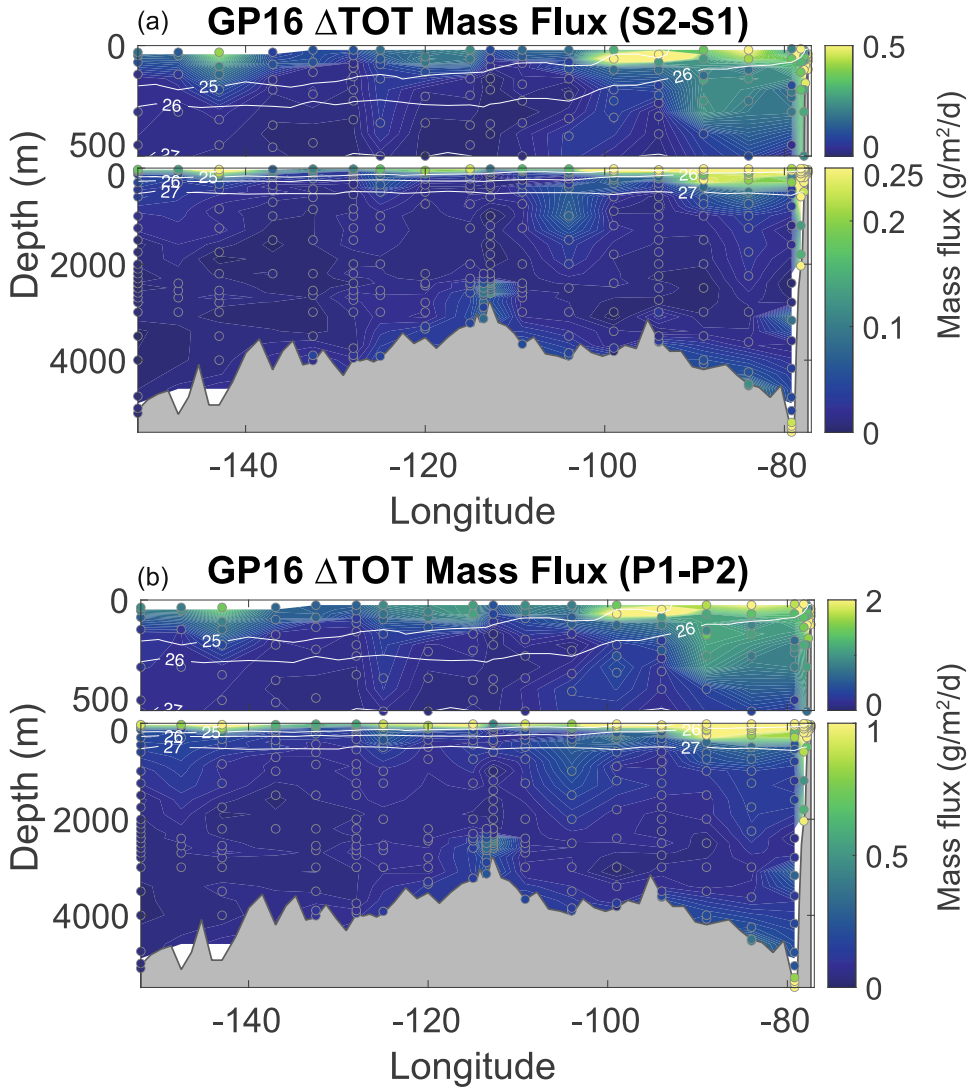

Appendix 3.8 Sensitivity studies. (a) the absolute differences in TOT mass flux between two upper size limits in the LSF (S2-S1), S2 as 10 mm and S1 as 5 mm; (b) the absolute differences in TOT mass flux between two porosity-size relationships (P1-P2), where P1 is the relationship from Alldredge & Gotschalk (1988) and P2 is the newly compiled one in this study. Note that (a) and (b), together with their upper (upper 500 m) and lower (the whole water column) panels, all have different color bars.

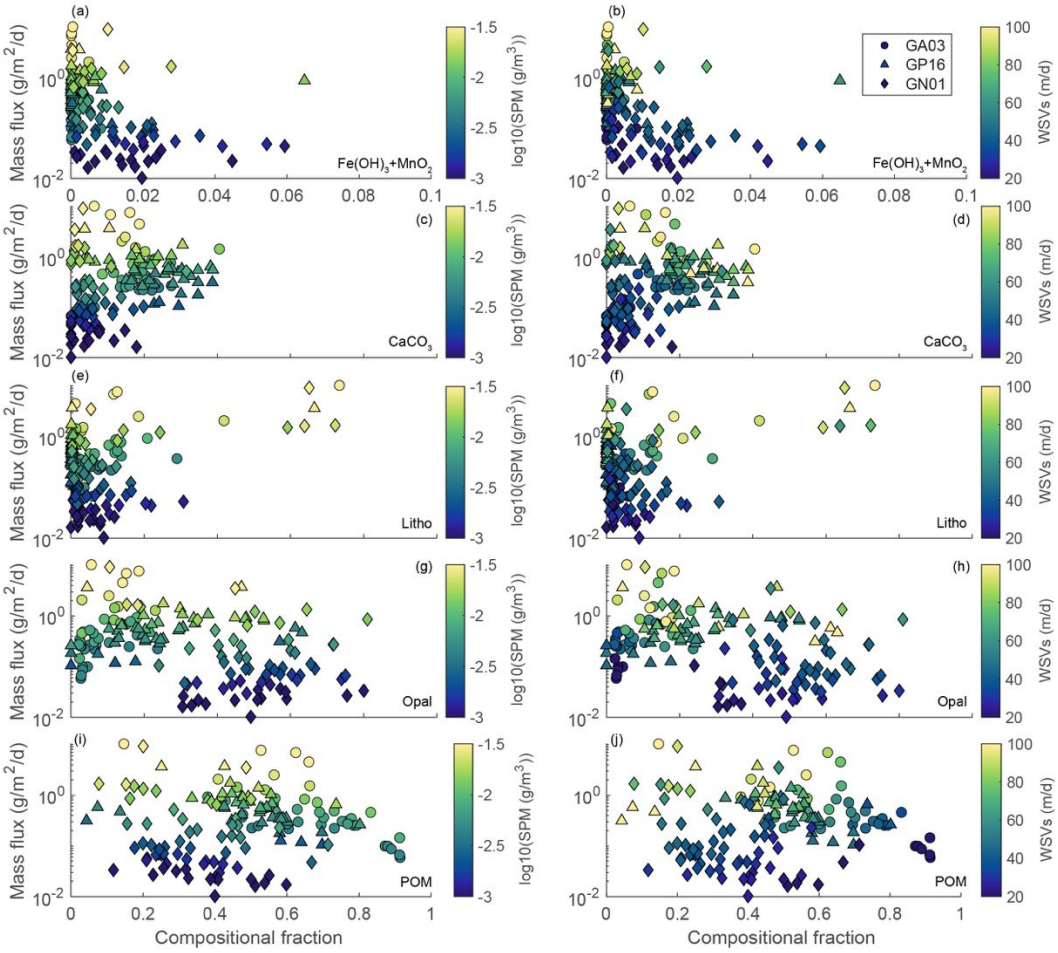

Appendix 3.9 Scatter plots between LSF compositional fractions and LSF mass flux in the upper 100 m of all non-shelf stations (bottom depth>200 m). The color bars are log10(SPM) on the left, and mass-weighted average sinking velocity (WSVs) on the right. Note that the color bar for SPM is in log scale. The first row of plots (a-b) are the compositional fractions of $Fe(OH)_3$+MnO_2, the second row (c-d) the fractions of $CaCO_3$, the third row (e-f) the fractions of Litho, the fourth row (g-h) the fractions of Opal, and the fifth row (i-j) the fraction of POM. The fractions of $Fe(OH)_3$+MnO_2 have different X scales (0-0.1) than other compositional fractions (0-1).

Appendix 3.10 Porosity-size Relationship Literature Compilation.

Sources	Size error (Y/N)	Porosity error (Y/N)	Particle Types	How	Size methods	Porosity methods	Data extraction method
Alldredge & Gotschalk, 1988[1]	N	N	Natural diatom & other marine snow	In situ SCUBA divers	Camera-based	Mass-based	Indirectly from Figure 2C
Logan & Alldredge, 1989[2]	N	Y	Natural diatom flocs	In situ SCUBA divers	Camera-based	Mass-based	Directly from Table 2
Lam & Bishop, 2007[3]	Y	N	Natural marine aggregates	In situ pump particles	UVP-based	Mass-based	Indirectly from Figure 14A & UVP PSD slopes
Ploug et al., 2008[4]	Y	Y	Various cultures, marine snow & fecal pellets	Lab roller tanks	Microscope-based	Mass-based	Directly from Table 1
Bach et al., 2016[5]	Y	N	Natural marine aggregates	In situ mesocosm	Camera-based	Mass-based	Personal comms
Ploug & Passow, 2007[6]	Y	Y	Diatom culture	Lab roller tanks	Microscope-based	Mass-based	Directly from Table 1
Engel et al., 2009[7]	Y	Y	*E. huxleyi* cultures	Lab roller tanks	Camera-based	Mass-based	Personal comms
Schmidt et al., 2014[8]	Y	Y	Diatom culture, coccoliths & foram tests	Lab roller tanks	Camera-based	Mass-based	Directly from text & indirectly from Figure 1B
Prairie et al., 2015[9]	Y	Y	Diatom cultures	Lab roller tanks	Microscope-based	Mass-based	Directly from Table 1 & 2
Iversen & Roberts, 2015[10]	N	N	<100 μm natural plankton	Lab roller tanks	Microscope-based	Mass-based	Personal comms
Laurencea u-Cornec et al., 2015[11]	N	N	Natural phytoplankton mixtures	Lab roller tanks	Camera-based	Mass-based	Personal comms
Laurencea u-Cornec et al., 2020[12]	Y	Y	Diatom cultures & zooplankton	Lab roller tanks	Microscope-based	Mass-based	Directly from Tables 2 & S1
Bach et al., 2019[13*]	Y	Y	Natural marine aggregates	In situ mesocosm	Camera-based	Optic-based	Directly from PANGAEA

*: The data from Bach et al. (2019) are not shown in Figure 3.2 in the main text, for it is optic-based and not calibrated with the mass-based method.

Appendix 3.11 Properties of Size Bins in the Model

Size bin	SSF			LSF		
	Size min (μm)	Size max (μm)	Center (μm)	Size min (μm)	Size max (μm)	Center (μm)
1	1.0	1.2	1.1	51.0	61.3	55.9
2	1.2	1.4	1.3	61.3	73.6	67.2
3	1.4	1.6	1.5	73.6	88.4	80.7
4	1.6	1.9	1.7	88.4	106.2	96.9
5	1.9	2.2	2.0	106.2	127.6	116.4
6	2.2	2.6	2.4	127.6	153.3	139.9
7	2.6	3.0	2.8	153.3	184.1	168.0
8	3.0	3.5	3.3	184.1	221.2	201.8
9	3.5	4.1	3.8	221.2	265.8	242.5
10	4.1	4.8	4.5	265.8	319.2	291.3
11	4.8	5.6	5.2	319.2	383.5	349.9
12	5.6	6.6	6.1	383.5	460.7	420.4
13	6.6	7.7	7.1	460.7	553.5	505.0
14	7.7	9.0	8.4	553.5	664.9	606.6
15	9.0	10.6	9.8	664.9	798.7	728.8
16	10.6	12.4	11.4	798.7	959.5	875.5
17	12.4	14.5	13.4	959.5	1152.7	1051.7
18	14.5	17.0	15.7	1152.7	1384.8	1263.4
19	17.0	19.8	18.3	1384.8	1663.5	1517.8
20	19.8	23.2	21.5	1663.5	1998.4	1823.3
21	23.2	27.2	25.1	1998.4	2400.7	2190.4
22	27.2	31.8	29.4	2400.7	2884.0	2631.3
23	31.8	37.2	34.4	2884.0	3464.6	3161.0
24	37.2	43.6	40.3	3464.6	4162.1	3797.4
25	43.6	51.0	47.1	4162.1	5000.0	4561.9